



**Bio-Mechatronic Implementation of a
Portable Upper Limb Rehabilitative Exoskeleton**

**Submitted By:
Mr Dasheek Naidu (BScEng, UKZN) – 207504291**

**Supervisors:
Dr Riaan Stopforth
Prof Glen Bright
Mr Shaniel Davrajh**

November 2011

Submitted in fulfilment of the academic requirements for the degree of Master of Science in Engineering at the School of Mechanical Engineering, University of KwaZulu-Natal.

Declaration

Declaration by Author

I, Dasheek Naidu, declare that

- (i) The research reported in this dissertation, except otherwise indicated, is my original work.
- (ii) This dissertation has not been submitted for any other degree or examination at any other university.
- (iii) This dissertation does not contain other persons' data, pictures, graphs or other information, unless specifically acknowledged as being sourced from other persons.
- (iv) This dissertation does not contain other persons' writing, unless specifically acknowledged as being sourced from other researchers. Where other written sources have been quoted then:
 - a) their words have been rewritten but the general information attributed to them has been referenced;
 - b) where their exact words have been used, their writing has been placed inside quotation marks, and referenced.
- (v) Where I have reproduced a publication of which I am an author, co-author, or editor, I have indicated in detail which part of the publication was written by myself alone and have fully referenced such publications.
- (vi) This dissertation does not contain text, graphics, or tables copied and pasted from the Internet, unless specifically acknowledged, and the source being detailed in the dissertation and in the References sections.

Signed: _____ Date: _____

Mr. Dasheek Naidu

Acknowledgments

Firstly I would like to thank God for giving me the strength and knowledge required to complete this research. I would like to acknowledge the love and support from my parents Robin and Usha and my brother Soshen without you all this would have not been possible, you guys are truly amazing.

I would like to thank my supervisors Prof Glen Bright, Dr Riaan Stopforth and Mr Shaniel Davrajh for their expertise and efforts. Special thanks to Professor Glen Bright for his constant motivation and enthusiastic approach to life. Your positivity, advice, direction and expertise have been invaluable in my research and life, thank you.

I would like to acknowledge all the staff of the School of Mechanical Engineering for the support and guidance they have provided. I would like to thank Ms Wendy Janssens, Mrs Kogie Naiker and Mrs Ooma Chetty for the administrative support they provided. I would like to thank Mr Danesh Singh and the rest of the workshop staff for their commitment in manufacturing the mechanical design.

I would also like to thank Dr Richard Loubser for his assistance and analysis with the kinematics of this research as well as overall opinions with the design.

I would like to acknowledge the final year project group 2 for their assistance with my research platform. I would like to thank my colleagues and friends: Mr Niven Raman, Mr Neolen Pillay, Mr Onashan Pillay, Ms Leeanne Elaine Sukhdeo, Mr Calvin Cunniffe, Ms Fiona Leverone, Mr Mike Pillay, Mrs Ooma Chetty, Mr Yogandra Naidu, Mr Yogianandh Naidoo, Mr Roland Dixon, Mr James Collins and Mr Jared Padayachee. You all have assisted me in my research in various ways and I would like to thank you for your motivation and advice. Special thanks to my friend Neolen Pillay who assisted me throughout my research with support and assistance.

Abstract

The rationale behind this research originates from the lack of public health care in South Africa. There is an escalation in the number of stroke victims which is a consequence of the increase in hypertension in this urbanising society. This increase results in a growing need for physiotherapists and occupational therapists in this country which is further hindered by the division between urban and rural areas. The exoskeleton device has been formulated to encapsulate methodologies that enable the anthropomorphic integration between a biological and mechatronic limb.

The physiotherapeutic mechanism was designed to be portable and adjustable, without limiting the spherical motion and workspace of the human arm. The exoskeleton was portable in the sense that it could be transported geographically and is a complete device allowing for motion in the shoulder, elbow, wrist and hand joints. The avoidance of singularities in the workspace required the implementation of non-orthogonal joints which produces extensive forward kinematics.

Traditional geometric or analytical derivations of the inverse kinematics are complicated by the non-orthogonal layout. This hindrance was resolved iteratively via the Damped Least Squares method. The electronic and computer system allowed for professional personnel, such as an occupational therapist or a physiotherapist, to either change an individual joint or a combination of joints angles. A ramp PI controller was established to provide a smooth response in order to simulate the passive therapy motion.

Table of Contents

1	Introduction.....	1
1.1	Physical Therapy Challenges in South Africa	1
1.2	Bio-Mechatronics.....	2
1.3	Motivation for Research.....	3
1.4	Research Objectives for the Exoskeleton device	4
1.5	Research Outcomes.....	5
1.6	Research Specifications	5
1.6.1	Safety requirements.....	6
1.6.2	Portability.....	6
1.6.3	Functional performance requirements.....	6
1.6.4	Adjustability.....	6
1.7	Research Contribution.....	7
1.8	Methodology Overview	7
1.9	Research Publications	8
1.10	Chapters of this Dissertation	9
1.11	Chapter Summary	9
2	Exoskeleton Literature Research	10
2.1	Introduction.....	10
2.2	The Upper Limb Anatomy and Kinematic Movements.....	10
2.2.1	Therapeutic Exercises	16
2.3	Previous Work in Exoskeletons	17
2.3.1	Existing Exoskeletons Movements and Descriptions	17
2.3.2	Exoskeleton Actuation	26
2.4	Chapter Summary	26
3	Mechanical Design.....	28
3.1	Introduction.....	28

Table of Contents

3.2	Shoulder Spherical Mechanism	29
3.2.1	Shoulder Spherical Motion	29
3.2.2	Shoulder Conceptual Designs	31
3.2.3	Shoulder Concept Selection	35
3.2.4	Exoskeleton Shoulder Joint Limits	37
3.2.5	Physical Configuration.....	39
3.2.6	Material and Link Structure	42
3.2.7	Actuators	44
3.2.8	Joints	47
3.2.9	Final Shoulder Design.....	48
3.3	The Wrist and Hand Mechanism	49
3.3.1	The Wrist Mechanism.....	50
3.3.2	Parameter analysis.....	51
3.3.3	The Hand Mechanism	53
3.4	Construction Overview	56
3.4.1	Shoulder Construction Overview	56
3.4.2	Wrist and Hand Construction Overview	58
3.4.3	User Interface and Final Prototype.	61
3.5	Chapter Summary	63
4	Exoskeleton Kinematic Models	64
4.1	Introduction.....	64
4.1.1	Kinematic Redundancy	65
4.1.2	Kinematic Model Relationship	66
4.2	Redundant Kinematic Model	66
4.2.1	Forward Kinematics.....	67
4.2.2	Inverse Kinematics.....	75

Table of Contents

4.2.3	Kinematic results.....	80
4.3	Non-Redundant Model.....	86
4.3.1	Forward Kinematics.....	86
4.3.2	Inverse Kinematics.....	89
4.4	Kinematic Error	93
4.5	Chapter Summary	94
5	Exoskeleton Electronic System.....	95
5.1	Exoskeleton Electronic Design Consideration.....	95
5.2	Exoskeleton Electronic Control System	95
5.3	Actuation Control Module	96
5.3.1	Microcontroller	97
5.3.2	Half-Bridge Motor Drivers	98
5.3.3	USB communication.....	101
5.3.4	Encoder sensor	101
5.3.5	Power Supply	102
5.3.6	Wiring	103
5.4	Chapter Summary	104
6	Exoskeleton Software System.....	105
6.1	Software Design Considerations.....	105
6.2	Graphical User Interface (GUI)	105
6.2.1	GUI operation	106
6.3	The Microcontroller	110
6.3.1	Receiving the Serial Protocol Data Packet.....	111
6.3.2	Processing Encoder Pulses.....	111
6.4	Chapter Summary	121
7	Exoskeleton Testing and Discussion.....	122

Table of Contents

7.1	Introduction.....	122
7.2	Manipulators Workspace	122
7.3	Load Tests.....	126
7.3.1	Shoulder and Elbow Test.....	126
7.3.2	Wrist Load Test.....	130
7.4	The Hand Mechanism	132
7.5	Positional Test.....	132
7.6	Encoder Testing	135
7.7	Protocol Adjustments.....	137
7.8	Stand Adjustability and Portability	138
7.9	Control Revision	139
7.10	Cost Break Down.....	140
7.11	Chapter Summary	140
8	Exoskeleton Research Conclusion.....	142
9	References.....	146
A.	Appendix.....	149
	Appendix A.1: Shoulder Conceptual 2 Design.....	149
	Appendix A.2: Lateral and Medial Rotation and Link 2's Length.	150
	Appendix A.3: Torque, Force and Deflection Calculations.....	152
	Deflection.....	153
	Torque.....	154
	Force	155
	Appendix A.4: Link Structure.....	155
	Stress Calculations.....	157
	Appendix A.4 – Doga Motor Catalogues.....	159
	Appendix A.5: Wrist Conceptual Designs.....	163

Table of Contents

Appendix A.6: C-gear Fatigue and Safety Factor Calculations.....	166
B. Appendix.....	168
Appendix B.1: Complex Jacobian Matrix and Positional Vector	168
Positional Vector.....	168
Jacobian Matrix.....	169
Appendix B.2: Matlab workspace code.	172
Appendix B.3: Calculation of the joint limited damping factor.....	174
Appendix B.4: Comparison between JLDLS and DLS methods	175
C. Appendix.....	176
Appendix C.1: Schematics of the ATmega 1280 and Arduino Board.	176
Appendix C.2: H-bridge Information.....	178
Appendix C.3: Schematic of the FT232.....	180
D. Appendix.....	181
Appendix D.1: Sample of the GUI code	181
Appendix D.2: Protocol Retrieval of the Microcontroller	185
Appendix D.3: C-Code of the Physiotherapy Ramp Control.....	186
Appendix D.4: Sample C-code	188
Appendix D.5: Arduino Board and Pin Layout	190
E. Appendix.....	192
Appendix E.1: Chauvenet's Criterion Sample Calculation for Encoder 4 Test.....	192

List of Acronyms and Abbreviations

GH- Glenohumeral Joint

MGA- Maryland Georgetown Army

ARMin II's- Arm Therapy in Strokes

PROM- Passive Range of motion

ADL- Activities of Daily Living

DOF- Degrees of Freedom

ROM- Range of Motion

CAD- Computer Aided Drawing

RPS- Revolute Prismatic Spherical

DC- Direct Current

UDL- Uniformly Distributed Load

HIS- Human Isometric Strength

FE- Finite Element

CNC- Computer Numerical Control

PCD- Pitch Circle Diameter

D-H- Denavit Hartenberg

DLS- Damped Least Squares

JLDLS- Joint Limited Damped Least Squares

Inv- Inverse

ACM- Actuation Control Module

PC- Personal Computer

List of Acronyms and Abbreviations

USB- Universal Serial Bus

H-bridge- Half Bridge

MIPS- Million Instructions Per Second

USART- Universal Synchronous/Asynchronous Receiver/Transmitter

ICSP- In-Circuit Serial Programmer

PCBs- Printed Circuit Boards

I/O- Input/Output

PWM- Pulse Width Modulation

PCB- Printed Circuit Board

GUI- Graphics User Interface

RO- Robotic One-way

PID- Proportional Integral Derivative

OCR- Output Compare Register

Nomenclature

a_i - link length

$c\vartheta_i$ - cosine(ϑ_i)

d_i - link length

$D(\lambda)$ - diagonal damping matrix

e - error vector

F- force

f_{clk} - clock frequency

f_{PWM} - PWM frequency

F_t- tangential force

I- identity matrix

I_{major} – moment about major axis

I_{minor} – moment about minor axis

I_{rect} – moment of inertia for a rectangle

J- Jacobian matrix

J- geometry

J^{-} - inverse jacobian

J^T - Jacobian transpose

K_d - derivative gain

K_i - integral gain

K_m - load distribution

K_o - overload factor

Nomenclature

K_p - proportional gain

K_v – dynamic factor

L1- length from GH joint to elbow joint

L3- length of GH to centre of end-effector

m- number of DOF in the joint space

n- number of DOF that correspond to the task space

N- number of DOF, pre-scalar value

p- exponential factor affecting motion range

S- positional vector

$s\vartheta_i$ - sine(ϑ_i)

T- Transformation matrix

TOP- highest PWM value

w_i - weighting factor of joint i

X0- X axis of base point

Z0- Z axis of base point

α_i - twist angle

$\Delta\vartheta$ - change in joint angle

δ_B - deflection in y direction

ϑ_i – mechanical joint value for joint i, kinematic joint value for joint i

ϑ_{max} – maximum kinematic joint limit

ϑ_{min} – minimum kinematic joint limit

Nomenclature

λ - damping factor

ρ - position vector

σ_b – bending stress

τ - torque

v - velocity

List of Figures

Figure 1.1: Graphical representation of a mechatronic system.....	2
Figure 1.2: Graphical representation of a bio-mechatronic system.	3
Figure 1.3: Sequence of Operations for Mechatronic Design Process.....	8
Figure 2.1: Graphical Representation of the Upper Limb Anatomy.....	11
Figure 2.2: Graphic representation of the human body motion planes.	12
Figure 2.3: (a) Posterior and (b) anterior views of the right radius and ulna.	14
Figure 2.4: Diagram illustrating the carry angle between the forearm and upper arm	15
Figure 2.5: Picture illustrating the 7 DOF in the upper arm	16
Figure 2.6: CAD drawing of the CADEN-7	20
Figure 2.7: Picture of the L-EXOS exoskeleton	21
Figure 2.8: Picture of the MAHI exoskeleton	22
Figure 2.9: CAD of the MGA exoskeleton design	23
Figure 2.10: CAD of ARMin II's elbow to hand support.....	24
Figure 3.1: Graphic illustrating a systematic integration of the joints (numbered circles), together with the number of DOF (arrows).....	28
Figure 3.2: Graphic representing the three joint axes, angles and the tool tip direction.....	30
Figure 3.3: Graphical representation of the spherical motion.....	31
Figure 3.4: CAD of the MGA, prototype I.	32
Figure 3.5: CAD of Concept One.	33
Figure 3.6: MGA's final shoulder mechanism Prototype IV	33
Figure 3.7: CAD of Concept Three.....	35
Figure 3.8: CAD of Shoulder and Elbow Conceptual Design on a Model of a Human Arm.....	37
Figure 3.9: CAD. of Maximum angle at joint 1.....	38
Figure 3.10 CAD of Maximum Joint 2 Angle	38
Figure 3.11: CAD of Maximum Angle of Joint 3.....	39
Figure 3.12: CAD Illustrating the Load on the Joints, in Worst Case Pose.....	40
Figure 3.13: Simplified Force Diagram of Upper Limb in Worst Case Pose	42
Figure 3.14: Physical Properties of Aluminium Compared With Other Common Materials	43
Figure 3.15: CAD Illustrating the Various Components to the Joint Design.	48
Figure 3.16: CAD of final shoulder and elbow mechanism.....	49
Figure 3.17: Spur gear concept- view one	51
Figure 3.18: Deflection analysis of the C-gear.	52
Figure 3.19: Stress analysis of the C-gear.....	52

List of Figures

Figure 3.20: Final Prototype design of the Hand mechanism.....	54
Figure 3.21: Stress analysis of the hand mechanism.....	55
Figure 3.22: Deflection analysis of the hand mechanism	56
Figure 3.23: (a) Final construction of link 1, (b) and a complete assembly of joint 1.....	57
Figure 3.24: Final construction of link 3a/b.....	57
Figure 3.25: Manufactured forearm link (link 4a/b/c).	58
Figure 3.26: (a) Pictures of the manufactured spur pinion gear, (b) C-gear, (c) and gear encasement with assembled components.	59
Figure 3.27: Picture of final machined key.....	59
Figure 3.28: (a) Picture illustrating the sheet metal pieces, (b) the grid for the fingers, (c) and the servo mounts.....	60
Figure 3.29: Picture of the complete hand mechanism.	61
Figure 3.30: Final exoskeleton prototype mechanism with stand support.	62
Figure 4.1: Kinematic joint schematic derived from final mechanical design and illustrates joint X and Z axes.	70
Figure 4.2: CAD of mechanical manipulator with respective Z axes.	71
Figure 4.3: The respective joint axes and origins	72
Figure 4.4: CAD Illustrating the Lengths at the Initial Position.	73
Figure 4.5: Achievable workspace of the exoskeleton arm.	74
Figure 4.6: Flowchart illustrating the iteration process of the DLS method.....	78
Figure 4.7: Damping factor curve for motion range of a joint. $\vartheta_{max}= 900$ and $\vartheta_{min} = -900$	80
Figure 4.8: Graph of the minimization of the X, Y and Z error values, against the number of iterations.	81
Figure 4.9: Graph illustrating the stabilisation of the joint angle values.	82
Figure 4.10: Graph illustrating the change in X, Y and Z positions of the end-effector in relation to the iteration count.	83
Figure 4.11: 3-D Kinematic trajectory of the end-effector position from initial position (green circle) to end position (red circle) illustrating the linear relationship produced by the DLS method.	84
Figure 4.12: Y-Z plane of position trajectory.	85
Figure 4.13: Kinematic schematic of the non-redundant model.....	87
Figure 4.14: Fundamental spherical motion produced by the shoulder mechanism.	89

List of Figures

Figure 4.15: Graph of the minimization of the X, Y and Z error values, against the number of iterations.....	90
Figure 4.16: Graph illustrating the stabilisation of the joint angle values.	91
Figure 4.17: Graph illustrating the change in X, Y and Z positions of the end-effector in relation to the iteration count.	92
Figure 4.18: Kinematic trajectory of the end-effector position from initial position (green circle) to end position (red circle) illustrating the linear relationship produced by the DLS method.	93
Figure 4.19: Flow Diagram of the Error Calculation between the Inverse and Forward Kinematic Models.	93
Figure 5.1: Basic overall exoskeleton electronic architecture.	96
Figure 5.2: Interaction of the actuation control module with the PC.....	97
Figure 5.3: Arduino board with integrated microcontroller and electronic interfacing.	98
Figure 5.4: Picture of the Pololu motor driver.	99
Figure 5.5: Picture of the Elechouse 50A motor driver.	100
Figure 5.6: (a) Top view of FT232 with access to USB communication, (b) bottom view illustrating actual FT232 chip.	101
Figure 5.7: (a) The two channel HEDS 5701 G00 encoder, (b) mounted onto the Doga Motor.	102
Figure 5.8: Diagrammatic layout of the power supply unit.	103
Figure 5.9: Picture illustrating the wire routing.	104
Figure 6.1: GUI Implemented in this Research.	106
Figure 6.2: Sample Protocol Data Packet for the above described values.	108
Figure 6.3: Flowchart illustrated the GUI processes with the Microcontroller,	110
Figure 6.4: Closed loop relationship between the GUI, microcontroller and other components of this research.	112
Figure 6.5: Graph Representing the Step Input.....	113
Figure 6.6: Graph Representing the Different Responses for Different Kp Gains.	114
Figure 6.7: Graph Representing the Different Responses for Different Ki Gains (Kp=5).	115
Figure 6.8: Graph Representing the Different Responses for Different Kd Gains (Kp=5 and Ki=0.2).	116
Figure 6.9: Graph Illustrating the Chosen PID Response.....	117
Figure 6.10: Graph Comparing the PID Theoretical and Practical Responses	118
Figure 6.11: Graph Illustrating the Ramp Input.....	119

List of Figures

Figure 6.12: Graph Comparison Between the Step and Ramp Response.	119
Figure 7.1: (a) Shoulder Abduction, (b) shoulder Flexion.	123
Figure 7.2: (a) Shoulder extension, (b) elbow flexion.	123
Figure 7.3: (a) Shoulder lateral rotation, (b) medial rotation.	124
Figure 7.4: (a) Wrist supination, (b) pronation.	124
Figure 7.5: (a) Shoulder flexion of 3 kg, (b) 5 kg mass.	126
Figure 7.6: Elbow flexion of 5 kg mass.	127
Figure 7.7: Graph of Time vs Mass for the Shoulder Joint.	128
Figure 7.8: Graph of Time vs Mass for the Elbow Joint.	130
Figure 7.9: Illustration of Placement of the Load on the C-gear.	130
Figure 7.10: Graph of Time vs Mass for the Wrist Motor.	132
Figure 7.11: X-Z plane of the Exoskeleton.	133
Figure 7.12: Y-Z Plane of the Exoskeleton.	134
Figure 7.13: Final Protocol Data Packet.	137
Figure 7.14: Stand Adjustability Allows for Variation in Height.	138
Figure 7.15: Comparison between Experimental Step and Ramp Responses.	139
Figure A.1: CAD of Concept Two.	149
Figure A.2: C.A.D illustrating maximum medial rotation for link 2 angle length = 45°, 60°, 75°, 90° at 90° abduction.	151
Figure A.3: CAD illustrating maximum lateral rotation for link 2 angle length = 45°, 60°, 75°, 90° at 90° abduction.	151
Figure A.4: Simplified Force Diagram of Upper Limb in Worst Case Pose.	152
Figure A.5: Torque and Force Calculation Spreadsheet.	152
Figure A.6: C-Section Dimensions.	156
Figure A.7: CAD of the Wrists Mechanism's Concept 1.	163
Figure A.8: CAD of the Wrists Mechanism's Concept 2.	164
Figure A.9: CAD of the Wrists Mechanism's Concept 3.	164
Figure C.1: Schematic of the AtMega1280 microcontroller.	176
Figure C.2: Schematic relationship between the AtMega1280 microcontroller and the arduino inputs and outputs.	177
Figure C.3: Pololu H-bridge input and output ports.	178
Figure C.4: Dual H-bridge input and output ports.	179
Figure C.5: Schematic diagram of the FT232 PCB.	180

Figure D.1: Arduino Mega 1280 Board 190

List of Tables

Table 2.1: Joint Movement in Degrees.....	18
Table 2.2: Location of Motion of Certain Exoskeletons Adapted from.....	25
Table 3.1: Advantages vs Disadvantages of the different designs.....	36
Table 3.2: Table of Comparison of the different designs.....	36
Table 3.3: Approximate Weight, Centre of Mass and Length of Large Male	42
Table 3.4: Human Isometric Strength.....	45
Table 3.5: Total Torque Requirements for Each Motor (Nm).....	46
Table 3.6: Doga Motors Selection Matrix	46
Table 3.7: Final Motor Selection	47
Table 4.1: Denavit-Hartenberg Parameter for final design.....	68
Table 4.2: Denavit-Hartenberg Parameter for final design without the elbow mechanism.....	87
Table 7.1: Comparison of Joint Movement in Degrees.....	125
Table 7.2: Test Values of Shoulder Joint Loads against Time.....	128
Table 7.3: Test Values of Elbow Joint Loads against Time.....	129
Table 7.4: Test Values of Wrist Joint Loads against Time.....	131
Table 7.5: Encoder Test Values.....	135
Table 7.6: Chauvenet's Criterion for Different Number of Measurements.....	136
Table 7.7: Cost Break Down for the Research.....	140
Table A.A.1: Moment of Area Calculator – C-section.....	156
Table A.A.2: Moment of Area Calculator – Solid Section.....	157
Table A.A.3: Concept selection matrix.....	165
Table B.B.1: Comparison of joint limited DLS and original DLS methods.....	175
Table C.C.1: Truth table for the Pololu H-bridge.....	178
Table C.C.2: Truth table for the Dual H-bridge.....	179
Table D.1: Pin Layout for this Research Exoskeleton Design.....	191
Table E.1: Chauvenet's Criterion Test for Encoder 4.....	192

1 Introduction

1.1 Physical Therapy Challenges in South Africa

The rationale behind this research originates from the need of improvement in South African health care services, in terms of rehabilitation. South Africa consists of a population of an approximate total of 49.9 million individuals with a rural population of approximately 25.95 million people. Only 9 million individuals have access to private or insurance funded care, the remaining 40.9 million can only afford care provided by the public sector [1]. The private sector is well served by 53 and 30 physiotherapists and occupational therapists respectively, per 100 000 people, as compared to 2.5 physiotherapists and 2.0 occupational therapists per 100 000 people in the public sector [1]. This shocking fact proves that there is a great need for an increase in rehabilitation in the public sector of South Africa. Therefore this research will allow for less skilled physiotherapists or occupational therapists to assist in the rehabilitation of the upper limb, resulting in an increase in public sector rehabilitation.

An exoskeleton arm is an external mechanical structure which has joints that correspond to the human arm. This correspondence allows for the transfer of mechanical power to the biological upper limb [2]. Such a device can be used to provide repeatability and anthropomorphic motion which will assist the rehabilitation process of injured upper limb individuals [3]. Rehabilitation exoskeletons can be classified into three groups which includes [4]:

- To assist disabled individuals with their daily activities
- To support mobility
- To assist therapy by providing mobility and therapeutic exercise.

The exoskeleton in this design was used to provide physiotherapeutic exercise. Literature research could not yield an exoskeleton upper limb specifically built for physiotherapy in South Africa. This demographic is important as poverty, health-care and the division between rural and urban areas are at large in South Africa. Traditional state of the art rehabilitation robots are bulky and consist of advanced actuation which results in high production costs. Their bulkiness limits geographic portability which would be useful for transportation from urban to rural South Africa as well as a joint layout which minimises the performance in terms of achievable workspace. It was therefore decided to design a prototype exoskeleton device that will assist in rehabilitation in South Africa; such an exoskeleton will result in a Bio-Mechatronic system.

1.2 Bio-Mechatronics

Mechatronics is the integration of mechanical engineering, electronic engineering and computer engineering. A representation of this combination of disciplines can be seen in Figure 1.1. This integration produces better system versatility, the capability to perform autonomous data receiving and transmission, and easier manipulations in terms of design and programming [5].

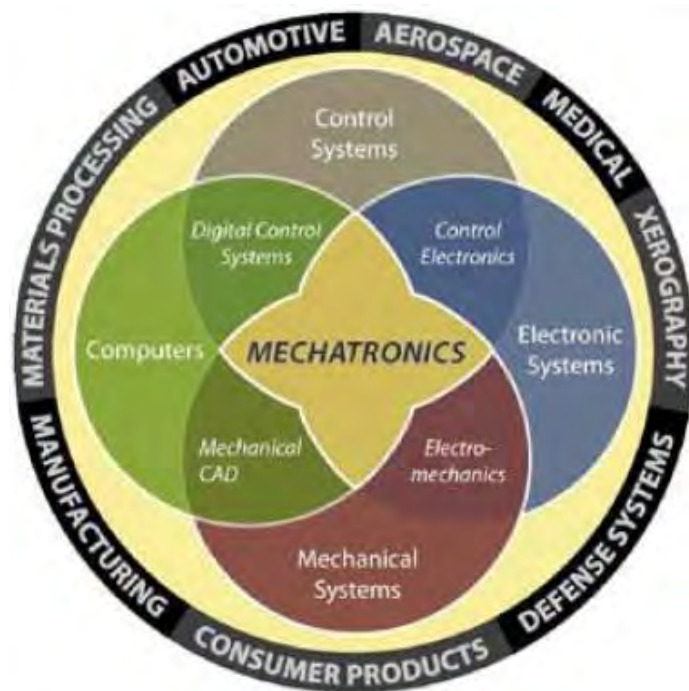


Figure 1.1: Graphical representation of a mechatronic system [6].

Mechatronics is an essential concept in the progress of this research as bio-mechatronics may be considered as an expansion to mechatronic engineering. Thus bio-mechatronics deals with the development of mechatronic engineering through bio-inspired designs; as well as the interaction of mechatronic systems with biological systems, e.g. the interaction of an exoskeleton arm with the human body [7]. An illustration of a bio-mechatronic system can be seen in Figure 1.2.

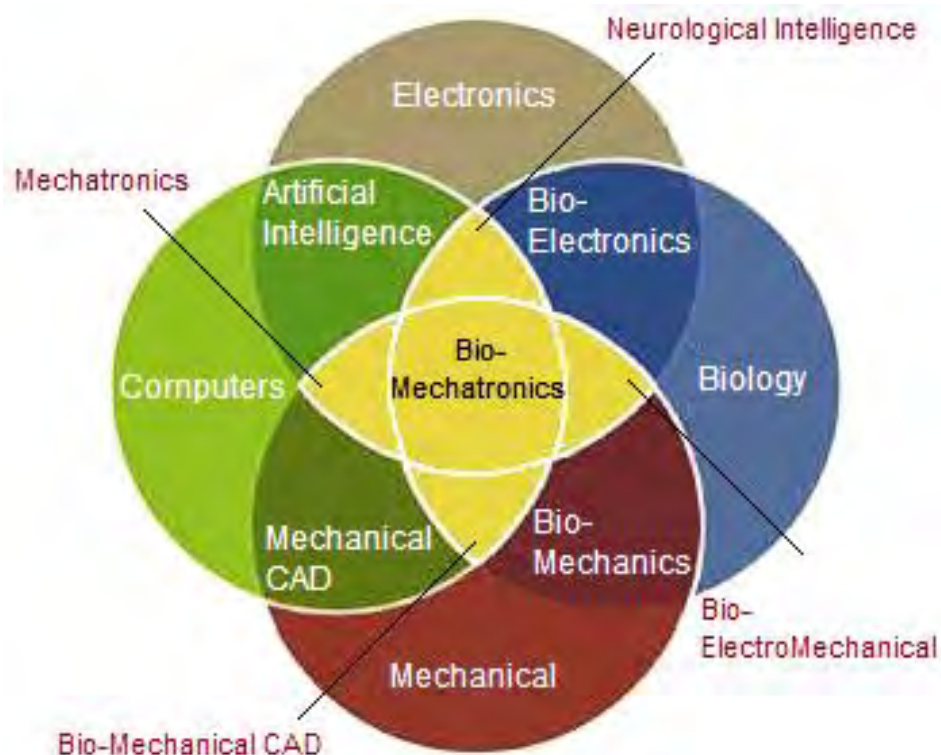


Figure 1.2: Graphical representation of a bio-mechatronic system.

1.3 Motivation for Research

Strokes are a leading cause of disability and death in developing countries, a study done by the Global Burden of Disease reveals that 80% of stroke fatalities arises in the low and middle income regions of a population [8]. This financial fact results in a high stroke rate in South Africa; as there is a minority of upper class individuals in the country. South Africa is experiencing a swift development into an urban society with strokes accounting for 6.5% of all deaths in the year of 2000 [8] [9]. This illness was the third most common cause of death in South Africa in year 2000 after HIV/AIDS and ischaemic heart disease [9]. In Africa, an individual's health is directly linked to their socio-economic standing and urbanisation [8]. Such development is directly related to an increase in hypertension which is the most influential and constant risk factor contributing to strokes with 71% of stroke victims in South Africa, having experienced hypertension [10] [11]. This increase in hypertension means that there will be an increase in strokes in the following years in South Africa, hence resulting in more disabled individuals as result of strokes. Approximately 55%-65% of these victims experience motor deficiency in their upper limb [12]. Such disabilities include spastic hemiparesis and shoulder subluxation. Spastic hemiparesis is the altered performance of muscle tone also known

as 'tightness of the muscle' and occurs in 39% of first stroke patients after 12 months [13]. Shoulder subluxation is medically defined as less than a dislocation and reported incidences reveal that up to 81% of stroke victims experience shoulder subluxation [14]. This side effect of stroke occurs when the muscle structure around the Glenohumeral (GH) joint weakens [15]. Shoulder pain is experienced by up to 40% of stroke victims as well as those patients which experience shoulder subluxation [16] [17]. An exoskeleton arm can accelerate the rehabilitation process by providing repeatability and accuracy. Clinical trials have proven that passive robotic therapy results in improved rehabilitation in the shoulder and elbow motion of spastic hemiparesis patients as compared to traditional physiotherapy [3]. Passive therapy is the movement of a limb segment created completely by an external force; it is a non-restrictive motion and will be implemented in this research. Previous studies also revealed that robotic exercises can improve upper limb motor functions in the chronic stage, post stroke [3]. Griffin and Reddin [17] stated that spasticity may result to shoulder subluxation and shoulder pain, therefore robotic rehabilitation may prevent shoulder subluxation and shoulder pains. Such statistics illustrate that there is a need for improvement in rehabilitation in South Africa and this is with regards to stroke alone, other injuries such as broken bones from everyday activities may increase the demand for physiotherapy.

An orthopaedic surgeon, Doctor S. Osman who practices at Life Entabeni Hospital in Durban, was consulted. Dr Osman explained that such an exoskeleton will be beneficial during post-operative rehabilitation for stroke victims. The reason being is that it is essential not to stretch the muscles during post-operative rehabilitation as this may result in further injury. Passive therapy will achieve mobility in the joints but not cause any stretching of the muscles [18]. The orthopaedic surgeon also explained that isometric rehabilitation can be achieved on such an exoskeleton device. Isometric rehabilitation is when the patient applies a force on a stationary object. This rehabilitation can be achieved by requesting the patient to apply a force on the stationary exoskeleton arm. Dr Osman explained that isometric rehabilitation will be beneficial at later stages of post-operative rehabilitation as these exercises will create tension in the muscles.

From the above described research and consultation it is evident that a physiotherapeutic exoskeleton will be beneficial to the South African society.

1.4 Research Objectives for the Exoskeleton device

The objectives of this research paper were:

- To research the mechanical operation of the biological arm.

- To research, design and develop an exoskeleton arm that had similar mechanical properties to those of a biological arm.
- Research and develop the kinematic models for the movement of the arm and integrate it with feedback control.
- Research, develop and integrate the models with electronic modules.
- Test the exoskeleton and validate the specifications.

1.5 Research Outcomes

The following outcomes were as a result of the topics investigated in the literature review:

- Three mutually intersecting non-orthogonal serial joints could achieve a spherical motion.
- The Maryland Georgetown Army (MGA) exoskeleton provided the fundamental shoulder motion without a singularity in the workspace.
- The Arm Therapy in Stroke's (ARMin II's) exoskeleton wrist mechanism provided the fundamental concept required to design the supination and pronation movements of the forearm.
- The shoulder mechanism was based on the concept illustrated by the MGA exoskeleton.
- The elbow mechanism was designed to be similar to that of the MGA and MAHI exoskeletons.
- Electric motors were implemented directly on the individual joints following the success of the MGA exoskeleton.
- Passive Range of Motion (PROM) therapy would require only positional motion.

1.6 Research Specifications

The following research specifications were implemented in this design:

- Safety
- Portability
- Functional performance
- Adjustability

1.6.1 Safety requirements

The exoskeleton must execute passive therapy in a safe manner; this will be achieved through a list of safety mechanisms. Mechanical, electronic and software safety will be implemented.

1.6.2 Portability

A portable mechanism must be designed in order to cater for the urban and rural segregation in South Africa. Factors influencing portability are as follows:

- The mechanical manipulator must be as compact as possible and weigh less than 10 kg.
- The system must be geographically portable.

1.6.3 Functional performance requirements

The exoskeleton manipulator must provide a range of physiotherapy motions. The structure must be capable of achieving these motions. The following characteristic which influences the exoskeleton's functionality must be taken into consideration.

- The exoskeleton should allow for a large workspace according to the Activities of Daily Living (ADL).
- The exoskeleton manipulator (shoulder, elbow and wrist mechanisms) must be capable of lifting a 2kg load at the end-effector. This specification was implemented as a safety factor and to assist with any future developments of the exoskeleton.

1.6.4 Adjustability

The exoskeleton must be adjustable as follows:

- The design must be adjustable for users with different dimension as rehabilitation will occur on different sized individuals. Adjustability will be based on the 95th percentile human being.

- Standing and sitting physiotherapy will assist in terms of patient preference or the type of injury.

These specifications were further complicated with a budget of ZAR 30 000. Designing a low cost exoskeleton prototype will assist with future implementation in to the public healthcare service.

1.7 Research Contribution

The contribution of this research was specified as follows:

- The exoskeleton mechanism did not consist of a singularity in the workspace of the ADL.
- The manipulator would be adjustable according to the 95th percentile human being.
- It would be geographically portable as specified.
- The exoskeleton would perform passive physiotherapy.
- A complete upper limb exoskeleton was designed this included a shoulder, elbow, wrist and hand mechanism. The shoulder and elbow mechanism was of priority with least priority placed on the hand and wrist mechanism.
- Inverse kinematics was implemented and catered for the complex joint layout.

1.8 Methodology Overview

It is important to have a design approach for this research. The mechatronics approach is illustrated in Figure 1.3 and will be adapted in this research and integrated biologically to produce a bio-mechatronic device as explained in section 1.1. The need for such research has been explained as a motivation of the research. The conceptual designs will be illustrated in the mechanical design chapter.



Figure 1.3: Sequence of Operations for Mechatronic Design Process.

It is essential to establish conceptual designs in order to compare the various trade-offs between the designs. This will allow for the selection of the optimal and effective design for this research purpose.

Implementation of kinematic models will allow for a correlation between joint space and end-effector positions. These models will have to be simulated and related to practical tests. Positional, workspace and load tests were executed.

1.9 Research Publications

- D. Naidu, R. Stopforth, G. Bright, S. Davrajh; "A 7 DOF exoskeleton arm: Shoulder, elbow, wrist and hand mechanism for assistance to upper limb disabled individuals," *AFRICON, 2011, Livingstone, Zambia*; IEEE, vol., no., pp.1-6, 13-15 Sept. 2011
- D. Naidu, C. Cunniffe, R. Stopforth, G. Bright, S. Davrajh; " Upper and Lower Exoskeleton Limbs for Assistive and Rehabilitative Applications," *CSIR International Conference Centre, Johannesburg, South Africa*; Robmech 2011, 23-25 Nov. 2011

1.10 Chapters of this Dissertation

Chapter one: Introduces the reader to the physiotherapy challenges in South Africa. The research is further motivated for a passive therapy application. The research objectives, outcomes, contributions and methodology are described.

Chapter two: Analyses the biological upper limb anatomy as well as several previous exoskeleton designs

Chapter three: The mechanical design process is illustrated for the exoskeleton shoulder, elbow, and wrist and hand mechanism. Movement of singularities result in complex kinematics.

Chapter four: Presents a solution to the complex inverse kinematic problem. A redundant and non-redundant model is presented as well as kinematic results.

Chapter five: Presents the electronic components in this research.

Chapter six: Presents the design and development of a GUI as well as an investigation in to two control models which is required for passive therapy.

Chapter seven: Testing on the mechanism is executed in this chapter.

Chapter eight: Conclusion to this research as well as the specification of future improvements in the design.

1.11 Chapter Summary

This chapter introduced the reader to the problem statement which was further motivated by the increase in stroke victims. The research objectives, outcomes, specifications and methodology were established. A summary of the chapters in this thesis was provided.

2 Exoskeleton Literature Research

2.1 Introduction

This chapter is a literature review on the human biological upper-limb and traditional exoskeleton designs. The Degrees of Freedom (DOF) in the upper limb are explained as well as their limits in their respective plane of motion. The analysis of the previous exoskeleton designs resulted in a tabulated list of their joint limitations and locations of motion.

2.2 The Upper Limb Anatomy and Kinematic Movements

A compact exoskeleton design requires an anthropomorphic layout, and the successful integration of an exoskeleton manipulator and the human arm, without producing any collisions between the two. The mechanical manipulator had to be capable of providing a large workspace according to the ADL in order to provide successful physiotherapy. The upper limb anatomy had to be researched extensively to achieve the above described characteristics. This research provided a relationship between the human arm bio-mechanics and the mechanics of the upper limb exoskeleton, which was essential in creating an anthropomorphic design. The biological arm consists of three main parts: the upper arm, the forearm and the hand which are connected together via three joints. The upper arm is connected to the trunk segment (torso) via the GH joint, which is commonly known as the shoulder joint. The forearm is connected to the upper arm via an elbow joint; and the hand is connected to the forearm via the wrist joint. These joints and connections are illustrated in Figure 2.1.

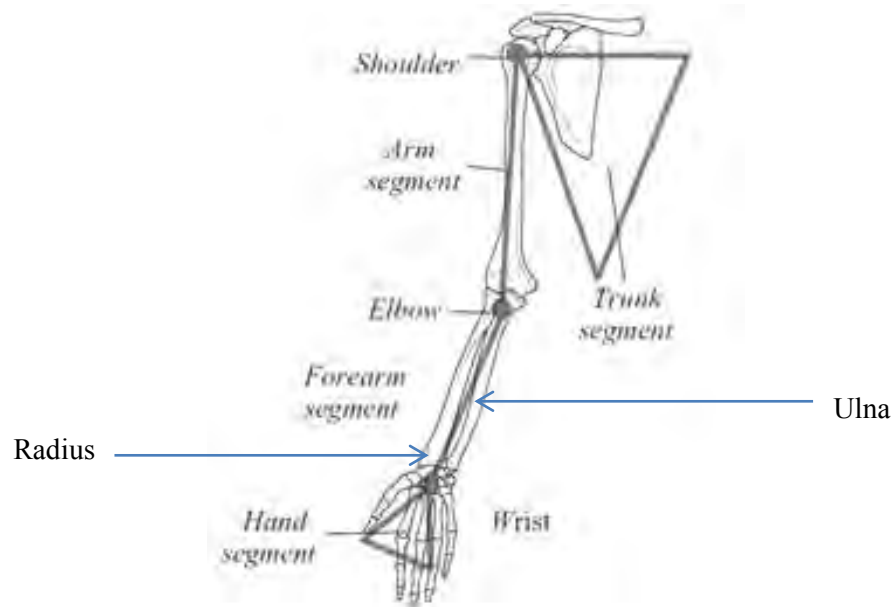


Figure 2.1: Graphical Representation of the Upper Limb Anatomy [7].

The above described joints had to be taken into consideration to provide the necessary passive therapy motion for the relative DOF. The DOF in the human biological arm can be imitated using seven mechanical DOF; these comprise of three DOF in the shoulder joint, two in the elbow joint and two in the wrist [19]. The design of the exoskeleton arm had to cater for majority of these motions in order to replicate the human workspace required to perform the ADL, as previously explained.

The human upper-limb locomotion in bio-medical terms was described in three planes. These included the frontal/coronal plane, the lateral/sagittal plane and the transversal plane. These planes were illustrated in Figure 2.2 and are according to the human anatomical position. This anatomical posture was positioned with the feet together; the arms rotated outwards and to the side; palms, eyes and head faced forward [7].

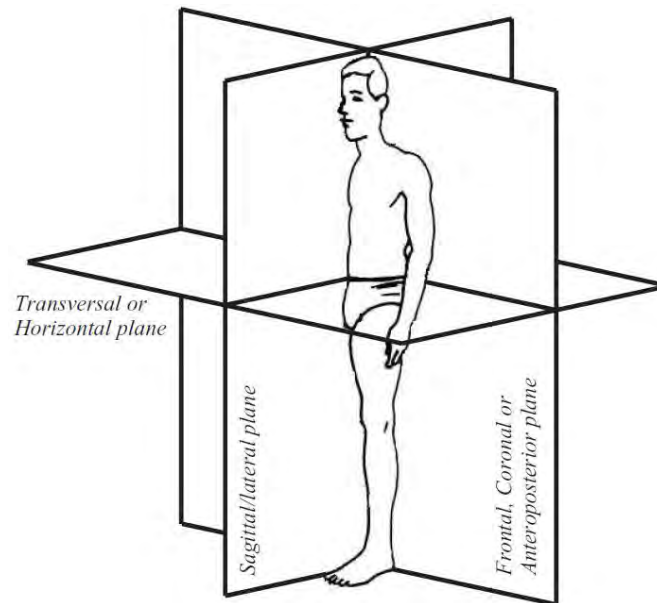


Figure 2.2: Graphic representation of the human body motion planes [7].

The different types of motion that occur in the three anatomical planes are: extension/flexion, abduction/adduction and supination/pronation; these terms are explained as follows.

- Extension and flexion occur in the sagittal plane, extension is movement in which the angle between the bones and body parts increase. Whereas flexion is movement in which this angle reduces.
- Abduction and adduction occur in the coronal plane. Abduction is the motion in which the angle between the bones and body parts increase. Whereas adduction is movement in which this angle reduces which results in the bone being closer to body.
- Supination and pronation is the rotation of the forearm. Supination is rotation so that the palm faces upwards whereas pronation is rotation such that the palm faces downwards [7].

With knowledge of these descriptions of motion, the movement of the specific joints were explained. Thus further analysis with regards to the angle specifics provided vital design information.

The GH joint was modelled mechanically as a ball and socket joint; which produced a spherical workspace [20]. This spherical motion was achieved using three DOF; these three DOF were separated and parameterised individually to provide the required mechanical spherical motion. The three degrees of freedom are:

- Flexion and extension, the workspace limits up to 180 degrees and 80 degrees respectively.

- Abduction and adduction, with work limits of up to 180 degrees and 50 degrees respectively.
- Rotation of the joint internally (medial) and externally (lateral). These movements have work limits of up to 90 degrees for both motions [7].

The elbow joint was represented as a mechanical hinge, and created the movement of flexion and extension [21].

- Flexion is the movement that brings the forearm towards the shoulder joint. The work limits of the flexion motion are up to 146 degrees and there is no extension [7].
- Pronation and supination is also experienced in the elbow joint but this mainly affects the movement of the palm, it is a complex motion and is explained below.

Supination and pronation are created by the radius and ulna bones. A detailed illustration of these bones can be seen in Figure 2.3. The radius and ulna form the basis of the forearm and are connected at the elbow and wrist joints. The radius is the shorter of the two bones and moves around the ulna. This motion is propagated to the lower regions of the forearm resulting in the pronation rotational movement. The movement of this radius is mainly noticeable at the wrist, which creates the rotational movement of the hand. It is important to understand this pronation and supination movement in order to create a design that can successfully mimic it.

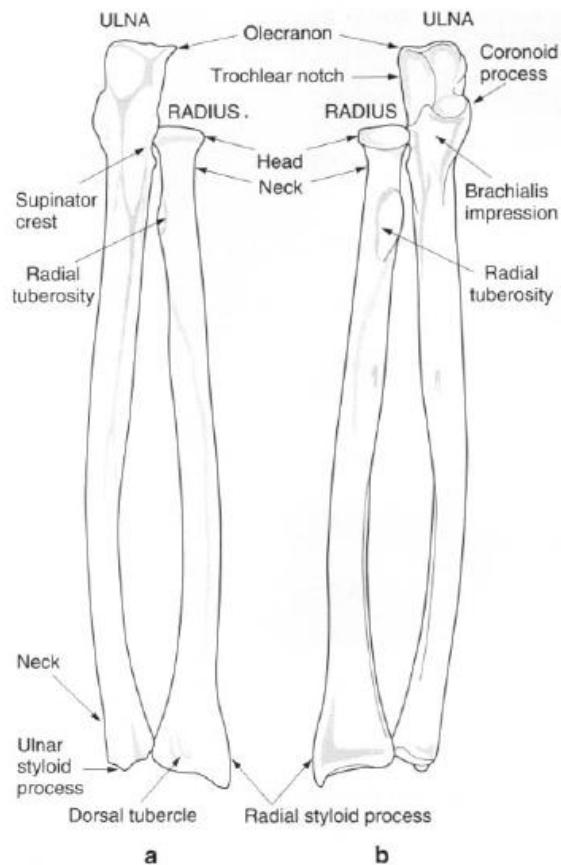


Figure 2.3: (a) Posterior and (b) anterior views of the right radius and ulna [22].

An important factor taken into consideration was that there was a carry angle between the forearm and the upper arm; which means that forearm and upper arm are not co-axial when fully extended. The carry angle results in the elbow joint axis being inclined in the transverse plane by an angle equal to half the carry angle [7]. Pons [7] informs of a carry angle of 5-6 degrees; whereas Palastanga, Field and Soams reports a carry angle of half 10-15 degrees and half 20-25 degrees in men and woman respectively [22]. This meant that the design of the exoskeleton had to cater for this in terms of mechanical adjustability. An illustration of the carry angle can be seen in Figure 2.4. The entire mechanism was adjustable according to the 95th human arm. The 95th percentile arm is statistical information on individuals that have larger arm dimensions than the average human being [23]. Adjustability will be explained in chapter 3.

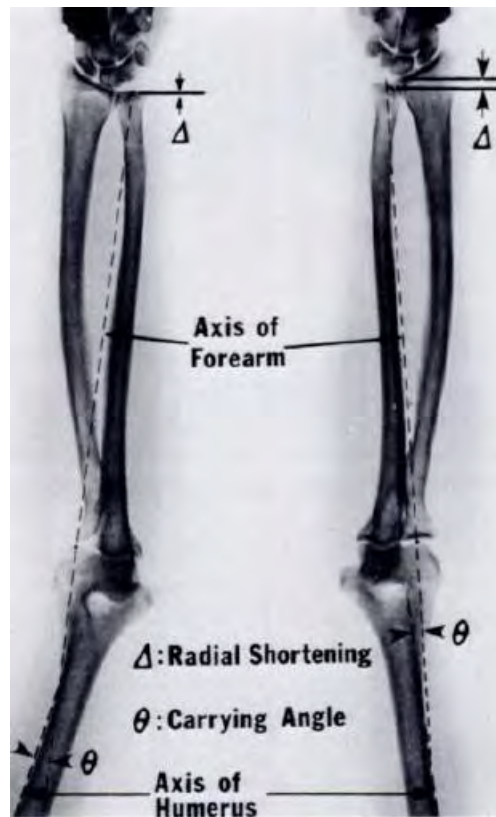


Figure 2.4: Diagram illustrating the carry angle between the forearm and upper arm [24].

The wrist joint experiences abduction/adduction and flexion/extension.

- Flexion is the bending of the wrist so that the palm approaches the forearm. This movement can be up to 90 degrees, whereas extension is up to 80 degrees.
- Adduction is the movement so that the palm moves towards the ulna and abduction is the movement of the palm so that the palm moves towards the radius. Approximately 30-40 degrees of adduction can be achieved and up to 15 degrees of abduction.

The wrist joint can be visualised as a spherical joint when coupled with the supination/pronation of the elbow joint. This concept has been adapted in industrial robots as it is easier to handle and control in terms of robotic kinematics [25]. However, the wrist adduction/abduction and extension/flexion degrees of freedom were not included in the design as it minimised the moment created by the excess weight, as well as reduced the number of degrees of freedom in the entire structure. This compromise is acceptable as the supination and pronation motion together with the gripping of the hand will rehabilitate the carpus region of the arm. This region is between the connection of the hand and ulna and radius bones [22]. The seven degrees of freedom are illustrated in Figure 2.5.

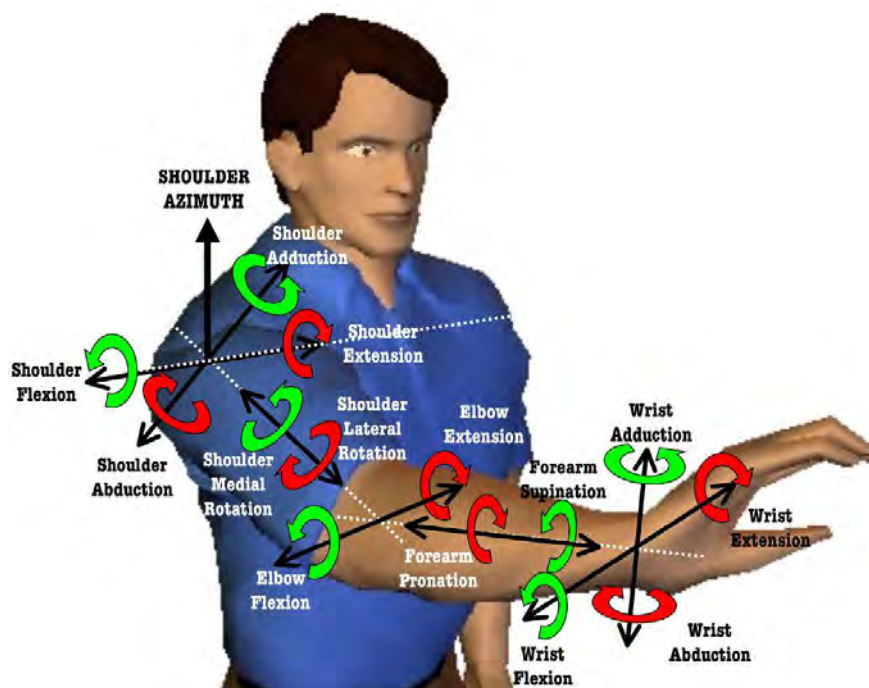


Figure 2.5: Picture illustrating the 7 DOF in the upper arm [19].

2.2.1 Therapeutic Exercises

There are three different types of therapeutic exercises that are carried out in the Range of Motion (ROM) of the specific joint, these exercises include [18]:

- Passive ROM
- Active ROM and
- Active-Assistive ROM

Passive ROM is the non-restricted motion of a limb segment which is created completely by external forces, as explained in Chapter 1. There is no muscular feedback from the patient. Active ROM is the non-restricted motion created by the contraction of muscles across that joint; the motion is created without any assistance from external forces. Active-Assistive ROM is a form of active ROM and occurs when external forces are applied to the limb segment because the prime moving muscles require assistance to complete the desired motion [18]. Active Assistive ROM was not implemented in this research as Passive ROM provided the necessary therapy required to fulfil the need as explained in the motivation of chapter 1. The benefits of Passive ROM are to [18]:

- Maintain muscular mechanical elasticity.

- Assist with the healing process after surgery or injury.
- Create better blood circulation and assist vascular dynamics.
- Provide motion for cartilage nutrition.
- Decrease or inhibit pain.
- Help maintain patient's awareness of movement.

Passive ROM is therefore beneficial to various other patients excluding stroke victims. Passive ROM is less costly to implement than Active Assistive ROM because it does not require feedback from the patient. Therefore the mechanism can be operated purely in positional terms as this change in position will provide the desired passive therapy.

2.3 Previous Work in Exoskeletons

This subchapter discussed previous exoskeleton designs in order to understand their joints movements, physical layout, DOF and actuation.

2.3.1 Existing Exoskeletons Movements and Descriptions

Current upper limb exoskeleton designs are mainly built for the purpose of haptic, tele-operations, rehabilitation and strength enhancement applications. Tele-operation is the process by which a slave robot is controlled, at a distance, via the replication of forces and movements performed by an operator using an exoskeleton arm [26]. Haptic interface is the interaction of the exoskeleton and the operator through human touch; which can be used to control virtual reality environments [27]. Strength enhancement is implemented in exoskeleton devices to aid individuals in bearing or carrying large loads [28]. Traditional rehabilitative exoskeletons are bulky and their mechanical manipulators are not designed to be portable. Although this exoskeleton arm research was designed for physiotherapeutic applications; previous haptic, tele-operations and assistive designs will provide valuable insight with regards to the design of the exoskeleton arm. Various exoskeleton arm designs was analysed and the joint specifics of the MGA, MAHI, L-EXOS and the CADEN-7 exoskeletons were obtained. The total range of motion of these exoskeletons was studied and tabulated, Table 2.1, according to the joint movements.

Table 2.1: Joint Movement in Degrees.

Joint	Motion	MGA [19]	MAHI* [29]	L-EXOS* [30]	CADEN-7* [31]	HUMAN** [23]	ADL*** [31]
SHOULDER	Extension /Flexion	210	-	135	180	236	110*
	Adduction /abduction	138	-	140	180	173.5	100*
	Rotation lateral /medial	131	-	135	160	160	135*
ELBOW	Flexion	142	120	105	150	138	115*
WRIST	Supination /Pronation	360 but not motor actuated	180	180	160	172	150*

*Values are mechanical joint capabilities for both directions (total) where applicable.

**Values are the 50th percentile of a test of 100 males. Female joints are more flexible [23].

*** ADL – Activities of daily living [31].

The tabulated values printed in red are joints that are capable of rotating more than that specific human joint can handle. This can cause severe damage; resulting in hyper extension or flexion of the human joints. Therefore safety is an essential factor in this design and the proper implementation will be discussed further in this dissertation.

It is also important to note that traditional exoskeletons consist of three mutually intersecting orthogonal joints which replicate the spherical motion of the shoulder joint, this is the fundamental motion required to create a large workspace according to the ADL [32]. However, this orthogonal layout is undesirable as it results in a singularity in the workspace. A singularity is created when two joint axes become co-linear; any further rotation regarding the joints will yield the same result. This results in a loss of a degree of freedom [33]. As a result the Jacobian, used in the kinematic model, reduces in rank and the subsequent matrix would command an infinite speed in the relative joint axes, which is not desired for obvious reasons [32]. As the mechanical structure approaches a singularity-larger changes in joint angles result in smaller changes in the end-effector position. This is the main

reason why one cannot work around a singularity in the middle of the workspace because the structure will always be in close proximity of the singularity [34]. A singularity cannot be removed from the mechanical design. However, it can be moved to a position which will not hinder the ADL, but this will result in a change in the orthogonal layout of the joints which will be explained in chapter 3. This change in joint layout will result in problematic kinematics which was discussed further in chapter 4.

2.3.1.1 CADEN-7 Exoskeleton.

The CADEN-7, by Perry and Rosen, could be used for four different applications which include physiotherapy, assistive, haptic and as a master device; this was achieved by changing the control algorithms [31]. This control architecture inspired this research as a similar approach can be used in future designs to allow physiotherapy as well as assistive algorithms. The CADEN-7 employs a drive pulley system which allowed the actuator weight to be positioned remotely in order to minimise the moments acting on the exoskeleton structure. However, this required the actuators to be externally fixed, which limited the portability of the system. The CADEN-7 exoskeleton also successfully imitated the three DOF in the shoulder joint and the supination/pronation rotation, as tabulated in Table 2.1. Good control bandwidths were achieved however the extra cable drives required more devices which added extra weight and complicated the structure in terms of adjustability.

Figure 2.6 is a Computer Aided Drawing (CAD) of the CADEN-7. It is visible from Figure 2.6 that the pulley actuation added extra mass to the system and therefore resulted in a bulky system [31].



Figure 2.6: CAD drawing of the CADEN-7 [31].

2.3.1.2 L-EXOS Exoskeleton.

The L-EXOS was similar to the CADEN-7 in terms of the pulley actuation and structural design. It consisted of three mutually intersecting orthogonal joints which emulated the spherical motion of the GH joint. This motion was desirable however the orthogonal joints produced a singularity in ADL as previously described. The L-EXOS could be configured to allow for the hand to be implemented into the end-effector, however this was purely for a virtual environment and only made use of the thumb and index finger [30]. This exoskeleton was designed for haptic purposes and its control architecture catered for forces which were applied by the user. This was not necessary for this research as positional control was only required to provide the passive therapy, as previously described. The L-EXOS can be seen in Figure 2.7.



Figure 2.7: Picture of the L-EXOS exoskeleton [30].

2.3.1.3 MAHI Exoskeleton.

The MAHI was a haptic exoskeleton designed for training and rehabilitation; it implemented an actuation layout that consisted of a Revolute Prismatic Spherical (RPS) parallel mechanism. This mechanical layout created the required pronation and supination rotation however the exoskeleton did not consist of any shoulder motions [29]. Its elbow design could have been implemented into this research, and although the 3 RPS layout may have been effective for the MAHI; the extra actuators combined with a shoulder mechanism added extra weight to this research design. It was decided to use one actuator for the supination and pronation movements. Figure 2.8 is a picture of the MAHI exoskeleton.



Figure 2.8: Picture of the MAHI exoskeleton [35].

2.3.1.4 MGA Exoskeleton.

The MGA exoskeleton, Figure 2.9, was designed to provide fixed (not geographically portable) physiotherapy to the scapula, shoulder and elbow joints. Scapula therapy added an extra degree of freedom to the design; this degree of freedom was not required in this research. However, its structure compensated for the spherical workspace; by allowing for a joint layout that was not mutually orthogonal. The MGA made use of Direct Current (DC) motors for the individual joints therefore did not require an external support for actuation. The structure had a hand support and not an exoskeleton hand, hence the exoskeleton did not accommodate for the full upper-limb but its joint layout and actuation setup was implemented in this design.

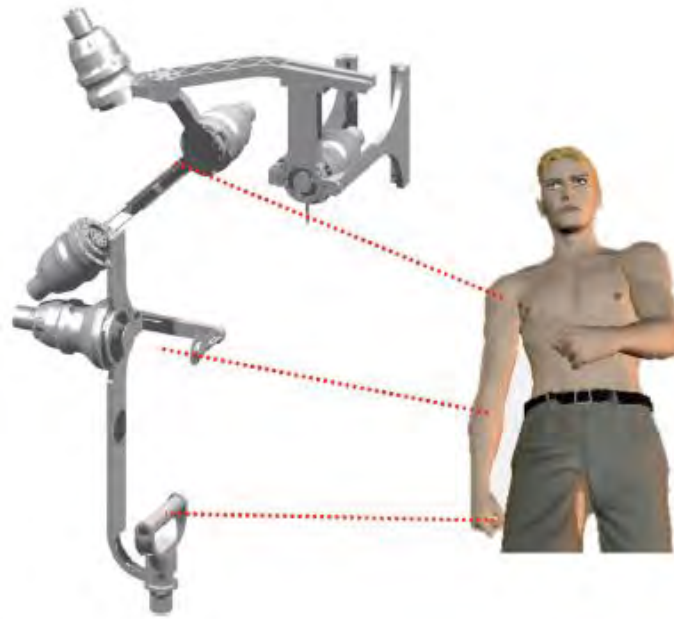


Figure 2.9: CAD of the MGA exoskeleton design [19].

2.3.1.5 ARMinII Exoskeleton.

Another exoskeleton that was researched was the ARMin II. It was a seven degree of freedom exoskeleton structure that was used for rehabilitation and provided motion from the shoulder to the wrist. The exoskeleton has an interesting wrist design that allowed for the supination/pronation motion of the wrist however it was bulky and mounted onto an external structure. The ARMinII consisted of a semi-circular guide and cart that was actuated using a steel cable which was attached to the outside of the guide and to a single DC motor [36]. This steel cable attachment could have proven to be hazardous as it was not encased and created unnecessary friction outside the guide [36]. A more direct method in terms of actuating would be preferred. The elbow, wrist and hand support mechanism is illustrated in Figure 2.10.

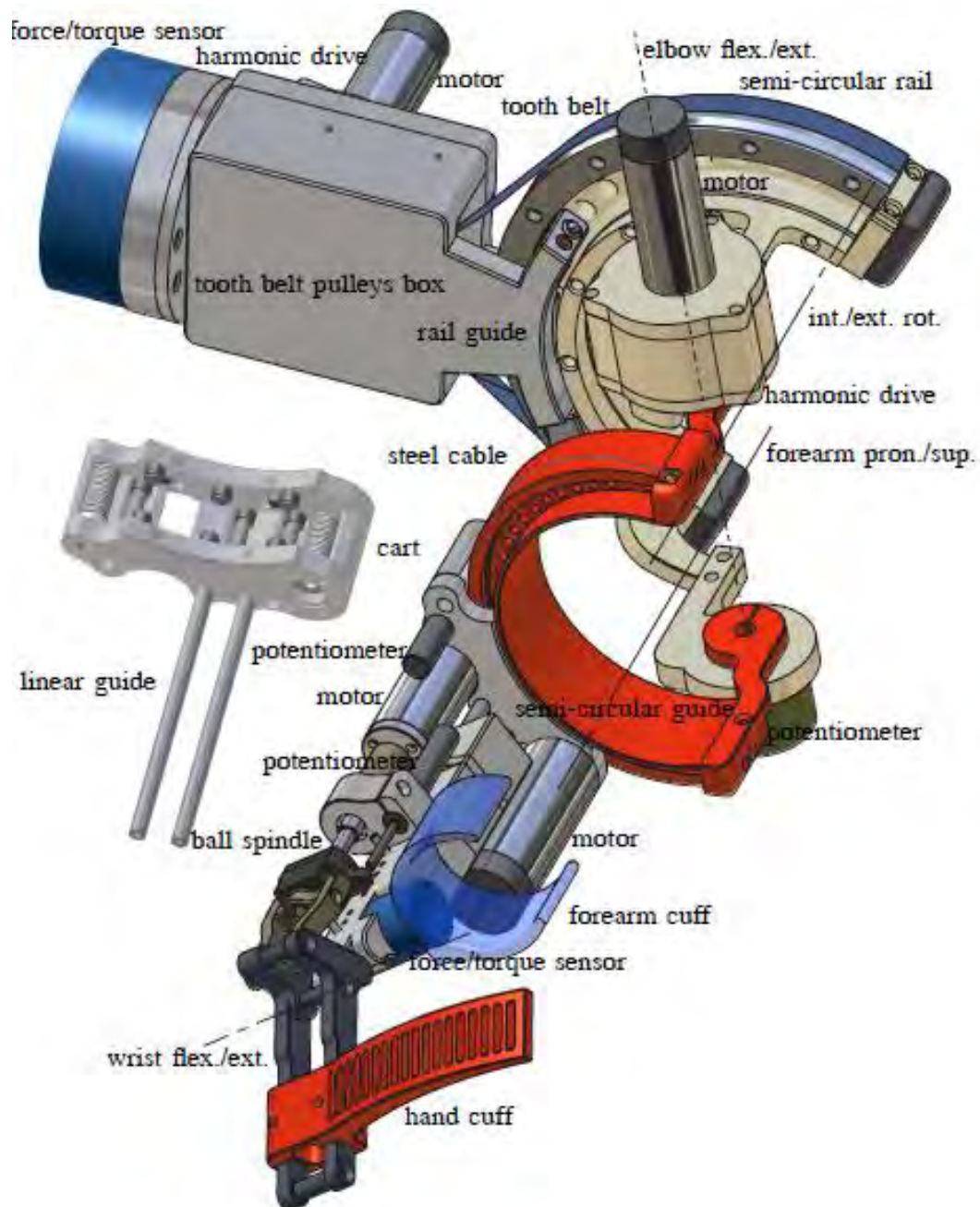


Figure 2.10: CAD of ARMin II's elbow to hand support [36].

The shoulder mechanism of the ARMin II employed a serial orthogonal layout with a prismatic joint for the flexion and extension of the elbow, this resulted in a fixed bulky mechanism as described above [36].

2.3.1.6 Exoskeleton Locational Motion

The location of motion in the above described exoskeletons and additional exoskeletons which were researched are tabulated in Table 2.2. This allowed for a comparison of a combination of movements.

Table 2.2: Location of Motion of Certain Exoskeletons Adapted from [37].

Exoskeletons*	Location of Motion
CADEN-7	Shoulder, elbow and wrist joints and forearm motion
7DOF “Soft-Actuated” Exoskeleton Design	Shoulder, elbow and wrist joints and forearm motion
Mechanical Design of Exoskeleton for Shoulder Vertical Height Adjustment: ARMin Robot	Shoulder and Elbow
Mechanical Design with Parallel Manipulators	Elbow and wrist joints and forearm motion
ASSIST	Wrist Joint
Mechanical Design of Exoskeleton for Hand and Fingers Motions	Wrist joint, fingers and forearm motion
ARMin II	Shoulder, elbow and wrist joints and forearm motion

* Where the name of the exoskeleton was not specified, the title of the literature paper was used.

From the exoskeletons tabulated in Table 2.2, none possessed the complete upper arm movement and hand movement to achieve desired the therapeutic effects. This allowed for the contribution of designing a portable physiotherapeutic design that provided movement in the location of the shoulder, elbow, wrist, and hand (gripping) joints.

2.3.2 Exoskeleton Actuation

Gopura [37] outlined several state of the art upper-limb exoskeletons that varied in the number of DOF; as a result of their various applications. Devices that replicated the motion of the shoulder varied in configuration as well as actuation. Therefore actuation was an important factor in the overall mechatronic design. The different types of actuation that were illustrated by Gopura included pneumatic, hydraulic and electric actuators.

The Sarcos Master Arm [38] was a seven degree of freedom exoskeleton arm that provided motion for the shoulder, elbow and wrist. It made use of hydraulic actuators and provided a large workspace [32]. The heavier pumps would result in additional costs and mass, which would increase the cost of geographical transportability.

Pneumatic actuators have a high power to weight ratio and are relatively light. However they required pressurised airflow which complicated the adjustability of the design. The usage of pressurised air required the control of solenoid valves which added weight and control complications [39].

Due to the flaws of the above actuators it was decided that electric motors would be the actuation of choice. Although heavier than pneumatic actuators of the same strength, it was smaller in size [39]. This allowed for flexibility in terms of adjustment, mechanical design and easier control architecture which proved successful in the MGA exoskeleton [32]. The rotary motion allowed for easier replication of the human joints and it will be easier to power the entire system (including other electronics) from a single electric power source.

2.4 Chapter Summary

This chapter explained the bio-mechanics of the biological human arm. It was essential to understand the mechanics and restrictions of the relative joints in order to design an acceptable mechanical structure that would be capable of providing the required workspace, without causing hypertension or hyper flexion to the wearer's joints. The various DOF at the relative joints were discussed, and complications such as the carry angle were taken into consideration. The different physiotherapy exercises were described and passive ROM was chosen as it satisfies the need of this research. Different exoskeleton mechanical structures were analysed, none of which possessed motion from the shoulder to the hand (gripping). The joint ranges of the described exoskeletons were tabulated. The shoulder mechanism of the MGA exoskeleton had favourable design aspects for this research application. The ARMin II wrist design was favourable however the steel cable actuation was not

desirable for this research and it needed to be re-designed. The various actuators were explored and it was decided that electric motors were to be used due to the required adjustability in the design. The research outcomes and contribution of this research were finally established as illustrated in chapter 1.

3 Mechanical Design

3.1 Introduction

The mechanical manipulator consisted of 5 DOF as explained in chapter 2. These DOF included three for the spherical workspace of the shoulder, one for the elbow and the last degree of freedom being the supination/pronation of the forearm. The hand (end-effector) consisted of an additional two DOF which provided the required gripping motion. A simple schematic of the design can be seen in Figure 3.1. Circles 1-4 in Figure 3.1 represent the shoulder, elbow, wrist and hand joints respectively; the arrows illustrate the DOF at the respective joints and the blue solid lines are the mechanical segments I-III.

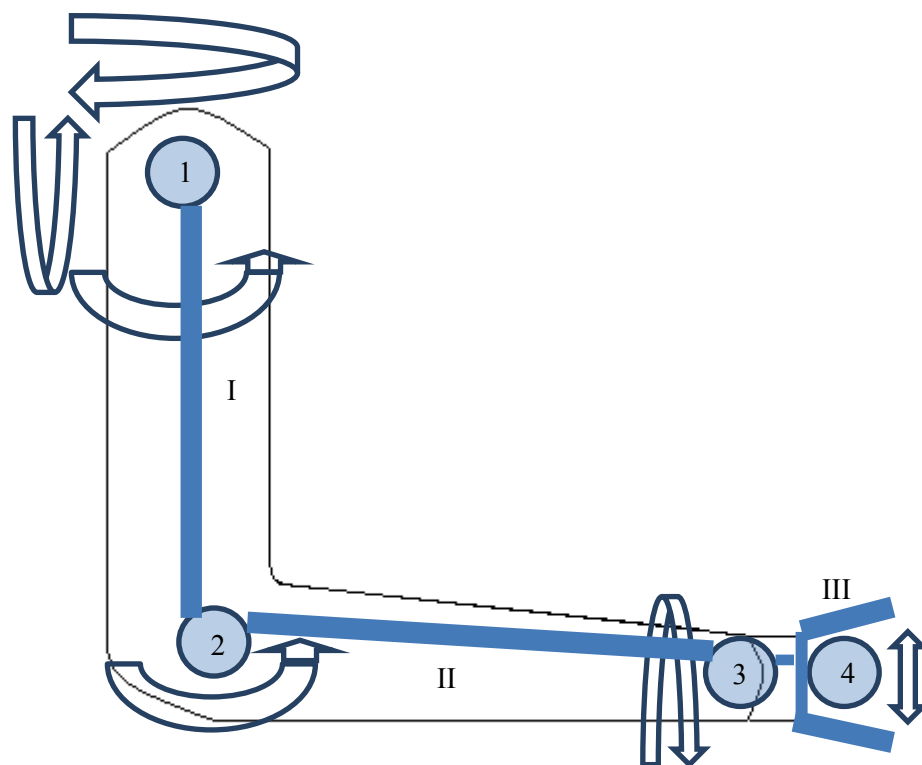


Figure 3.1: Graphic illustrating a systematic integration of the joints (numbered circles), together with the number of DOF (arrows).

The fundamental spherical motion was produced by the shoulder mechanism. The integration of the shoulder and elbow mechanisms would result in the translational positioning of the end-effector. The supination/pronation of the wrist merely modified the orientation of the end-effector and the hand exercised the gripping function of the patient. The wrist and end-effector mechanisms did not change the translational position of the end-effector. It was of a greater priority that the spherical motion of the GH joint was possessed in the shoulder mechanism as this would provide the large translational workspace. The wrist and end-effector design were to be designed around the shoulder and elbow mechanism. This design arrangement would ensure that priority was placed on the shoulder and elbow mechanism to cater for the spherical motion and the carry angle as discussed in chapter 2. The priority of the shoulder and elbow mechanism ensured that passive therapy of the patient would be carried out successfully by creating the desired spherical workspace.

Another important factor which was explained in chapter 2 was the singularity. This singularity had to be addressed and moved to a position that did not hinder the workspace of the ADL.

This chapter covers the above described factors as well as a brief overview of the construction of the components that make the exoskeleton.

3.2 Shoulder Spherical Mechanism

3.2.1 Shoulder Spherical Motion

The spherical nature of the shoulder joint was replicated by three external serial revolute DOF. The joint axes may have been mutually orthogonal in order to create the spherical motion. However, mutually orthogonal joints produced a singularity in the workspace of the ADL. Inequalities 3.1 and 3.2 had to be satisfied in order to achieve the spherical motion without implementing orthogonal joint axes. It was important to understand that the three joint axes needed to intersect at the same position of the GH joint to create a spherical workspace about the point of intersection [32].

$$\frac{180^0}{2} - \theta_3 \leq \theta_2 \leq \frac{180^0}{2} + \theta_3 \quad (3.1)$$

$$180^0 - \theta_2 - \theta_3 \leq \theta_1 \leq \theta_2 + \theta_3 \quad (3.2)$$

All angles lay between 0 and 180° . θ_1 , θ_2 and θ_3 represent the angles between *joint axes 1* and 2; *joint axes 2* and 3 and *joint axis 3* and the tool tip, these angles are 90° , 75° and 45° degrees respectively. The tool tip was the direction of the end-effector away from the GH joint. The above described angles can be seen in Figure 3.2; these angles were illustrated on the final design later in this chapter for better clarity.

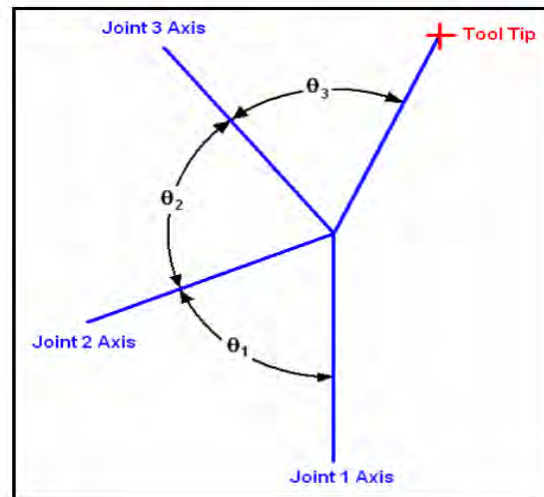


Figure 3.2: Graphic representing the three joint axes, angles and the tool tip direction [32].

By rotating the tool tip around *joint axis 3* a circular path was outlined, this path is represented by the green circle in Figure 3.3 (b). A further rotation of this circle around *joint axis 2* resulted in a spherical surface bounded by *joint axes 2* and 3. The orange sphere in Figure 3.3 (c) represents this surface. The rotation of this orange structure around *joint axis 1* resulted in a complete sphere. Inequalities 3.1 and 3.2 needed to be satisfied in order to obtain the required spherical workspace [32].

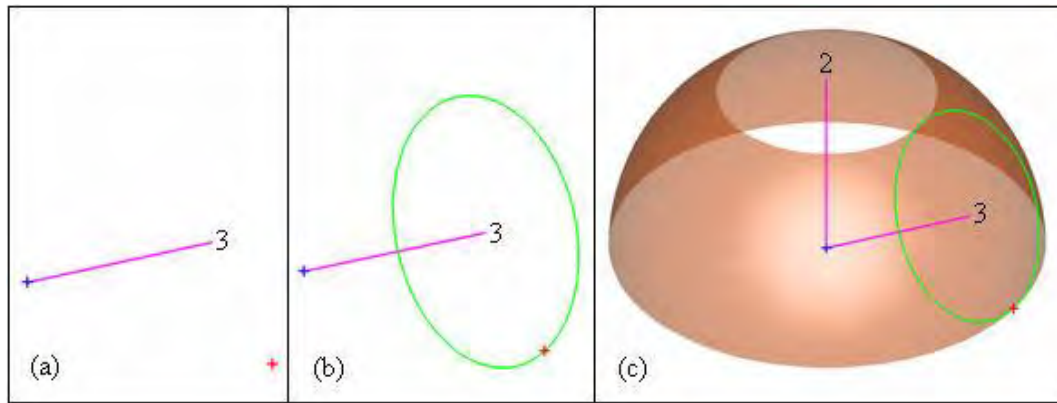


Figure 3.3: Graphical representation of the spherical motion [32].

3.2.2 Shoulder Conceptual Designs

The conceptual designs were based on the different MGA exoskeleton versions. This exoskeleton consisted of four different prototypes. For clarity purposes the MGA designs were referred as their respective prototypes and the conceptual designs would be the designs created for this research.

The *MGA prototype I* was analysed and it consisted of an additional scapula DOF which was not a requirement of this research. This prototype was favourable because it was a simple anthropomorphic mechanism. However, it consisted of a singularity which occurred at a position that required the upper limb to be stretched out forwards at 90 degrees to the torso. This position lies within the workspace of the ADL. *Joint axis 3* was co-linear with the upper limb which increased the complexity of the actuation design. The *MGA prototype I* can be seen the CAD in Figure 3.4.

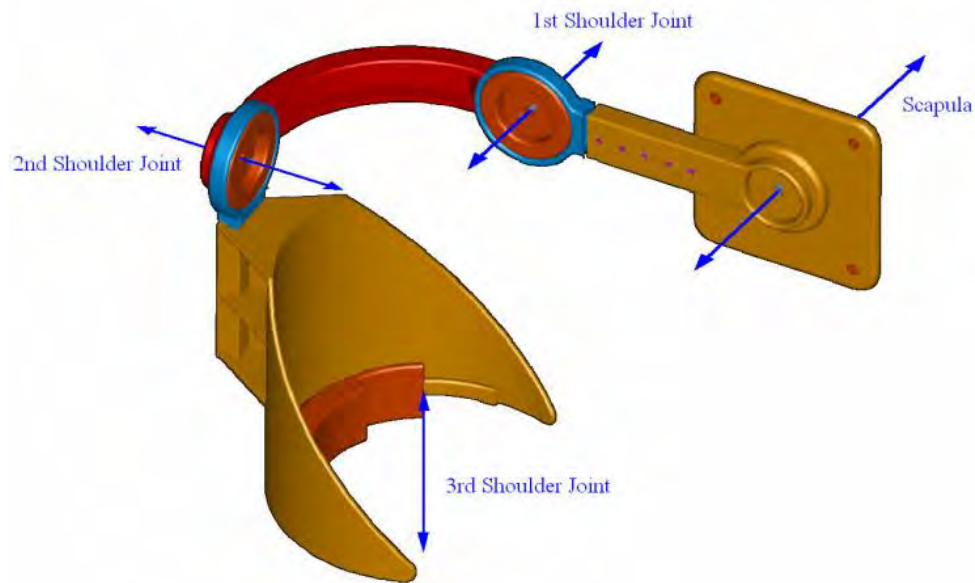


Figure 3.4: CAD of the MGA, prototype I [32].

The first conceptual design of this research was created by removing the additional DOF and modifying the position of *joint axis 3* of the *MGA's prototype I*. *Joint axis 3* was re-designed to be 45° to *joint axis 2* and the upper arm. This modification resulted in the elimination of the complex actuation for *joint 3* because *joint axis 3* was positioned to be inside the upper arm, instead of outside. The design did not have two collinear axes at 90° of flexion and the singularity was thought to be moved. However, further analysis revealed that the three joint axes were co-planar which resulted in a singularity at 90 degrees of flexion. This is in the middle of the workspace of the ADL and is undesirable. A CAD of concept one can be seen in Figure 3.5.

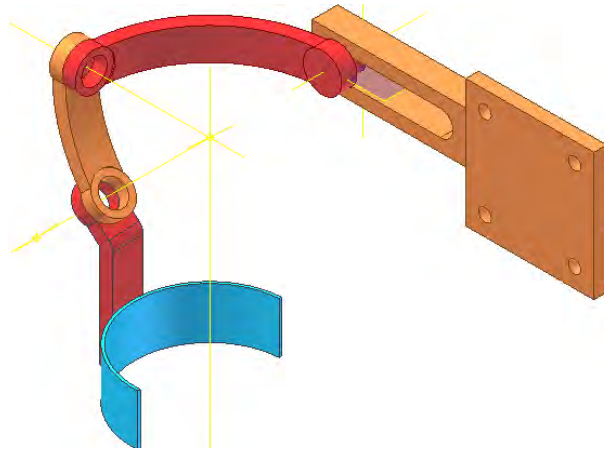


Figure 3.5: CAD of Concept One.

A second conceptual design can be seen in Appendix A.1 as Figure A.1. This conceptual design was created to solve the singularity problem however the axis of joint three was still co-linear.

The final *MGA's Prototype IV* was the solution to the singularity in the middle of the workspace as well as the joint actuation complexity. *Joint axis 3* was not co-axial with the upper arm and the singularity was moved out of the human workspace, which was at an unattainable position. The singularity was present when the arm is rotated 90° laterally, from the forward position, and 45° from *joint axis 1*.

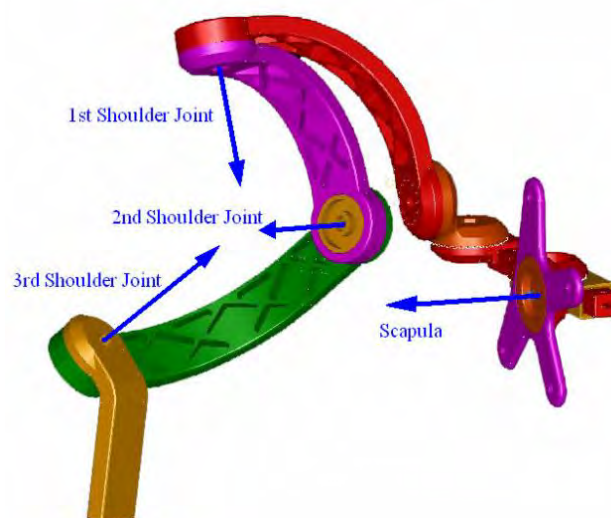


Figure 3.6: MGA's final shoulder mechanism Prototype IV [32].

This was not attainable in majority of human beings and would be uncomfortable for people that could achieve this position. The *MGA Prototype IV* can be seen in Figure 3.6. Although the singularity was in an unattainable position the Prototype IV was still not a favourable choice. The reason being was that the radius of the link curvature was large; this was acceptable with MGA because the fixed physiotherapy application did not limit this criterion. The minimum angle between two links was limited as the radius of curvature was decreased. Minimising the angle between two links increased the chances of link collision. The MGA employed larger link radii because of this link collision. The *MGA Prototype IV* also had the extra assistance from the scapula motion; which added an extra 30° during abduction. This meant that the MGA could abduct to 105° hence 75° without the scapula motion. This was below the ADL of abduction of 100° , which was stated in Table 2.1.

In order to address the above described factors a third conceptual design was created. The first joint angle was abducted by 30° in order to make up for the loss of the extra DOF. *Joint axis 1* was now co-axial with the vertical axis (azimuth) and this increased the abduction by 30° . However, it moved the singularity nearer to the workspace of the ADL. Another factor was that the workspace did not cater for various combinations of simultaneous joint orientation. The MGA was designed to exercise a certain muscle or a specific position of the arm. This meant that moving a certain combination of links caused collisions of the links with either the wearer or other links on the exoskeleton structure. This was a detrimental flaw in terms of this research design because a combination of movements is a contribution of this research. This detriment was intensified by the requirements of smaller link curvature radii in order to minimise the manipulator's weight. This collision occurred with link 1 and link 2 during abduction and medial or lateral rotation as illustrated in Appendix A.2. This type of collision also limited the *MGA Prototype IV's* movement when connected to a stand. This limitation was prominent at 90° of abduction and collision of the links with the stand would occur. Appendix A.2 explains and illustrates how the optimal length of link 2 was achieved through CAD modelling.

A 75° angle was chosen for link 3 because the smaller the angle the closer the singularity was to the anatomical position of the arm, as previously explained. Although full rotation of this link could not be achieved; it allowed for majority of the human workspace. This was the finalisation to concept three which can be seen in Figure 3.7.

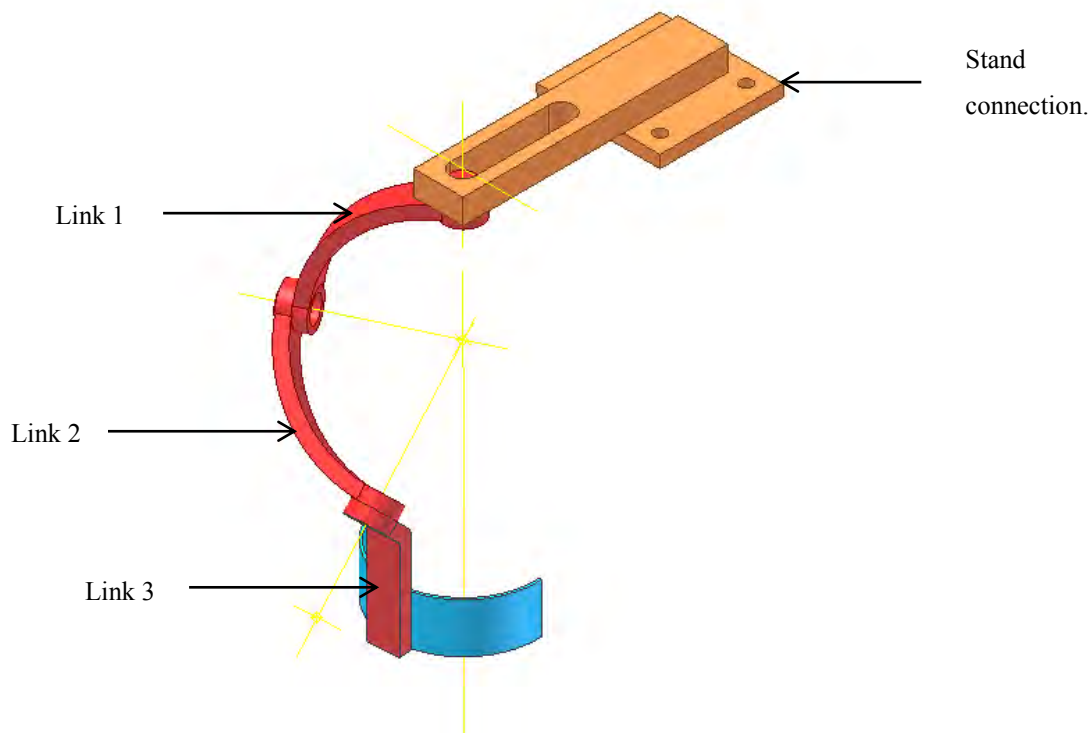


Figure 3.7: CAD of Concept Three.

The above chosen link size created an uncomfortable singularity when the upper arm was at an angle of 30° to the vertical plane with the forearm oriented 90° to the azimuth. This position did not fall in the ADL. It was important to realise that the collision of links were for design safety purposes and all possible collisions would be prevented by means of electronic and software safety stops. This also meant that the spherical workspace, determined in the concept models, would be slightly smaller by a set tolerance for safety purposes.

3.2.3 Shoulder Concept Selection

The selection of the correct concept, in relation to the required application, was essential. Table 3.1 and Table 3.2 have been created to display the advantages, disadvantages as well as weight the different conceptual designs. Table 3.1 illustrates the more conceivable advantages and disadvantages, whereas Table 3.2 encapsulates the various concepts' criteria in terms of weighting.

Table 3.1: Advantages vs Disadvantages of the different designs

	Advantages	Disadvantages
Prototype I	Simple design.	Joint three is difficult to actuate and there is a singularity in the middle of the workspace.
Concept I	Resolved actuation problem.	Singularity in the middle of the workspace.
Concept II	Singularity not in the workspace.	Joint three is difficult to actuate.
Prototype IV	Resolved actuation problem and singularity is not in the workspace.	Large link radii. Difficult to mount on to stand due to the position of Joint 1. Full work space is achieved by adding an extra scapula DOF.
Concept III	Achieves desired workspace. Allows for backpack attachment. Resolved Actuation problem. Smaller link radii compared to Prototype four.	Kinematics yield complex equations.

Concept three had a disadvantage in terms of kinematic complexity; the reason for this would be explained in chapter 4. It was advantageous in terms of the workspace, smaller link sizes; it allowed for a stand attachment and resolved the actuation problem in joint three. The single main disadvantage is outnumbered by the advantages. This weighting is illustrated in Table 3.2 which ranks conceptual design number three as the best design from the others. The final design would be based on concept three.

Table 3.2: Table of Comparison of the different designs

Selection Criteria	Weight (%)	Prototype I	Concept I	Concept II	Prototype IV	Concept III
Workspace extent	20	2	2	3	3	4
Kinematic complexity	10	3	3	5	3	3
Mechanical complexity	20	3	4	2	3	4
Comfort	10	3	4	3	4	4
Cost	5	3	4	3	4	4
Bulk/weight	15	3	3	3	3	3
Safety/collisions expected	20	4	3	4	3	3
WEIGHTED AVERAGE		3.00	3.15	3.20	3.15	3.55
RANK		5	3	2	3	1

The elbow design did not require a selection process as it consisted of only one degree of freedom which could be represented by a revolute joint. This degree of freedom had to align with the elbow joint axis and the exoskeleton joint could be positioned either medially or laterally (inside or outside) to the human joint. This design would consist of a simple extension of link 3 with a joint at the human elbow joint and a link to support the forearm (link 4). The elbow conceptual design together with the shoulder can be seen in Figure 3.8.

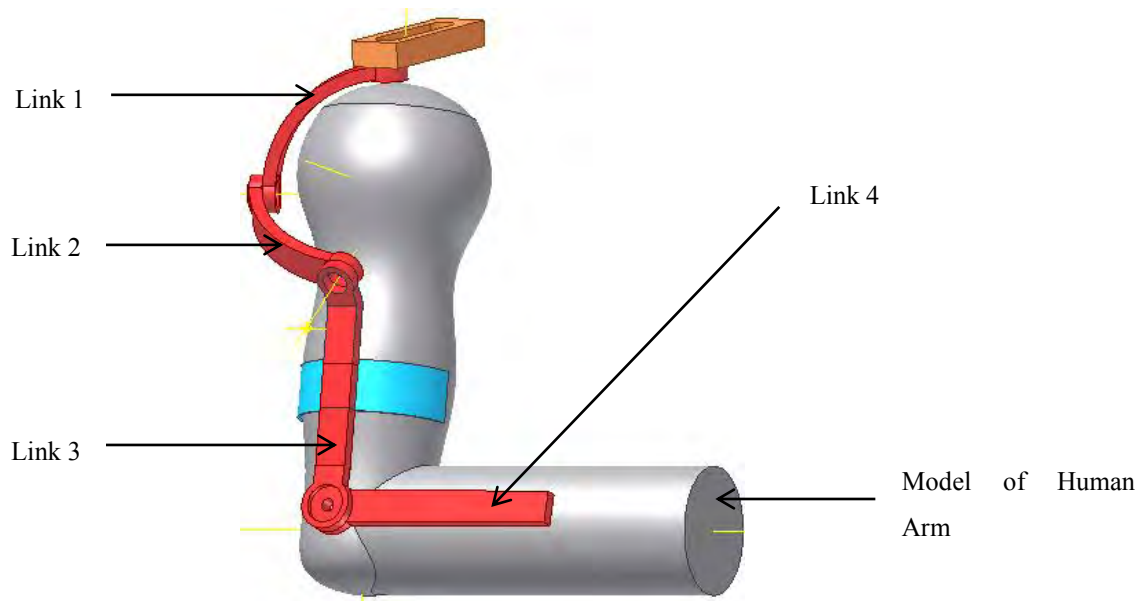


Figure 3.8: CAD of Shoulder and Elbow Conceptual Design on a Model of a Human Arm.

3.2.4 Exoskeleton Shoulder Joint Limits

The various joints were limited in order to prevent injury to the upper limb. These limits were explored via a CAD analysis. Figure 3.9 illustrates the maximum angle that is achieved by turning *joint 1* clockwise. The range of motion for *joint 1* was $\{-60^{\circ}; 120^{\circ}\}$; which was measured counter-clockwise from the frontal plane from above.

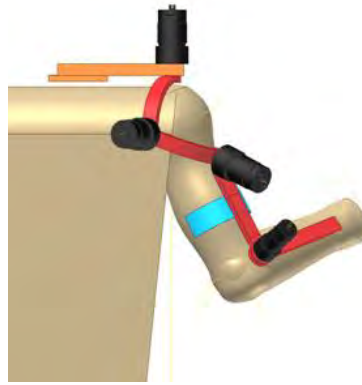


Figure 3.9: CAD. of Maximum angle at joint 1.

Flexion at *joint 2*, which was the anti-clockwise rotation of link 2 with respect to link 1, was inherently limited due to the collision of links 1 and 2 at the borders of the workspace therefore acting as mechanical stops. The extension of *joint 2* (clockwise rotation of link two relative to link one) was limited to 150° in order to prevent collision of the patients arm with their torso. Therefore the range of *joint 2's* motion was $\{30^{\circ}: 150^{\circ}\}$, measured anti-clockwise from link 1. The above described collision can be seen in Figure 3.10.

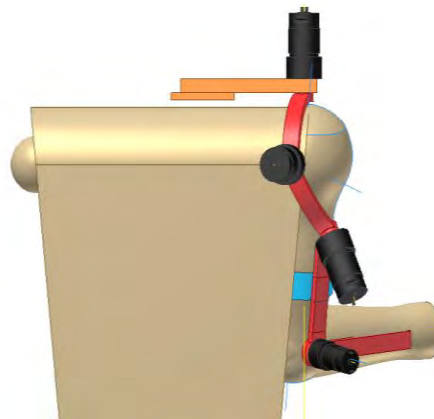


Figure 3.10 CAD of Maximum Joint 2 Angle

Joint 3's angle was measured as a clockwise rotation of link 3 relative to link 2. Link two collided with the users arm during maximal medial rotation (Figure A.2). The lateral rotation and flexion of the upper arm was as a result of decreasing *joint 3's* angle. This joint was limited to prevent hyper

rotation of the shoulder (collision does not occur). This joint angle range was about $\{135^{\circ}: 300^{\circ}\}$. The maximum *joint 3's* angle can be seen in Figure 3.11.

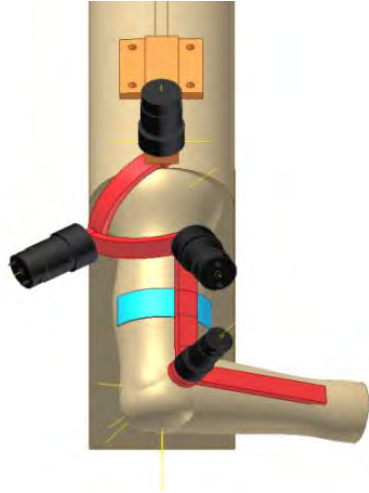


Figure 3.11: CAD of Maximum Angle of Joint 3

3.2.5 Physical Configuration

This subsection provided an overview on the design in terms of its adjustability, mechanical loading and the torques and forces acting on the exoskeleton.

3.2.5.1 Adjustability

The angles between *joints 1* and *2* and *joints 2* and *3* are 90° and 75° , respectively. These joints were mutually intersecting and were connected by curved links. This link layout allowed for a maximum user size of dimension according to the 95th percentile human being. The first shoulder joint was vertically above the GH joint. This would be attached to the stand which supported the exoskeleton mechanism. Link 3 which joined the shoulder and elbow mechanisms was adjustable to accommodate various upper arm lengths up until the 95th percentile. This was easily achieved using a slot and two bolts with the two links sliding into each other. The carry angle adjustable mechanism was created by adding a joint in between the link that connected joint three and the elbow joint (link three). This joint would effectively act as a hinge and would be fastened tightly at the desired position. The

forearm (link 4) was also adjustable and was designed so that two pieces of square tubing could slide concentrically and then be fastened at the desired position. This was further explained in the construction overview section.

3.2.5.2 Mechanical Loading

A major inconvenience with a serial arrangement was that the entire load was endured by a single serial arm. Hence the moments/torques created by the exoskeleton and the upper limb would propagate through the mechanical structure. Each joint experienced either a rotating torque or a bending moment that was created by the various loads acting along a moment arm. The orientation of the joints would determine whether the load would act as a joint rotation (torque rotation) or as a bending moment across the joint axis. The difference can be seen in Figure 3.12, below, by joint one and two. The greatest moments would be experienced when the arm was out stretched and flexed or abducted along the horizontal plane of the GH joint. Figure 3.12 illustrated that *joint 1* would experience a bending moment across the joint axis, whereas *joint 2* would encounter a torque load that would be endured by the actuator drive. The third and fourth joints would experience a combination of torque loads and bending moments because their axes were not orthogonal to the horizontal plane along which the upper limb is positioned (Figure 3.12). This meant that the joints had to be designed to withstand both axial and radial loads as a result of the respective high torque and bending moments. These joints had to be designed and engineered to handle these loads.

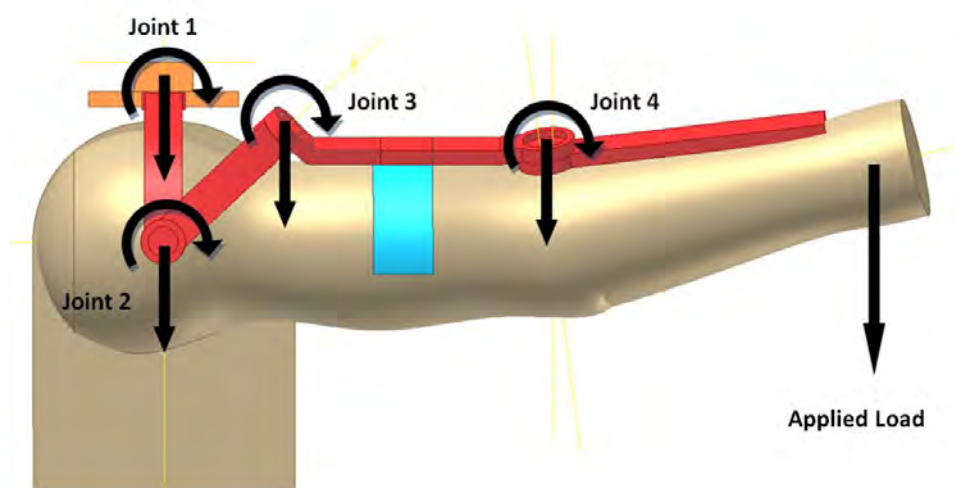


Figure 3.12: CAD Illustrating the Load on the Joints, in Worst Case Pose

3.2.5.3 Torque and Force Calculations

The worst case pose was illustrated in Figure 3.12, and modelled as a cantilever beam along a horizontal plane. Any manipulation of this pose (arm extended) along that plane would result in a maximum loading condition. The research was designed around the 95th percentile being which accommodated a larger and heavier arm. An excel document was created in order to calculate the moments of the exoskeleton at the worst case position (Figure 3.12). The exoskeleton was modelled as a cantilever beam with a negligible cross-sectional area as compared to the length. This meant that the structure was more likely to fail in bending than by shear forces, which was realistic in this research. The loading conditions were applied making reasonable assumptions as follows.

- The weight of the human arm was applied as point loads for the individual segments and positioned at their relevant centres of mass. The weight would be propagated to the exoskeleton arm at the relative points of attachment (the retainers and wrist device). This meant that total generated torque would be equivalent when stationary as illustrated in Figure 3.13. The total moments about the joints could be calculated; this assumption was valid and may have yielded a slight error in the deflection calculations. However the deflection calculations did not need to be very accurate because the tolerance for error with respect to the amount of deflection before failure was less conclusive than the margin of error with respect to that for failure of components due to yielding. The 95th percentile parameters of men are illustrated in Table 3.3.
- The motors and geared drives were responsible for majority of the weight of the exoskeleton structure. Therefore in order to do calculations the motor weights and the frame were estimated and updated throughout the research until the motors were chosen and only then were these values accurately known. Each motor was named according to their relative joint e.g. the motor for *joint 1* would be called motor 1. The motor weights were modelled as point loads and the exoskeleton structure as a Uniformly Distributed Load (UDL). An Excel spread sheet was created to obtain the bending moments; this allowed for easy change in parameters (such as motor weights) and retrieval of the according results. This spread sheet can be seen in Appendix A.3 together with the relative formulae and abbreviations used to perform the calculations. The deflection calculations were also calculated in the spread sheet. Involuntary muscle responses due to neurological damaged was considered to be momentarily. These responses were omitted from the calculations has the instantaneous nature of the response may only result in a stall of the motor for the duration of the response. This stall was considered to be the worst case situation which will not have an impact in this research.

- The 2 kg research specification load was applied as appoint load at the hand (end effector). This value was included in the Excel spread sheet and was used for the selection of the motors.

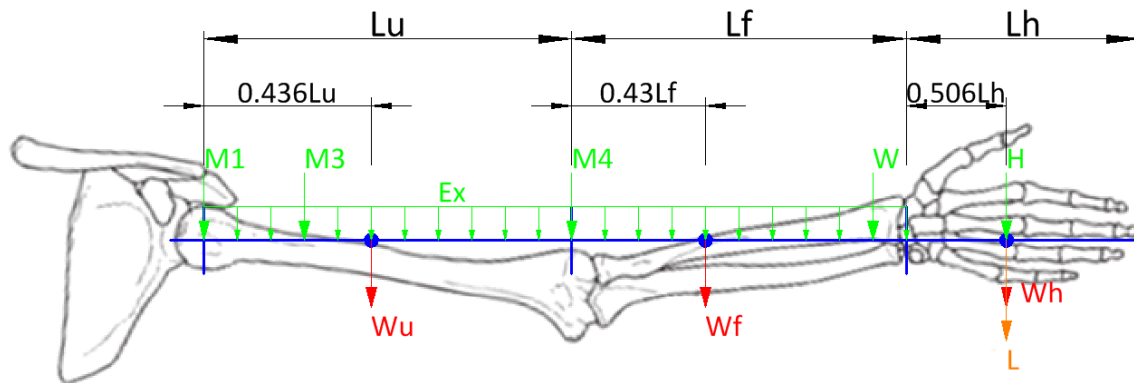


Figure 3.13: Simplified Force Diagram of Upper Limb in Worst Case Pose

Figure 3.13 is further explained in Appendix A.3. The above described excel spreadsheet would be referred to as the *Torque and Forces Calculation Spreadsheet*.

Table 3.3: Approximate Weight, Centre of Mass and Length of Large Male

	Approximate weight of body segment (N) [40]	Position of centre of mass (% of length proximal) [7]	95 th percentile man approximate length, joint to joint (mm) [7]
Upper Arm	26.5	0.436	355
Forearm	15.2	0.43	310
Hand	5.3	0.506	205

3.2.6 Material and Link Structure

This subsection described the chosen material as well the structure of the links.

3.2.6.1 Material

The choice of material required for manufacturing of the exoskeleton mechanism was affected by a few factors. These factors included cost, stiffness, weight and corrosion. The specific strength of the material could be calculated by dividing the material's strength by its density [41]. A high specific strength resulted in a high strength to weight ratio. Materials such as titanium and composites were considered however these materials were expensive and difficult to machine. Aluminium was favourable according to the above described factors. This metal was compared to other materials from a Hulam product catalogue as illustrated in Figure 3.14. The specific strength of aluminium, copper, steel and plastic was 25.5, 14, 27 and 2 MPa/(kg/m³), respectively. Steel and aluminium were both within the budget of the research. However, the density of steel and aluminium were 8900 and 2700 kg/m³, respectively. This made aluminium more favourable as it was approximately three times lighter with a similar strength to weight ratio. Other benefits of aluminium included its resistance to corrosion under atmospheric conditions due to the passive oxide layer formed, good machinability, availability and affordability. Therefore aluminium was chosen for the exoskeleton manipulator design and the wrist and hand mechanism as these components needed to be machined and manufactured as well.

	Aluminium 6063	Copper	Steel 371	Plastic
Strength / Breaking strength MPa	225	250	400	50
Ductility / Expansion %	10 to 24	25	20	25
Elasticity E, Young's modulus MPa	69 000	125 000	210 000	3 000
Density kg/m ³	2 700	8 900	7 800	1 400
Melting point °C	600 to 655	1 080	1 500	80
Working temperature range	-250 to 150	-200 to 300	-50 to 500	-50 to 80
Electrical conductivity m/Ohm-mm ²	35	55	7	-
Heat conductivity W/mK	200	400	76	0,15
Coefficient of linear expansion x 10 ⁻⁶ /°C	23	17	12	60 to 100
Non-magnetic	Yes	Yes	No	Yes
Weldable	Yes	Yes	Yes	Yes

Figure 3.14: Physical Properties of Aluminium Compared With Other Common Materials[42].

3.2.6.2 Link Structure

Structures were commonly used to withstand high bending loads [41]. The moment of area could be increased by implementing a 'structural' cross section which maximised stiffness and bending resistance while minimising the weight as compared to a solid structure. A trade-off between a high moment of area and a compact design needed to be made due to space constraints. The minimum moment of area allowing less than 5 millimetres of deflection was 18134 mm^4 . This was calculated using the *Torque and Forces Calculation Spreadsheet*, Appendix A.3.

A C-section structural design was chosen as it could be easily machined at a radius and it fitted most appropriately into the joint design. The dimensions of the C-section were chosen according to Table A.1 in Appendix A.4. These dimensions yielded a major moment of area of approximately four times that of the minor moment of area. The C-section was therefore positioned with the major axis and minor axis perpendicular to the human arm and tangent to the outside of the human arm respectively. A description of the C-section was illustrated by Figure A.6 in Appendix A.4. The reserve factor, determined as the maximum yield stress over the material yield strength, for yielding was found to be 2, which proved that material yielding of the structure, was not a problem; this is shown in Appendix A.4 as well.

3.2.7 Actuators

Electric actuation was chosen for the reasons outlined in chapter 2, it was essential that the motors were geared in order to provide the high torque requirements, which would be further discussed in this section. The *Torque and Forces Calculation Spreadsheet* in Appendix A.3 yielded the following moments at the individual joints for a 2kg end-effector load (rounded off to the nearest unit):

- Motor 1 = 48 Nm
- Motor 2 = 48 Nm
- Motor 3 = 38 Nm
- Motor 4 = 18 Nm

However, these were not the true actuation requirements for example, motor 1 referred to the bending moment experienced by the shaft and not the torque required by the motor. The motor torques could be calculated by basing the joint torques according to the human isometric strength (HIS). The HIS referred to the strength at which motion no longer occurs- analogous to the stall torque of a motor. The required output strength was between 1/8 and 1/4 of the average HIS [32]. Therefore the motor's

operating torque and stall torque would be taken as 1/8 and 1/4 of the HIS respectively. The human arm was considered in the HIS and only the torques created by the exoskeleton manipulator needed to be investigated. The HIS of each motion of the shoulder and elbow is specified in Table 3.4.

Table 3.4: Human Isometric Strength [Adapted from [43]].

	DOF	Torque (Nm)
Shoulder	Flexion/Extension	110
	Abduction/Adduction	125
	Medial/Lateral Rotation	-
Elbow	Flexion/Extension	72.5
	Supination/Pronation	9.1

The shoulder joints would provide a combination of therapy motions; it was therefore decided that each actuator would have the same strength. From this strength analysis the motor torques (M1, M2, M3 and M4) required were:

- M1, M2, M3 = 15.6 - 31.3 Nm
- M4 = 9.1 - 18.1 Nm

The *Torque and Forces Calculation Spreadsheet* was adjusted to obtain the weight moments created by the exoskeleton manipulator, these values are tabulated in Table 3.5. The weight moment at *joint 1* had no effect on the required motor torque. *Joint 2* experienced the entire moment at the worst case pose. *Joint 3* reached a minimum of 45 degrees to the weight moment axis, and the added torque was adjusted accordingly. The elbow mechanism was assumed to be parallel to the weight moment axis.

The torque requirements for each motor were tabulated in Table 3.5.

Table 3.5: Total Torque Requirements for Each Motor (Nm)

	Weight moment of Exoskeleton	Required Torque Moment of Exoskeleton	Required Torque 1/8 Human Strength	Required Torque 1/4 Human Strength	Required Operating Torque	Required Stall Torque
Motor 1	17.2	0.0	15.6	31.3	15.6	31.3
Motor 2	17.2	17.2	15.6	31.3	32.8	48.5
Motor 3	13.2	9.3	15.6	31.3	24.9	40.6
Motor 4	5.3	5.3	9.1	18.1	14.4	23.4

Electric DC motors manufactured by Kollmorgen, Maxon, Parvalux and Doga were investigated and compared. The Maxon and Kollmorgen motors were not affordable because separate gear drives were required. These motors also became bulky with attachment of the additional drives and were not used. A 12 V power supply was implemented because a wide range of this voltage source were commercially available to provide high current supplies. The Doga motors that were considered for selection was therefore 12 V in order to be powered by a 12 V power supply. The torque, speed and weight of the motors were tabulated in Table 3.6 in order to select the desired motor.

Table 3.6: Doga Motors Selection Matrix

Class Code	Weight (kg)	Torque(Nm)				Nominal speed (rpm)	Transmission Ratio
		Nominal	Short Operation	Start	Stall		
316	0.9	2	5	10	13	38	62:1
111	1.25	6	12	25	25	25	62:1
319	1.7	8	30	50	60	45	81:1
119	2.5	8	16	30	40	40	50:1
258	3	15	35	80	80	25	52:1

Friction was included in the torque speed curves provided by the manufacturer and this included the gearbox. Therefore all the friction was taken into account and the net torque values were read from the torque speed curves. The motors were chosen to match the requirements tabulated in Table 3.5

The chosen motors are illustrated in Table 3.7 and their catalogue information can be seen in Appendix A.4.

Table 3.7: Final Motor Selection

	Chosen Motor	Motor Short Operation Torque	Motor Stall Torque	Required Operation Torque	Required Stall Torque
Motor 1	111	12	25	15.6	31.3
Motor 2	319	30	60	32.8	48.5
Motor 3	319	30	60	24.9	40.6
Motor 4	111	12	25	14.4	23.4

3.2.8 Joints

The shaft bearing of the 111 and 319 Doga motors could only withstand a radial load of 3 Nm and 5 Nm respectively [44]. This meant that the bending moments had to be transferred to the joints and not the motor shaft. This problem was solved by placing a ball bearing in the joint at a distance from the motor bearing. This placement resulted in smaller radial loads between the two bearings which minimised the force acting on the motor shaft. The final joint design is illustrated in Figure 3.15 with all parts rigidly connected to the motor rotor and stator was hatched in blue and red respectively. The links needed to move independently without self-collision and these links were then mounted on different spherical planes, with link 1 on the outside of link 2.

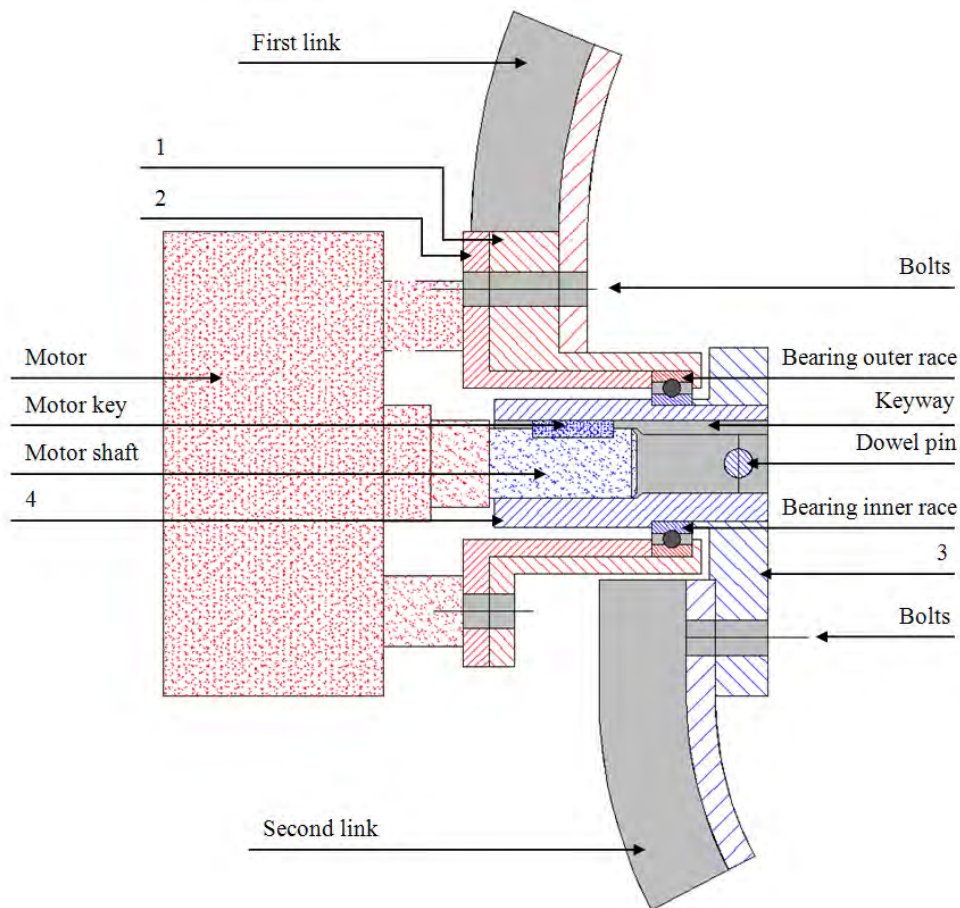


Figure 3.15: CAD Illustrating the Various Components to the Joint Design.

The motor was mounted on part one and two which were also responsible for holding the bearing in place. A tight rigid fit was created by using the same bolts to mount the motor, fasten the two parts and connect the link. Part three provided the connection of the next link and the joint rotor. A dowel pin joined part three and part four with the inner race of the bearing clamped between the two parts. The second link was connected to the motor shaft through a coupling which was interfaced via a key and keyway. The first link was connected to the second link only through the bearing.

3.2.9 Final Shoulder Design

The final shoulder and elbow mechanism is illustrated in Figure 3.16. The 90° , 75° and 45° angles represent θ_1 , θ_2 and θ_3 respectively and these angles satisfied inequalities 3.1 and 3.2.

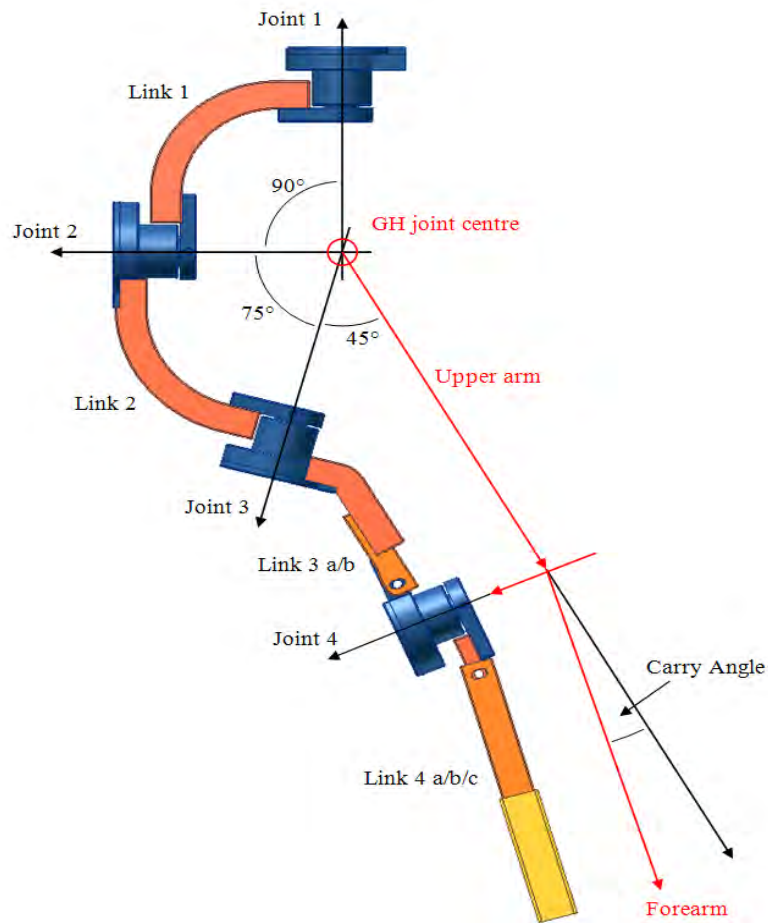


Figure 3.16: CAD of final shoulder and elbow mechanism.

Figure 3.16 also illustrates the accommodation for the carry angle. This accommodation can be varied by adjusting link 3a and link 3b relative to each other as previously explained.

3.3 The Wrist and Hand Mechanism

The wrist and hand mechanism were designed around the shoulder and elbow mechanism. The reason for this was because supination/pronation and the opening and closing of the hand were less complicated as compared to the shoulder and elbow mechanism. Also the spherical workspace was dependent on the shoulder and elbow mechanism and not the wrist and hand mechanism. The following sub sections will discuss the design of the wrist and hand mechanism. The wrist mechanism was based on the ARMin II exoskeleton as discussed in chapter 2.

3.3.1 The Wrist Mechanism

The steel cable actuation in the ARMin II was modified and a more direct method was preferred as explained in chapter 2. A number of conceptual designs were created these designs can be seen in Appendix A.5. The spur gear concept was chosen according to a selection matrix which is also illustrated in Appendix A.5 as Table A.3. The spur C-gear rotates about an axis which was co-linear to the patients forearm. This common axis allowed for the transfer of mechanical power to the end-effector which resulted in the supination and pronation movements. The final design consisted of a semi-circular gear which rotated within a slot about the co-linear axis. The C-gear was meshed with the pinion gear which provided a 5:1 gear ratio. This ratio was created for dimension purposes according to the 95th percentile being and not as a torque or speed requirement. The pinion gear was powered by a DC motor via a coupling and a keyway. The gears were encased in a gear cover which prevents exposure of the gear teeth and provided a mounting in which the forearm mechanism can be joined to the wrist mechanism via a U-tube. The pinion gear was designed to have an extended shaft which was supported by a ball bearing. This minimised any load on the motor shaft which resulted in a minimal torque application, as the wrist mechanism only provided the rotational movement. This mechanism can be seen in Figure 3.17. The gear concept without the gear cover is illustrated by Figure A.9 in Appendix A.5. The C-gear can be seen in the construction section of this chapter.

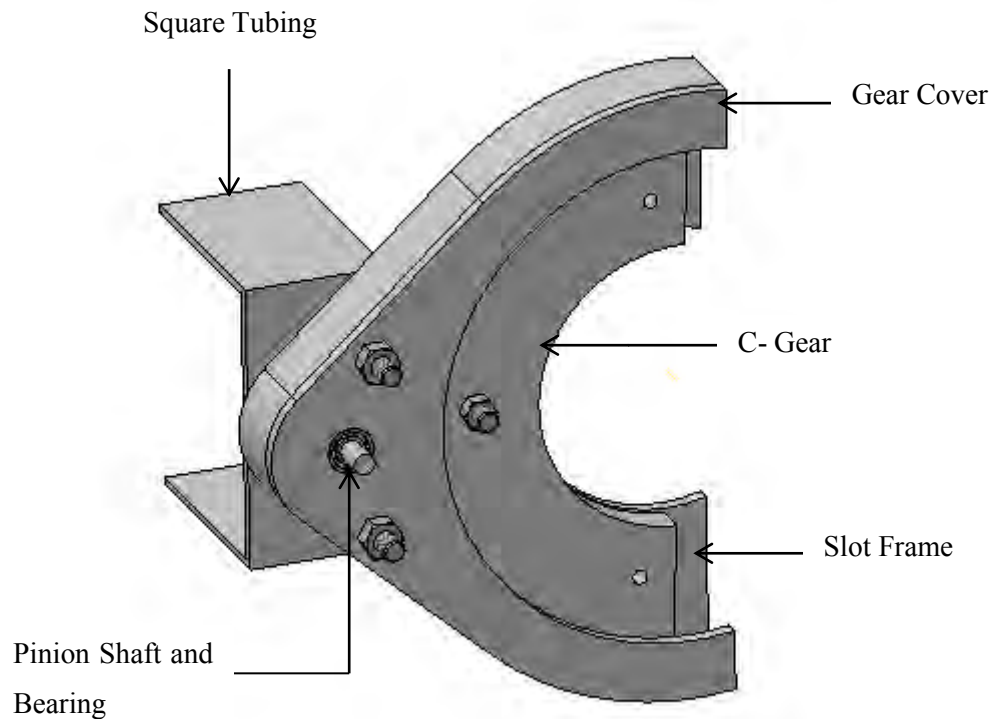


Figure 3.17: Spur gear concept- view one

3.3.2 Parameter analysis

Finite Element (FE) analysis was conducted in order to verify that minimal loads and deflections were experienced by the C-gear. The FE analysis modelled the tangential and radial forces produced by the pinion gear as well as the end-effector load of 2 Kg. The radial and tangential forces were taken according to a motor that would supply 0.59 Nm of torque. This motor torque would apply a rotational force of 8.85 Nm which was 97.25% of the HIS and is more than required as explained in the shoulder design. The motor chosen was a Solar Robotics 360 Miniature Motor it was chosen for its small dimensions and required torque output. The deflection and stress analysis can be seen in Figure 3.18 and Figure 3.19 respectively. A displacement of 0.1433mm in the Z axis was produced which was acceptable in this research design.

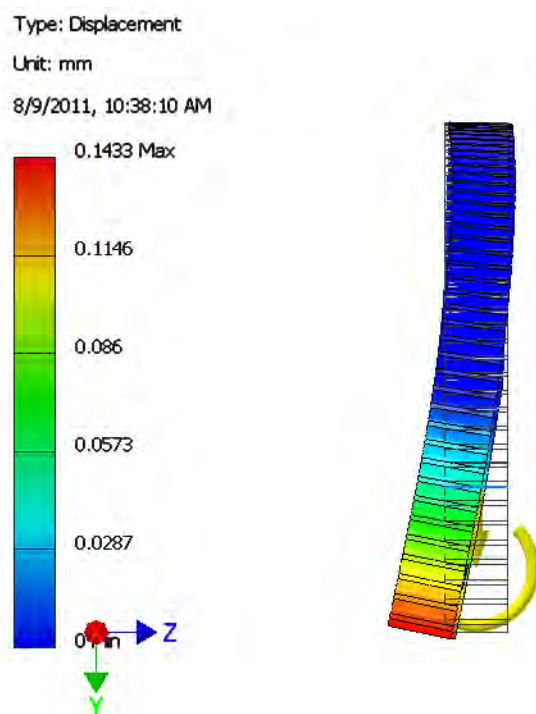


Figure 3.18: Deflection analysis of the C-gear.

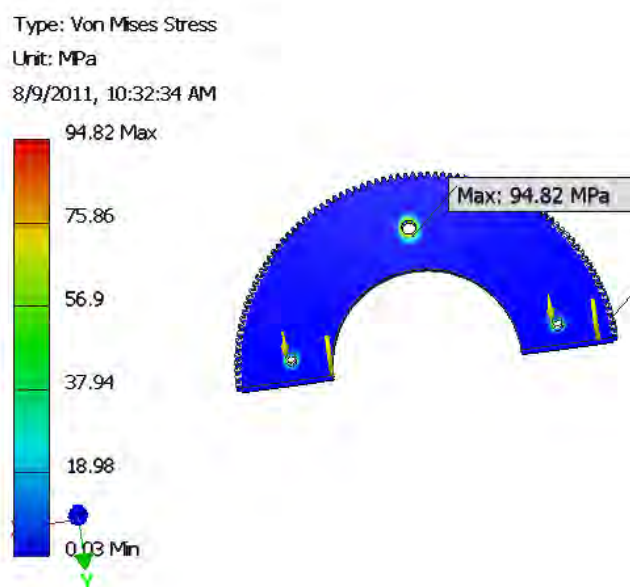


Figure 3.19: Stress analysis of the C-gear

The stress analysis produced a Von Mises Stress of 94.82 MPa which was well within the range according to the aluminium properties specified in Figure 3.14.

Fatigue calculations are shown in Appendix A.6 and it was concluded from these calculations that the C-gear would not fail under fatigue loading conditions.

3.3.3 The Hand Mechanism

The prototype hand mechanism was of the lowest priority and it provided the physiotherapy of the gripping motion. This mechanism was built around the biological hand to provide physiotherapy and physical gripping which may be useful in future developments. The supination and pronation movements were further propagated through the hand mechanism. The design catered for connection between the wrist and hand mechanisms. The movement of the thumb and fingers were necessary for rehabilitation of the gripping function, therefore physiotherapy to these regions would be provided by this mechanism.

The patient's thumb and fingers slot into two separate curved tubes, which consisted of a circular slot for the thumb and a grid which allowed for insertion of the individual fingers. The connection to the wrist mechanism allowed for movement of the thumb encasement as well as the supination and pronation rotation. The prototype hand design concept can be seen in Figure 3.20.

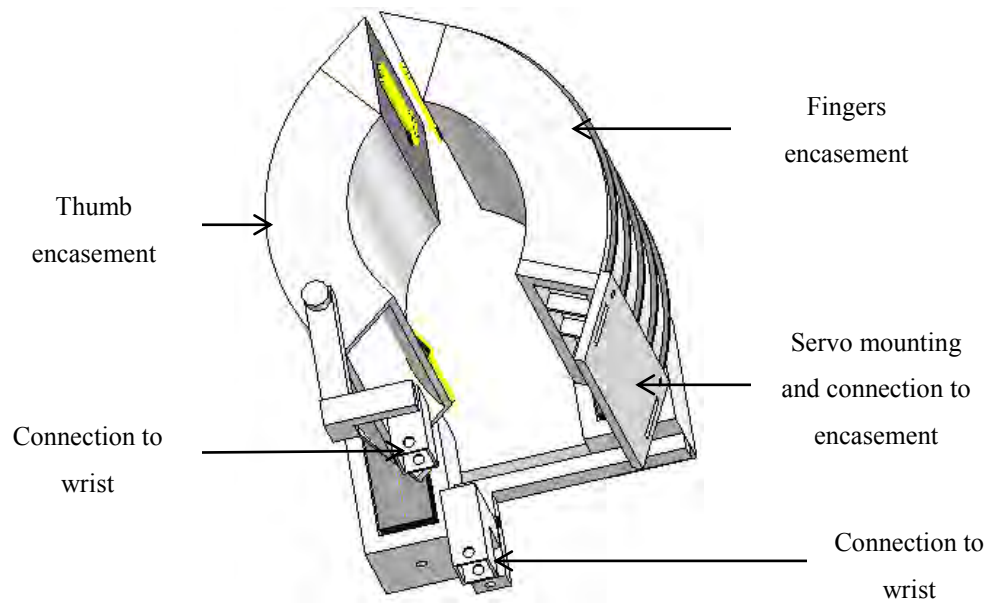


Figure 3.20: Final Prototype design of the Hand mechanism.

A FE analysis was conducted in order to verify that minimal loads and deflections are experienced by the mechanism. The stress and deflection analysis was modelled for a load of 2 kg end-effector load. However, this load was purely for illustrative purposes, the primary objective of this mechanism was to produce the movement in the gripping region as well as propagate the wrist motion. The stress analysis yielded a minimal stress of 1.815 MPa which can be seen in Figure 3.21.

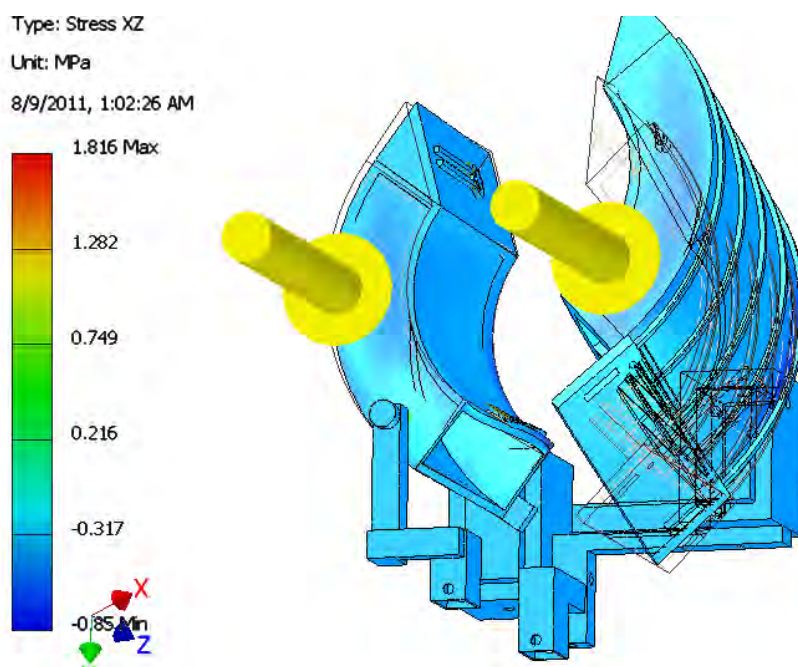


Figure 3.21: Stress analysis of the hand mechanism

A deflection of 0.026 mm in the load direction was experienced by the mechanism under the, above described, loading condition. This deflection was minimal and can be seen in Figure 3.22.

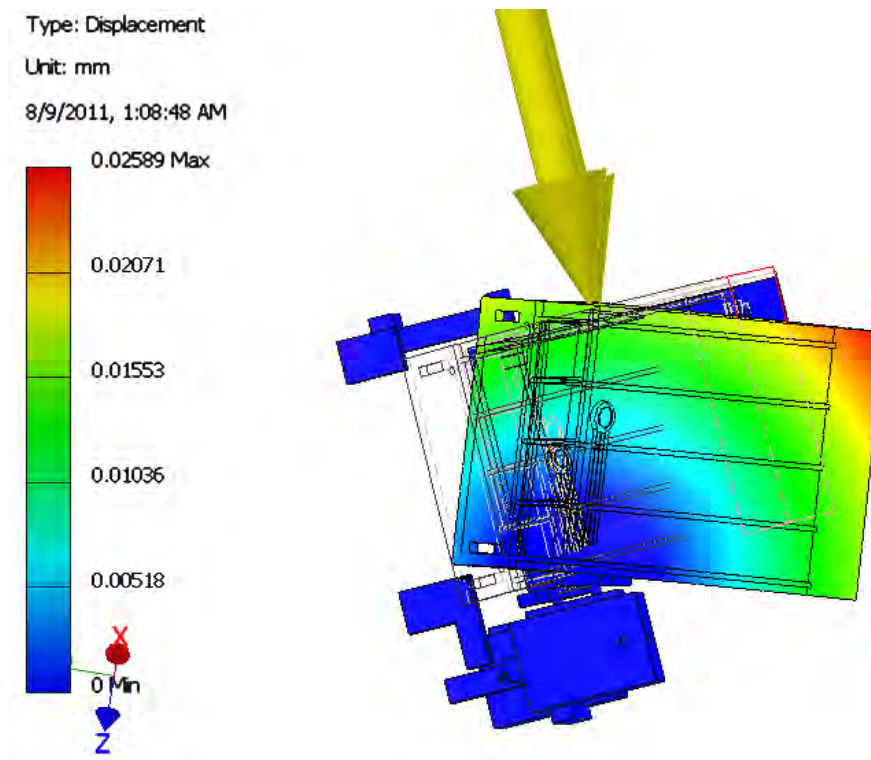


Figure 3.22: Deflection analysis of the hand mechanism

3.4 Construction Overview

3.4.1 Shoulder Construction Overview

The profile of the links of the shoulder mechanism was wire cut and then CNC milled to produce the C-shaped structure. The joint couplings were turned from a 22 mm round bar and their relative key ways were cut using a vertical broaching machine. The dowel pin was press fitted. The final link 1 component can be seen in Figure 3.23 (a) and a complete joint assembly is illustrated in Figure 3.23 (b).

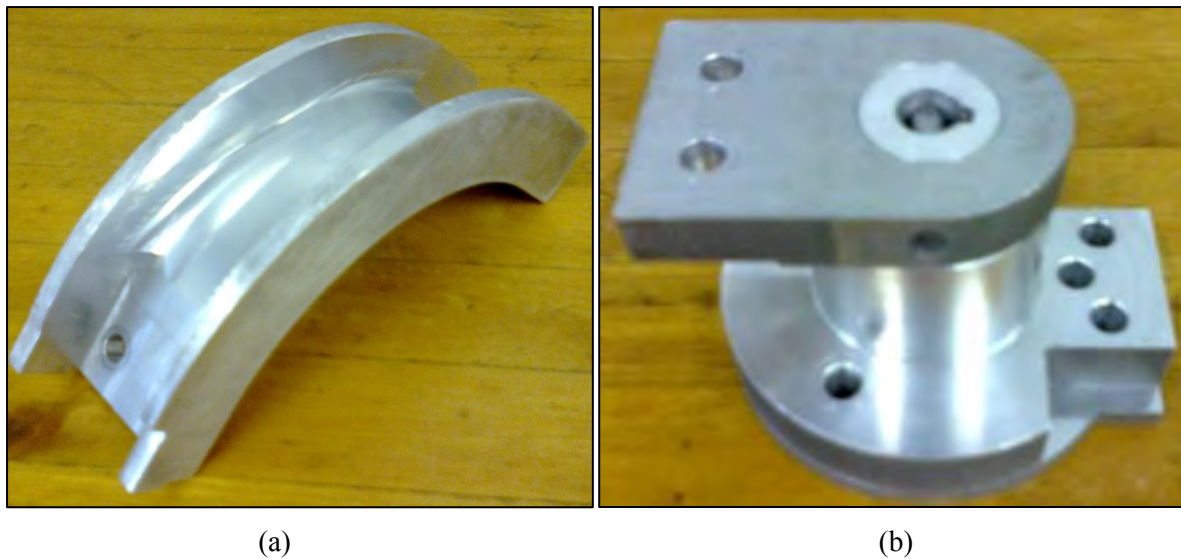


Figure 3.23: (a) Final construction of link 1, (b) and a complete assembly of joint 1.

The link 3a/b catered for length and carry angle adjustability. The bolt that joined joint 4 and link 3b was allowed to move in a slot which could be fastened to the desired position using the bolt and a washer. This movement in the slot provided the carry angle adjustability and can be seen in Figure 3.24.



Figure 3.24: Final construction of link 3a/b.

The forearm link was wire cut in order to achieve the vertical slot along which the square tubing would slide along and fasten at the desired position by 2 bolts and washers. The manufactured forearm link, link 4a/b/c, is shown in Figure 3.25.

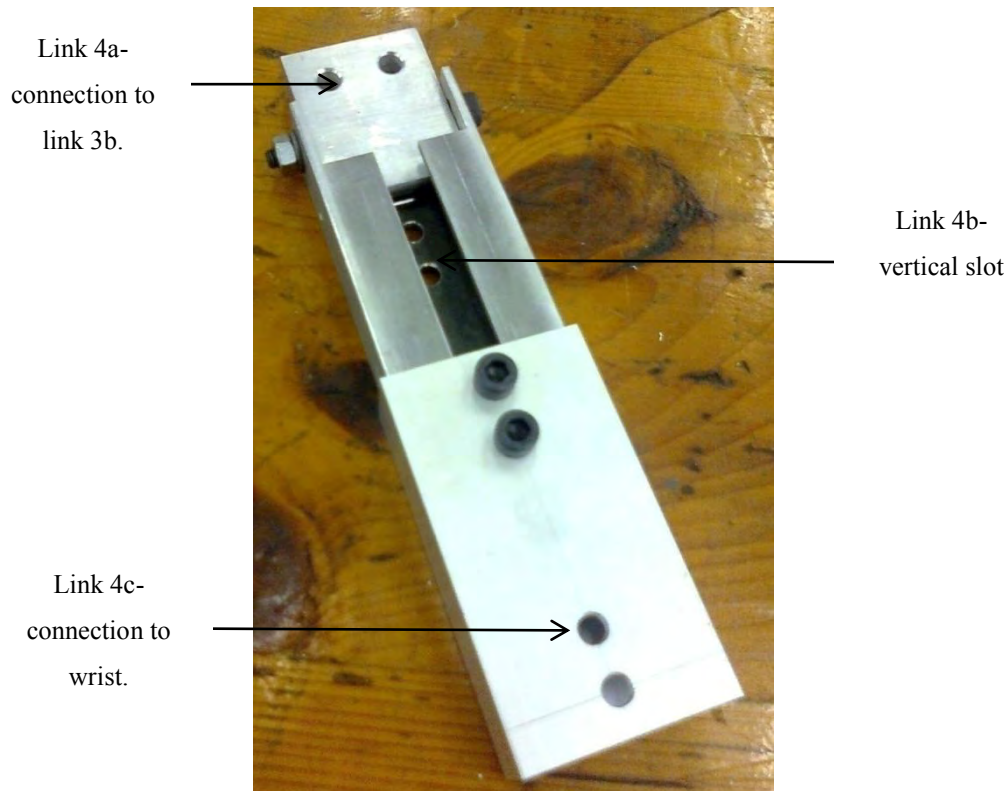


Figure 3.25: Manufactured forearm link (link 4a/b/c).

3.4.2 Wrist and Hand Construction Overview

The pinion and C- gears of the wrist mechanism were wire cut with a pitch circle diameter (PCD) of 32 mm and 160 mm respectively. Both gears consisted of a module of one. The gear casing was machined using a CNC machine. The pinion gear, the C-gear and the gear casing can be seen in Figure 3.26 (a), (b) and (c) respectively.

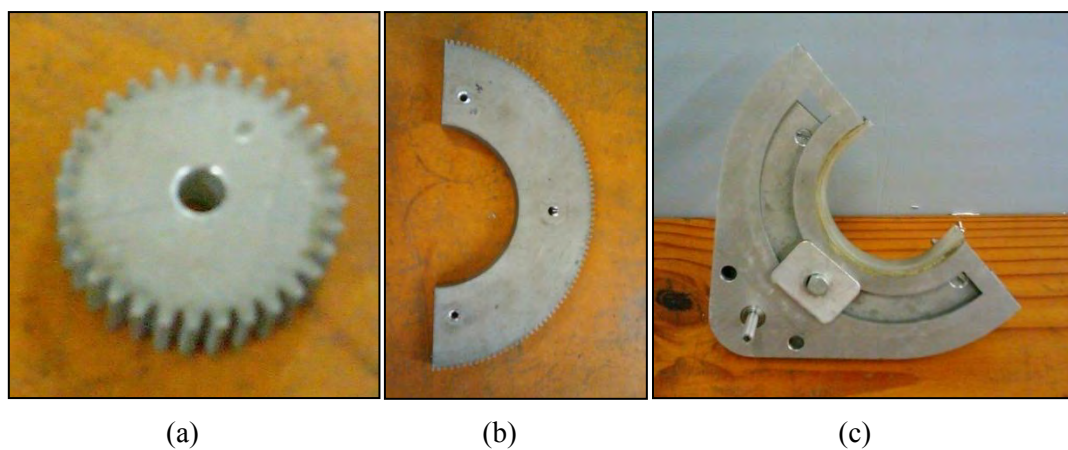


Figure 3.26: (a) Pictures of the manufactured spur pinion gear, (b) C-gear, (c) and gear encasement with assembled components.

Figure 3.27 illustrates the machined key which runs within the slot and prevents the C-gear from deviating away or out of the slot.



Figure 3.27: Picture of final machined key

The hand mechanism was manufactured by bending sheet metal into an arc of the required length and radius. The bent sheets were then welded to flat arced shape sheets which were 25 mm wide. A grid was designed to allow for the insertion of the four fingers and solid sheet with a singular hole for the thumb, which was machined. The servo mountings were welded together from sheet metal and they connect to the C- gear and the arced tubes. The arced sheet, the bent arcs, the grid and servo mounts can be seen in Figure 3.28 (a), (b) and (c) respectively.

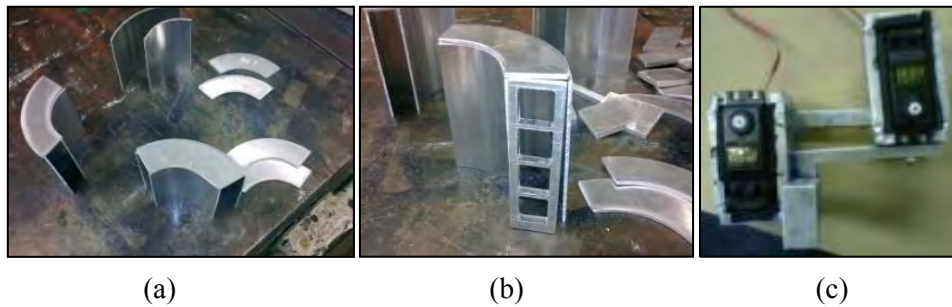


Figure 3.28: (a) Picture illustrating the sheet metal pieces, (b) the grid for the fingers, (c) and the servo mounts.

The assembled hand mechanism is shown in Figure 3.29. Melamine foam (sponge-foam) was placed inside the tubing to provide more contact between the walls of the tubing and the biological fingers and thumb, and proved to be successful.

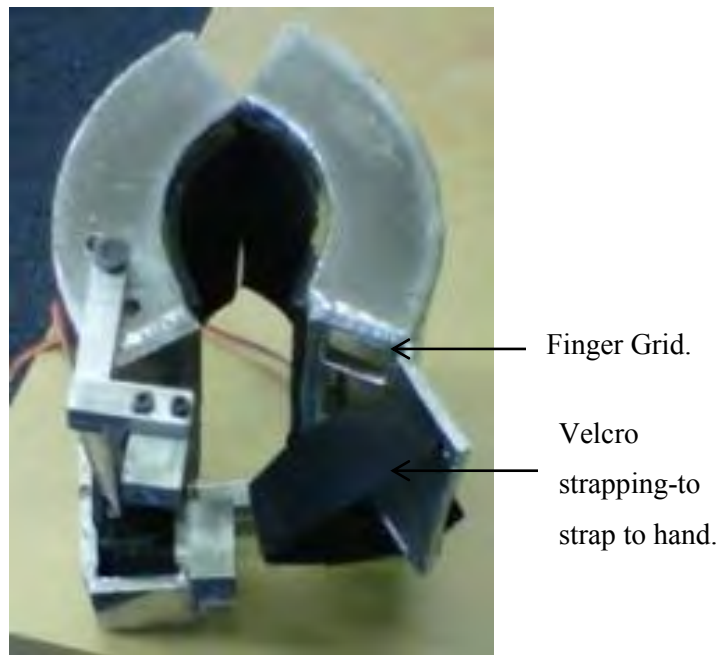


Figure 3.29: Picture of the complete hand mechanism.

3.4.3 User Interface and Final Prototype.

The exoskeleton mechanism had to interact with the user comfortably. This was achieved by using support retainers that could be attached to the user using Velcro straps. These retainers were placed at the upper arm and forearm. All sharp edges of the exoskeleton were filed and smoothed.

A portable stand was created and it allowed for adjustability via a telescopic layout of square tubing. The stand supports the exoskeleton mechanism and allows for physiotherapy while standing or sitting. The stand, the retainers and the entire exoskeleton mechanism can be seen in Figure 3.30 as a final prototype. The stand experiences a maximum moment of 52.4 Nm which is slightly greater than that that experienced by joint 2 at the worst case pose. The main concern was to balance the stand and this was easily achieved by designing a base that was greater than the centre of mass of the exoskeleton device.

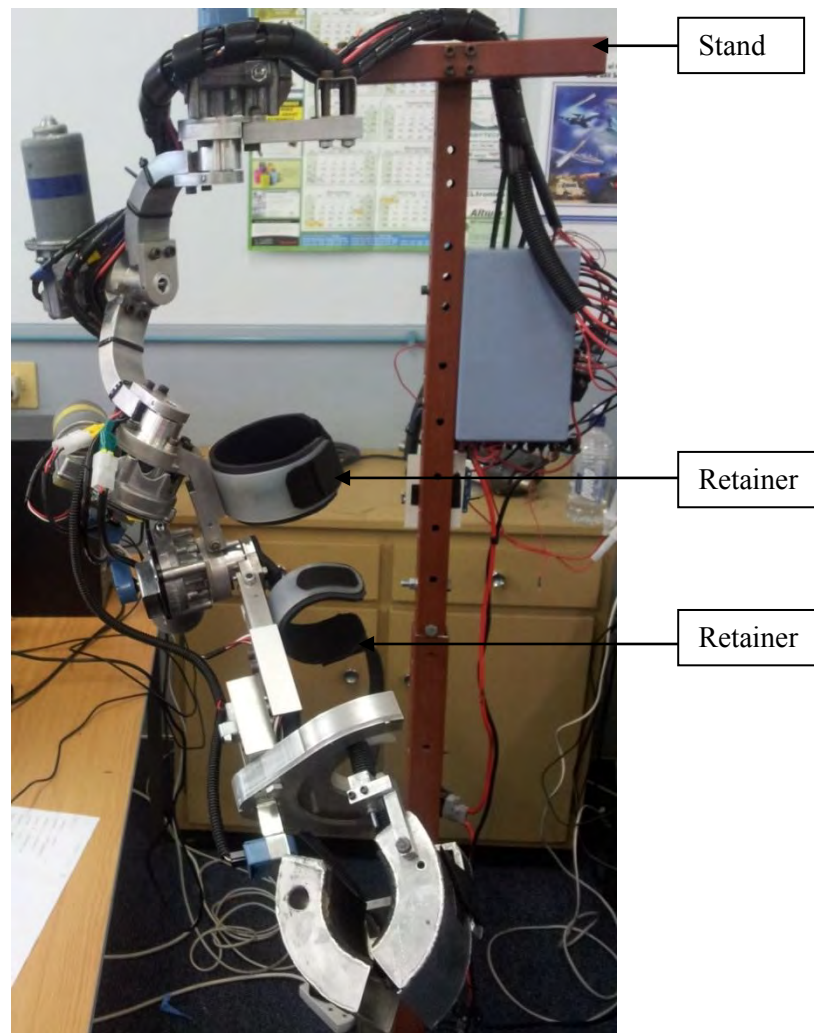


Figure 3.30: Final exoskeleton prototype mechanism with stand support.

3.4.3.1 Mechanical Stops

With the mechanical structure assembled, the finer details could be completed. The mechanical stops were the major final adjustments that had to be made. These stops were put in to place to ensure that if the control system malfunctioned the arm would not be driven beyond the human arm's workspace, thus preventing hyper extension/flexion of the joints. A decision was made in the design phase, not to include the mechanical stops in the joint design, but to use the bolts and other parts of the assembly to act as the mechanical stops when they collide. This may not have been the most elegant approach, but it substantially simplified the already complex joint design, and allowed for a more flexible way of fine-tuning the joint limits to suit the desired workspace which still had to be tested with this prototype.

The mechanical stops for each of the four joints were implemented individually, but the three bolts used to mount the motors were used in most cases. This was done by selecting the use of washers, or shortening bolts, or filing away the edge of the links. The only joint limitation that could not be done this way was the joint 4 minimum angle. Joint 4 was inherently limited by the two cuffs clashing with each other. If the two cuffs gave way there was a point not too far beyond that at which link 4 would clash with link 3 and stop the mechanism before elbow hyper-flexion occurred. With a bit of custom modification, the joint limits were tuned; these joint limit values are evaluated in the workspace test of the mechanism in chapter 7.

3.5 Chapter Summary

The design of the exoskeleton mechanical structure was illustrated in this chapter. The mechanical manipulator was designed to achieve passive therapy by obtaining a workspace according to the ADL. The shoulder and elbow mechanism was prioritised as it was these mechanical structures that affected the workspace of the device as well as the position of singularities. The MGA exoskeleton was analysed and conceptual designs based on this exoskeleton were created and modified in order to create simpler actuation and a workspace that was unhindered by singularities. The spherical workspace of the mechanism was created without the need of mutually orthogonal joints; this was achieved by satisfying inequalities 3.1 and 3.2. The chosen concept met the established criteria and allowed for a platform on which the wrist and hand mechanism could be developed. The wrist and hand mechanism were of a lower priority when compared to the shoulder and elbow mechanism and were designed to integrate with the exoskeleton shoulder and elbow mechanism. A brief overview of the construction of the components was discussed and the final exoskeleton design was illustrated.

4 Exoskeleton Kinematic Models

4.1 Introduction

Kinematics is the scientific motion of a mechanism and it involves the position, velocity and acceleration variables of this motion. It does not take into consideration the forces or torques that cause this motion; these forces and torques constitute to the problem of dynamics [45]. This research investigates the relationship of the joint space and task space position of the exoskeleton manipulator and this relationship involves purely the kinematic analysis. The torque requirements at the joints have been calculated in chapter 3 and therefore any further dynamic analysis is not required to obtain the maximum torque values at the joints. The angular velocity is relatively low, less than one revolution per second, and accelerates and decelerates at a low gradient at start and finish respectively. This minimised the inertia created by the mechanism. The aim of this chapter is to derive the forward and inverse kinematics of the chosen manipulator in chapter 3. These kinematic models were implemented to allow singular joint motion as well as a combination of joint movements. Therefore the occupational therapist or physiotherapist would be capable of controlling individual or combinational joint movements. The combination of joint movements was a list of end-effector positions in the workspace and was initiated via a graphics user interface (GUI), which is described in chapter 5. The inverse kinematics assists the medical professional in positioning the end-effector at a position that would exercise a combination of joints. This model may also prove useful in any further development of this research.

The Denavit-Hartenberg (D-H) notation was used to create the fundamental kinematic models of the exoskeleton device and is a well-established method [34]. The D-H method involved setting up the individual joint frame axes and geometrically solving the D-H parameters. From this joint setup, the individual joint matrices relative to the previous joints could be solved; this allowed for the derivation of the forward kinematics and a further complex solution to the inverse kinematics, which was required for a combination of joint movements.

Forward and inverse kinematics are two positional kinematic models that allow for a relationship between the change in the joint angles and in the co-ordinate axes of the end effector. Forward kinematics is the calculation in X, Y and Z co-ordinates of the end effector by defining the desired joint angles. Whereas inverse kinematics is the opposite of forward kinematics and consists of complex calculations. These calculations compute the relative joint angles which will position the end

effector at the desired co-ordinate space relative to the base frame [34]. The base frame originates at the GH joint which was the intersection of joints 1, 2 and 3 as explained in chapter 3.

The exoskeleton was considered as an industrial manipulator as they both perform a similar task that of manipulating the position and orientation of the end effector. However, traditional exoskeletons or industrial robots consist of three mutually intersecting serial orthogonal joints which replicate the spherical motion produced by the GH joint. This joint layout places a singularity in the workspace of the mechanism but allows for more zero terms (cosine and sine terms are eliminated) in the transformation matrices, which will be explained further in this chapter. However this traditional layout was not implemented in the final design, in order to avoid placing a singularity in the manipulator's workspace, as explained in chapter 3. Avoidance of this singularity resulted in joints 3 and 4 being placed 75 and 45 degrees apart to joints 2 and 3 respectively. This joint layout resulted in more non-zero terms in the transformation matrices, which resulted in an extensive kinematic model. This chapter will introduce the method of forward kinematics and its benefits as well as inverse kinematic solver which was implemented in this research.

4.1.1 Kinematic Redundancy

In this chapter m represented the number of DOF in the joint space of the manipulator and n , the number of DOF that correspond to the task space in which the end-effector is positioned. The three shoulder joints and the elbow joint results in $m = 4$ and the positioning of the mechanism in the X, Y and Z co-ordinates resulted in $n = 3$. A redundant system occurs when $(m - n) > 0$ [46]. This redundancy results to multiple inverse kinematic solutions, as there are many different postures the manipulator could take to achieve the same end-effector position [34]. A non-redundant system is also known to be over constrained whereas a redundant system is an under constrained entity. A redundancy may be beneficial in a system especially in an iterative solutions as it may be used to enhance the proficiency of the manipulator's kinematics in terms of obstacle avoidance [47]. However the manipulator in this research did not need to avoid obstacles as there would not be an obstruction during the physiotherapy. This redundant advantage was therefore not further explored in the dissertation.

4.1.2 Kinematic Model Relationship

A kinematic model is described by its joints, link segments and joint constraints. Such a model is related according to a hierarchy structure. This meant that every joint can be related to the previous joint which can be further related to the base joint. As previously explained the base joint was positioned at the GH joint and is illustrated by axes X0 and Z0 later in this chapter. Each joint consists of its own frame axes, which related its orientation and translation to the previous joint [34]. Mathematically these joint frames are represented by transformation matrices, and each joint i consists of a transformation matrix ${}^{i-1}T_i$. Concatenating the joints allows for a joint to be related to a previous joint or for the joint to be related to the base co-ordinates. The relation was done in hierarchy order; from the base joint towards the end-effector. Thus the end-effector could be related to the base co-ordinates. This concatenation is achieved mathematically by matrix multiplication and is illustrated by equation 4.1 [34].

$${}^0T_N = {}^0T_1 {}^1T_2 \dots {}^{N-1}T_N \quad (4.1)$$

Where N is the number of DOF, the end-effector consisted of two degrees of freedom for the gripping function; however this function was to be activated separately from the kinematic model. The reason being that the kinematic model is purely for positioning the end-effector at the required rehabilitative position relative to the base frame. Therefore the DOF on the end-effector was omitted from this kinematic model but it would be implemented into the control software.

Equation 4.1 was used to create the forward kinematics which is the fundamental foundation of the kinematic model; as it would be used to determine the workspace and derive the Jacobian which was subsequently used to solve the inverse kinematic problem. These aspects will be examined further in this chapter.

4.2 Redundant Kinematic Model

The exoskeleton manipulator was redundant; however for rehabilitation methods it was essential that the mechanism could provide motion in the elbow and shoulder, as these are the dominant joints in the upper limb. The combination of these four joints resulted in a redundant positional task space of

the mechanism. It was therefore decided to derive both redundant and non-redundant kinematic models and provide separate control for the elbow in the non-redundant model. The control of the elbow in the non-redundant model would be explained in the control architecture chapter.

4.2.1 Forward Kinematics

The forward kinematics was used to determine the end-effector position, p , as a function of the joint angles $\vartheta = \vartheta_1, \dots, \vartheta_N$. The position, p , was an $(m \times 1)$ vector, in this case it was (3×1) which represented the X, Y and Z co-ordinates. This forward kinematic model is illustrated by equation 4.2 [48].

$$p = f(\vartheta) \quad (4.2)$$

The D-H method was employed to derive the forward kinematics. It involved the rotation and translation of the relative joints, as explained in section 4.1.2, and separated the translation and rotation of each joint frame into four parameters. These parameters were α_i , a_i , d_i and ϑ_i which represented the twist angle, link length, link offset and the joint angle of joint i respectively [34]. The transformation matrices for each joint were established, according to equation 4.3.

$${}^{i-1}T_i = \begin{bmatrix} c\vartheta_i & -s\vartheta_i & 0 & a_{i-1} \\ s\vartheta_i c\alpha_{i-1} & c\vartheta_i c\alpha_{i-1} & -s\alpha_{i-1} & -s\alpha_{i-1} d_i \\ s\vartheta_i s\alpha_{i-1} & c\vartheta_i s\alpha_{i-1} & c\alpha_{i-1} & c\alpha_{i-1} d_i \\ 0 & 0 & 0 & 1 \end{bmatrix} \quad (4.3)$$

Where $c1$ and $s1$ are $\cos(\vartheta_1)$ and $\sin(\vartheta_1)$ respectively. Table 4.1 illustrates the D-H parameters for the final design.

Table 4.1: Denavit-Hartenberg Parameter for final design.

i	α_{i-1}	a_{i-1}	d_i	ϑ_i
1	0	0	0	ϑ_1
2	$-\frac{\pi}{2}$	0	0	ϑ_2
3	$\frac{5\pi}{12}$	0	$L1.\sqrt{2}$	ϑ_3
4	$\frac{3\pi}{4}$	0	L1	ϑ_4
5	$-\frac{\pi}{2}$	0	L3	ϑ_5

These parameters were substituted in to equation 4.3 which resulted in the frame transformations of the manipulator and are illustrated by equations (4.4)-(4.8). L1 and L3 were the length parameters and represented the distances from the GH joint to the elbow joint and the elbow joint to the center of the end-effector respectively, these parameters varied with changes in adjustability and are illustrated in Figure 4.1.

$${}^0_1T = \begin{bmatrix} c1 & -s1 & 0 & 0 \\ s1 & c1 & 0 & 0 \\ 0 & 0 & 1 & 0 \\ 0 & 0 & 0 & 1 \end{bmatrix} \quad (4.4)$$

$${}^1_2T = \begin{bmatrix} c2 & -s2 & 0 & 0 \\ 0 & 0 & 1 & 0 \\ -s2 & -c2 & 0 & 0 \\ 0 & 0 & 0 & 1 \end{bmatrix} \quad (4.5)$$

$${}^2_3T = \begin{bmatrix} c3 & -s3 & 0 & 0 \\ s3.c\frac{5\pi}{12} & c3.c\frac{5\pi}{12} & -s\frac{5\pi}{12} & -s\frac{5\pi}{12}.L1.\sqrt{2} \\ s3.s\frac{5\pi}{12} & c3.s\frac{5\pi}{12} & c\frac{5\pi}{12} & -c\frac{5\pi}{12}.L1.\sqrt{2} \\ 0 & 0 & 0 & 1 \end{bmatrix} \quad (4.6)$$

$${}^3_4T = \begin{bmatrix} c4 & -s4 & 0 & 0 \\ s4.c\frac{3\pi}{4} & c4.c\frac{3\pi}{4} & -s\frac{3\pi}{4} & -s\frac{3\pi}{4}.L1 \\ s4.s\frac{3\pi}{4} & c4.s\frac{3\pi}{4} & c\frac{3\pi}{4} & c\frac{3\pi}{4}.L1 \\ 0 & 0 & 0 & 1 \end{bmatrix} \quad (4.7)$$

$${}^4_5T = \begin{bmatrix} c5 & -s5 & 0 & 0 \\ 0 & 0 & 1 & L3 \\ -s5 & -c5 & 0 & 0 \\ 0 & 0 & 0 & 1 \end{bmatrix} \quad (4.8)$$

The mathematical calculation of the forward kinematics can be seen in equation 4.9 and was according to equation 4.1. Equation 4.9 illustrates the orientation and position of the end-effector relative to the base frame. Figure 4.1, is a kinematic joint schematic according to the chosen conceptual design and represent the frame axes as explained in section 4.1.2.

$${}^0_5T = {}^0_1T {}^1_2T {}^2_3T {}^3_4T {}^4_5T \quad (4.9)$$

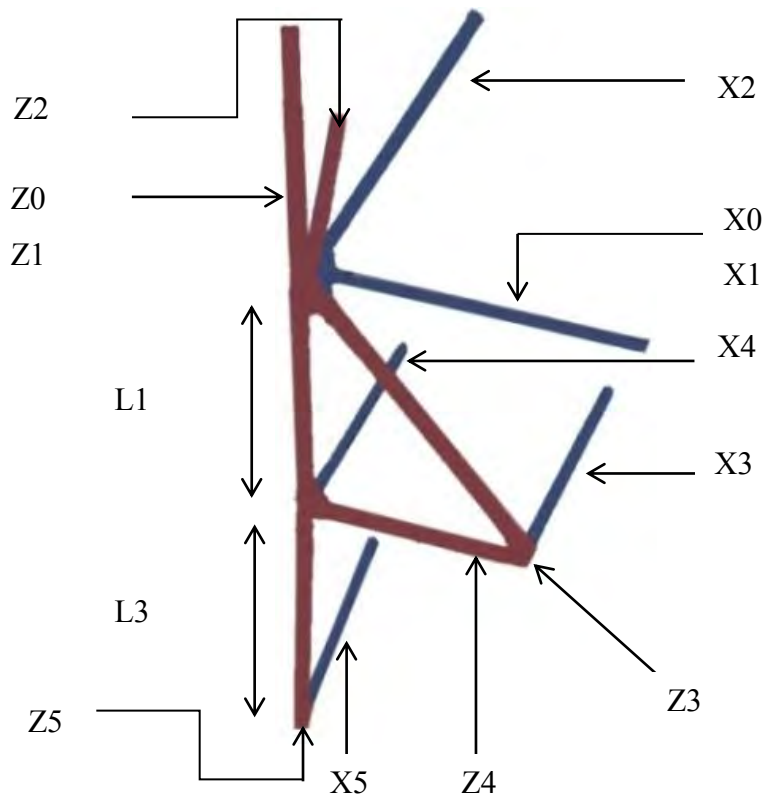


Figure 4.1: Kinematic joint schematic derived from final mechanical design and illustrates joint X and Z axes.

Figure 4.2 was established to assist the understanding of Figure 4.1 by representing only the Z axis on the mechanical manipulator, X_i was normal to Z_i and Z_{i+1} . X_i and Z_i were the joint frame axes of $joint_i$. The axes X_0 and Z_0 , which were at the same initial position as X_1 and Z_1 , represented the base axes. Y_0 was according to the right hand rule and pointed in the direction of X_3 and X_4 in Figure 4.1. The Z axes were also the respective joint's axis of rotation, and the intersection of a set of Z and X axes is the origin of the respective joint. The transformation matrices consisted of ϑ_i which referred to the rotation from X_{i-1} to X_i about Z_i [34]. This was a different representation of the mechanical constraints specified in chapter 3.

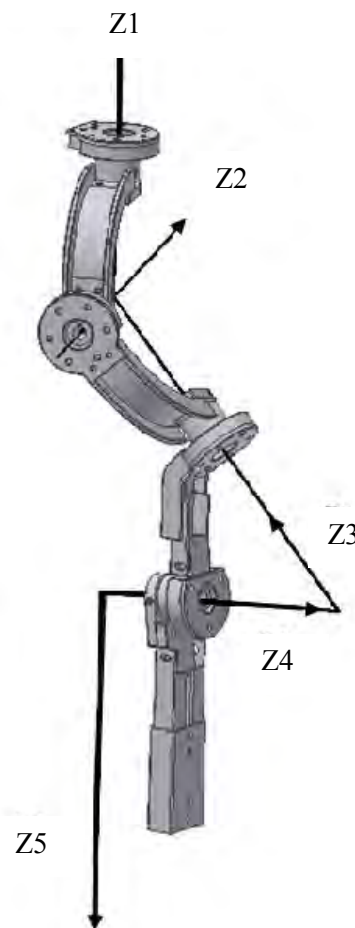


Figure 4.2: CAD of mechanical manipulator with respective Z axes.

The computation of equation 4.9 yielded the transformation matrix of the final joint relative to the base point, it was noticed that the elements of the matrix were relatively complex, which resulted in a problematic kinematic model. The first three rows of the last column of this transformation matrix yielded the X, Y and Z co-ordinates of joint 5 relative to the base frame and were displayed as the positional vector in Appendix B.1. This was the $m \times 1$ vector, as described above, and was essential for further derivation of the Jacobian, which will be explained further on. The L3 distance in the kinematic model was offset such that the position of the middle of the end-effector was the point of reference instead of the position of joint 5.

Figure 4.3 confirms the accuracy and derivation of the forward kinematic model and relates to the schematic illustrated in Figure 4.1 and the Z axes in Figure 4.2. The circular points illustrated the kinematic frame's origins; the first origin represented the base frame and joint 1 and 2's origins. The green, red and yellow represent joint frame origins 3, 4 and 5 respectively. Where joint frame origin 5 represented the supination and pronation movements and was offset such that the position was

referenced at the centre of the end-effector as described above. Figure 4.3 relates the origins with joint axes 3, 4 and 5 which corresponds to Z3, Z4 and Z5 in Figure 4.1.

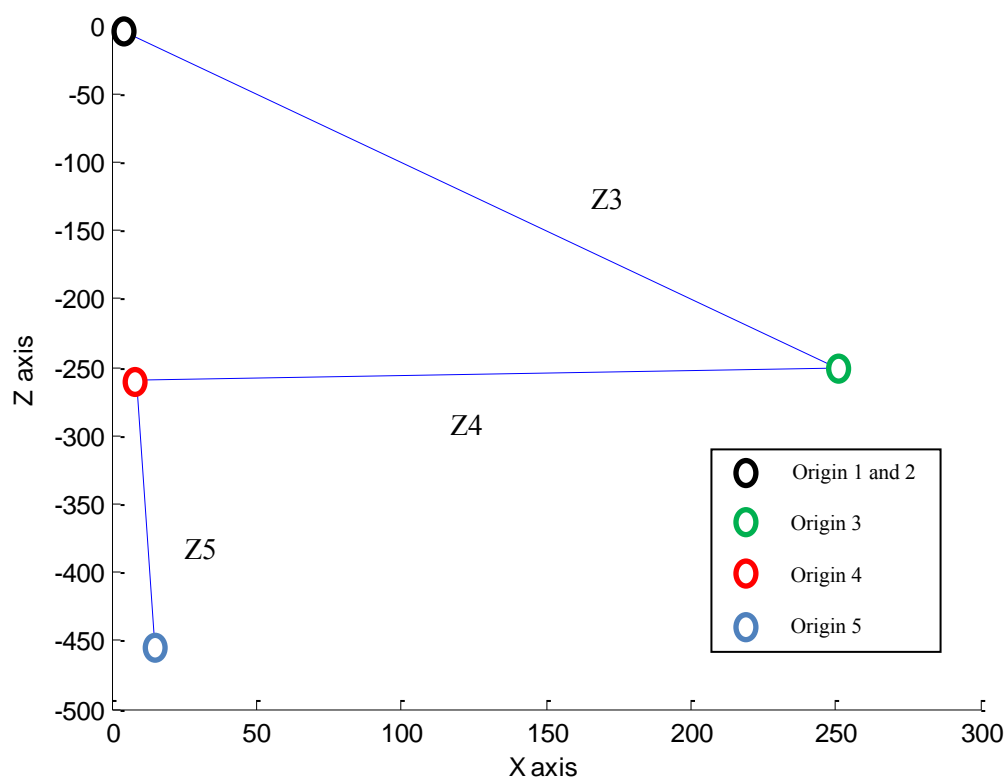


Figure 4.3: The respective joint axes and origins

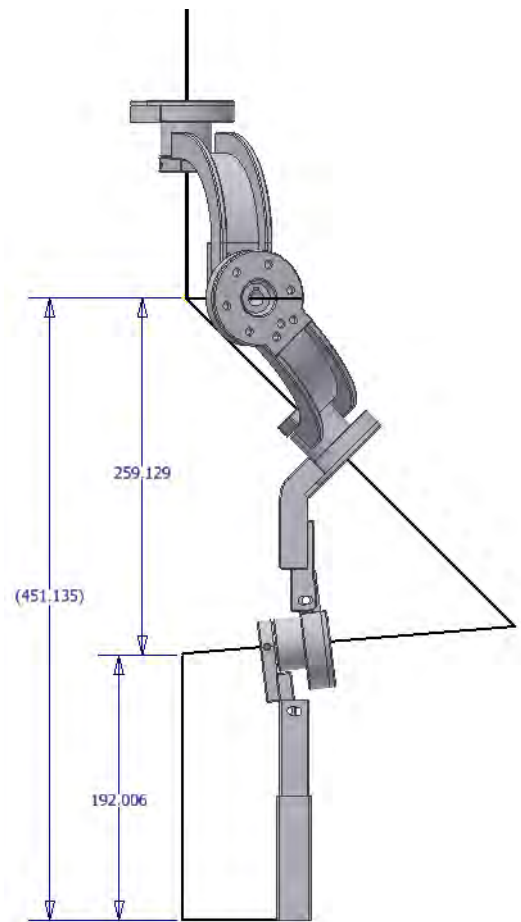


Figure 4.4: CAD Illustrating the Lengths at the Initial Position.

Figure 4.4 was the initial position of the mechanism with $\vartheta_1 = 0^\circ$, $\vartheta_2 = 45^\circ$, $\vartheta_3 = 75^\circ$ and $\vartheta_4 = 0^\circ$. L1 and L3 were taken to be 259.129 mm and 192.006 mm respectively. The forward kinematics produced a Z end-effector position of -450.8671 mm which is illustrated in Figure 4.3. However, the CAD in Figure 4.4 represented a Z distance of 451.135 mm which is 0.27 mm different to the kinematic model; this is an inaccuracy of 0.06 %.

4.2.1.1 The Workspace of the Exoskeleton Arm.

The X, Y and Z co-ordinates of the end-effector were used to obtain the various positions of the combination of different joint angles. A Matlab® simulation of a combination of different joint angles was created with the implementation of the joint constraints. $\vartheta_1, \vartheta_2, \vartheta_3, \vartheta_4$ and ϑ_5 were constrained to -30° to 150° , -150° to -30° , 0° to 137° , 0° to 120° and 0° to 175° respectively and were

according to the kinematic model illustrated in Figure 4.1. The simulation of this combination was created using a nested ‘for loop’ and an array layout, and this can be seen in Appendix B.2, which was the Matlab® source code for this simulation. The ‘for loop’ ranges from the minimum to the maximum joint limits of joints 1-4 by which the condition incremented by 20 degrees for joints 1, 2 and 3. Joint 4 was incremented by 10 degrees to achieve a better resolution. The forward kinematic position of each simulated point was then plotted as illustrated in Figure 4.5. The implementation of the joints constraints allowed for an illustration of the workspace of the exoskeleton arm with L1 and L3 taken to be 280 mm and 350 mm respectively.

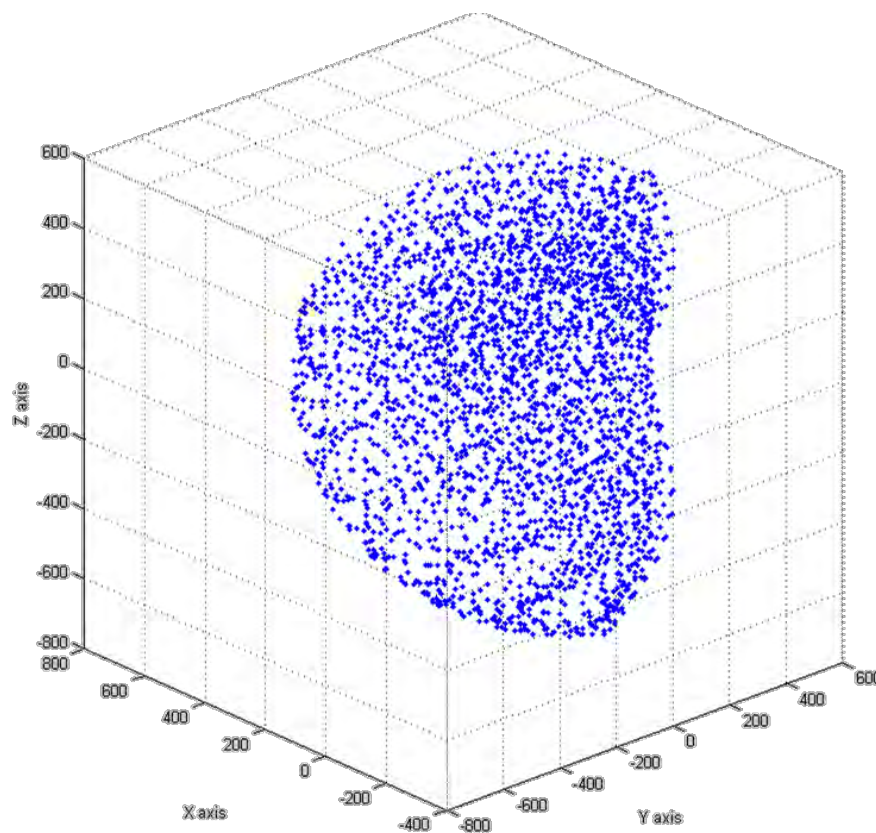


Figure 4.5: Achievable workspace of the exoskeleton arm.

Notice the spherical motion created by the mechanism in Figure 4.5. This motion allowed for a large workspace, therefore successfully imitating the GH joint’s spherical motion which is governed by equations 3.1 and 3.2. This imitation concludes that the angles chosen in the shoulder design yielded a successful anthropomorphic spherical motion. This motion was obtained without the need of three

serial orthogonal joints therefore resulting in a workspace according to the ADL which did not consist of a singularity.

4.2.2 Inverse Kinematics

The non-orthogonal layout produced problematic analytical and geometric solutions which were further coupled by a 3-dimensional problem which was evident from the methods illustrated in [34]. Buss [49] proposed several inverse kinematic iterative methods of which the Damped Least Squares (DLS) method was superior around singularities and complex designs. Its robustness around singularities allowed for successful computational implementation in all the conceptual designs; however conceptual design 3 was chosen for the reasons previously explained in chapter 2. The DLS method implemented the Jacobian of the positional vector of the mechanism; and was required to solve the change in ϑ_i [49].

Matrix 0T was in the form of equation 4.3 and the X, Y and Z terms of the end-effector, relative to the base frame, were represented by the first 3 rows of the last column illustrated in red by equation 4.3. This position of the end-effector was represented by S, equation 4.10, and was a function of $\vartheta_1, \vartheta_2, \vartheta_3$ and ϑ_4 . The desired supination and pronation movements were created by ϑ_5 which only affected the orientation of the end-effector and not the X, Y and Z position.

$$S = \begin{bmatrix} X(\vartheta_1 \dots \vartheta_i) \\ Y(\vartheta_1 \dots \vartheta_i) \\ Z(\vartheta_1 \dots \vartheta_i) \end{bmatrix} \quad (4.10)$$

The iteration of small angle change was a function of the Jacobian and resulted in a linear derivation of the inverse kinematics [49].

The Jacobian is represented by equation 4.11 [49].

$$J_{i,j} = \frac{\partial S[j]}{\partial \vartheta_i} \quad (4.11)$$

This Jacobian resulted in an (m x n) matrix and in this model m = 3 and n = 4, this expanded Jacobian was represented by equation 4.12. The final computed redundant Jacobian matrix can be seen in Appendix B.1.

$$J = \begin{bmatrix} \frac{\partial X}{\partial \theta_1} & \frac{\partial X}{\partial \theta_2} & \frac{\partial X}{\partial \theta_3} & \frac{\partial X}{\partial \theta_4} \\ \frac{\partial Y}{\partial \theta_1} & \frac{\partial Y}{\partial \theta_2} & \frac{\partial Y}{\partial \theta_3} & \frac{\partial Y}{\partial \theta_4} \\ \frac{\partial Z}{\partial \theta_1} & \frac{\partial Z}{\partial \theta_2} & \frac{\partial Z}{\partial \theta_3} & \frac{\partial Z}{\partial \theta_4} \end{bmatrix} \quad (4.12)$$

The inverse solution was initially represented by equation 4.13 which can only be implemented for a square Jacobian matrix [49]. However, the Jacobian in this research was not square and it was singular at a singularity which reduced the rank of the Jacobian therefore resulting in a non-invertible singular matrix [49]. The mechanical manipulator chosen in chapter 3 did not consist of a singularity in the workspace of the ADL but it consisted of a singularity in the workspace of the mechanical manipulator. Although this singularity may be rarely achieved, it was decided to implement the robust inverse kinematic solution achieved through the DLS method.

$$\Delta\theta = J^{-1} \text{error} \quad (4.13)$$

The error value was the difference between the initial position and the target position. This error value was updated iteratively according to the calculated position at any given time. Hanafusa and Nakamura [50] proposed the DLS method as a solution of the inverse kinematics, the DLS is implemented in order to provide robustness around singularities. The overcoming of singularities is achieved by finding the best $\Delta\theta$ which minimises the quantity illustrated by formula (4.14).

$$\|J\Delta\theta - \text{error}\|^2 - \lambda^2 \|\Delta\theta\|^2 \quad (4.14)$$

Where λ was the damping factor and was implemented to compensate for the computational problems produced by the singularities [51], it is explained further in this chapter. The minimisation illustrated in equation 4.14 was equivalent to minimising the quantity represented by formula (4.15) [49].

$$\| \begin{pmatrix} J \\ \lambda I \end{pmatrix} \Delta\theta - \begin{pmatrix} e \\ 0 \end{pmatrix} \| \quad (4.15)$$

Where I represented the identity matrix. The normal equation that corresponded to formula (4.15) is shown in equation 4.16 [49]. Equation 4.16 was achieved by using elementary matrix algebra and the multiplication of the $\begin{pmatrix} J \\ \lambda I \end{pmatrix}^T$ vector.

$$\begin{pmatrix} J \\ \lambda I \end{pmatrix}^T \begin{pmatrix} J \\ \lambda I \end{pmatrix} \Delta\theta = \begin{pmatrix} J \\ \lambda I \end{pmatrix}^T \begin{pmatrix} e \\ 0 \end{pmatrix} \quad (4.16)$$

Equation 4.16 can be equivalently represented as equation 4.17 [49] after elementary column multiplication.

$$(J^T J + \lambda^2 I) \Delta\theta = J^T * error \quad (4.17)$$

Where J^T represented the Jacobian transpose. Buss [49] illustrated that $(J^T J + \lambda^2 I)$ was non-singular and therefore could be inverted. Hence, the DLS inverse solution was represented in equation 4.18. This solution overcame the problem experienced by equation 4.13.

$$\Delta\theta = (J^T J + \lambda^2 I)^{-1} * J^T * error \quad (4.18)$$

The multiplication of the Jacobian with its transpose produced a square matrix which allowed for the computation of the inverse of this multiplication. The algorithm of the DLS method is illustrated by Figure 4.6. The iteration process was depended on the error value which was initially calculated. The angle change was then iteratively solved and the error value and joint angles were updated. This process is repeated until the error value was reduced to a desired tolerance. $J^T J$ was an $(n \times n)$ matrix which was more computationally expensive in redundant manipulators due to the DOF in the joint space being greater than the DOF in task space. Equation 4.18 was manipulated in the form of equation 4.19 to produce a $(m \times m)$ matrix.

$$\Delta\theta = J^T (J J^T + \lambda^2 I)^{-1} * error \quad (4.19)$$

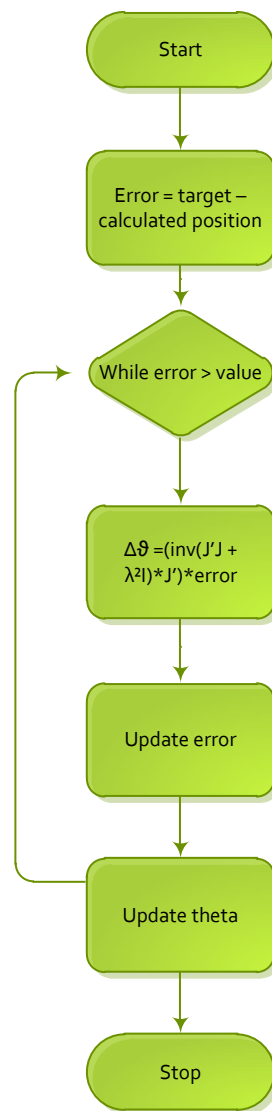


Figure 4.6: Flowchart illustrating the iteration process of the DLS method.

4.2.2.1 Joint Limits

Na, Yang and Jia [51] proposed a method to limit the joints according to the desired constraints, with a weighting which related to the joint flexibility. This was implemented by modifying the damping factor by inserting an $(n \times n)$ diagonal matrix which is illustrated by equation 4.20 [51].

$$D(\lambda) = \begin{bmatrix} \lambda_1 & \cdots & 0 \\ \vdots & \ddots & \vdots \\ 0 & \cdots & \lambda_n \end{bmatrix} \quad (4.20)$$

The individual damping factors are represented by equation 4.21 [51].

$$\lambda_i = \left[\frac{2\vartheta_i - \vartheta_{max} - \vartheta_{min}}{\vartheta_{max} - \vartheta_{min}} \right]^p + \frac{1}{w_i} \quad (4.21)$$

Where p was an even number and ϑ_i was the angle of joint i during the iteration process which was updated as the error decreased, according to Figure 4.6. The maximum and minimum limits of their respective joints were represented by ϑ_{max} and ϑ_{min} respectively. Where w_i was the user defined weighting according to the flexibility of each joint, the higher the value the lower flexibility was allowed in the joint [51]. The original DLS method implemented a constant damping factor. However, equation 4.15 produced a small damping factor when within joint constraints and a large damping factor when near or just away from joint limits. When the damping factor, λ_i , was equal to 1 the angular position, ϑ_i , was restricted as illustrated in Figure 4.7 [51]. This change in damping factor was mathematically shown, in Appendix B.3 for clarity purposes. It was visible from Figure 4.7 that a lower p value allowed for a wider range of motion. Therefore a value of 4 was chosen in this research which will enabled a larger range of motion, with regards to the joint angles

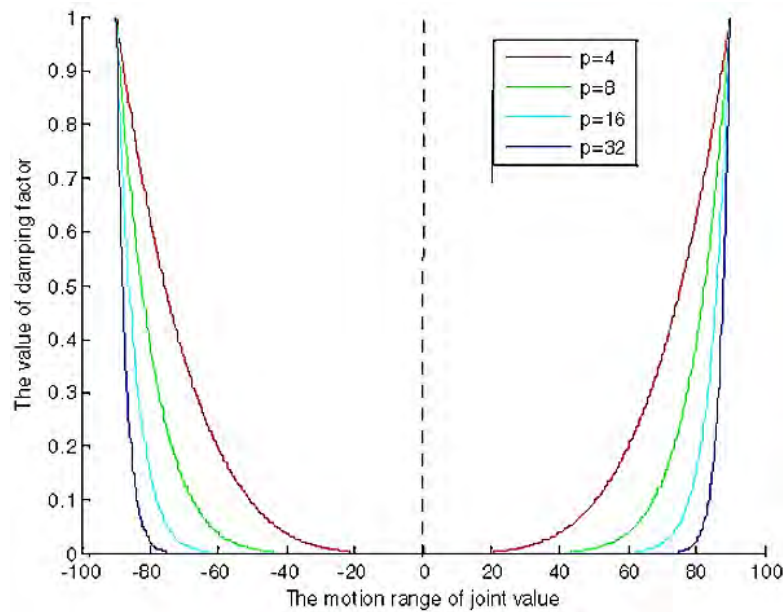


Figure 4.7: Damping factor curve for motion range of a joint. $\vartheta_{max} = 90^0$ and $\vartheta_{min} = -90^0$ [51].

The diagonal matrix, equation 20, is a $(n \times n)$ matrix and therefore was implemented into equation 4.18 and not 4.19. This implementation allowed for the addition of $J^T J + D(\lambda^2)$ which resulted in an $(n \times n)$ matrix. This matrix was inverted and then multiplied by the Jacobian transpose and the error values, which resulted in the respective change in joint positions. The implementation of the diagonal matrix into the DLS method resulted in equation 4.22.

$$\Delta\vartheta = ((J^T J + D(\lambda^2))^{-1} * J^T) * error \quad (4.22)$$

4.2.3 Kinematic results

Figure 4.8 and Figure 4.9 represents the minimisation of the error value for each axes and the change in joint angles respectively. The error value was reduced to 0 at approximately 250 iterations of the algorithm depicted in Figure 4.6. This convergence to zero was illustrated by Figure 4.8 and the joint angles become stable at their respective values as the error values approached zero. The stabilisation of the joint values and the minimisation of the error were dependent on the iteration count. The iteration count could be further increased by minimising the tolerance of the error value; this resulted

in a more accurate solution. The tolerance was chosen to be within 1×10^{-9} of the absolute error in the Cartesian co-ordinate system. This error resulted in an accurate model which was required in order to achieve a successful passive positional system. The tolerance value produced a high accuracy as well as a relatively low iteration count. The stabilisation of the joint values, Figure 4.9, as the error values minimise illustrated that a successful Joint Limited Damped Least Squares JLDLS was implemented on a redundant manipulator.

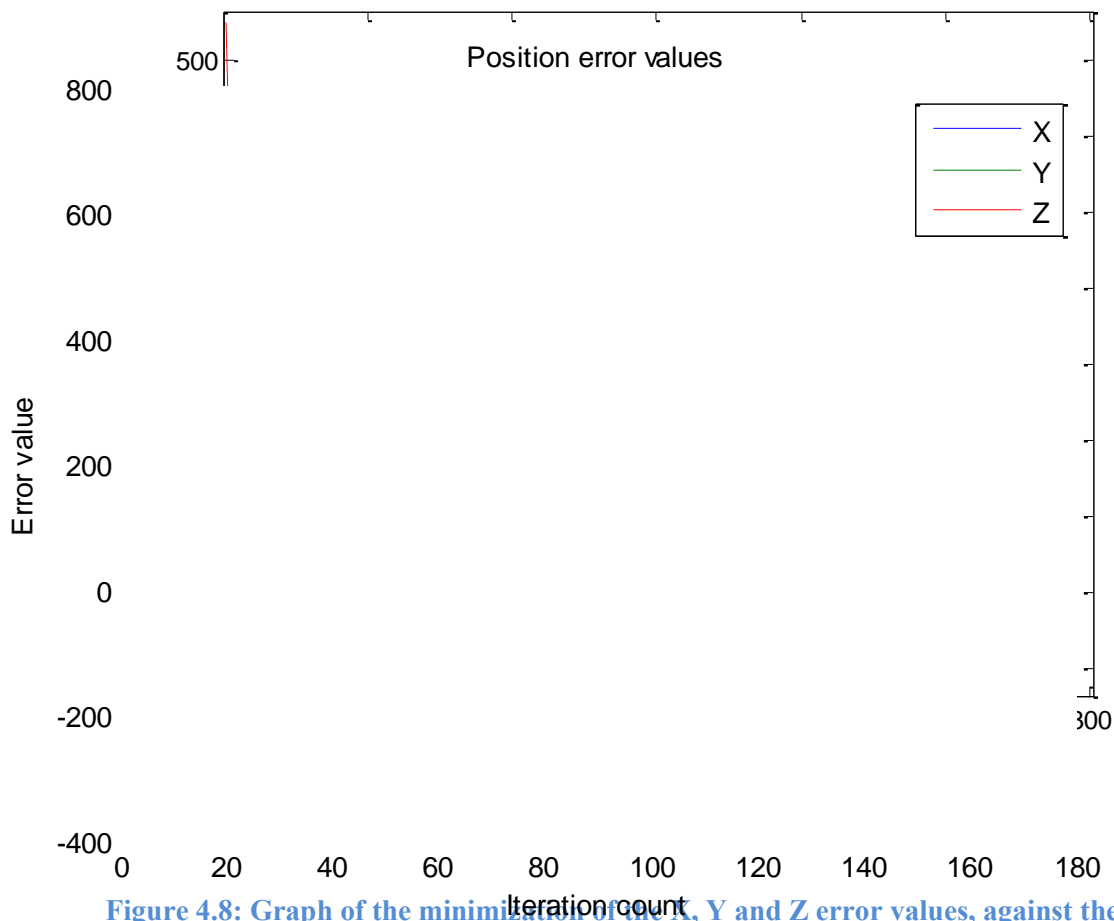


Figure 4.8: Graph of the minimisation of the X, Y and Z error values, against the number of iterations.

Figure 4.8 and Figure 4.9 were derived by changing the end-effector position to X, Y and Z co-ordinates of -90 mm, 400 mm and -30 mm respectively from initial joint angles of $\vartheta_1 = 0^\circ$, $\vartheta_2 = -45^\circ$, $\vartheta_3 = 75^\circ$ and $\vartheta_4 = 0^\circ$. This initial joint space position corresponds to an end-effector position of X, Y and Z of 21.1 mm, -3.9mm and -629.6 mm respectively. These values were obtained for L1 and L3 of 280 mm and 350 mm respectively.

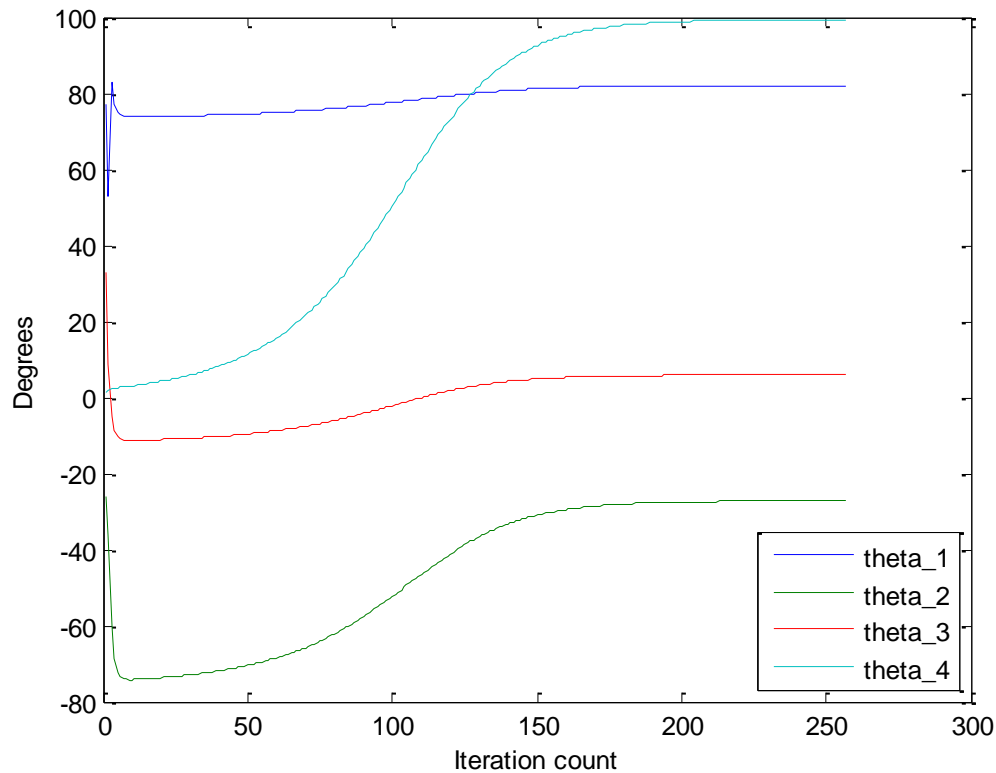


Figure 4.9: Graph illustrating the stabilisation of the joint angle values.

Figure 4.10 is a graph of the X, Y and Z positions of the end-effector relative to the iteration count. The positions were damped early in the iteration count, at approximately ten iterations. It could be compared to Figure 4.8, the two figures are linearly related, as the error decreased the change in position stabilised by an equivalent amount. This equivalence could be seen approximately between iterations 100 and 200, it was noticed that the change in error and position of the Y axis were of the same value.

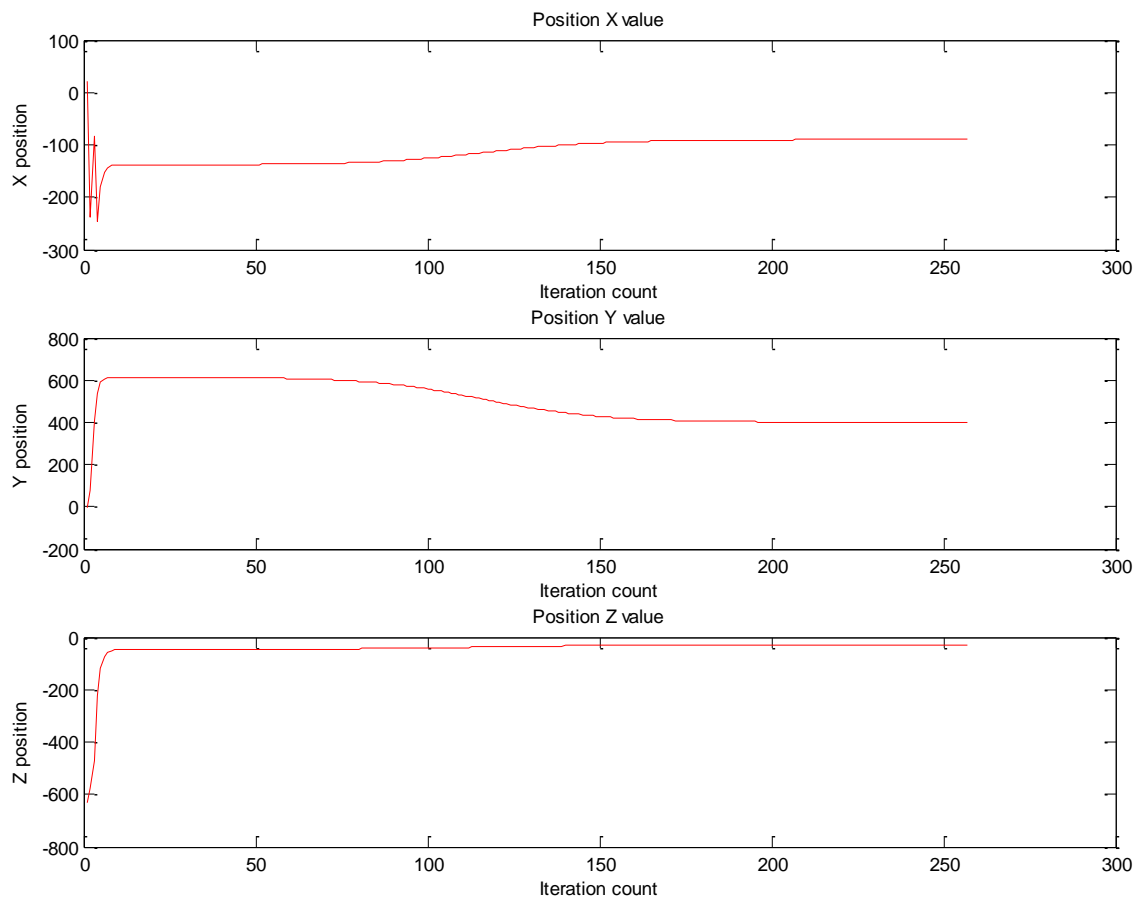


Figure 4.10: Graph illustrating the change in X, Y and Z positions of the end-effector in relation to the iteration count.

The kinematic trajectory of the end-effector from the initial to end position was simulated and plotted in 3-D, this plot is illustrated in Figure 4.11. The trajectory plot corresponded to the values in the graphs illustrated by Figure 4.10. These values are depicted differently in Figure 4.11 due to the absence of visual depth. Figure 4.12 is the Y-Z planar trajectory of Figure 4.11 and it was plotted to illustrate the accuracy of the model. The kinematic trajectory was a plot of the iteration values derived by the kinematic values. These iteration values were not implemented individually in the software design. Instead, the total change in the joint values was implemented. These trajectories were illustrated in order to indicate the linear derivation achieved by the kinematic model.

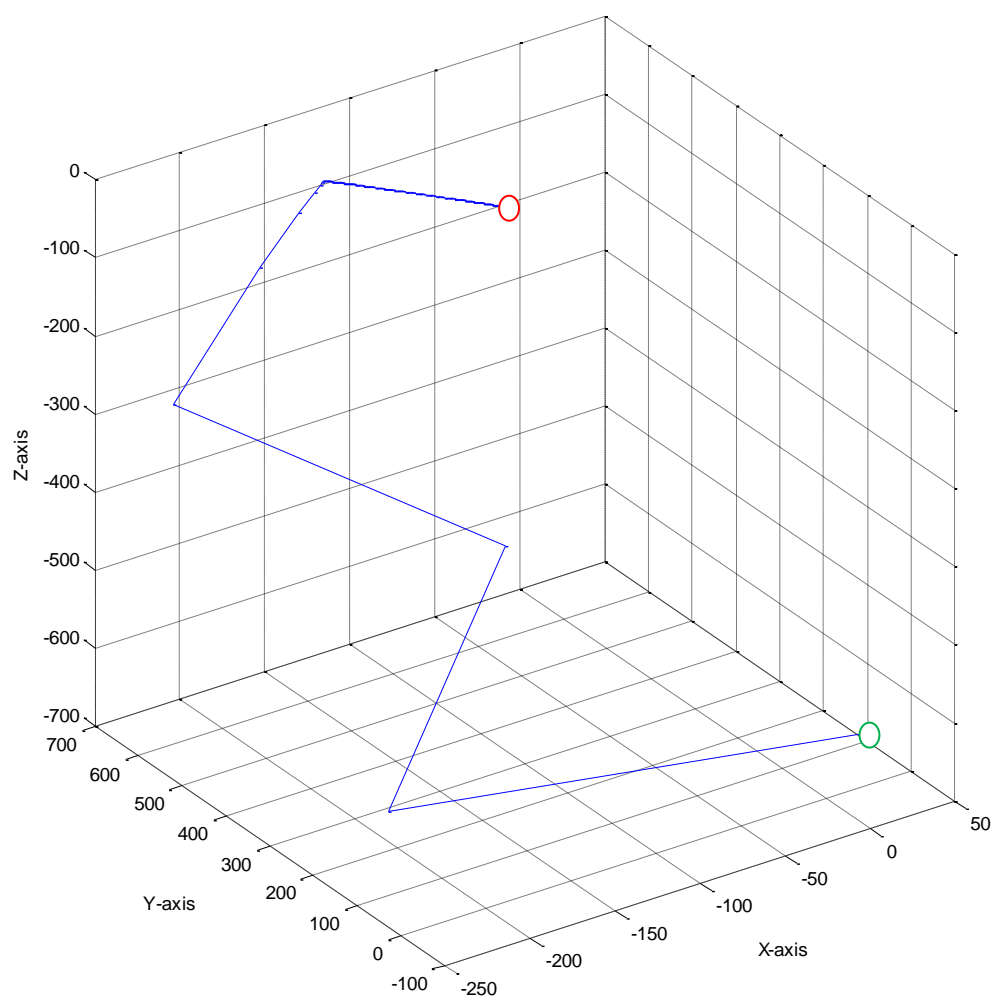


Figure 4.11: 3-D Kinematic trajectory of the end-effector position from initial position (green circle) to end position (red circle).

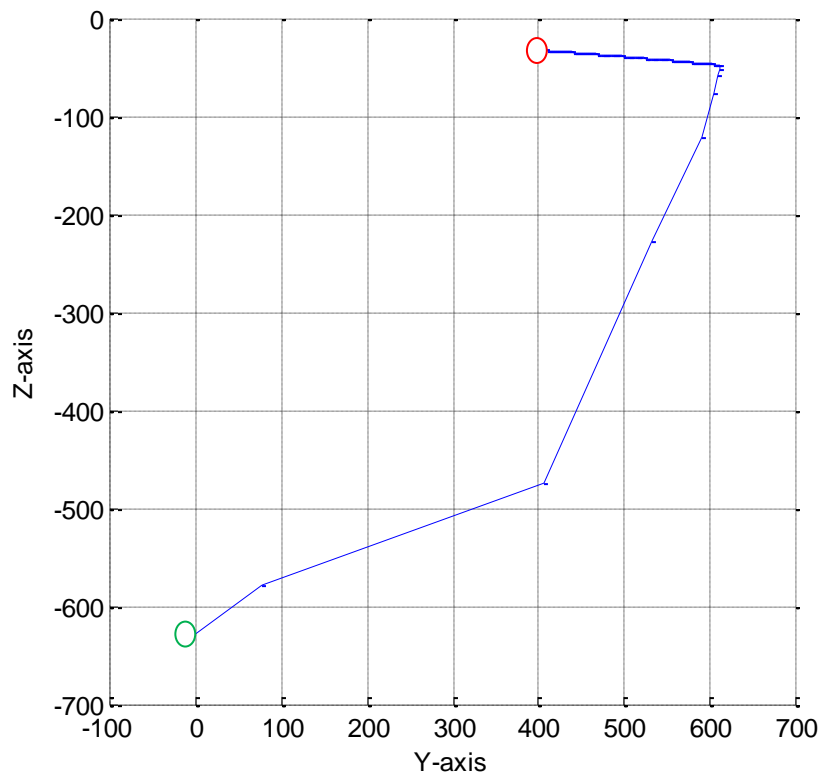


Figure 4.12: Y-Z plane of position trajectory.

The redundant model was not limited in terms of relating one joint angle to another or keeping a joint angle constant, this resulted in a non-square Jacobian matrix as illustrated in equation 4.12. The consequence of this redundancy was an infinite number of solutions to an inverse problem which resulted in certain solutions not obeying the joint constraints. The JLDLS method minimised joint angles which did not obey the joint constraints. This comparison between the joint limitation technique and the normal DLS was tabulated in Appendix B.4. However, certain values in the workspace were not achievable due to the redundancy. It was desired to create a non-redundant model although the redundant model would provide the necessary joint motion. The non-redundant model would not limit the workspace of the mechanism because there was a unique solution for every task space combination, which was in the workspace of the mechanical structure.

4.3 Non-Redundant Model

The non-redundant model resulted in ($m - n = 0$); which meant that the DOF in the joint space were equal to the DOF in the task space. The non-redundant analyses lead to the isolation of the shoulder mechanism and the development of a separate kinematic model. This would improve the rehabilitation of the shoulder joint as a combination of the 3 DOF could be achieved throughout the workspace. A non-redundant solution resulted in a single inverse solution therefore converging with fewer iterations than the redundant solution but with a minimal error, which was experienced from simulations.

4.3.1 Forward Kinematics

The kinematic schematic changed slightly as compared to the redundant model, there was a common origin which lies at the GH joint. Z4 and X4 were created to offset the position of the final forward kinematics from the GH joint to the elbow joint, which was the end-effector in this model. The D-H parameters are tabulated in Table 4.2 and the kinematic schematic is illustrated in Figure 4.13.

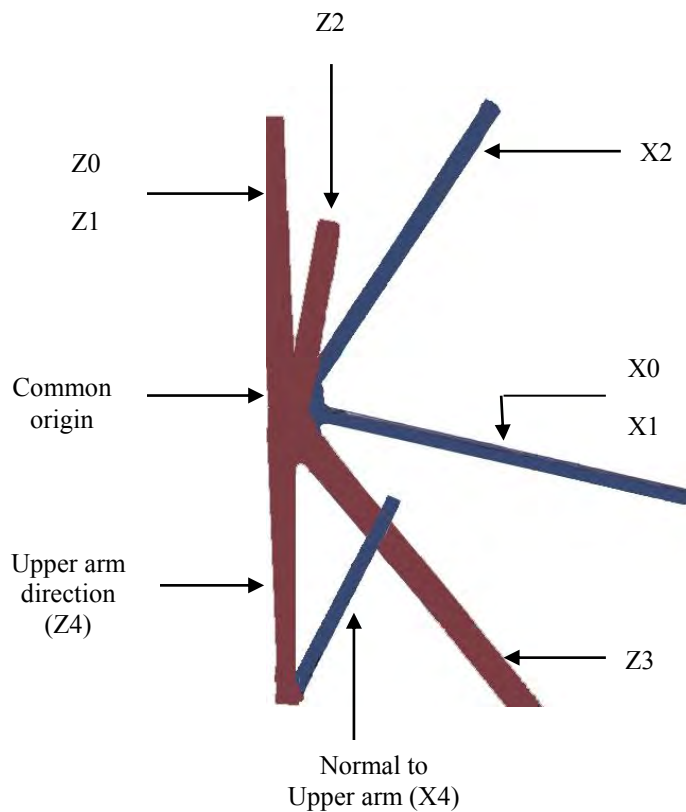


Figure 4.13: Kinematic schematic of the non-redundant model

Table 4.2: Denavit-Hartenberg Parameter for final design without the elbow mechanism.

i	α_{i-1}	a_{i-1}	d_i	ϑ_i
1	0	0	0	ϑ_1
2	$-\frac{\pi}{2}$	0	0	ϑ_2
3	$\frac{5\pi}{12}$	0	0	ϑ_3
4	$-\frac{3\pi}{4}$	0	$L1$	ϑ_4

Transformation matrices 0_1T and 1_2T remained the same when compared to the redundant model, 2_3T and 3_4T change and are represented by equations 4.23 and 4.24 respectively. $L1$ represented the distance from the GH joint to the elbow joint.

$${}^2_3T = \begin{bmatrix} c3 & -s3 & 0 & 0 \\ s3.c\frac{5\pi}{12} & c3.c\frac{5\pi}{12} & -s\frac{5\pi}{12} & 0 \\ s3.s\frac{5\pi}{12} & c3.s\frac{5\pi}{12} & c\frac{5\pi}{12} & 0 \\ 0 & 0 & 0 & 1 \end{bmatrix} \quad (4.23)$$

$${}^3_4T = \begin{bmatrix} c4 & -s4 & 0 & 0 \\ s4.c\frac{-3\pi}{4} & c4.c\frac{-3\pi}{4} & -s\frac{-3\pi}{4} & -s\frac{-3\pi}{4}.L1 \\ s4.s\frac{-3\pi}{4} & c4.s\frac{-3\pi}{4} & c\frac{-3\pi}{4} & c\frac{-3\pi}{4}.L1 \\ 0 & 0 & 0 & 1 \end{bmatrix} \quad (4.24)$$

The forward kinematics were obtained by equation 4.25, although reduced by one degree of freedom it still produced many non-zero terms. This was a result of twist angles two and three which still required solving of the inverse kinematics iteratively.

$${}^0_4T = {}^0_1T {}^1_2T {}^2_3T {}^3_4T \quad (4.25)$$

The spherical motion was fundamentally produced by the shoulder mechanism as previously explained. This motion is visible in Figure 4.14 and it resulted in the motion produced in Figure 4.5. Hence a successful shoulder mechanism was designed.

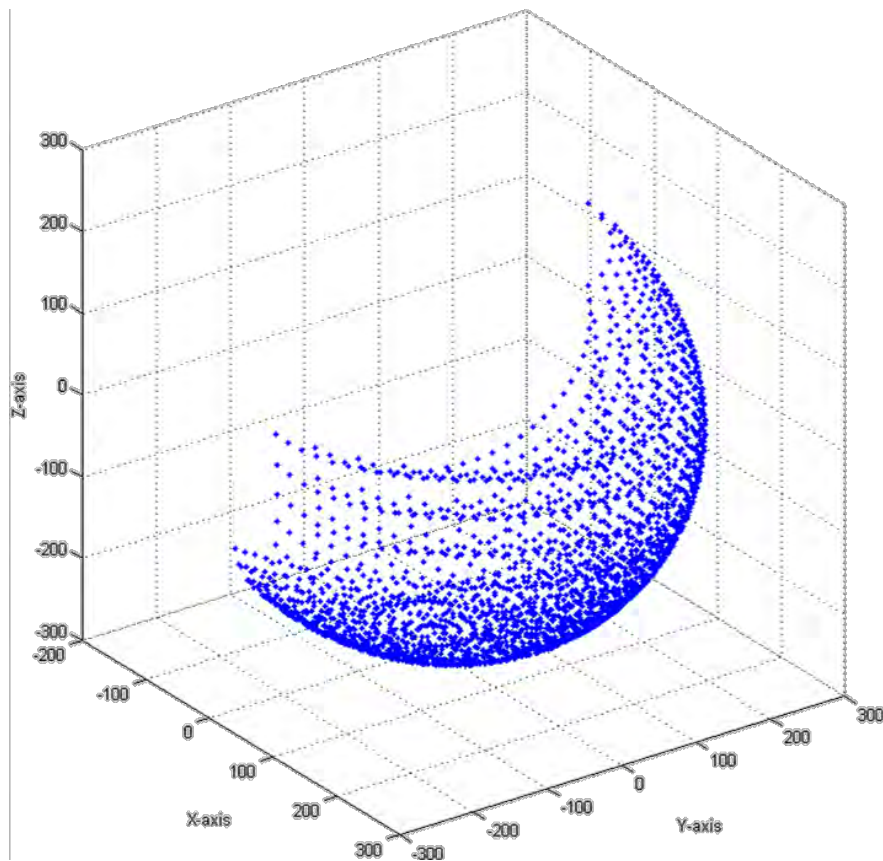


Figure 4.14: Fundamental spherical motion produced by the shoulder mechanism.

4.3.2 Inverse Kinematics

The inverse kinematics were solved iteratively as specified in section 4.3.2 however the Jacobian matrix was now a square matrix and is represented by equation 4.26. This square matrix resulted in lower computational cost as compared to the redundant Jacobian [49].

$$J = \begin{bmatrix} \frac{\partial X}{\partial \theta_1} & \frac{\partial X}{\partial \theta_2} & \frac{\partial X}{\partial \theta_3} \\ \frac{\partial Y}{\partial \theta_1} & \frac{\partial Y}{\partial \theta_2} & \frac{\partial Y}{\partial \theta_3} \\ \frac{\partial Z}{\partial \theta_1} & \frac{\partial Z}{\partial \theta_2} & \frac{\partial Z}{\partial \theta_3} \end{bmatrix} \quad (4.26)$$

The low computational expense is visible by the iteration count illustrated in Figure 4.15 and

Figure 4.16 as compared to Figure 4.8 and Figure 4.9. The new model converged to a final solution and produced a linear relationship within 10 iterations for all solutions. Kinematic testing yielded an absolute convergence error of less than 1 mm as compared to an error of less than 1×10^{-9} mm for the redundant model. The non-redundant error was minimal especially for physiotherapy purposes and therefore was taken to be acceptable.

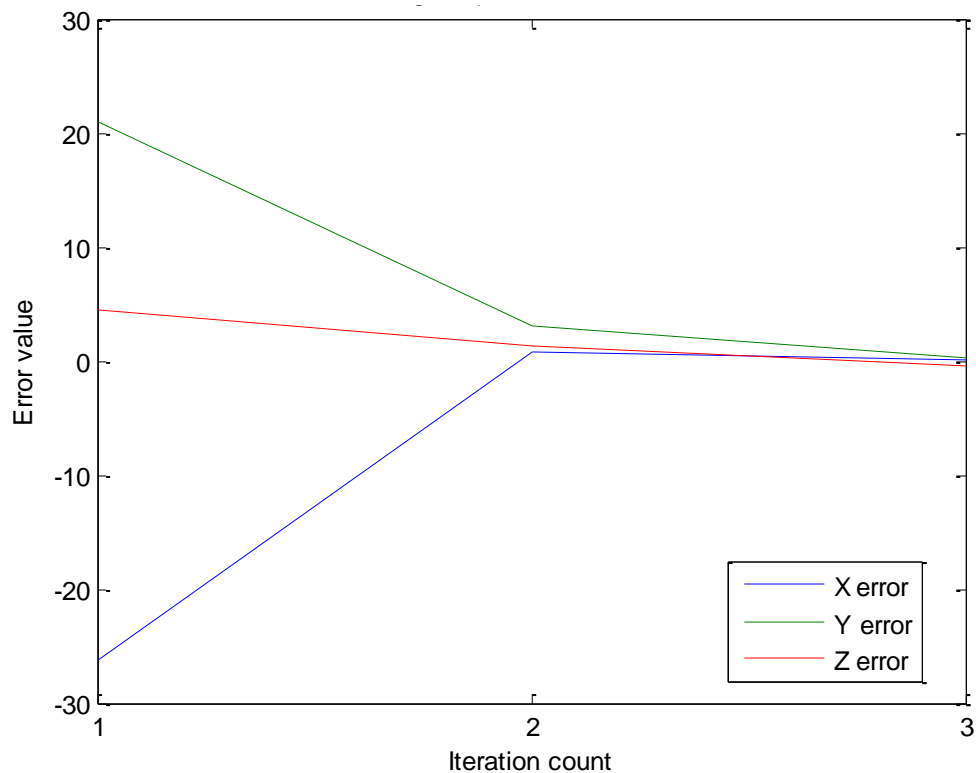


Figure 4.15: Graph of the minimization of the X, Y and Z error values, against the number of iterations.

The DLS produced joint stabilisation at the convergence of an absolute error of zero which is illustrated by Figure 4.15 and Figure 4.16

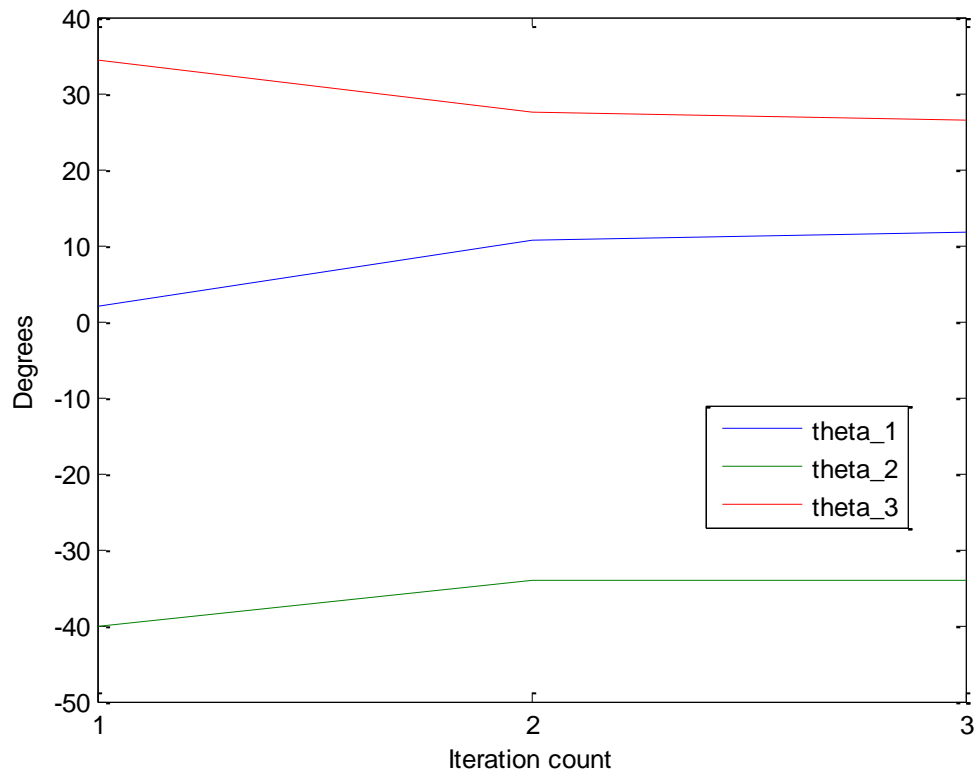


Figure 4.16: Graph illustrating the stabilisation of the joint angle values.

The change in X, Y and Z positions of the end-effector, which in this model was the elbow joint, was graphed in Figure 4.17 and was related to Figure 4.15 as explained in section 4.2.3. The linear relationship of this model was visible in Figure 4.18 which is the kinematic trajectory of the end-effector, from joint space position of $\vartheta_1 = 0^\circ$, $\vartheta_2 = -45^\circ$ and $\vartheta_3 = 75^\circ$ to a final X, Y and Z task space of 35 mm, 130 mm and -246 mm respectively. A 2-D plot was not illustrated as the values could be seen to be accurate from the 3D trajectory and the same concept was applied as the redundant model. The final joint change was implemented in the control software as described with the redundant model.

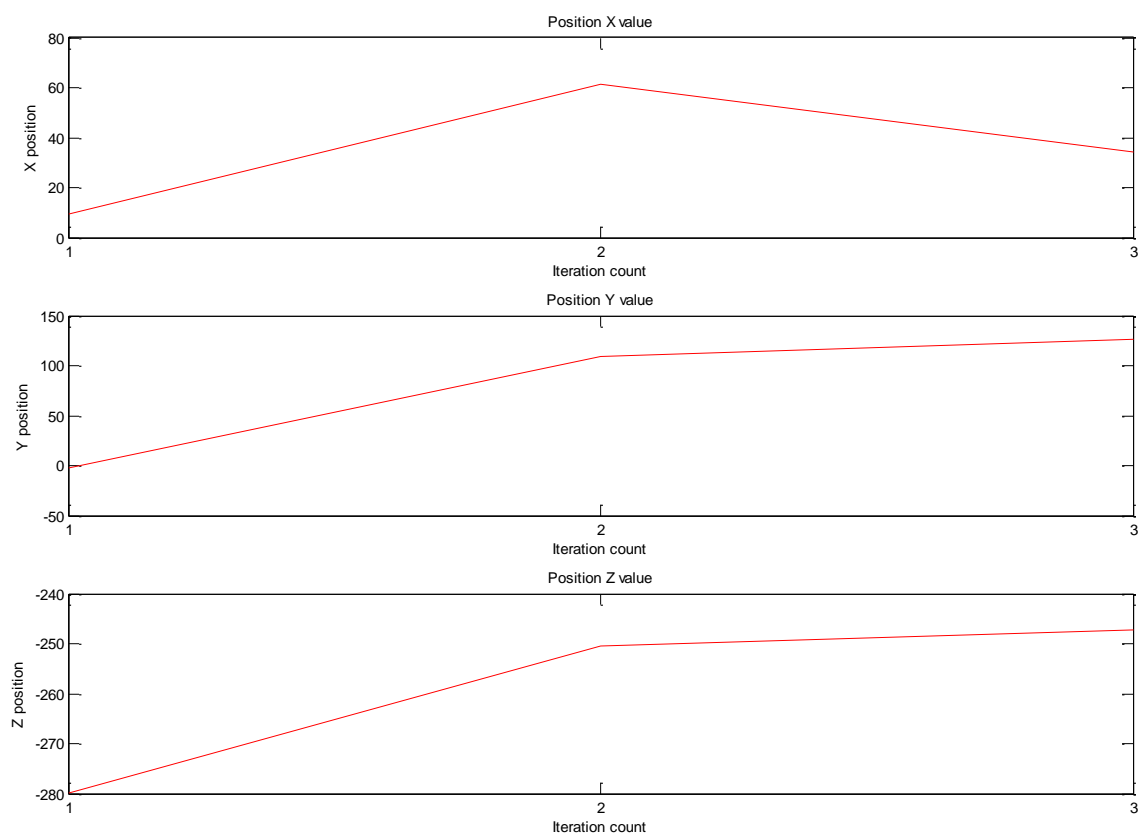


Figure 4.17: Graph illustrating the change in X, Y and Z positions of the end-effector in relation to the iteration count.

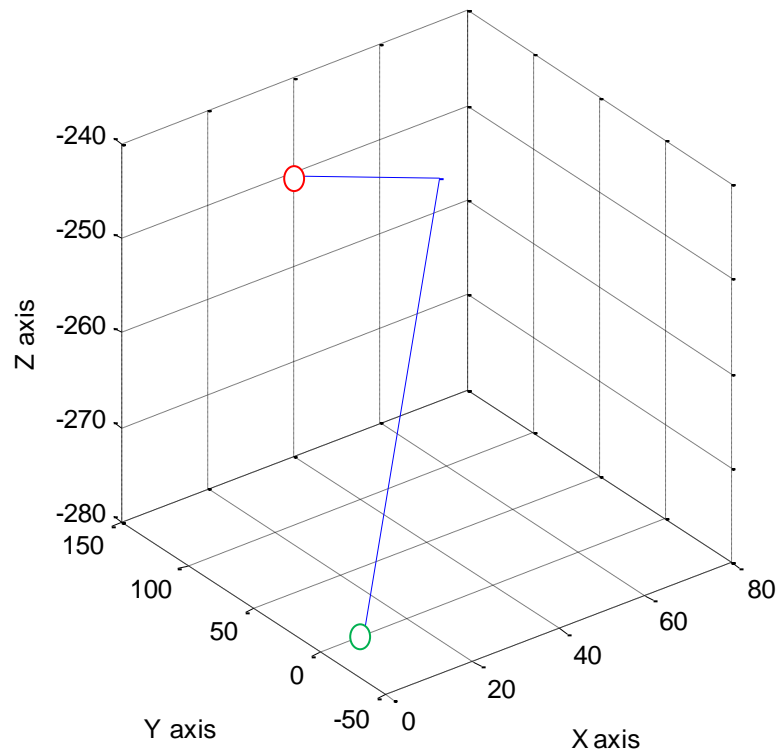


Figure 4.18: Kinematic trajectory of the end-effector position from initial position (green circle) to end position (red circle).

4.4 Kinematic Error

The inverse kinematic joint angles solution was used as an input into the forward kinematic model this was achieved manually for a number of values. The errors for the X, Y and Z values were then calculated. Figure 4.19 illustrates the above described procedure.

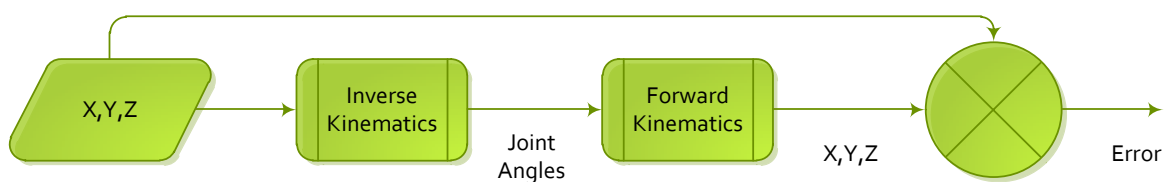


Figure 4.19: Flow Diagram of the Error Calculation between the Inverse and Forward Kinematic Models.

This error calculation was done for both the redundant and non-redundant models. The redundant model was more accurate in achieving the values. The error for the X, Y and Z co-ordinates ranged from 0.01-0.09 mm as compared to the 0.08-0.4 mm for the non-redundant model. The difference between these errors in the two models was as a result of the computational iterations. The non-redundant model had an iteration count within 10 iterations as compared to over 200 iterations with the redundant model. This was as a result of the number of DOF in the model; the extra iterations were as a result of the additional degree of freedom.

4.5 Chapter Summary

The kinematic models and analysis were essential in order to monitor and control the behaviour of the exoskeleton mechanism. Mechanical joints were positioned in a non-orthogonal manner due to the avoidance of workspace singularities. This resulted in problematic forward kinematics which complicated the solution to inverse kinematics via analytical or geometric methods. Hence, the inverse kinematics was solved iteratively. This iterative solution resulted in the implementation of the DLS method in an exoskeleton manipulator. A joint limitation technique was also used and proved successful in minimising hyper extension or flexion in human joints.

The forward and inverse kinematic models were derived for both redundant and non-redundant manipulators and the errors between the two models were compared. The mechanical workspace of both models were simulated and plotted. The redundant model could be used for rehabilitation but with restrictions to the achievable workspace. These restrictions were overcome with successful implementation of a non-redundant model and a complete spherical workspace was obtained with the inverse kinematics. The successful implementation of the DLS was illustrated by error convergence and joint stabilisation graphs. A further linear relationship between the convergence error and the change in position was established as well as the linear derivation which was expressed in terms of the kinematic end-effector trajectory. The kinematic model was implemented with the mechanical, electronic and computer components to establish a successful upper limb exoskeleton for physiotherapy.

5 Exoskeleton Electronic System

5.1 Exoskeleton Electronic Design Consideration

The design consideration of the electronic hardware required a mechatronic design approach which resulted in a subsystem that was integrated with the mechanical and software components of this research. The Actuation Control Module (ACM) consisted of all the electronic hardware, excluding the personal computer (PC), of this research and was the subsystem focused in this chapter. The electronic design considerations that would assist with this integration are as follows:

- **Integrability-** This sub-system must display ‘plug –in’ system capabilities to assist with quick integration of the bio-mechatronic design.
- **Diagnosability-** Implementation of sensors that facilitate with movement of the exoskeleton and user feed-back.
- **Portability-** The electronic components must be compact as possible in order to assist with the geographical portability requirement.
- **Mobility-** The electronic components and their respective wiring must not limit the motion or adjustability aspects of the exoskeleton structure.

5.2 Exoskeleton Electronic Control System

The basic layout of the exoskeleton electronic architecture, shown in Figure 5.1, was implemented in this research. A PC was at the head of this architecture. The development of computers allowed for faster processing, better user interaction and electronic interfacing. Such characteristics made the PC a suitable control station for exoskeleton physiotherapy [19]. The PC was implemented as it already consists of hardware and software support for Universal Serial Bus (USB) and Ethernet communication [52]. The USB provided the required electronic interfacing which allowed for quick plug and play architecture. This interfacing was implemented together with the USB 2.0 protocol due to existing software and support for data rates of up to 12 Mb/s [53], which was more than required in this research as data was transferred at the rate of approximately 32 bytes per second, noise was not considered in the transfer rate.

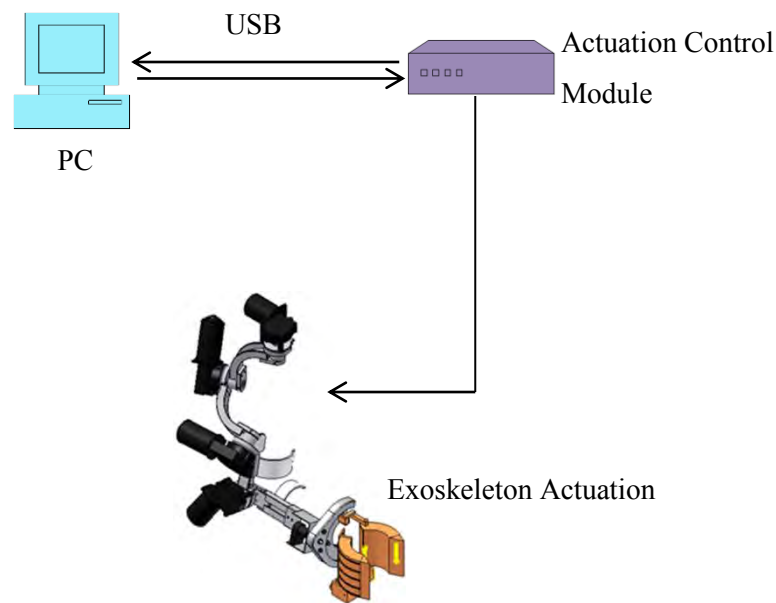


Figure 5.1: Basic overall exoskeleton electronic architecture.

5.3 Actuation Control Module

The ACM provided the necessary positioning of the upper limb exoskeleton and it consisted of various electronic components that made up this module. These include the:

- Microcontroller
- H-bridge motor drivers
- USB communication
- Sensors
- Power supply
- Wiring

Figure 5.2 illustrates a basic interaction of the ACM with the PC, the solid blue lines indicates the power lines and the solid red lines indicate the direction of the electronic signal flow.

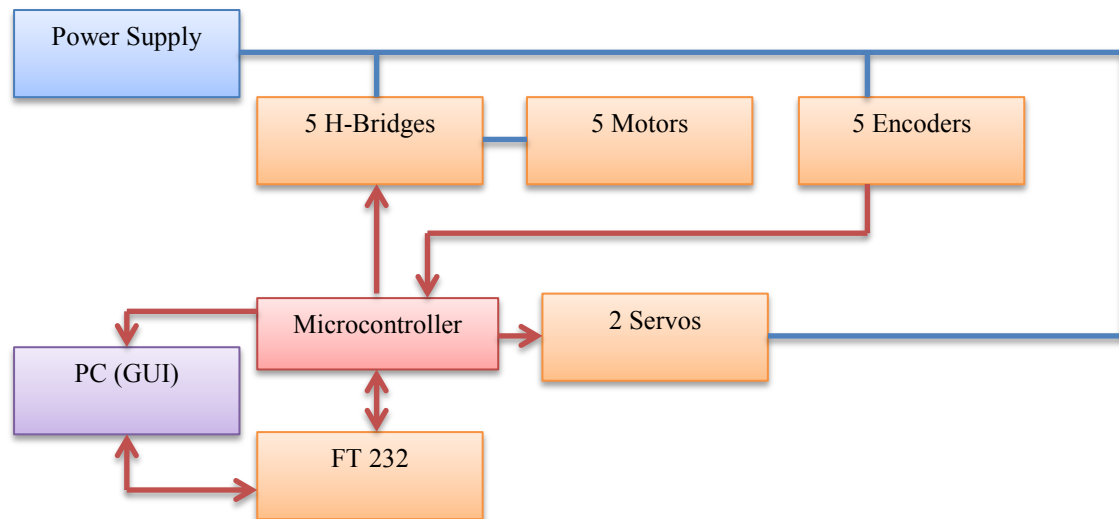


Figure 5.2: Interaction of the actuation control module with the PC.

The power supply provided power to the H- bridges, the servos and the encoders. The motors were powered via the H-bridges.

5.3.1 Microcontroller

The microcontroller was an important factor in this research because the positioning of a manipulator with multiple degrees of freedom required a high number of external interrupts for encoder sensing. The ATmega 1280 microcontroller provided such a solution and was implemented in this research. The microcontroller was used to process the encoder signals and control the actuators according to the feedback received from the encoders. The ATmega 1280 consisted of (but was not limited to) the following features [54]:

- Up to 16 MIPS throughput at 16MHz
- Four programmable serial USART
- 12 PWM outputs
- 7 external interrupts
- 256 KBytes of in-system self-programmable flash
- Two 8-bit timer/counters with separate prescaler and compare mode
- Four 16-bit timer/counters with separate prescaler, compare- and capture mode.

The above features of the microcontroller are essential in order to provide the processing power, positional control and serial communication which are required for this research.

A schematic of the AtMega 1280 can be seen in Appendix C and is represented by Figure C.1. The microcontroller was implemented in the form of an Arduino board, which can be seen in Figure 5.3. This board consisted of In-Circuit Serial Programmer (ICSP) pins, which allowed for real time programming, and a FT232 that provided the required USB interface between the PC and microcontroller. The Arduino allowed for easy electronic interfacing as additional Printed Circuits Boards (PCBs) were not required for microcontroller interconnections. The relationship between the Arduino and the AtMega 1280 input/output (I/O) pin layout can be seen in the schematic illustrated by Figure C.2 in Appendix C.



Figure 5.3: Arduino board with integrated microcontroller and electronic interfacing.

5.3.2 Half-Bridge Motor Drivers

Motor drivers were required in order to electronically change the polarity and speed of the motors. These drivers were essential and needed to be capable of operating under the motor loads. The second and third joints were driven by the high torque motors, the first and fourth joints were driven by motors of lower torque capacity. The high torque and lower torque motors required 43 and 11 Amps respectively at stall, both at 12 Volts. The motor drivers are chosen to operate the system under these those conditions. The Pololu 15 Amp motor driver was used for the lower torque motors, this motor driver can be seen in Figure 5.4, below. The Pololu motor drivers were more than capable of

controlling the lower torque motors, without the requirement of additional cooling. This half-bridge consisted of the following features (but not limited to):

- Operation voltage 5.5V-30V (recommended max at 24V)
- Can supply 15 A of continuous current
- 40KHz maximum PWM frequency
- Maximum logic voltage is 5.5 V
- It is 3.25 cm X 2 cm in size.

The above features are essential in producing a compact electronic motor control architecture that are capable of handling the chosen motors at a wide range of frequencies.

The control and polarity of the Pololu motor driver are illustrated in Appendix C.2 by figure C.3 and table C.1.

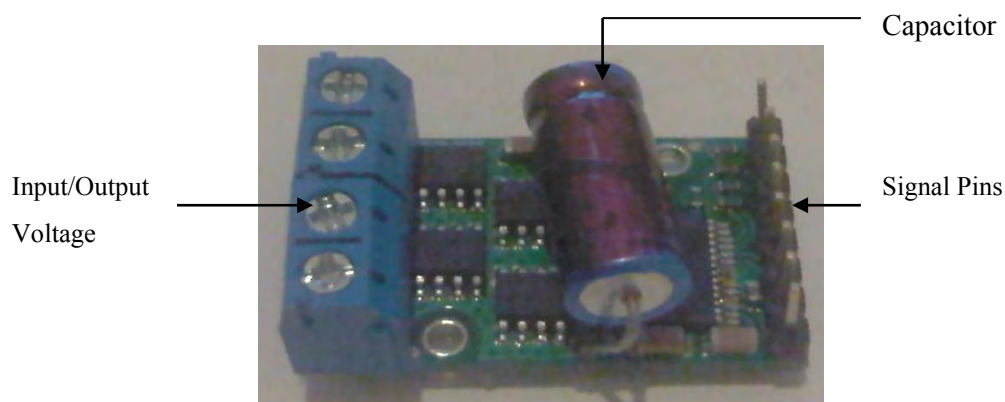


Figure 5.4: Picture of the Pololu motor driver.

A Pololu H-bridge model was also used for the supination and pronation movements as this H-bridge was capable of being supplied by a 6 V power source. This motor driver was referred to as the 6 V H-bridge and the motor used was for a low torque and current application, as previously explained.

An Elechouse 50 Amp motor driver was used for the high torque motors. It consisted of a dual output which allowed for the operation of two motors with a single motor driver. Generally, motor drivers of this capacity are bulky and require cooling however this motor driver was 60.5 mm x 45.5 mm and could provide a continuous current of 50 Amps without the need of external cooling. This half-bridge consisted of (but not limited to) the following features [55]:

- Dual motor output.

- Operation voltage 3.0V-15V
- Could supply 50 A of continuous current
- Peak Current of 100A
- It was 60.5 mm x 45.5 mm in size
- It allowed for a PWM duty of 0%-98%.

The 50 Amp motor driver is illustrated in Figure 5.5, below, and the control and polarity layout is illustrated in Appendix C2 by figure C.4 and table C.2.

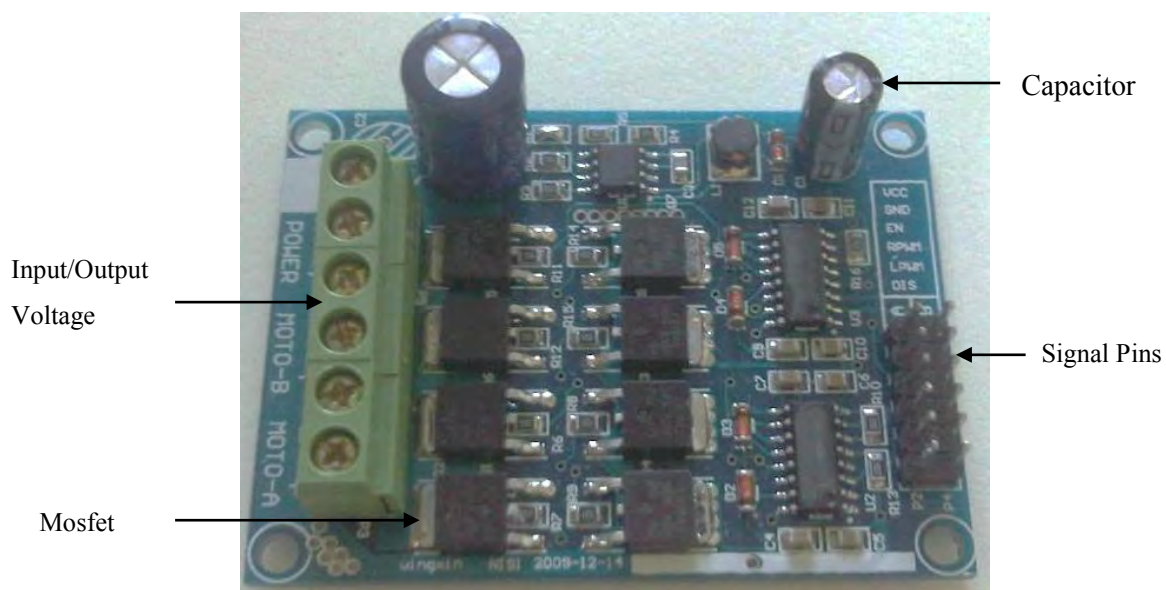


Figure 5.5: Picture of the Elechouse 50A motor driver.

The H-bridges were chosen for the required current ratings and their respective sizes. These compact motor drivers facilitated with the portable aspect of this research. Both H-bridges provide a braking torque using the back EMF from the motors. This brake is useful and allows the arm to fall gradually with some resistance to gravity in the case that there is a loss in power. However, the H-bridges do not freeze the motors at the desired position when power is lost. Future work may consider implementing motor brakes.

5.3.3 USB communication

An additional FT 232 was required for testing although there is one built into the Arduino. The FT 232 allowed for communication between the PC and the microcontroller. During testing it was essential to monitor the data transmitted from the PC and the data transmitted from the microcontroller. An individual FT 232 used one of the communication ports of the PC and only a single program could have access to a communication port. Therefore two FT232s were required since Matlab® was used to transmit data to the microcontroller and CodeVisionAVR's Terminal was used to monitor this data. The schematic of the FT232 on a printed circuit board (PCB) is illustrated in Appendix C.3 as Figure C.5. This PCB board is illustrated in Figure 5.6.

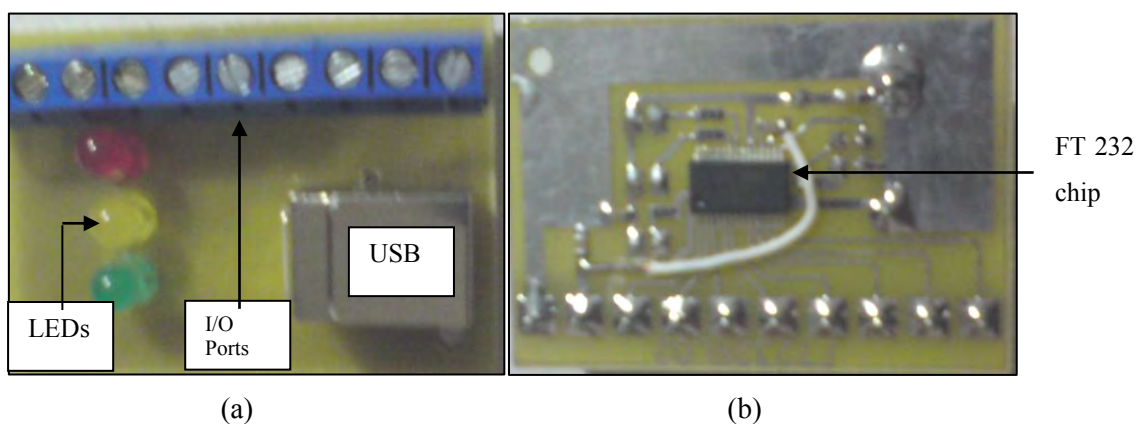


Figure 5.6: (a) Top view of FT232 with access to USB communication, (b) bottom view illustrating actual FT232 chip.

The USB communication medium provided a plug and play medium which assisted with the entire integration of the system as well as user-feedback to the PC.

5.3.4 Encoder sensor

HEDS-5701 G00 incremental encoders were implemented in the design which allowed for the actuation positioning. Absolute encoders would have been preferably, however were rejected due to higher cost. The HEDS encoder consisted of 360 pulses per revolution which related one degree to one pulse this relationship resulted in an accuracy with a total possible error of 0.5 degrees for every activation. It was a two channel incremental encoder with a high quality shaft which only allowed for movement about its axis. The two channels of the encoder were out of phase by 90 degrees in

frequency. Channel A leads channel B during a clockwise motion and vice versa during an anti-clockwise motor. Channel A was connected to an interrupt of the microcontroller whereas channel B in connected to an input pin of the microcontroller. This connection allowed for the counting of pulses in the relative direction. The encoder that was used can be seen in Figure 5.7 (a) and it was mounted on to the shaft of the motor via a simple coupling design. The device was initially referenced at start up by moving the joints to their relative joint limits and then offsetting the joint angles to correspond with the initial respective angles in the kinematic model. The offset angle was calculated using the encoder count.

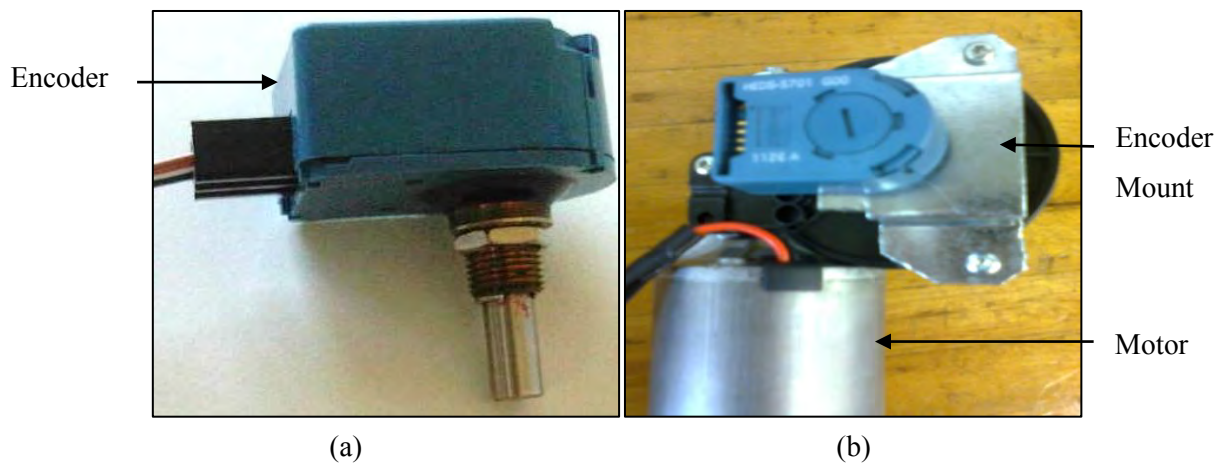


Figure 5.7: (a) The two channel HEDS 5701 G00 encoder, (b) mounted onto the Doga Motor.

5.3.5 Power Supply

A 12 Volt (V) lead acid battery, that provided 80 amps per hour continuously, was used to power the actuation. Parallel power distribution was implemented for the different actuators and components. The 12 V signal was regulated to 6 V and 5 V in order to supply the servo motors and the sensors respectively. A LM7805 (5 volts) and LM7806 (6 volts) voltage regulators were used to regulate the 12 V supply to 5 V and 6 V respectively. Both these regulators could supply a maximum current of one amp. Figure 5. is a diagrammatic layout of the power supply unit with the positive and negative terminal supplies represented by the red and black solid lines respectively. The 12 V power supply was split via a con-block (vertical orange column in Figure 5.8) in order to neatly create a parallel distribution. This then supplied the 3 H-bridges (including the dual H-bridge), a 6 V regulator and a 5 V regulator. The 6 V regulator supplied the 6 V motor's H-bridge; this motor drew a stall current of 692 mA. The output was spilt using a con-block (not illustrated in Figure 5.8) to supply the 5

encoders and 2 servo motors. The encoders and servo motors required a combined maximum current of 800 mA which was supplied by the 1 A regulator. A 120 A fuse was placed after the battery before the parallel distribution as illustrated in Figure 5.8. This was to protect the battery in the event of a short circuit. The battery was capable of distributing a maximum output of 140 A. There were fuses before each H-bridge in order to protect the motor drivers; these included two 15 A fuses, a 50 A fuse and a 1 A fuse for the Pololu, dual and 6 V H-bridges respectively. A safety switch was also implemented in the power supply unit and was situated before the parallel distribution.

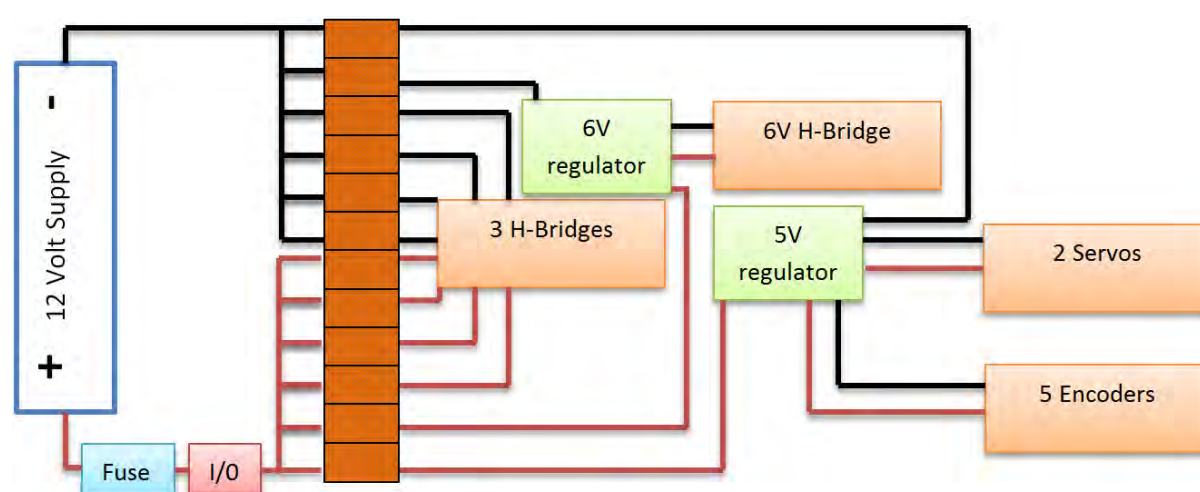


Figure 5.8: Diagrammatic layout of the power supply unit.

5.3.6 Wiring

The wiring of the electronic hardware was essential; it had to be routed through the exoskeleton device without hindering manoeuvrability. The wiring had to also be compact to assist portability but at the same time allow adjustability. The encoder signal wires were wrapped in spiral tubing and routed through the exoskeleton C-channel links together with the motor wiring. Figure 5.9 illustrates the routing of the wiring through the link. The electronic components were housed in a plastic polystyrene box. The signal wiring consisted of pins at the ends which allowed for a relatively fixed placement into the Arduino board, these pins reduced the chance of the wiring becoming loose. An additional con-block was used to provide a common ground between the electronic components. The polystyrene housing was mounting at the top of the stand such that the stand could be adjusted. The housing could also be unbolted and placed on a table if maximum adjustability is required.

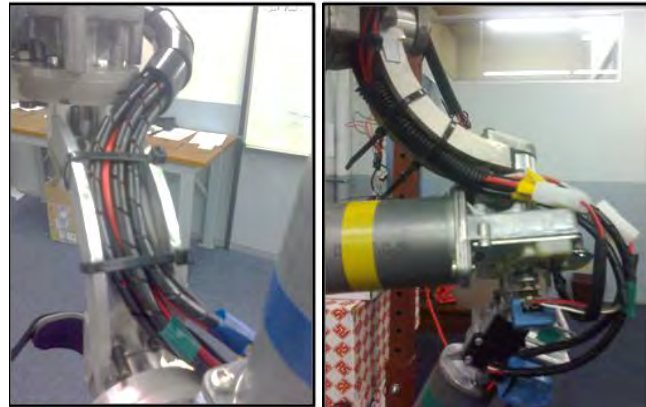


Figure 5.9: Picture illustrating the wire routing.

5.4 Chapter Summary

The ACM together with the PC formed an essential sub-system of the bio-mechatronic research which was integrated with the mechanical and software components of this design. The choice of a single microcontroller as well as compact motor drivers minimised the maximum size and weight of the research design which satisfied the portability criteria of this subsystem. The diagnosability and integrability aspects of the design were satisfied by a combination of the encoder sensors as well as the plug and play feature provided by the USB communication medium. The wiring was routed through the exoskeleton's links which did not limit the mobility or adjustability of the exoskeleton. A successful electronic exoskeleton system was designed which satisfied the electronic design considerations.

6 Exoskeleton Software System

6.1 Software Design Considerations

The exoskeleton software was designed with the consideration of four important features, these included user interaction, software safety, communication protocol and therapeutic passive control. The characteristics were implemented as an integration of the entire design in order to provide the physical therapy requirement. The software characteristics were elaborated as follows:

- **User interaction** – It was important to provide a Graphical User Interface (GUI) to assist the medical professional. The GUI allows for positioning of the end-effector in the X, Y and Z co-ordinates or the joints may be controlled individually without the knowledge of the kinematic models.
- **Software safety**- Joint limitation was implemented in the software stages, this was essential in order to prevent hyper extension or hyper flexion of the joints.
- **Communication protocol**- A protocol was established to transfer data between the GUI and the microcontroller.
- **Therapeutic passive control**- Proportional Integral Derivative (PID) and Proportional Integral (PI) control was investigated in order to provide the required passive positioning with accuracy and smoothness.

This chapter will discuss the development of the above described characteristics and illustrate their implementation in this research and design.

6.2 Graphical User Interface (GUI)

The GUI was created using Matlab®. The choice of software was essential as Matlab® allowed for easier linkage of the GUI and the code of the inverse kinematic model. The GUI creates the necessary interface between the user, the kinematic model and the hardware. This interface was created in order to perform the following tasks:

- User input and feedback
- Access Kinematic model
- Convert to the necessary protocol and

- Ensure joint values were within their limits.

The GUI implemented in this research is illustrated in Figure 6.1. The blue text in the GUI is to assist the user in supplying the correct information.

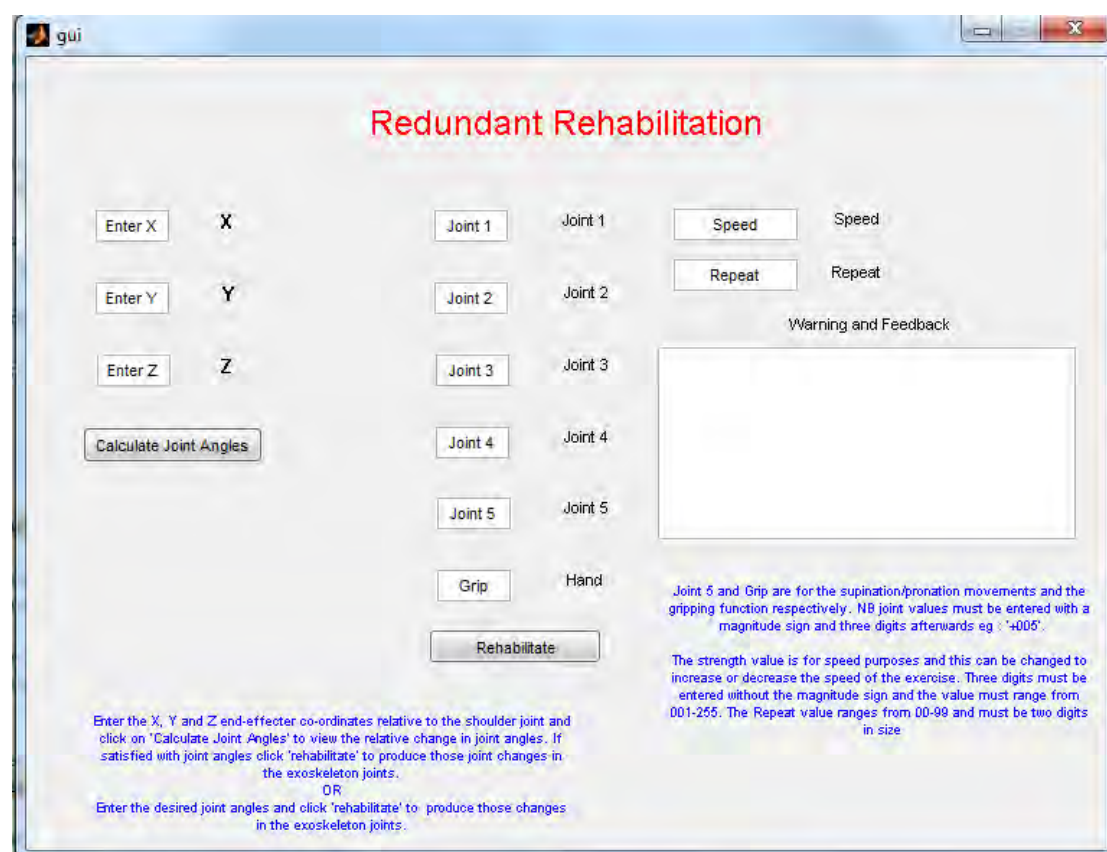


Figure 6.1: GUI Implemented in this Research.

6.2.1 GUI operation

The medical professional is allowed to enter a desired end-effector co-ordinate position that he/she may think is suitable for a combination of movements. The 'Calculate Joint Angles' button accessed the inverse kinematic model and use the desired co-ordinates specified by the user as a reference. The model then calculated the joint values for joints 1 to 4 and placed them in the relative joint text boxes which are illustrated in Figure 6.1. The medical professional could edit these values if necessary and

then enter the desired joint 5, hand and speed values. The 'Rehabilitate' button will then check if these values are within the joint limits and either display a warning or send the command to the microcontroller in order to perform physiotherapy on the upper limb. The two different kinematic models were accessed separately via two different GUIs. The layout was exactly the same however the non-redundant model only solved the three shoulder joint values and it positioned the manipulator according to the elbow joint as explained in chapter 4.

6.2.1.1) Protocol

A protocol had to be established in order to successfully communicate with the microcontroller. Serial communication was used and data was sent as a Robotic One-way (RO) packet. A RO packet is when data is sent from one station to another without the confirmation of data being received [57]. This was acceptable as the system was designed such that the exoskeleton would become mobile as soon as the data packet was received by the microcontroller. The data packet was sent as a 30 character string. The 5 joint values, the gripper joint value, the speed value and a start byte form the 30 characters. The start byte was chosen to be the character '#' and each joint contained 4 characters of which the first determined its magnitude and the remaining three characters represented the change in joint value, from the initial position. The speed value was 3 characters in length and represents a Pulse Width Modulation (PWM) value in the range of 0-254. The speed value was the maximum PWM value that the passive controller could achieve. This value affected the strength as well as the speed of the exoskeleton's motors during operation. A repeat number input was also specified in the GUI. This number specified the numbers of times the mechanism would move from the initial to the desired point. An example of this protocol can be seen in Figure 6.2, below, for the following values:

- Joint 1 : 45
- Joint 2 : -100
- Joint 3 : 9
- Joint 4 : 81
- Joint 5 : -20
- Grip : 19
- Speed : 99
- Repeat : 07

The angles determined by the inverse kinematic model were rounded off to the nearest degree; which would result in a maximum error of 0.5 degrees. This rounding off was implemented because the

encoders chosen had a resolution of one pulse per degree and therefore a fraction of a degree could not be achieved. This was acceptable as such accuracy is not necessary for physiotherapy.

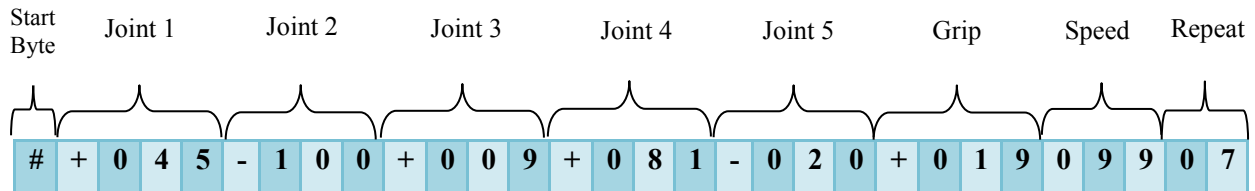


Figure 6.2: Sample Protocol Data Packet for the above described values.

The angles determined by the model were then placed in the format illustrated by the above described protocol, e.g. if the angle was a unit then two zeros and the magnitude sign had to be added to the unit string, as shown in the sample protocol data packet. A sample code (Matlab®) for this modification is illustrated below for joint 1 (referred to in the code as 'n1').

```

if str2num(n1) > 100 || str2num(n1) < -100
    if str2num(n1) < 0
        n1=num2str(abs(str2num(n1)));
        count1=count1+1;
    end
end
if str2num(n1) < 100 && str2num(n1) >-100
    if str2num(n1) < 10 && str2num(n1) >-10
        if str2num(n1)>0
            n1=['0',n1];
        else
            n1=num2str(abs(str2num(n1)));
            n1=['0',n1];
            count1=count1+1;
        end
    end
    if str2num(n1)>0
        n1=['0',n1];
    else
        n1=num2str(abs(str2num(n1)));
        n1=['0',n1];
        count1=count1+1; % count 1 is further used to determine the
% magnitude sign that will be placed in the string

    end
end
if str2num(n1)==0
    n1=['0',n1];
end

```

6.2.1.2) Joint limits

The GUI checked the individual joint limits before sending the data packet. A warning was sent to the 'Warning and Feedback' window in the GUI if any of the joints did not obey the joint constraints specified in chapter 4. The GUI will also adjusted those unconstrained joint values to the nearest joint limit and place those values in the relative joint text boxes. This adjustment and placement allowed for a quick continual from the disruption of the unconstrained joints, which resulted in the warning, and allowed the user to 'Rehabilitate' again, if desired. The GUI safety was necessary as a joint limit could be breached by 0.5 degrees during the round off or for any unaccountable reasons.

6.2.1.3) GUI Interaction with Microcontroller

The interaction of the above described processes with the microcontroller is illustrated in Figure 6.3, there is feedback from the microcontroller but this is not illustrated in figure 6.3. The GUI serially communicates with the microcontroller via the USB communication medium which was implemented in the PC.

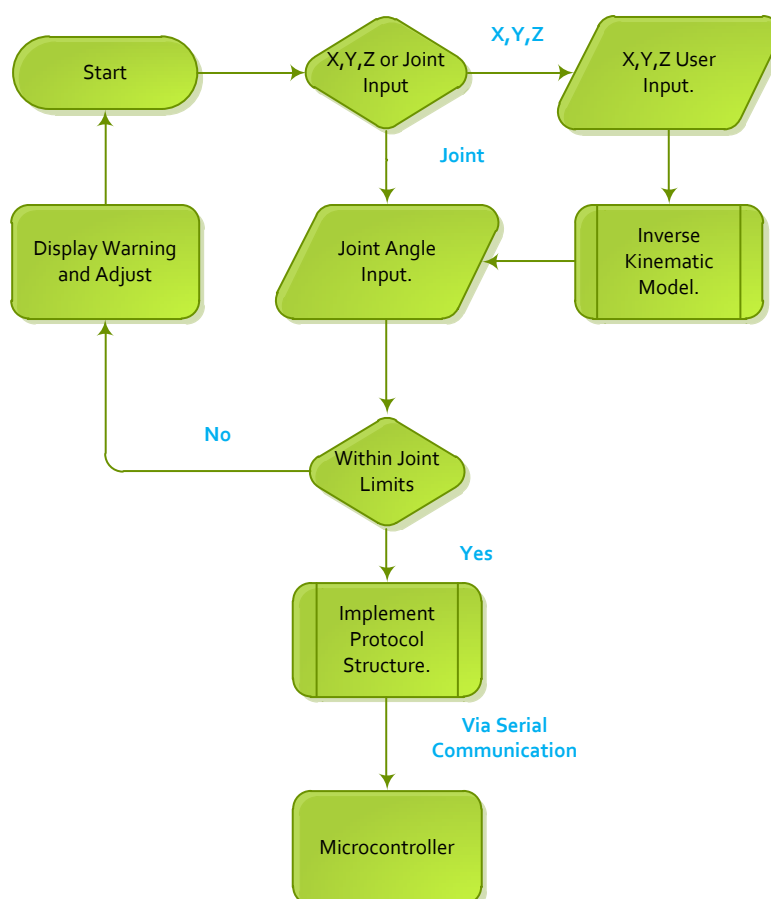


Figure 6.3: Flowchart illustrated the GUI processes with the Microcontroller,

A sample code of the GUI can be seen in Appendix D.1. The entire GUI code can be seen in the supplementary CD

6.3 The Microcontroller

The microcontroller was responsible for performing several tasks which included:

- Receiving the Serial Protocol
- Processing Encoder Pulses
- Executing the therapeutic passive control
- Applying the correct PWM signals and
- Collision detection.

6.3.1 Receiving the Serial Protocol Data Packet

The data packet which was sent serially from the GUI needed to be accessed. This was done using the Rx interrupt of the microcontroller. The buffer size of the microcontroller was set to 30 in order to receive the 30 character string successfully. The string was stored into a buffer variable which was then incrementally analysed from the first character using If Then statements. If the microcontroller identified a '#', which was the start byte of the protocol, it stopped processing and assigned the Joint 1 part of the protocol to an array variable called ref. This was done for all the joints and the speed part of the protocol was assigned to a strength variable. This part of the microcontroller C-code can be seen in Appendix A.2. The entire microcontroller code can be seen in the supplementary CD.

6.3.2 Processing Encoder Pulses

There were five encoders in this system and these were processed simultaneously through 5 external interrupts on the microcontroller. This processing was acceptable as the motors were operated at a relatively low speed of less than 0.5 revolutions per second. However, the external interrupt code had to be as minimal as possible since the encoders interrupted the microcontroller simultaneously during a joint combination movement. The minimisation of the interrupt code resulted in a short time allocated to the external interrupt as shown in the sample code below for the encoder 1 (referred to in the code as 'current [1]').

```
// External Interrupt 1 service routine
interrupt [EXT_INT1] void ext_int1_isr(void)
{
  /*Code for encoder1 counting every rising edge of channel A
  if(PINA.1) current[1]--; // if channelB == 1; rotation = CCW, else if channelB == 0; CW.
    else current[1]++;
  change[1]=1;
}
```

This current value together with the ref values is used to perform the passive control.

6.3.2.1 Passive Control Therapy

The passive therapy was achieved by investigating the responses of different positional control implementations; these included a combination of Proportional, Integral and Derivative positional control. It was essential to emphasise that the system's stability was more important than the response

time; the reason being was that having a quick response was more likely to reduce the stability of the system [58]. An unstable system would have either had an overshoot or a change in direction [59]. This was not desirable as an overshoot could result in movement which was not within the joint limits and a change in direction could have resulted in a response that was not smooth. It was concluded that the controller consists of a smooth and accurate motion. The PID control theory was a closed loop system which is illustrated using the schematic represented by Figure 6.4.

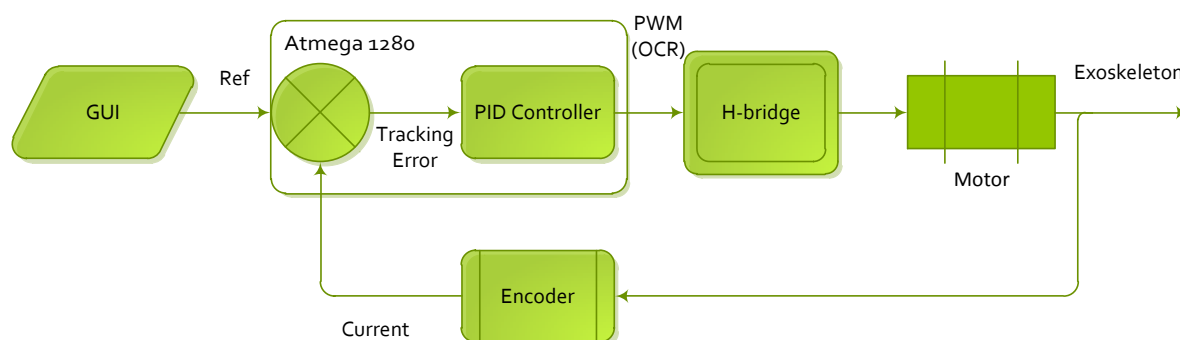


Figure 6.4: Closed loop relationship between the GUI, microcontroller and other components of this research.

The tracking error, which was the difference between the ‘ref’ position and the ‘current’ position, was calculated. This error was then sent to the PID controller which calculated the integral and derivative of this error. The output from this controller was the PWM signal which is calculated according to equation 6.1 [59].

$$\text{PWM} = (\text{tracking error} * K_p) + (\text{integral error} * K_i) + (\text{derivative error} * K_d) \quad (6.1)$$

Where K_p , K_i and K_d were the proportional, integral and derivative gains respectively. These gain values were essential in producing the desired stable response. A Matlab® program was created in order to analyse and establish these gain values which were tuned and implemented in the microcontroller. A linear relationship between the current and PWM values were established in order to provide a theoretical response. It was determined, experimentally, that a PWM of 20 did not create movement of the motor under minimal load. It was therefore decided to increment the current value for PWM values greater than 20. This Matlab® code can be seen in Appendix D.3.

PID theory reveals that the proportional gain would have the effect of reducing the rise time, which was the time it took to go from the initial to the reference value. This gain would also reduce the steady state error which was the difference between the input and output values (the tracking error). However, the proportional gain could not completely eliminate this error. The integral had the capability of eliminating the steady state error but at the same time it could hinder the transient response. The integral factor in the PID control resulted in an integral windup. An integral wind up is the build-up of error through successive loops [59]. This build up was useful in the system especially when the initial PWM is not large enough to create a movement against a load. The integral wind-up allowed for the PWM to increase in a stationary system which would increase the chances of motion in a high load operation. The derivative gain could improve the systems stability, transient response and reduce over shoot. It was therefore decided to investigate the different gains and their impact on the response. The responses was analysed according to the iteration count (number of loops) and not according to time, as this allowed for better observation of the looping structure.

The PID terms was analysed for a step input which can be seen in Figure 6.5. The proportional term was investigated for different values and their responses are plotted in Figure 6.6. The steady state error was not completely eliminated as noticed in Figure 6.6.

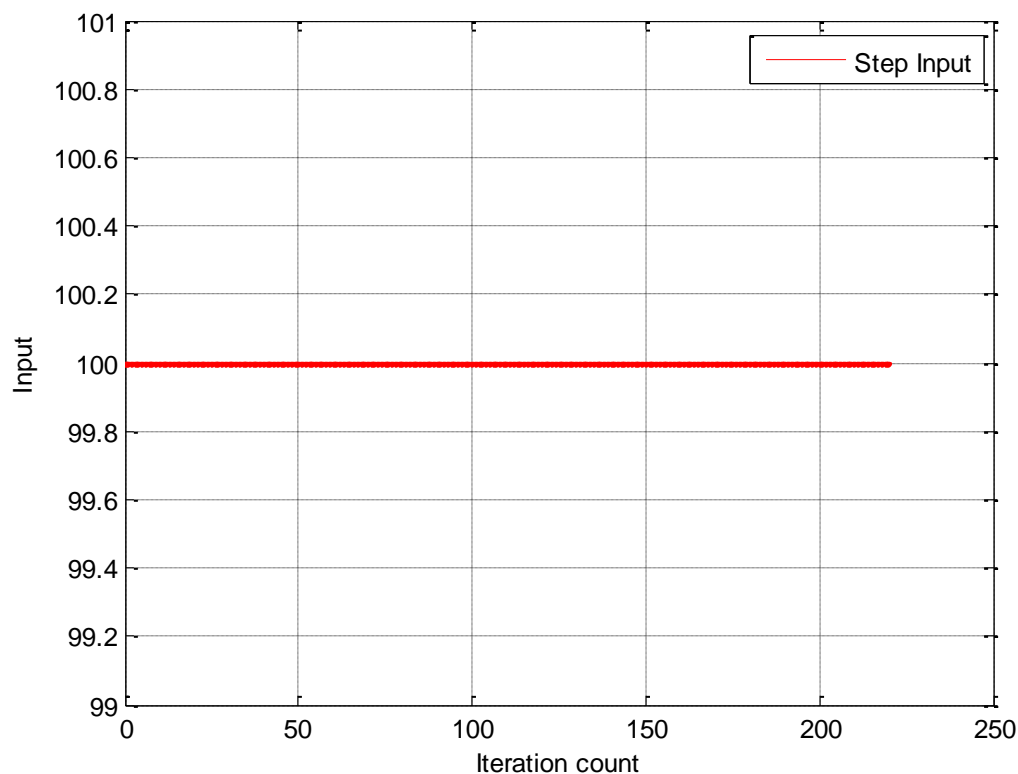


Figure 6.5: Graph Representing the Step Input.

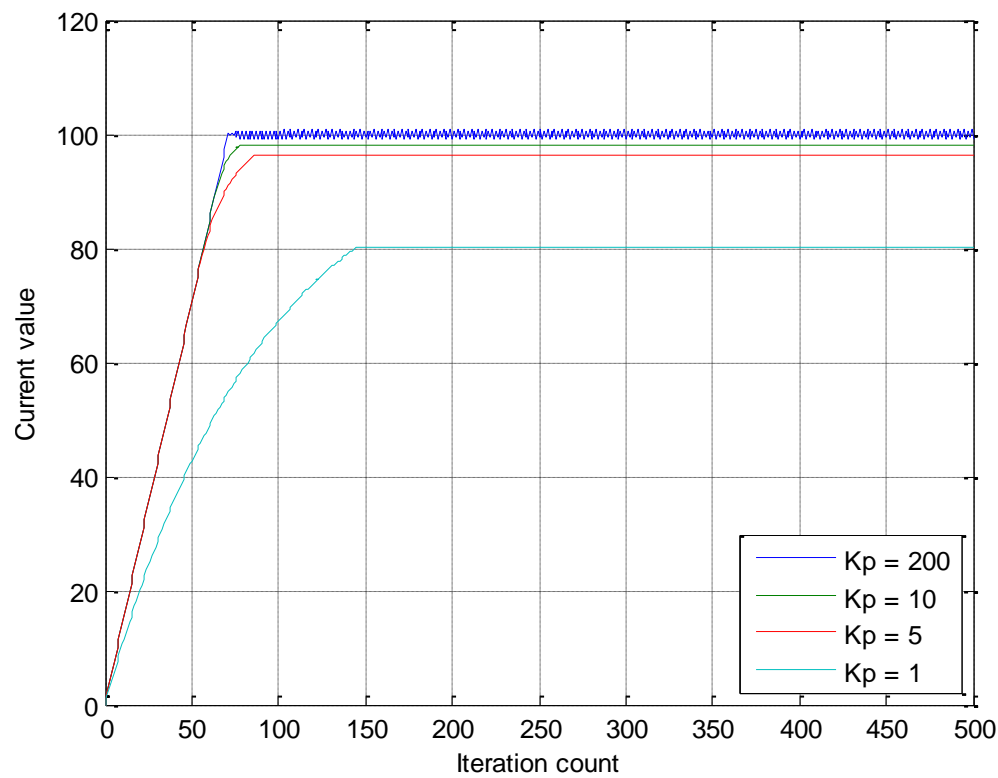


Figure 6.6: Graph Representing the Different Responses for Different K_p Gains.

Figure 6.7 illustrates the different K_i values that were plotted for a K_p of 5. It was noticed that the transient response was affected by the oscillations, and that the steady state errors were eliminated (except for $K_i = 0.1$).

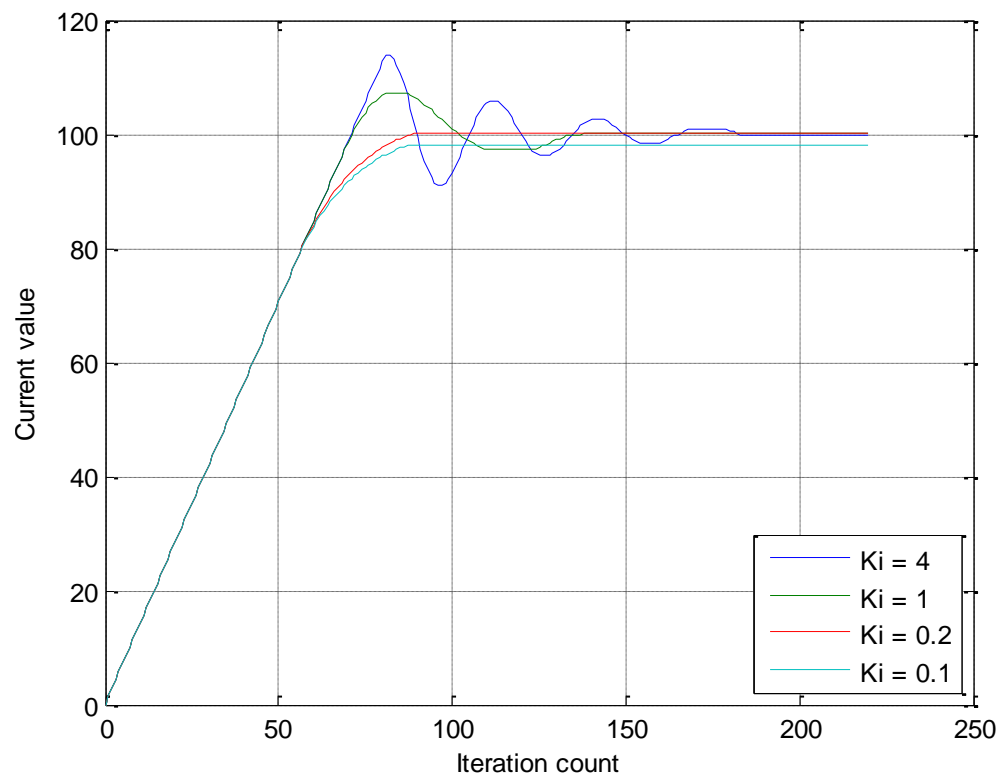


Figure 6.7: Graph Representing the Different Responses for Different K_i Gains ($K_p=5$).

Figure 6.8 illustrates the different responses for different K_d values with a constant K_p and K_i of 5 and 0.2 respectively. The derivative gain increased the curvature of the step response and reduced the response before settling which was for a negative derivative gain. This curvature can be seen in Figure 6.8.

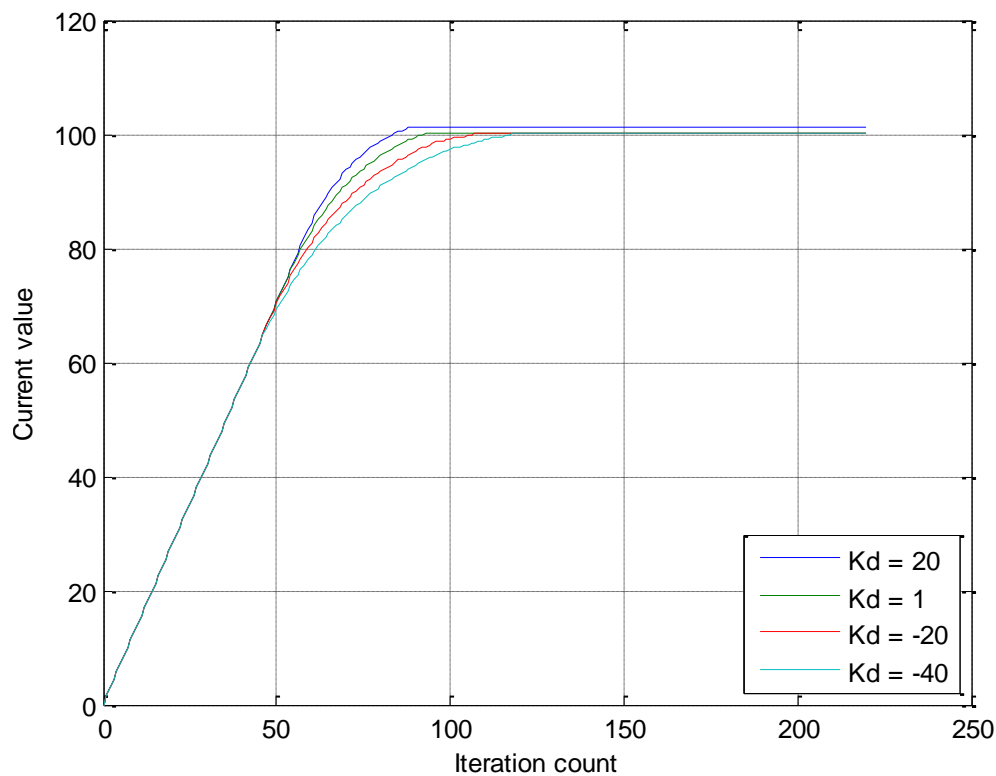


Figure 6.8: Graph Representing the Different Responses for Different K_d Gains ($K_p=5$ and $K_i=0.2$).

Gains were then chosen in order to give a smooth stable response without the need of a rapid response; the chosen step response is illustrated in Figure 6.9. This response is for K_p , K_i and K_d of 1.5, 0.2 and -20 respectively. The proportional gain was decreased from 5 as a lower K_p provided a larger curved response, hence a smoother step response.

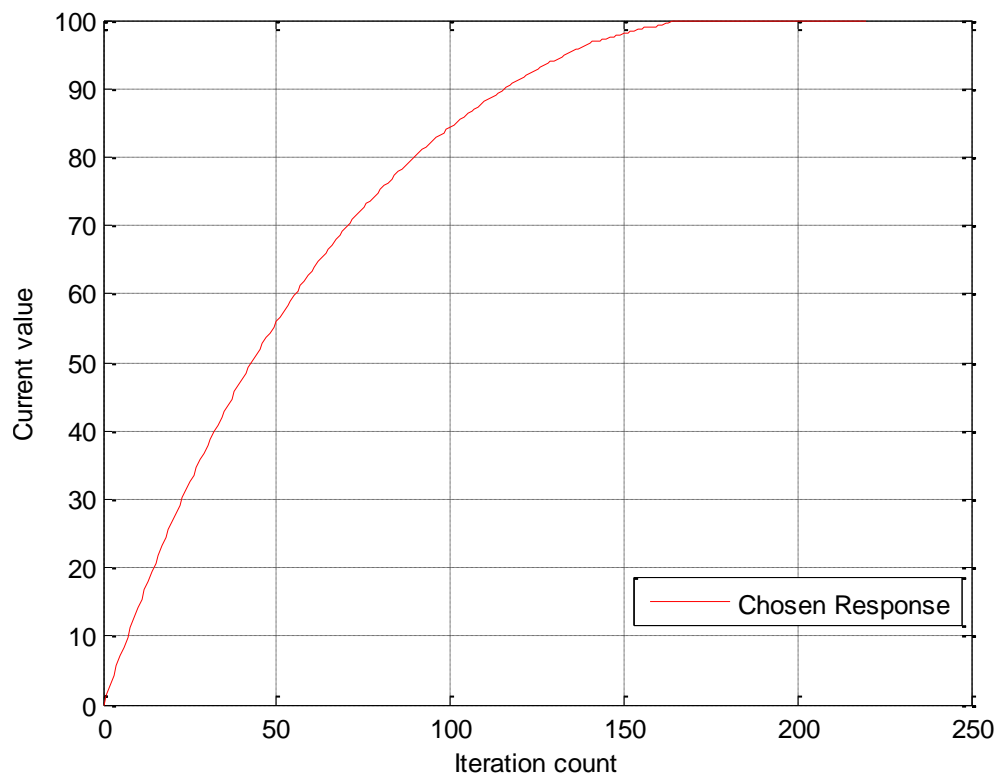


Figure 6.9: Graph Illustrating the Chosen PID Response.

The practical testing of the control system was illustrated in this chapter in order to express the implementation of the system in a more conclusive approach. The actual practical step response of the PID controller was compared to the theoretical step response in Figure 6.10. The experimental line was more jagged; this is due to the fact that the encoder resolution was accurate to a degree and not to fractions of a degree. The practical response closely matched the theoretical response. The slight offset in the responses could be as a result of the theoretical relationship between the PWM and the current value as compared to the practical encoder readings. Both responses resulted in stability and an elimination of the steady state error with no overshoot, which is as desired. However, the response on the initial movement was jerky. This was a result of the step response which supplied a high initial PWM for large error values.

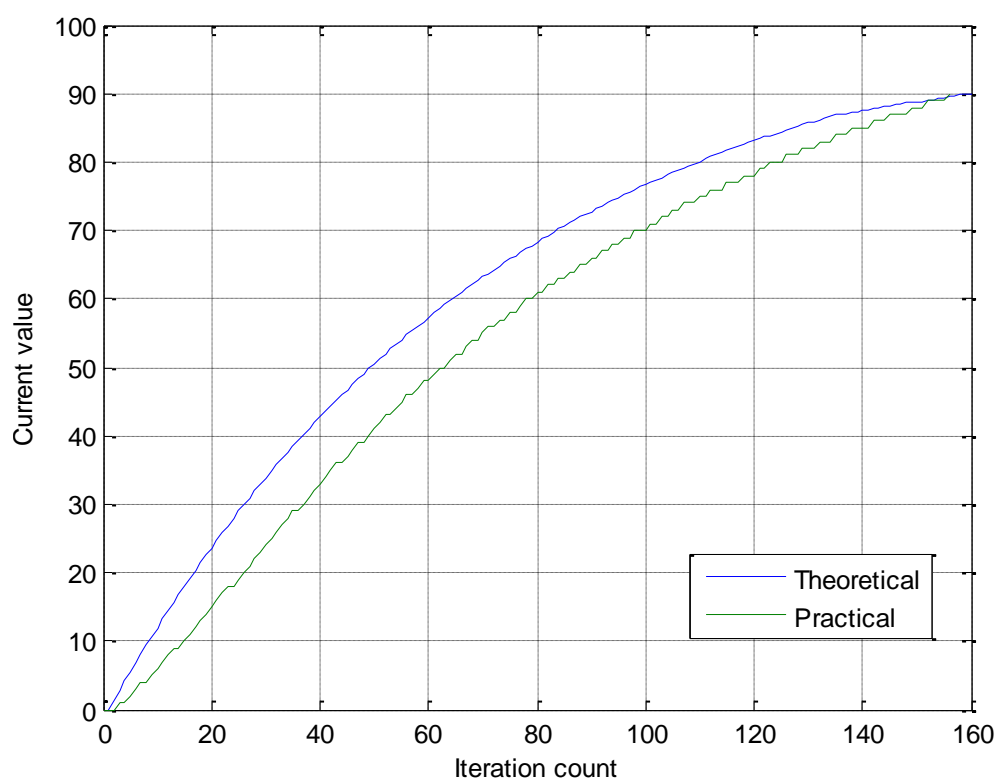


Figure 6.10: Graph Comparing the PID Theoretical and Practical Responses

This jerky motion was overcome by implementing a ramp input which increased linearly with every successive loop. This ramp input is shown in Figure 6.11, and the corresponding practical ramp response was compared with the above described practical step response. This comparison was illustrated in Figure 6.12. The initial gradient of the ramp response is much less than that of the step response which resulted in a smoother control system. The ramp response resulted in a control system that consists of no overshoot, no steady state error and it was stable and smooth. Therefore, the ramp response was implemented as the control system that provided the required passive physiotherapy. The derivative gain was not implemented in the ramp response. The ramp input incremented by a value of one for every successive loop. This small resolution required no additional damping; therefore a PI ramp controller was implemented. The C-code for this controller can be seen in Appendix D.4. It is extracted from the main C-code which can be seen in the supplementary CD.

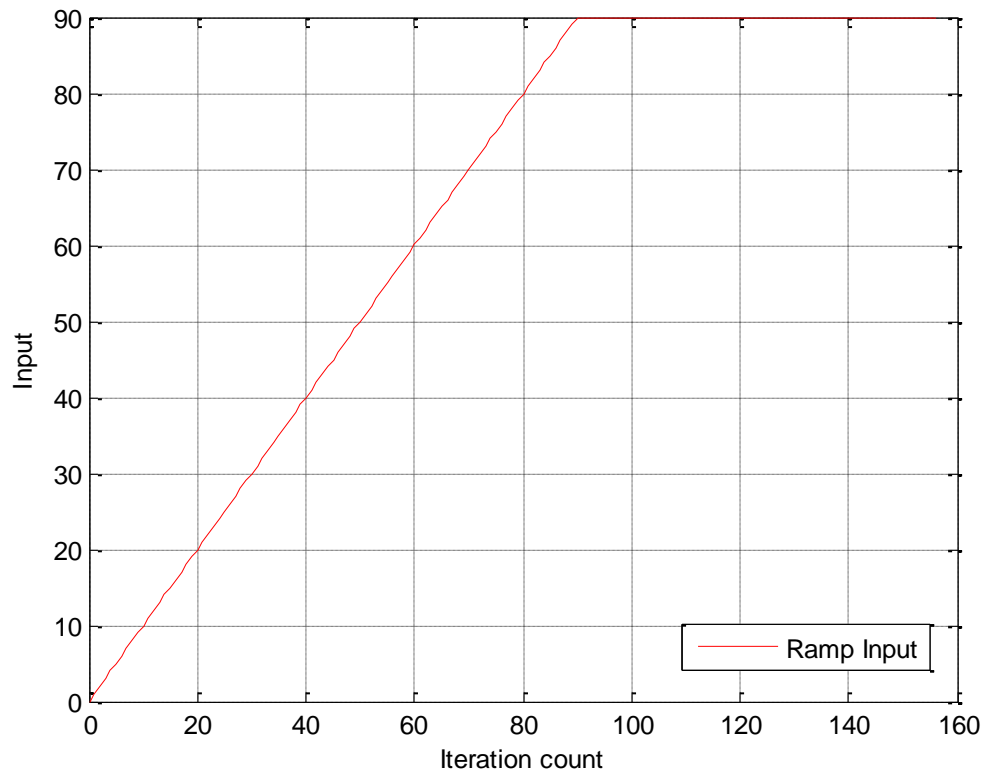


Figure 6.11: Graph Illustrating the Ramp Input.

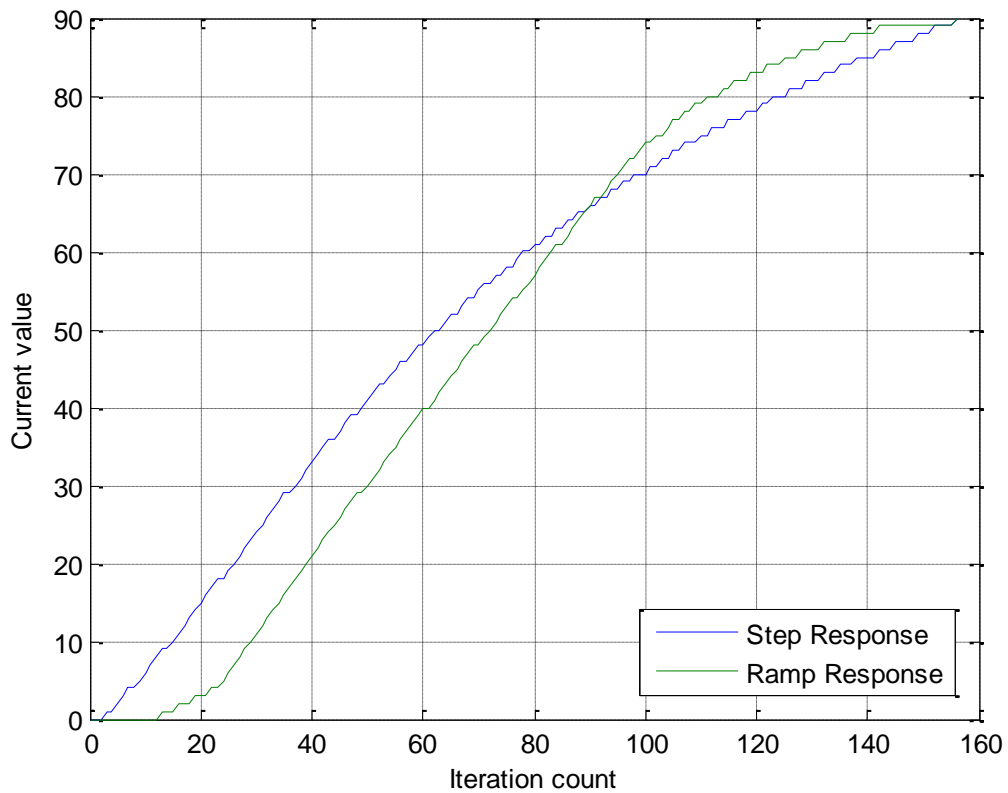


Figure 6.12: Graph Comparison Between the Step and Ramp Response.

6.3.2.2 Pulse Width Modulation (PWM)

The PWM signal was created using both 8 and 16 bit timers. This signal was calculated according to equation 6.1 and its frequency was calculated according to equation 6.2 [54]. Where N is the pre-scalar value and was chosen to be 1. The clock frequency, f_{clk} , was adjusted to 62500 Hz. The TOP value was set to 255. The TOP value is the highest PWM value that could be achieved and it determines the resolution of the duty cycle. A frequency of 122.5 Hz was achieved and this resulted in a smooth motor movement, therefore there was no need to increase the frequency. This frequency was within the maximum ranges of the chosen H-bridges.

$$f_{PWM} = \frac{f_{clk}}{2.N.TOP} \quad (6.2)$$

Phase and frequency correct PWM was executed on the ATmega 1280 microcontroller. The Output Compare Register (OCR) corresponded to the PWM signal and only the low bits had to be changed on the 16 bit timer as the maximum value was chosen to be 255. The duty cycle of the PWM was calculated by equation 6.3.

$$Duty\ Cycle = \frac{OCR}{255} \times 100 \quad (6.3)$$

The duty cycle was increased gradually from an initial value of 0 to a maximum value equal to that of the speed value.

6.3.2.3 Collision Detection

A 16 bit over flow internal interrupt was created to monitor the position of the joints every 1.05 seconds. This time value was chosen as it was easily obtained by changing the clock value to 62500 Hz without the need of adjusting any pre-scalar values. A collision detection message would be sent to the 'Warning and Feedback' box in the GUI if any of the joints experienced an initial movement but was at a constant position for 1.05 seconds without reaching the reference value. This routine would stop the generation of all the PWM signals. The pin layout for this research and the Arduino Mega 1280 board is illustrated in Appendix D.5.

6.4 Chapter Summary

This chapter presented the software system of the exoskeleton research and design. A GUI interface was created to allow user interaction with the exoskeleton mechanism. This GUI provided access to the kinematic model without any complications to the user. The GUI provided the necessary protocol in order to communicate with the microcontroller as well as joint limit detection for safety purposes. The microcontroller analysed the protocol successfully which allowed for the continual of the physiotherapy control. This control was investigated using a step and ramp response. The different types of controllers were compared practically and a ramp PI controller was chosen and implemented in the design. Collision detection was integrated and this sent a warning message to the user and stopped any further motor movement.

7 Exoskeleton Testing and Discussion

7.1 Introduction

This chapter will indicate the type of testing that was executed on the exoskeleton device. This analysis includes the following tests:

- Testing of the manipulators mechanical workspace
- Mechanical loading tests
- An Empirical positional test
- Portability test
- Control Revision.

The controls response was explained in chapter 6 and was part of the testing procedure.

7.2 Manipulators Workspace

The different range of joint motions were tested and compared to the researched joint ranges that were established by table 2-1. The exoskeleton manipulator was driven to its joint limits in order to determine its workspace angles, the exoskeleton joints were mechanically limited as described in chapter 3. The following joint motions were analysed:

- Shoulder abduction
- Shoulder flexion/extension
- Shoulder medial/lateral rotation
- Elbow flexion/extension.
- Wrist Pronation/Supination

The DOF as described above were tested and photographed. Shoulder abduction and flexion/extension is illustrated in Figure 7.1 (a) and Figure 7.1 (b) respectively.



Figure 7.1: (a) Shoulder Abduction, (b) shoulder Flexion.

Figure 7.2 (a) and Figure 7.2 (b) illustrates the maximum shoulder extension and elbow flexion respectively.

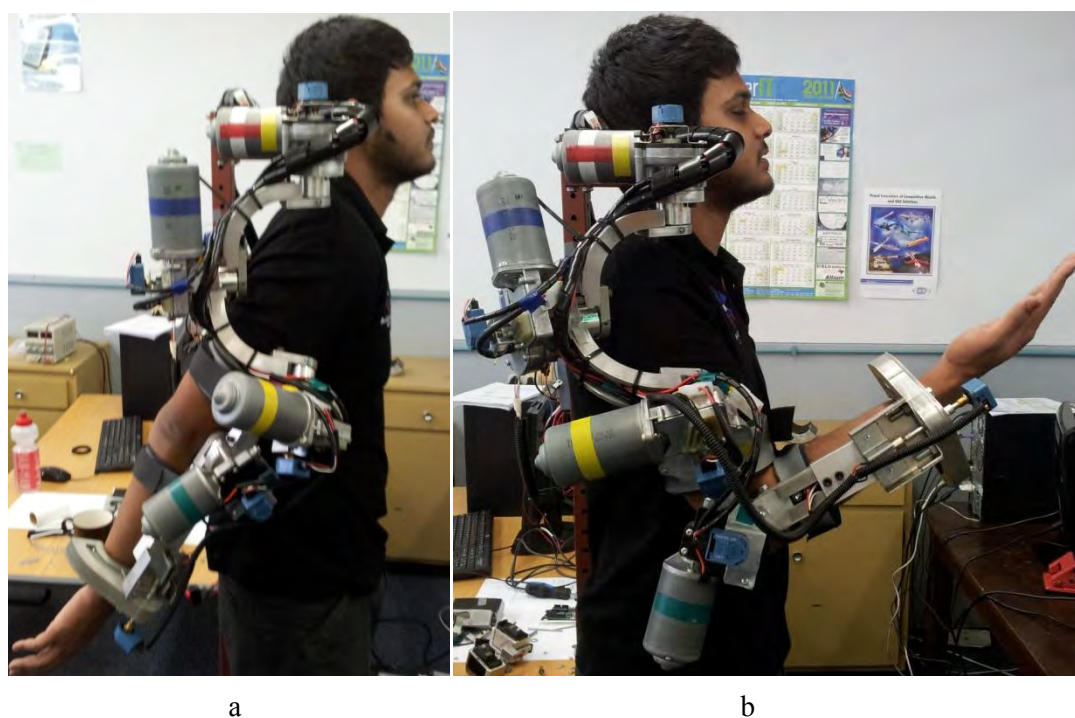


Figure 7.2: (a) Shoulder extension, (b) elbow flexion.

Shoulder lateral and medial rotation is illustrated in Figure 7.3 (a) and Figure 7.3 (b) respectively.

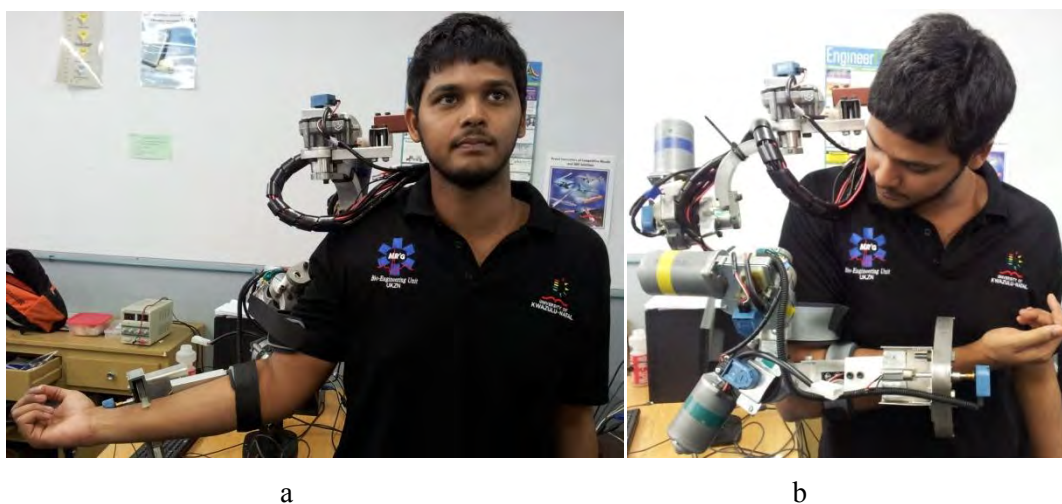


Figure 7.3: (a) Shoulder lateral rotation, (b) medial rotation.

Figure 7.4 (a) and Figure 7.4 (b) illustrated the supination and pronation movements respectively.



Figure 7.4: (a) Wrist supination, (b) pronation.

The workspace tests were concluded as follows in degrees.

- Shoulder abduction/adduction – $110^{\circ}/45^{\circ}$
- Shoulder Extension/Flexion – $30^{\circ}/135^{\circ}$
- Shoulder Lateral/Medial Rotation- $40^{\circ}/90^{\circ}$
- Elbow Flexion – 120°
- Wrist Pronation/Supination – $85^{\circ}/85^{\circ}$

Table 2.1 was edited to include the joint angles ranges of the DOF in this research. These values are tabulated in Table 7.1 under ‘UKZN Exo’ as a total range of motion in that specific degree of freedom.

Table 7.1: Comparison of Joint Movement in Degrees.

Joint	Motion	MGA [19]	MAHI* [29]	L- EXOS* [30]	CADEN- 7* [31]	HUMAN** [23]	ADL*** [31]	UKZN Exo
SHOULDER	Extension /Flexion	210	-	135	180	236	110*	165
	Adduction /abduction	138	-	140	180	173.5	100*	155
	Rotation lateral /medial	131	-	135	160	160	135*	130
ELBOW	Flexion	142	120	105	150	138	115*	120
WRIST	Supination /Pronation	360 but not motor actuated	180	180	160	172	150*	170

*Values are mechanical joint capabilities for both directions (total) where applicable.

**Values are the 50th percentile of a test of 100 males. Female joints are more flexible [23].

*** ADL – Activities of daily living [31].

The exoskeleton device in this research was capable of achieving more than the majority of the workspace of the ADL. It was deficient in shoulder rotation (lateral/medial) but was still capable of achieving 96.3% of this degree of freedom’s motion. The achievable workspace could be considered as a success as the exoskeleton utilised more than the combinational workspace of the ADL.

7.3 Load Tests

This chapter discusses the load tests of the shoulder, elbow and wrist mechanism. The hand mechanism was not designed to withstand a perpendicular load and was purely for exercising the gripping function.

7.3.1 Shoulder and Elbow Test

A load of 1 kg was placed on the end of the elbow mechanism, link 4, the elbow was fully extended and only the shoulder mechanism was mobilised to produce the worst case pose as illustrated in chapter 3. The load was repeatedly incremented by 1 kg until a load of 5 kg was achieved and the shoulder mechanism repeatedly moved from the anatomical position to the worst case pose. The elbow mechanism was tested by moving the elbow from the anatomical position to 90 degrees of flexion. This test was repeated from 1 kg to 5 kg with an increment of 1 kg during each test. Photographs of the shoulder test at the worst case pose with a 3 kg and 5 kg load can be seen Figure 7.5. The elbow test of 5 kg is shown in Figure 7.6.

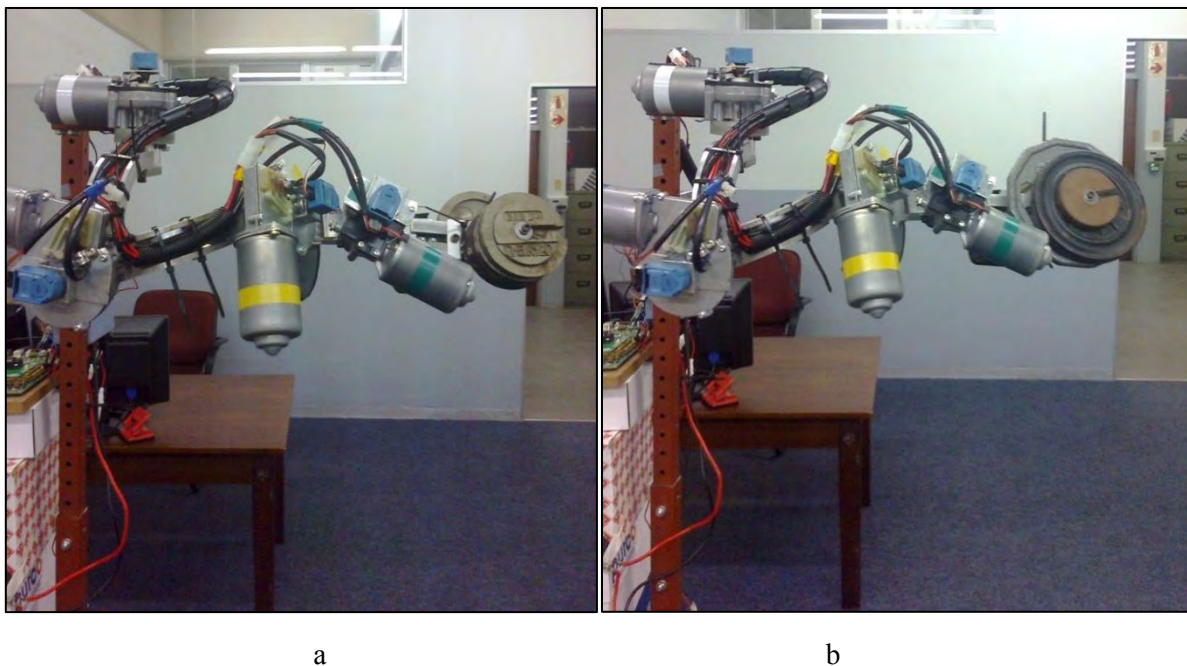


Figure 7.5: (a) Shoulder flexion of 3 kg, (b) 5 kg mass.



Figure 7.6: Elbow flexion of 5 kg mass.

The 1kg-3 kg loads were tested using a speed value of 150 PWM whereas the 4kg-5kg loads were tested using a speed value of 254 PWM. These PWM values corresponded to a duty cycle of 59% and 100% respectively. The loads were held at their respective positions for ten seconds. This was done by changing the timer values in the microcontroller. It was held for that duration to monitor the heat of the components. During the 5 kg test there was no noticeable heating in any of the components.

The 5 kg load at the end of link 4 produced a much larger combined moment, as a result of the summation of moments induced by the 95th percentile human arm, the wrist and hand mechanisms as well as an end-effector load of 2 kg. This resulted in external strength achievability for the shoulder and elbow flexion of 33 Nm and 15 Nm respectively. These torque values resulted in an HIS of 0.27 and 0.21 which was approximately the $\frac{1}{4}$ stall torque as specified. The stall requirements were met since the motors did not stall during normal operation. Higher loads were not tested as a safety measure although the 5 kg weight was lifted without signs of stalling.

There exists a linear relationship between load and time [60]. It was therefore decided to obtain this relationship in order to determine the consistency of the motion as well as verify the controller's response to different loads. These load tests were executed on joints 2 and 4 and the mass was applied as illustrated in Figure 7.5. These joints were both individually flexed by 90 degrees from the

anatomical position. The tests were done from no load up to 5 kg at a constant user defined PWM value (speed) of 254. The different loads for the shoulder joint were executed several times as seen in Table 7.2 which allowed for an average value to be obtained. These average values were plotted in Figure 7.7 and a trend line was obtained. This trend line produced a linear equation which is represented by equation 7.1.

Table 7.2: Test Values of Shoulder Joint Loads against Time.

Voltage (V)	Time (s)	Mass (kg)
12	3.49	0
12	3.43	0
12	4.50	1.6
12	4.46	1.6
12	4.43	1.6
12	5.37	2.8
12	5.25	2.8
12	5.52	2.8
12	6.95	5
12	7.22	5
12	7.13	55

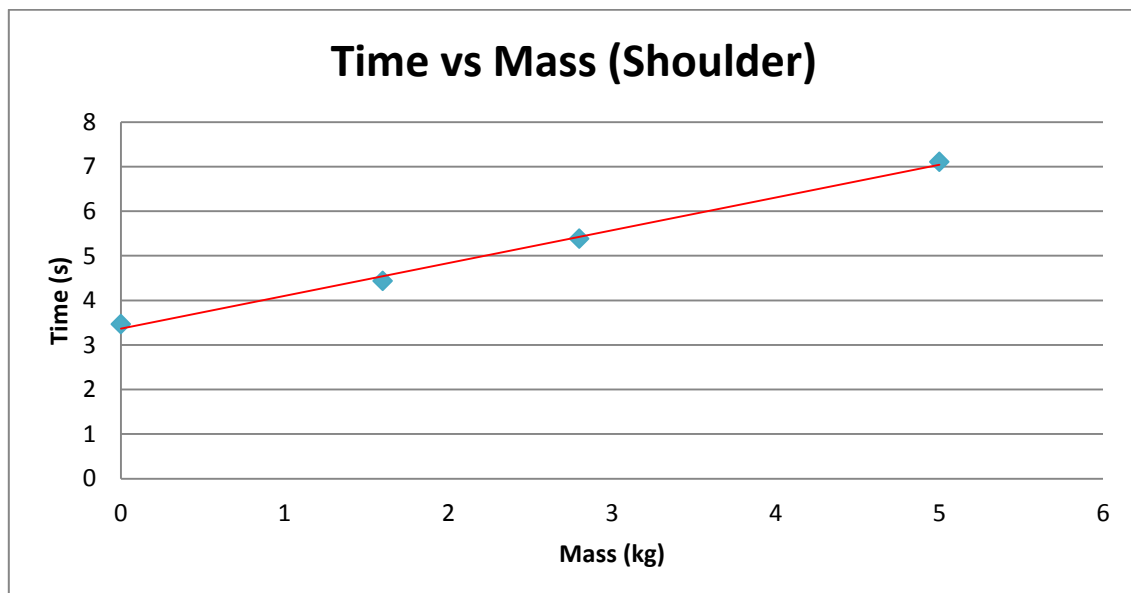


Figure 7.7: Graph of Time from 0-90 degrees vs Mass for the Shoulder Joint.

$$y = 0.735x + 3.3653 \quad (7.1)$$

The above described method was executed for joint 4 as well. The varying time and mass results are tabulated in Table 7.3 and the trend line is illustrated in Figure 7.8. The resulting linear equation is represented by equation 7.2.

Table 7.3: Test Values of Elbow Joint Loads against Time.

Voltage (V)	Time (s)	Mass (kg)
12	3.81	0
12	3.99	0
12	4.12	0
12	4.71	1.6
12	4.78	1.6
12	4.67	1.6
12	4.49	2.8
12	4.90	2.8
12	4.77	2.8
12	6.05	5
12	6.17	5
12	6.22	5

$$y = 0.4292x + 3.9863 \quad (7.2)$$

The varying load tests on joints 2 and 4 resulted in a linear relationship between time and mass. This verified that the controller's response was constant through varying loads that did not cause the motors to stall. The controller produced the same response in a longer period of time. Had the controller produce varying responses, a linear relationship would have not been derived. It was further noticed that joint 2 achieved the same angle change in a longer period of time. This could have been as a result of the larger gearbox reduction or the different moments acting on the joints.

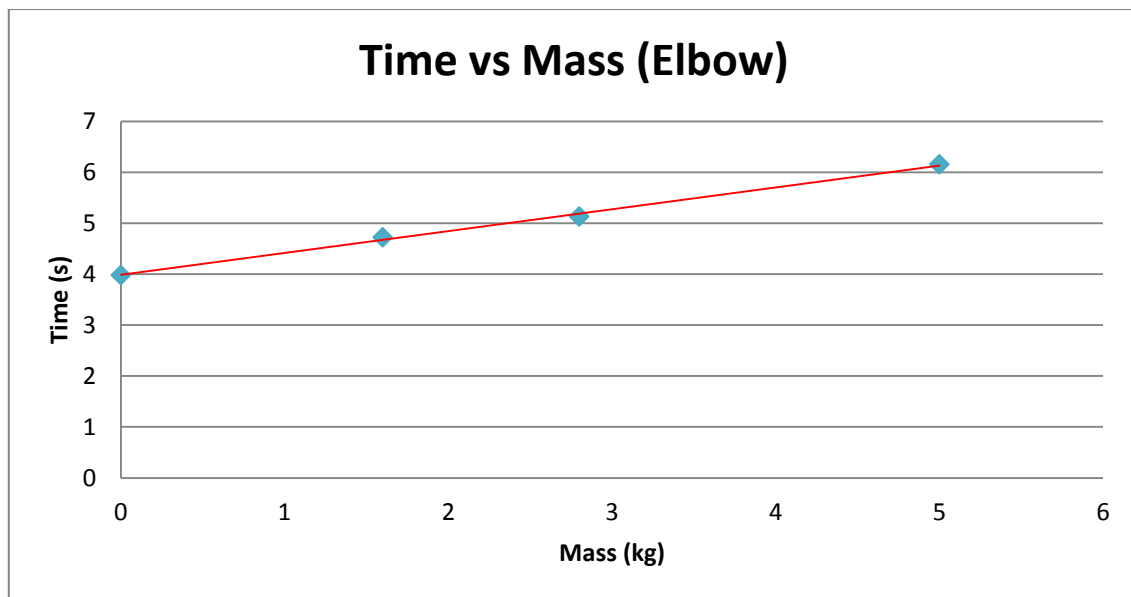


Figure 7.8: Graph of Time from 0-90 degrees vs Mass for the Elbow Joint.

The angular velocity varied according to the change in load however the duty cycle for the loads were varied from 59% to 100%. Acceleration was considered and a smooth start and stop was required, therefore the initial acceleration and the final deceleration were varied according to the ramp controller.

7.3.2 Wrist Load Test

The wrist mechanism was tested to rotate various loads which were acting against its rotation. The load was position as illustrated in Figure 7.9. Figure 7.9 is purely to illustrate the positioning of the load on the C-gear. The C-gear was rotated 90 degrees such that the C gear was positioned above its horizontal axis- this resulted in the load acting against the rotation.

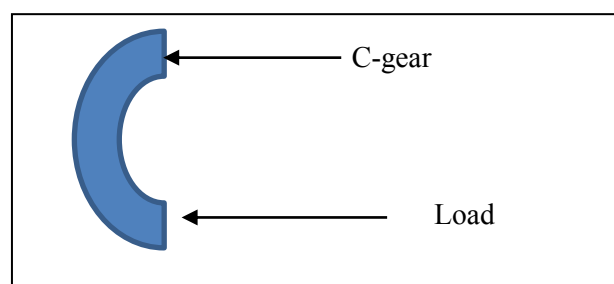


Figure 7.9: Illustration of Placement of the Load on the C-gear.

Loads ranging from just the weight of the C-gear up to 2 kg were timed and a trend line was produced as executed with joints 2 and 4. These tests are tabulated in Table 7.4 and the average of these tests was plotted in Figure 7.10.

Table 7.4: Test Values of Wrist Joint Loads against Time.

Voltage (V)	Time (s)	Mass (kg)
6	3.1	0.2
6	3.4	0.2
6	3.6	0.2
6	5	1
6	4.8	1
6	6	1.5
6	5.1	1.5
6	4.9	1.5
6	6.3	2
6	6	2
6	5.9	2

An equation for the trend line was created in Microsoft Excel this equation allows for a time and load relationship. This formula is represented by equation 7.3.

$$Y = 1.4471x + 3.2172 \quad (7.3)$$

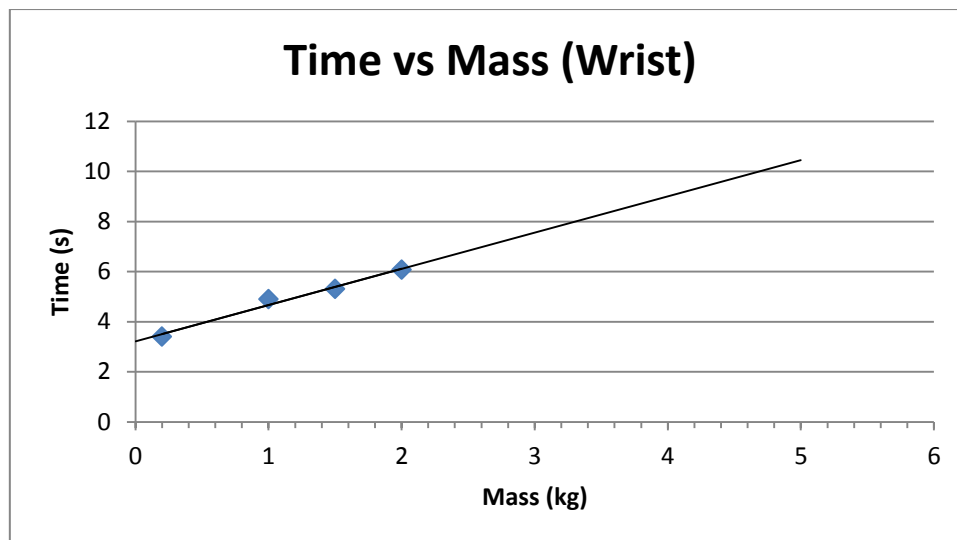


Figure 7.10: Graph of Time from 0-90 degrees vs Mass for the Wrist Motor.

The exoskeleton wrist mechanism was capable of handling the loading conditions without showing signs of stall. The time for a 90 degree revolution under a 2kg load was approximately 6 seconds this may seem long but it was appropriate for providing passive therapy to the wrist.

7.4 The Hand Mechanism

The hand mechanism was filled with foam in order to allow for better contact between the thumb and the inner walls of the left arced tubing. The servo created the required gripping motion for both the thumb and fingers and the wrist motion was propagated through the design. However, future developments should focus on reducing its size. This design accommodated for movement of the thumb and fingers and propagation of the wrist motion which was achieved.

7.5 Positional Test

The inverse kinematic model was tested using a digital image scaling empirical method. It was difficult to achieve a high accuracy by physically measuring the position of the exoskeleton. This empirical method is widely adopted in the measurements of objects or distances from satellite images, aerial photographs as well as digital images and involves making use of a scaling system [61]. This

digital scaling was implemented in the testing by taking images of two different planes. The cameras used to do the tests were calibrated to take the same pixelated images. The digital devices were placed at the same height and at the same distance away from the exoskeleton. These distances were measured with an accuracy of 0.5 mm. The cameras were also orthogonal to the plane in which they were capturing. The exoskeleton was then moved to an X, Y and Z position of 340 mm, 590 mm and 380 mm respectively. Videos of the X-Z and Y-Z planes were taken simultaneously to minimise any errors as a result of depth. A snap shot of the final position from the videos was taken. Specific positions on the picture were measured and these positioned were measured on the actual mechanism. This allowed for the creation of a scale for each picture. The pictures were printed to a larger scale to allow for greater accuracy. These pictures are illustrated by Figure 7.11 and Figure 7.12. The X and Z direction scales in Figure 7.11 were created by measuring 'a' and 'b' respectively. This produced a distance scale between the picture and actual measurements as follows:

- X direction - 10:60
- Z direction - 12:100

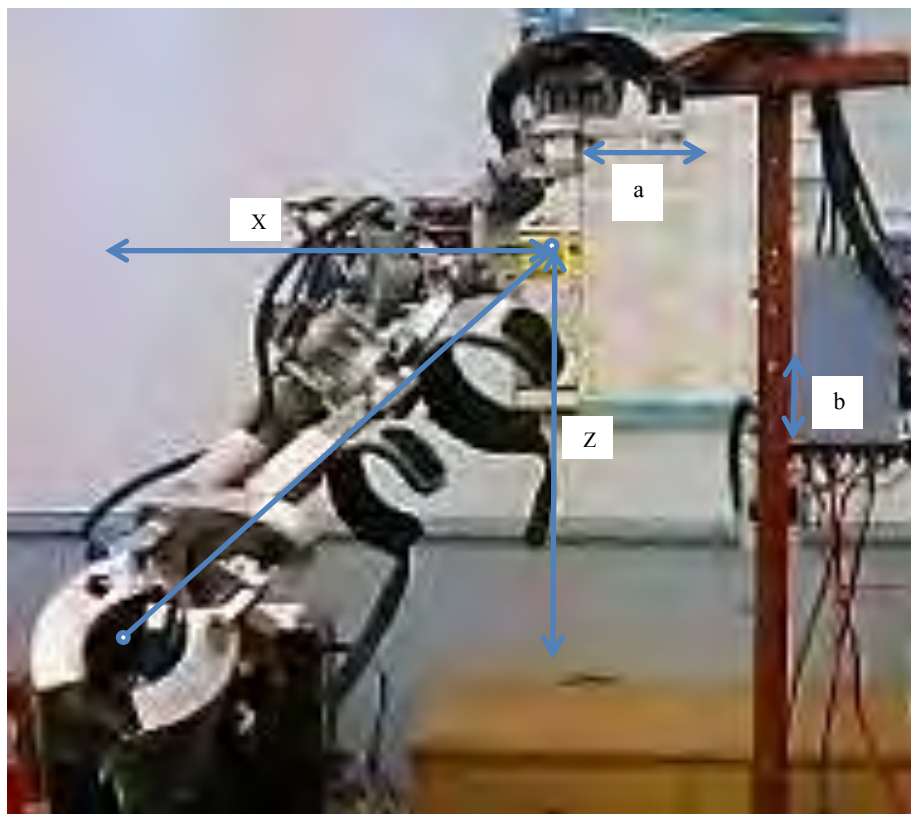


Figure 7.11: X-Z plane of the Exoskeleton.

The X and Z directions was measured in the Figure 7.11 to be 48 mm and -53 mm respectively. This resulted in an actual X and Z position of 288 mm and 441.67 mm. These values were mathematically rounded off to the nearest one hundredth of a millimetre and the mathematical calculations were carried out to minimise the round off error and does not suggest that the vision system is accurate to one hundredth of a millimetre. The Y and Z direction scales in Figure 7.12 were created by measuring 'c' and 'd' respectively. This produced a scale as follows:

- X direction - 07:50
- Z direction - 17:100

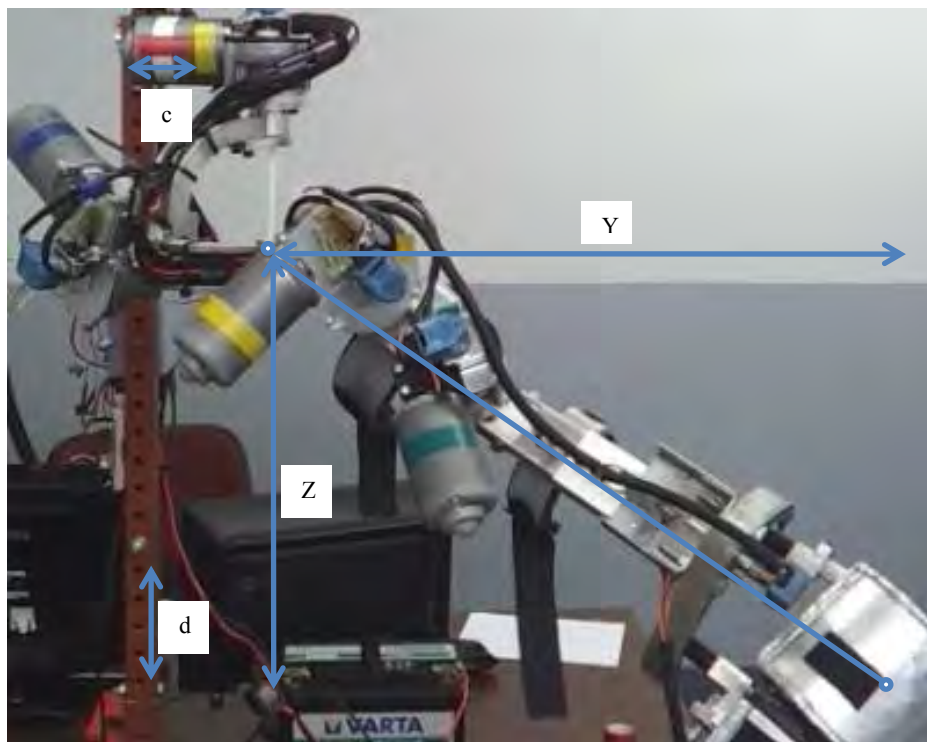


Figure 7.12: Y-Z Plane of the Exoskeleton

The Y and Z directions were measured in the Figure 7.12 to be 87 mm and -61 mm respectively. This resulted in an actual Y and Z position of 621.43 mm and 437.76 mm respectively. It was noticed that the Z values were within 99.1% each other therefore this empirical measurement method is acceptable. These measured values for X, Y and Z were 288mm, 621.43mm and 439.72 (average) respectively. This resulted in an X, Y and Z error 15.3 %, 5% and 13.6% respectively. This produced an average error of 11%.

This error could have been as a result of the encoder resolution as well as the round off error in the GUI model. The calibration of the camera setup may have induced minimal errors in the

calculation with regards to the heights and the distance of the cameras. Mechanical error may have contributed to this error as well. The initial position was set by driving the links to their joint limits then moving the respective joints to their positions which were referenced from the joint limits. This positioning as well as the above described possible errors needs to be investigated in future developments in order to minimise the error.

7.6 Encoder Testing

The encoders were tested for joints 1 to 4. This test was executed by moving the joints a constant 30 degrees several times and the final encoder count was read from CodeVision's terminal. The values are tabulated in Table 7.5.

Table 7.5: Encoder Test Values

Test Number (x_i)	Encoder 1	Encoder 2	Encoder 3	Encoder 4
1	29	30	27	28
2	30	29	30	30
3	30	29	29	30
4	30	30	30	31
5	30	28	30	29
6	29	29	30	29
7	30	30	29	29
8	30	30	31	29
9	30	29	30	30
10	30	30	30	30

A statistical approach was applied in order to decide if any of the above tabulated measurements had to be discarded. The Chauvenet's Criterion was implemented this statistical method produces a probability in which an acceptable scatter of data is defined. The Chauvenet's Criterion was analysed as follows [62]:

- Calculate the mean value, \bar{x} , for all the measurements

- Calculate the standard deviation, σ , according to equation 7.4
- Calculate $d_i = (x_i - \bar{x})$ for each measurement
- Calculate $\frac{|d_i|}{\sigma}$ for each measurement and compare to the Chauvenet's Criterion which was tabulated in Table 7.6.

$$\sigma = \left(\frac{1}{N-1} \sum (x_i - \bar{x})^2 \right)^{0.5} \quad (7.4)$$

Where N is the total number of measurements and was equivalent to 10 in the encoder test. If $\frac{|d_i|}{\sigma}$ was greater than $\frac{d_{max}}{\sigma}$ of 1.96, as shown in Table 7.6, then that measurement could have been considered as 'bad data' and should be rejected.

Table 7.6: Chauvenet's Criterion for Different Number of Measurements [61]

Number of measurements (N)	$\frac{d_{max}}{\sigma}$
2	1.15
3	1.38
4	1.54
5	1.65
6	1.73
7	1.8
10	1.96
15	2.13

A sample calculation was executed in Microsoft Excel for the encoder 4 values this calculation is illustrated in Appendix E.1. The calculation was achieved for all the encoders and none of the measurements tabulated in Table 7.5 were considered as 'bad data'. Therefore all the measurements were taken into consideration.

The encoder values only overshoot twice in forty tests and this was by one degree. The values that undershot the mark were possibly as a result of the settling of the mechanism or inertia. This offset was possible because the controller switches off once the destination was achieved and any change in the angles would result in an encoder change which would not be corrected by the controller. This was implemented as a safety mechanism in order to stop power to the motors once the destination was reached. The values differed by a majority of 1 degree with a maximum value of 3 degrees. A combination of joint errors could have resulted in the positional error illustrated by the empirical test. This encoder error together with the possible errors described in section 7.5 must be investigated in future developments.

7.7 Protocol Adjustments

During testing it was detected that there was signal noise between the FT 232 and the microcontroller. This was as a result of a loose connection between the common grounds of the microcontroller and the FT 232. The signal noise added additional symbols or characters in-between the protocol and this noise produced errors as the buffer size was set to a specific value. It was decided to implement an end character in the protocol for better data analysis. The microcontroller would then check for this end character and whether or not it was in the end position. If the start and end characters were in their respective positions then the microcontroller would assign the joint angles, the speed value and the repeat value. The end character was chosen to be '*'. The adjusted protocol for the example in shown in chapter 6 is illustrated by Figure 7.13. The buffer size was changed to 31.

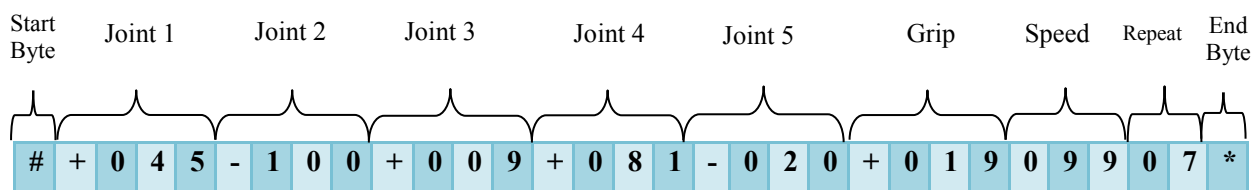


Figure 7.13: Final Protocol Data Packet

7.8 Stand Adjustability and Portability

The stand was adjustable such that it allowed for physiotherapy in the standing up and sitting down position. The workspace testing was executed in the standing position. Figure 7.14 illustrates the exoskeleton at a seated position.



Figure 7.14: Stand Adjustability Allows for Variation in Height.

The exoskeleton manipulator, the electronic components and the wiring was placed in a bag. The exoskeleton, the electronic components, the wiring and the stand were disassembled and transported to a vehicle where it was easily stowed for geographical relocation. The overall weight of the aluminium mechanical structure was 1.927 kg (shoulder and elbow) and including the motors the value totalled to 7.828 kg. With the wiring, hand and wrist mechanism and the arm cuffs added, the total weight did not exceed 9.3 kg, which was below the weight specification.

7.9 Control Revision

The exoskeleton control was illustrated in chapter 6. The step response was accurate however it produced a jerky initial movement. This problem was solved by implementing a ramp input which incremented with every successive loop. The comparison between the ramp and step response was illustrated in Figure 7.15. The ramp response is smoother during the initial motion. This resulted in a PI controller as the derivative term was not required to dampen the response.

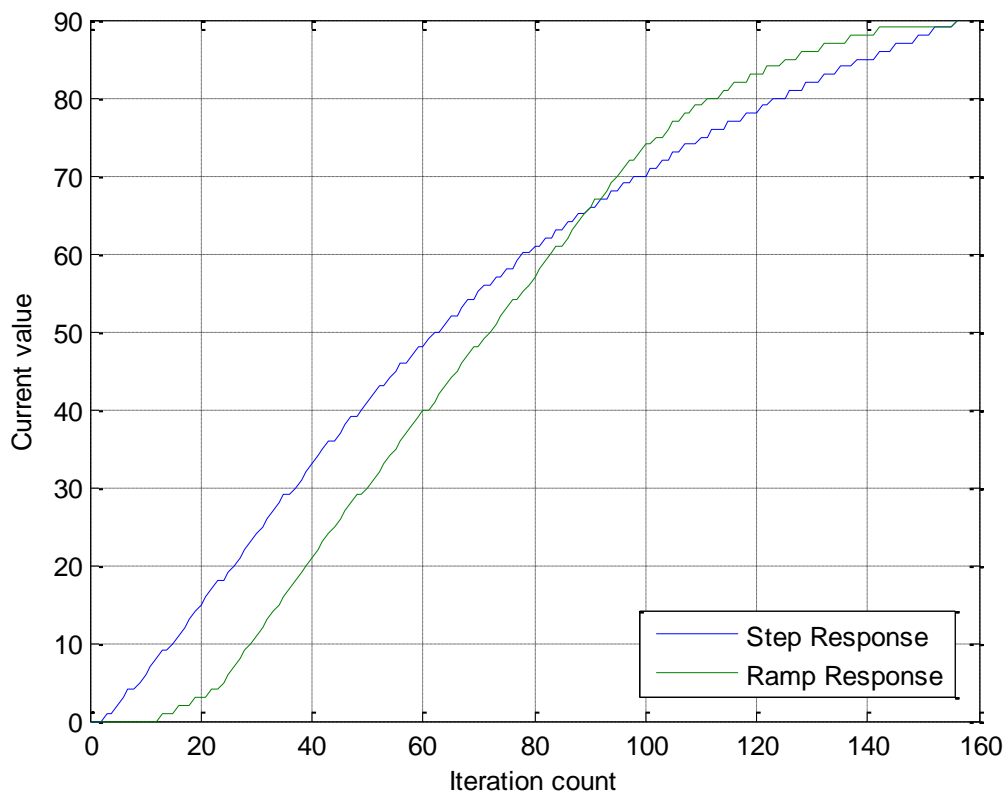


Figure 7.15: Comparison between Experimental Step and Ramp Responses.

7.10 Cost Break Down

A cost break down for the total design of a single exoskeleton arm was illustrated in Table 7.7. A total cost of under ZAR 20 000 was obtain. This cost was significantly low (economically viable) and therefore applicable to a developing country such as South Africa.

Table 7.7: Cost Break Down for the Research

Item #	Item Description	QTY	Manufacturer	Supplier/Distributor	Total Cost (incl. VAT)
1	Aluminium 6082 block (Material)	750x130x40	Hulamin	Euro Steel Natal	R 500.12
2	NSK 6804 ZZ Ball Bearing	8	NSK	BMG	R 747.02
3	DOGA motor 119 - 12Vdc 25rpm 6Nm	2	DOGA	RS Components	R 3 187.17
4	DOGA motor 319 - 12Vdc 45rpm 8Nm	2	DOGA	RS Components	R 5 094.30
5	HEDS 5107 360ppr	4	Avago	RS Components	R 2 393.04
6	Orthotic Materials Miscilaneous	-		Propaedics	R 0.00
7	Aluminium 6082 wrist and hand	400x130x40	Hulamin	Euro Steel Natal	R 350.23
8	Aluminium 6082 rod for couplings	380xÆ22	Hulamin	Euro Steel Natal	R 31.87
9	M6/M8 Bolts assorted +nuts&washers	aprox. 50		SA fasteners	R 44.00
10	40mm 5ø Dowel pins	8		SA fasteners	R 19.00
11	Keyway cutting (machineing process)	2		Gearwise	R 80.00
12	Long M6 bolts for stand			SA fasteners	R 22.00
13	Wiring + 15A fuses&fuse holders	6x4m + 2x1m		A1 Radio	R 90.41
16	Assorted Electronics			A1 Radio	R 377.97
16	Hand and Wrist Electronics	3		Netram	R 800.00
15	Cables, tape etc.			A1 Radio	R 229.66
16	Stand and miscellaneous cost			Various	R 600.00
16	Microcontroller and FT 232's			Netram	R 800.00
16	H bridges	3		Netram	R 1 840.00
16	Aluminium Polish			MIDAS	R 198.00
	TOTAL				R 17 404.78

7.11 Chapter Summary

The workspace of the exoskeleton manipulator was larger than that of the ADL. The shoulder rotation was 3.7% lower than desired however this was acceptable. Load tests on the shoulder and elbow mechanism were conducted. These tests were done for a load of 5 kg without out any noticeable

heating to any of the components. The stall requirements according to the normal operation HIS specifications were satisfied. The wrist mechanism was capable of moving a 2kg direct load without any signs of stalling; this test resulted in a linear relationship between time and mass. This linear relationship was derived for the shoulder and elbow joints as well. The relationship verified the consistency of the system. The gripping function of the hand mechanism was achieved however future designs must focus on a size reduction. The inverse kinematic model was tested and an accuracy of 88.7% was achieved. Encoder counts were statistically analysed and errors were detected. These error could result in the positional error however future investigations need to be executed in order to analyse the positional error. The protocol that was sent to the microcontroller was edited to cater for any noise. The stand allows for physiotherapy to be conducted with the patient either standing or sitting. Pictures illustrating the geographical nature of the design were shown. A ramp PI controller was created as explained in chapter 6, this produced a smoother response. A cost break down illustrated that the cost of the exoskeleton design was under ZAR 20 000 rand this is significantly low and is applicable in South Africa.

8 Exoskeleton Research Conclusion

This research began with the introduction of the problem statement which was applicable in South Africa. The division between rural and urban areas addressed the factor of portability. This factor was implemented in the design process in order to produce a physiotherapeutic exoskeleton that focused on assisting medical professionals in rehabilitating stroke victims. The biological upper limb anatomy was investigated and the DOF and joint limits were analysed in order to develop an anthropomorphic mechanical structure. A number of previous exoskeleton designs were then analysed. The joint motion ranges of these exoskeleton designs were then compared to human and ADL joint ranges. A further tabulation of the exoskeleton positions of motion lead to the design of a complete exoskeleton upper limb. The designs of the MGA, MAHI and ARMin II exoskeletons provided vital information with regards to the mechanical design of this research.

An exoskeleton mechanism was designed to consist of a 5 DOF manipulator with a 2 DOF end-effector. The shoulder and elbow mechanism was of higher priority as these were the mechanisms that affected the positional task space of the mechanism relative to the workspace environment. A spherical motion was required in order to imitate the workspace of the GH joint. A spherical workspace was generally achieved by 3 serial orthogonal mutually intersecting joints. This layout resulted in a singularity in the human workspace. A singularity hindered the motion in this workspace. Movement of a singularity was achieved by the change in joint orientation however this affected the workspace of the mechanism. The MGA exoskeleton research provided two useful inequalities which allowed for the change in joint orientation without compromising the spherical workspace. This resulted in a non-orthogonal joint orientation and the singularity was positioned in a non-achievable location for most human beings. The wrist mechanism was based on the ARMin II and the hand mechanism was purely designed for producing movement which related to the gripping function. The exoskeleton manipulator was designed to be less than 10 kg, portable and adjustable.

Forward kinematics of the mechanism was derived using the D-H notation. This method required the setup of individual joint axes which was required to determine the D-H parameters. These parameters were then used to solve the relative joint transformation matrices which were mathematically computed to produce the forward kinematics. This kinematic model was used to determine the spherical workspace of the design. The change in the non-orthogonal layout resulted in extensive forward kinematics. This complicated the inverse kinematics problem which could not be solved algebraically or geometrically as this problem was further complicated by its 3 dimensional nature. The solution to the inverse kinematics problem was obtained iteratively via the Damped Least Squares method. This iterative solution may prove useful in future developments as it could be

implemented in obstacle avoidance. A redundant and non-redundant kinematic model was created. A joint limitation technique was implemented in both the redundant and non-redundant model. This resulted in the implementation of the Joint Limited Damped Least Squares method in a redundant system. The non-redundant model allowed for a larger workspace and for separate control of the shoulder mechanism. A linear derivation of the inverse kinematics was illustrated through kinematic trajectories. Change in position was plotted against iteration count and it was shown to stabilise as the error approached zero. This change in position was dependent on the initial position. The inverse kinematics model was shown to produce minimal error; this was achieved by sending the inverse kinematic results into the forward kinematic model.

The electronic components were chosen to be compact in order to assist with the portability aspect. The motor drivers were chosen for the relative stall loads, and fuses were placed to protect the components of the system. A 12 V lead acid battery was implemented as the power supply of the system and proved to be successful in terms of geographical portability and power supply. A single microcontroller successfully received information from 5 encoders simultaneously while processing PI motor control. The implementation of a single microcontroller assisted with the portability criteria. The wiring of the controller mechanism was routed through the channels of the exoskeleton but at the same time catered for the mechanism's adjustable nature. The electronic architecture implemented quick 'plug and play' which allowed for easier integration with the software system.

A GUI was created to allow the user to access the kinematic model as well as the control architecture without the prior knowledge of how these systems worked. This allowed the user to input values which were computed via the kinematic models and sent to the microcontroller or they were sent without kinematic computation. The GUI provided a protocol which permitted serial communication between the GUI and microcontroller via the USB interface. The microcontroller then analysed the protocol and assigned the relative joints a value in order to produce the passive therapeutic motion. Two control responses were investigated in order to create this motion. Initially, theoretical gain values for a step PID response were analysed and obtained. These values were then practically implemented to produce an accurate positional response. However, the initial movement was not smooth and did not produce the desired passive therapy motion. A ramp input which incremented every successive loop was applied to a PI controller. This provided an initial smooth and accurate response. The derivative gain was set to zero as the response did not need to be dampened.

A workspace test was achieved by driving the exoskeleton to the limits of each of its joints (limited by mechanical stops). The combined workspace was larger than the workspace of the ADL with the shoulder rotation not achieving 3.7 % of the desired motion in that joint alone. Load tests on the shoulder, elbow and wrist mechanism were carried out. The shoulder and elbow mechanism lifted loads that produced approximately $\frac{1}{4}$ of the HIS without the motors demonstrating any signs of

stalling during normal operation. During the tests none of the fuses were damaged and there was no noticeable heating amongst the components of the design. The load tests on the wrist mechanism produced a linear time and mass relationship. The wrist rotational motion was approximately 6 seconds for a 90 degrees rotation; although this motion was slow it was still be acceptable as it provided passive therapy which would assist with reducing spasticity of the joint. The hand mechanism provided the required gripping motion and propagated the wrist rotation however future developments must consider a more compact design. An empirical measurement was done in order to measure the inverse kinematic model. This measurement yielded an error of 11.3%. This error could be as a result of the encoder resolution, rounding off during the GUI calculations, encoder errors and mechanical manufacturing errors. These errors need to be investigated in future development in order to provide a physiotherapeutic exoskeleton device. The protocol was adjusted to accommodate for noise. The portability aspect of the exoskeleton was illustrated as well as the ability of the support stand to accommodate for standing or sitting physiotherapy. The mass of the exoskeleton manipulator was weighed to be 9.3 kg which was below the specified weight.

The operation of the biological arm and previous exoskeletons were researched. The mechanism was designed and developed such that exoskeleton had similar mechanical properties to those of the biological arm. This research, design and development met the first two research objectives specified in chapter one. The research and development of the kinematic models together with feedback control from the software system satisfied the third research objective. The electronic components were researched and the complete electronic layout was developed. The electronic layout was then integrated with the rest of the system and this achieved the fourth research objective of this paper. The safety specification was achieved through mechanical, electronic and software implementations. The workspace of the mechanism was analysed and achieved a combinational workspace better than that of the ADL. The workspace and load tests resulted in achieving the functionality aspects. The mechanism was adjustable and the stand accommodated for the standing and sitting positions. This met the adjustability specification of the research. The cost was below 2/3 of the ZAR 30 000 budget. This was a substantially low cost design which will enhance applicability in the South African society. These tests and achieved specifications satisfied the final research objective specified in chapter 1. Therefore the research objectives of this dissertation were successfully analysed and achieved.

An exoskeleton prototype was developed to be geographically portable, adjustable, provide a spherical workspace according to the ADL and consist of a complete upper limb. This was further complicated with movement of the singularity which lead to an extensive kinematic model which was solved iteratively and integrated with the software and electronic components.

This prototype provided an acceptable foundation for future rehabilitative developments, by the University of Kwa-Zulu Natal, and therefore was considered to be a successfully researched design.

9 References

- [1] M. Mars, "Telerehabilitation in South Africa- Is there a Way Forward?," *International Journal of Telerehabilitation*, vol. 3, pp. 11-17, 2011.
- [2] S. Panich, "Kinematic Analysis of Exoskeleton Suit for Human Arm," *Journal of Computer Science*, vol. 6, pp. 1272-1275, 2010.
- [3] G. Fazekas, M. Horvath, T. Troznai, and A. Toth, "Robot Mediated Upper Limb Physiotherapy for Patients with Spastic Hemiparesis: A preliminary Study " *Foundation of Rehabilitation Information*, vol. 39, pp. 580-582, 9 March 2007 2007.
- [4] E. Akdogan and M. A. Adli, "The design and control of a therapeutic exercise robot for lower limb rehabilitation:Physiotherobot," *Mechatronics*, vol. 21, pp. 509-522, 12 February 2011.
- [5] W.Bolton, *Mechatronics- electronic control systems in mechanical and electrical engineering*, 4th ed. Essex: Pearson Education Limited, 2008.
- [6] A. Prasetyo. (2008, 20th May). *Mechatronic's Engineering*. Available: <http://ryryf.blogspot.com/>
- [7] J. L. Pons, *Wearable Robots: Biomechatronic Exoskeletons*. Chichester,West Sussex: John Wiley & Sons Ltd., 2008.
- [8] S. Wasserman, L. d. Villiers, and A. Bryer, "Community-based care of stroke patients in a rural African setting," *SAMJ*, vol. 99, pp. 579-583, August 2009.
- [9] S. Afr, "Stroke in the community," *SAMJ*, vol. 99, p. 545, August 2009.
- [10] P. Degaute and P. Bovet, "Stroke Prevention, Treatment, and Rehabilitation in Sub-Saharan Africa," *American Journal of Preventive Medicine*, vol. 29, pp. 95-101, 2005.
- [11] M. Connor and A. Bryer, "Stroke in South Africa," *Chronic Diseases of Lifestyle in South Africa*, pp. 195-203, 2005.
- [12] A. Henderson, N. Korner-Bitensky, and M. Levin, "Virtual Reality in Stroke Rehabilitation: A Systematic Review of its Effectiveness for Upper Limb Motor Recovery.," *Topics in Stroke Rehabilitation*, pp. 52-61, March-April 2007.
- [13] D. K. Sommerfeld, E. U.B, A.-K. Svensson, L. W. Holmqvist, and M. H. v. Arbin, "Spasticity After Stroke Its Occurrence and Association With Motor Impairments and Activity Limitations," *Journal of the American Heart Association*, vol. 35, 18 December 2004.
- [14] S. L. Linn, M. H. Granat, and K. R. Lees, "Prevention of Shoulder Subluxation After Stroke With Electrical Stimulation," *Journal of the American Heart Association*, vol. 30, pp. 963-968, 18 February 1999.
- [15] Editor. (2010, 18 September 2010). Shoulder Subluxation after stroke- exercises and treatment. Available: <http://strokerehabonline.com/tag/shoulder-subluxation/>
- [16] I. Lindgren, A.-C. Jo'nsson, B. Norrving, and A. Lindgren, "Shoulder Pain After Stroke A Prospective Population-Based Study," *Journal of the American Heart Association*, vol. 38, pp. 343-348, 21 December 2006.
- [17] J. Griffin and G. Reddin, "Shoulder pain in patients with hemiplegia," *Physical therapy*, vol. 61, pp. 1041-1045, July 1981.
- [18] C. KISNER and L. A. COLBY, *Therapeutic Exercise foundations and techniques*, 5th ed. Philadelphia: F. A. Davis Company, 2007.
- [19] C. Carignan and M. Liszka, "Design of an Arm Exoskeleton with Scapula Motion for Shoulder Rehabilitation," *IEEE*, pp. 524-531, 2005.
- [20] P. B. a. R. Boulic, "Parametrization and range of motion of the ball-and-socket joint."
- [21] J. P. Loan, "A graphics-based software system to develop and analyze models of musculoskeletal structures.," vol. 25, pp. 21-34, 1995.
- [22] N. Palastanga, D. Field, and R. Soames, *Anatomy and human movement- structure and function*, 4th ed. Edinburgh: Butterworth Heinemann, 2002.

- [23] A. N. Standard, "Human factors engineering –Design of medical devices ", ed. 1110 N. Glebe Road, Suite 220, Arlington: Association for the Advancement of Medical Instrumentation, 2009.
- [24] B. F. Morrey, E. Y. Chao, and F. C. Hui, "Biomechanical Study of the elbow following excision of the radial head," *The Journal of Bone and Joint Surgery*, 1979.
- [25] Y. Tsumaki, et al... "Singularity-consistent inverse kinematics of a 6 D.O.F. manipulator with a non-spherical wrist," presented at the International conference on robotics and automation, Albuquerque, New Mexico, 1997.
- [26] L. Bosio, et al... "An arm exoskeleton system for teleoperation and virtual environments applications," *IEEE*, pp. 1449-1454, 1994.
- [27] V. Hayward, et al... "Haptic interfaces and devices," *Emerald Group Publishing Limited*, vol. 24, pp. 16-29, 2004.
- [28] J.E. Pratt, et al, "The roboknee: an exoskeleton for enhancing strength and endurance during walking," presented at the International Conference on Robotics and Automation, New Orleans, LA, 2004.
- [29] A. Gupta and M. K. O'Malley, "Design of a Haptic Arm Exoskeleton for Training and Rehabilitation," *IEEE*, vol. 11, p. 280, 3 June 2006.
- [30] A. Frisoli and F. Rocchi, "A new force-feedback arm exoskeleton for haptic interaction in Virtual Environments," presented at the Proceedings of the First Joint Eurohaptics Conference and... 2005.
- [31] J. C. Perry and a. J. Rosen, "Design of a 7 Degree of Freedom Upper-Limb Powered Exoskeleton " presented at the BioRob 2006- The first IEEE / RAS-EMBS International Conference on Biomedical Robotics and... Tuscany, Italy, 2006.
- [32] M. Liszka, "Mechanical Design of a Robotic Arm Exoskeleton for Shoulder Rehabilitation," University of Maryland, 2006.
- [33] S. K. Ider, "Singularity robust inverse dynamics of parallel manipulators.," *InTech*, pp. 373-390, April 2008.
- [34] J. J. Craig, *Introduction to Robotics -Mechanics and Control* 3rd ed. Upper Saddle River: Pearson Prentice Hall, 2005.
- [35] A. Gupta and M. K. O'Malley, "Robotic Exoskeletons for Upper Extremity Rehabilitation," *InTech*, pp. 371-396, August 2007.
- [36] M. Mihelj, "ARMin II-7 DoF rehabilitation robot: mechanics and kinematics," presented at the International Conference on Robotics and Automation, Roma, Italy, 2007.
- [37] K. Kiguchi, "Mechanical Designs of Active Upper-Limb Exoskeleton Robots- State-of-the-Art and Design Difficulties," presented at the 11th International Conference on Rehabilitation Robotics, Japan, 2009.
- [38] S. M. Mistry, "An exoskeleton robot for human arm movement study," presented at the International Conference on Intelligent Robots and Systems, 2005.
- [39] D. G. Caldwell, "Development and Control of a 'Soft-Actuated' Exoskeleton for Use in Physiotherapy and Training," *Autonomous Robots*, vol. 15, pp. 21-33, 2003.
- [40] S. Plagenhoef and T. Abdelnour, "Anatomical data for analyzing human motion. Research Quarterly for Exercise and Sport," *Research Quarterly for Exercise and Sport*, vol. 54, 1983.
- [41] J. M. Gere, *Mechanics of Materials*, 6th ed. Belmont: Thomson Learning, 2004.
- [42] H. Extrusions, "Standard Profile Catalogue," ed. Midrand, August 2007.
- [43] N. Tsagarakis, D.G. Caldwell, and G.A. Medrano-Cerda, "A 7 dof pneumatic Muscle Actuator (pMA) powered Exoskeleton," presented at the International Workshop on Robot and Human Interaction, Pisa, Italy, 1999.
- [44] Doga, "Dc Motors with Gears," ed, 2009.
- [45] M. Vidyasaga, *Robot Dynamics and Control*: John Wiley and Sons, 1989.
- [46] O. Egeland, J. R. Sagli, and I. Spangelo, "A Damped Least- Squares Solution to Redundancy Resolution," presented at the International Conference on Robotics and Automation, Sacramento, California, 1991.
- [47] K. T. Ge, "Solving Inverse Kinematics Constraint Problems for Highly Articulated Models," University of Waterloo, Ontario, 2000.

- [48] R. Nilsson, MSc programmes in engineering, Luleå University of Technology, 2009.
- [49] S. R. Buss, "Introduction to Inverse Kinematics with Jacobian Transpose, Pseudoinverse and Damped Least Squares methods," 17 April 2004.
- [50] Y. Nakamura and H. Hanafusa, "Inverse Kinematics Solution with singularity robustness for robot manipulator control," *Journal of Dynamics systems with singularity robustness for robot manipulator control*, vol. 108, pp. 163-171, September 1986.
- [51] M. Na, B. Yang, and P. Jia, "Improved damped least squares solution with joint limits, joint weights and comfortable criteria for controlling human-like figures.," *IEEE*, pp. 1090-1095, 2008.
- [52] J. Padayachee, "Development of a Modular Reconfigurable Machine for Reconfigurable Manufacturing Systems," MSc Engineering, School of Mechanical Engineering, The University of Kwa-Zulu Natal, 2010.
- [53] "USB 2.0 Specification."
- [54] A. Corporation, "ATmega640/1280/1281/2560/2561," ed, 2011.
- [55] ElecHouse, "Freescale 50A Dual-channel H bridge motor drive module."
- [56] P. Control. (2008). *Incremental Encoders*. Available: http://www.pc-control.co.uk/incremental_encoders.htm
- [57] R. Stopforth, G. Bright, S. Davrajh, and A. Walker, "Improved communication between manufacturing robots," *South African Journal of Industrial Engineering*, vol. 22, pp. 99 - 107, 2011.
- [58] F. Haugen, *Basic DYNAMICS and CONTROL*: TechTeach, 2010.
- [59] K. Ogata, *Modern Control Engineering*, 4 ed. New Jersey: Prentice Hall, 2002.
- [60] W. E. Johns. (2003, 02 November). *Notes on Motors*. Available: <http://www.gizmology.net/motors.htm>
- [61] J. Pickle. (2008, 19 March). Measuring Length and Area of objects in Digital Images Using AnalyzingDigital Images Software. Available: <http://umassk12.net/ipy/materials/2008Summer/Pickle/Measurement.pdf>
- [62] P. D. Sherman and L. Lin. (2007, 02 November). *Cleaning Data the Chauvenet Way*. Available: <http://analytics.ncsu.edu/sesug/2007/SA11.pdf>

A. Appendix

Appendix A.1: Shoulder Conceptual 2 Design

A second conceptual design was created; this was created with intentions of only moving the singularity to a more suitable position. The actuator complexity of joint three was not considered as it was the singularity that needed to be analysed in depth. The singularity was moved by designing the first joint to be 45 degrees about *joint axis 2*, below the horizontal. This resulted in the singularity being placed at 135 degrees of flexion, when joint angle two is 180 degrees. The restriction on the flexion movement was tolerable as it was on the borderline of the human workspace but was more than the required workspace for the ADL. In concept two the joints angles were 90° , 90° and 0° for *joint angles 1, 2 and 3* respectively. This satisfied the spherical condition bounded by equation 3.1 and equation 3.2. The second conceptual design is illustrated in Figure A.1.

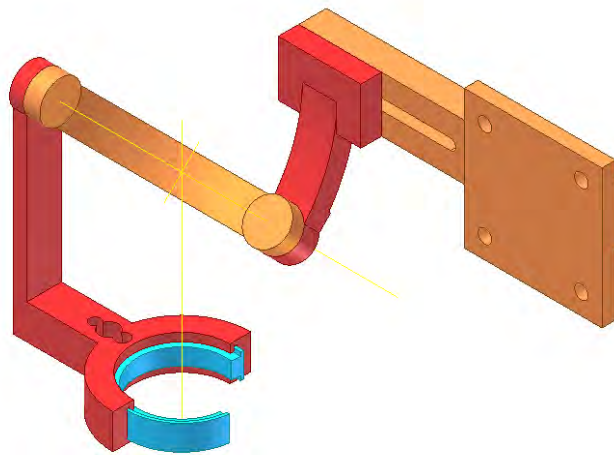


Figure A.1: CAD of Concept Two.

Appendix A.2: Lateral and Medial Rotation and Link 2's Length.

The permissible angle of rotation before collision could be varied by adjusting the angle-length of link 2. Numerous three dimensional CAD of concept three were analysed. In order to determine the optimal link length models with angle-lengths of 45° , 60° and 75° were compared with the original 90° configuration. A smaller angle-length for link two produces a singularity closer to the required workspace until the singularity exists at zero abduction and zero flexion. This is the anatomical position and occurs at an angle length of 45° .

Figure A.2 shows the collision during abduction at 90° . Figure A.3 shows the maximum medial rotation for the different angle length configurations of 45° , 60° , 75° and 90° (left to right respectively). At the maximum medial rotation collision between link two and the back of the wearer's upper arm occurs. It can be seen that further medial rotation, before collision, can be achieved with the larger angles. This is a qualitative comparison between the different configurations and gives an estimate of the maximum angles. However, the precise maximum angles will depend on the wearer's arm dimensions and the final exoskeleton design.

The comparison of the maximum angles of lateral rotation at 90° abduction before collision is shown in figure A.3. The results oppose those for maximum medial rotation. The 90° link has a maximum rotation of 45° above the horizontal whereas the 45° link does not ever come in contact with the back of the upper arm. So there has to be a compromise in link length selection to accommodate both medial and lateral rotation. The various link sizes have approximately 90° of link motion. However, the best choice in terms of a size will be the angle length that permits motion which replicates the human arm. The 60° and 75° angle length links accomplish this and would be suitable. Figure A.2 and Figure A.3 consist of a conceptual elbow design which can be seen by the extra joint, joint four.

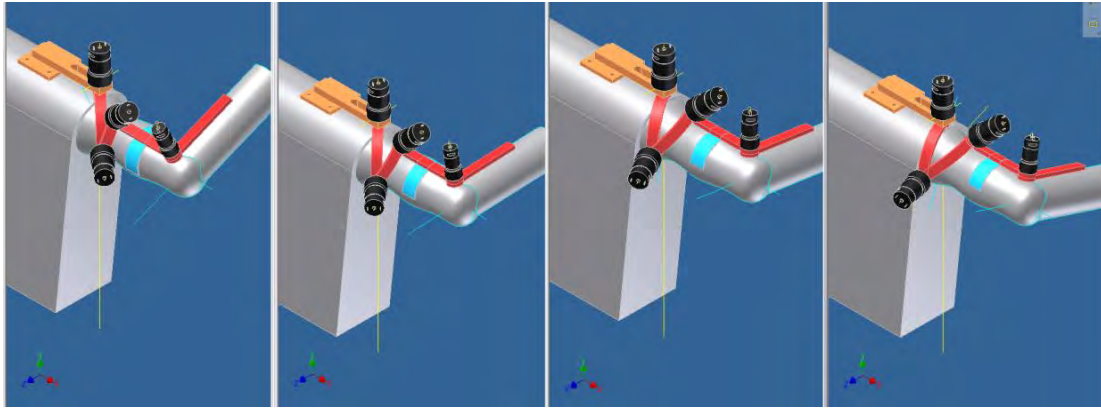


Figure A.2: C.A.D illustrating maximum medial rotation for link 2 angle length = 45° , 60° , 75° , 90° at 90° abduction

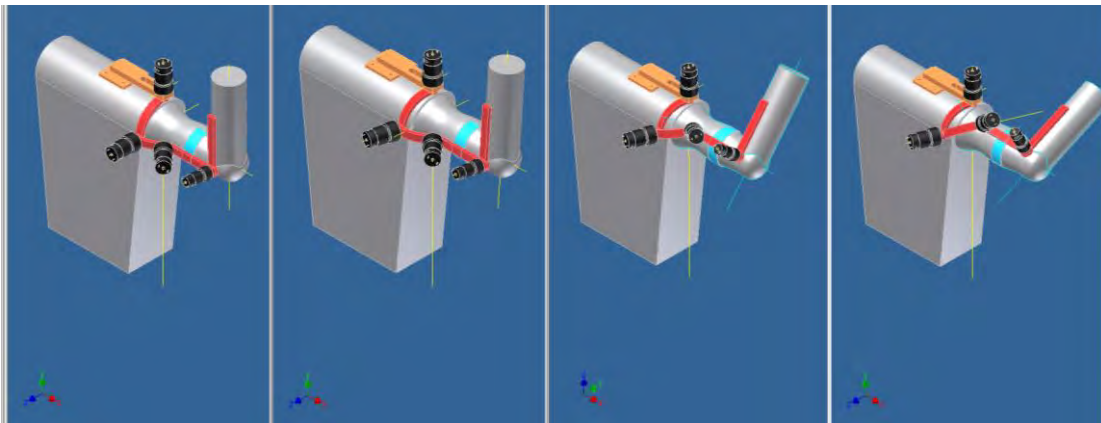


Figure A.3: CAD illustrating maximum lateral rotation for link 2 angle length = 45° , 60° , 75° , 90° at 90° abduction.

Appendix A.3: Torque, Force and Deflection Calculations

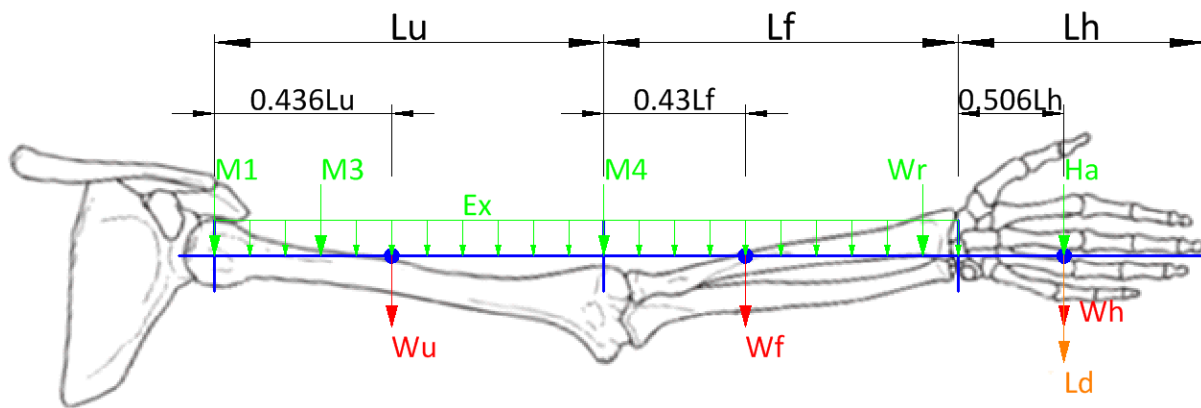


Figure A.4: Simplified Force Diagram of Upper Limb in Worst Case Pose

	a (mm)	b (mm)	P (N)	q (N/mm)	dB (mm)	T1,T2 (Nm)	T3 (Nm)	T4 (Nm)	F1, F2 (N)	F3 (N)	F4 (N)
M1	0	665	16.677	-	0	0			16.677		
M2	0	665	16.677	-	0	0			16.677		
M3	85	580	16.677	-	0.030655	1.417545	0		16.677	16.677	
M4	355	310	12.2625	-	0.337587	4.353188	3.310875	0	12.2625	12.2625	12.2625
Wr	635	30	7.3575	-	0.537431	4.672013	4.046625	2.0601	7.3575	7.3575	7.3575
Ha	768.73	-103.73	7.3575	-	0.710183	5.655931	5.030543	3.044018	7.3575	7.3575	7.3575
Ex	665	0	-	0.004905	0.095828	1.084557	0.825021	0.235685	3.261825	2.8449	1.52055
Wu	154.78	510.22	26.5	-	0.155615	4.10167	1.84917		26.5	26.5	
Wf	488.3	176.7	15.2	-	0.727361	7.42216	6.13016	2.02616	15.2	15.2	15.2
Wh	768.73	-103.73	5.3	-	0.511583	4.074269	3.623769	2.192769	5.3	5.3	5.3
Ld	768.73	-103.73	19.62	-	1.893821	15.08248	13.41478	8.117383	19.62	19.62	19.62
TOTAL					5.000	47.864	38.231	17.676	146.890	113.119	68.618

Figure A.5: Torque and Force Calculation Spreadsheet

In Figure A.5 each row corresponds to one load, represented by a symbol in the first column pointing to the cause of the load, for example M1 is the weight of motor one. The next block of four columns contains the parameters of the load, and the rest of the columns are the results of that load. All the symbols are described in full below:

M1, 2, 3, 4 Motors at each respective joint, motor 1 and 2 were assumed to be positioned at the GH joint

Wr Wrist mechanism

Ha	Hand mechanism
Ex	Exoskeleton framework (UDL)
Wu	Human upper arm
Wf	Human forearm
Wh	Human hand
Ld	Load at end effector
a	The distance to the load from the shoulder joint
b	The distance from the load to the end of the arm, chosen to be the wrist
P	Load value (eg. The weight of the component)
q	UDL value
dB (δ_B)	Deflection at end in the y direction
T1, 2, 3, 4	Torque experienced at each joint (required by each motor)
F1, 2, 3, 4	Force experienced at each joint

Some of the above symbols are used in the equations that follow; they can be taken to have the same meaning as described above, therefore only the terms that have not been described above will be explained after the equations appear. The units used in the equations will also correspond to those used above (N and mm as base units, i.e. N/mm² or MPa for stress).

Deflection

The deflection at the end of the arm, caused by the load of each component is calculated and displayed in the column headed 'dB', Figure A.5. The deflection caused by each component is then simply summed based on the superposition theorem to reach a total deflection at the end, displayed in the 'TOTAL' row of Figure A.5. The end was taken at the wrist because the free human wrist will be able to relocate in the hand mechanism without any obstruction. However, the deflection at the wrist is limited by the deflection which can be catered for in the fitting between the wrist mechanism and the human wrist. This value was agreed not to exceed 5mm. The value for the moment of area was adjusted iteratively until the calculated deflection was 5mm. This value of 18134 mm⁴ then became the aim for the moment of area of the structure cross section.

The equation used to calculate the deflection of a cantilever beam under a UDL applied from the fixed point to a length 'a', is as follows:

$$\delta_B = \frac{qa^3}{24EI} (4L - a)$$

Where: E is the Young's modulus of elasticity (For Aluminium E = 69 GPa)
 I is the moment of area of the 'beam' cross section
 L is the length to the point of deflection (the wrist in this case)

Ex, the exoskeleton framework, was the only UDL, so it shall be used for the sample calculation, the result of which is in the cell where the 'Ex' row coincides with the 'dB' column in Figure A.5:

$$\delta_B = \frac{qa^3}{24EI} (4L - a) = \frac{0.004905 \times 665^3}{24 \times 69000 \times 18134} (4 \times 665 - 665) = 0.0958 \text{ mm}$$

To calculate the deflection of a cantilever beam under the effect of a point load at a length 'a' from the fixed point, the following equation is used [41]:

$$\delta_B = \frac{Pa^2}{6EI} (3L - a)$$

The deflection caused by the weight of the upper arm will be selected for the sample calculation, displayed in the cell where the 'Wu' row coincides with the 'dB' column:

$$\delta_B = \frac{Pa^2}{6EI} (3L - a) = \frac{26.5 \times 154.78^2}{6 \times 69000 \times 18134} (3 \times 665 - 154.78) = 0.1556 \text{ mm}$$

'L' is the distance at which the deflection is measured. In this case the deflection in interest is taken to be at the wrist. The distance from the shoulder to the point at which the load is acting is 'a'. The above calculation, calculates the deflection caused at the wrist, distance 'L' away from the shoulder, by the weight of the upper arm which acts at distance 'a'. The individual deflections are calculated and summed up. 'L' is a fixed value at 665 mm whereas 'a' ranges according to the position of the respective load. L is fixed because the deflection is taken at the wrist which is a distance 665 mm away from the shoulder joint.

Torque

The moment caused by each component at each joint is calculated and displayed in the cells in the columns headed by 'T#' where # represents the joint number. The moment caused by each component can then be simply added using superposition theorem to arrive at a total for the joint. For each component, the equation used was simply the definition of a torque, the force multiplied by the moment arm, in this case:

$$\tau = \frac{P \times a}{1000}$$

The solution is divided by 1000 to convert the units to Nm. For the UDL the centre of mass was simply found and used as the moment arm, and multiplied by the product of the UDL and the UDL length. The sample calculation for the moment produced by the weight of the upper arm on joint 1/2 is shown below:

$$\tau = \frac{P \times a}{1000} = \frac{26.5 \times 154,78}{1000} = 4.102 \text{ Nm}$$

Force

The force caused by each component at each joint is already known, it is the determined weight. For the UDL the q value was multiplied by the UDL length, distal of the joint, to get the weight of the structure on the respective joints. All the force values were then simply added to arrive at a total for each joint.

Appendix A.4: Link Structure

The dimensions of common aluminium C-section were placed in a spreadsheet and the moment of area, in each direction, was calculated. The results are displayed in Table A.1, where the dimensions a, b and T are defined in Figure A.6. 'I major' is the larger moment of area, about the major axis, coincident with the central horizontal axis of the C-section. 'I minor' is the smaller moment of area, about the minor axis, perpendicular to the major axis. A is the cross-sectional area and the last column is the approximate mass per unit length in kg/m. The cells highlighted in red are below the required minimum of 5mm deflection at the wrist, while those in green yield less than 2mm deflection at the wrist.

Table A.1: Moment of Area Calculator – C-section

C-section beam

a	b	T	I major	I minor	A	kg/m
30	10	5	19167	2292	200	0.542
30	15	5	27083	6771	250	0.6775
30	20	5	35000	14375	300	0.813
35	10	5	29219	2656	225	0.60975
35	15	5	40573	7760	275	0.74525
35	20	5	51927	16302	325	0.88075
40	10	5	42083	3021	250	0.6775
40	15	5	57500	8750	300	0.813
40	20	5	72917	18229	350	0.9485

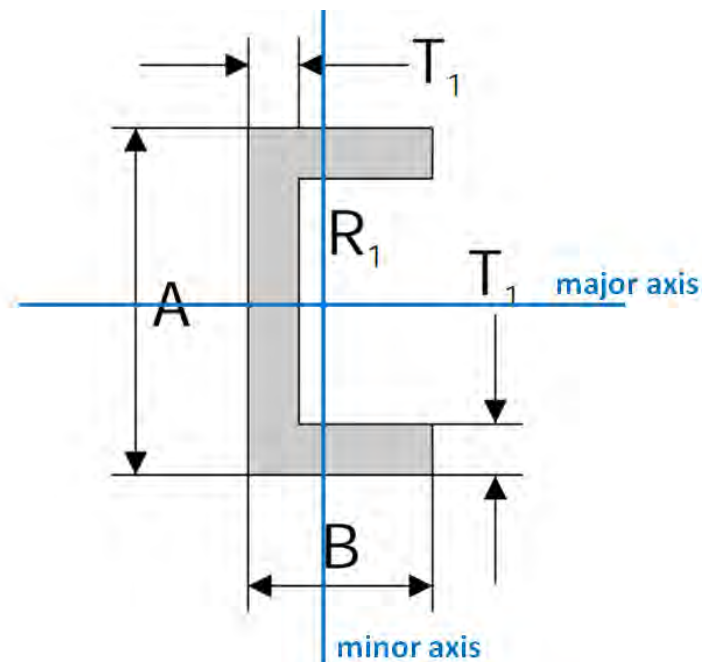


Figure A.6: C-Section Dimensions[42].

The only size that achieves the required maximum deflection in both directions is the 40x20x5 section. The effectiveness of the C-section in increasing the moment of area can be seen if a cross section of solid rectangle with identical area and therefore length density is compared. The values

attained for a solid section of 35x10 are shown in Table A.2. The minor moment of area is significantly less which would be a problem.

Table A.2: Moment of Area Calculator – Solid Section

Solid section						
a	b	T	I major	I minor	A	kg/m
35	10		35729	2917	350	0.9485

The equations used for the moment of area calculations for the C-section are adaptations of the standard rectangular section:

$$I_{rect} = \frac{a^3b}{12}$$

The specific forms of the equations are shown below, together with a sample calculation of the last beam section 40x20x5:

$$I_{major} = \frac{a^3b - (a - 2T)^3(b - T)}{12} = \frac{40^3 \times 20 - (30)^3 \times (15)}{12} = 72917 \text{ mm}^4$$

$$I_{minor} = \frac{ab^3 - (a - 2T)(b - T)^3}{12} = \frac{40 \times 20^3 - (30) \times (15)^3}{12} = 18229 \text{ mm}^4$$

Stress Calculations

The standard formula for bending stress σ_b experienced by a beam with an applied static bending moment of M is :

$$\sigma_b = \frac{My}{I}$$

Where: y is the distance from the neutral axis
I is the moment of area

The higher stress will be found, using the minor moment of area of 18229 mm⁴. The moment used will be the maximum moment experienced at joint 1, calculated in the Torque and Forces Calculation Spreadsheet as approximately 48 Nm. The highest value of y is not readily known, but need not be calculated; it will not exceed 20 mm, therefore 20 mm can be used as an over designed parameter.

$$\sigma_b = \frac{My}{I} < \frac{48 \times 1000 \times 20}{18229} = 52.7 \text{ MPa}$$

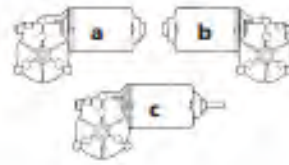
For a low grade of Aluminium alloy, 6061 tempered T4, the 0.2% proof stress is 110 MPa. Therefore the reserve factor is larger than 2, which makes it acceptable.

Appendix A.4 – Doga Motor Catalogues

111



motor with gear motorreductor



Reference code # referencia	Nominal voltage Tensión nominal		Nominal torque Par nominal		Nominal speed Velocidad nominal		Nominal current Corriente nominal		Load capacity Carga máxima		Gear Engranaje	Gear ratio Cambio de engranaje	Insulation Clase de aislamiento	Inertia Momento de inercia	Approximate weight Peso aproximado	Front flange Código de identificación	Material Material	Length Longitud	Code Código
	V (V)	Min (Watt / Nm)	Max (rpm)	Min (A)	Max (Nm / Kg.m)	Min (rpm)	Max (A)												
11.1.371.1.20.00	12	5 / 44.2	40	5	25 / 221.2	25	E22	C25	EE2	62-1	1.25 / 3.34	IP53	PLA	a	1				
11.1.371.1.30.00	24	5 / 44.2	40	2.5	25 / 221.2	13	E22	C25	EE2	62-1	1.25 / 3.34	IP53	PLA	a	1				
11.1.3761.20.00	12	5 / 44.2	40	5	25 / 221.2	25	E23	C25	EE2	62-1	1.25 / 3.34	IP53	PLA	a	1				
11.1.3761.30.00	24	5 / 44.2	40	2.5	25 / 221.2	13	E23	C25	EE2	62-1	1.25 / 3.34	IP53	PLA	a	1				
11.1.3761.20.00E	12	5 / 44.2	40	5	25 / 221.2	25	E23	C25	F2	62-1	1.25 / 3.34	IP53	PLA	a	1				
11.1.3761.30.00E	24	5 / 44.2	40	2.5	25 / 221.2	13	E23	C25	F2	62-1	1.25 / 3.34	IP53	PLA	a	1				
11.1.3763.20.00	12	6 / 53.1	25	4	25 / 221.2	15	E23	C25	EE2	62-1	1.25 / 3.34	IP53	PLA	a	3				
11.1.3763.30.00	24	6 / 53.1	25	2	25 / 221.2	8	E23	C25	EE2	62-1	1.25 / 3.34	IP53	PLA	a	3				
11.1.4761.30.00	24	5 / 44.2	40	2.5	25 / 221.2	13	E23	C25	EE2	62-1	1.25 / 3.34	IP53	PLA	b	1				
11.1.9031.20.00	12	3 / 26.5	70	6	25 / 221.2	34	E23	C25	EE2	62-1	1.25 / 3.34	IP53	PLA	a	2				
11.1.9031.30.00	24	3 / 26.5	70	3	25 / 221.2	17	E23	C25	EE2	62-1	1.25 / 3.34	IP53	PLA	a	2				
11.1.9033.30.00	24	1.5 / 13.2	240	4	14 / 123.9	23	E23	C26	EE1	40-4	1.25 / 3.34	IP53	PLA	a	4				
11.1.9041.30.00	24	5 / 44.2	40	2.5	25 / 221.2	13	E24	C25	EE2	62-1	1.30 / 3.48	IP53	BRD	a	1				
11.1.9094.20.00	12	5 / 44.2	40	5	25 / 221.2	25	E52	C2	EE2	62-1	1.25 / 3.34	IP53	PLA	a	1				
11.1.9107.30.00	24	1.5 / 13.2	240	4	14 / 123.9	23	E24/ES2	C26	EE1	40-4	1.25 / 3.34	IP40	CEL	c	4				
11.1.9114.30.00	24	3 / 26.5	70	3	25 / 221.2	17	E24/ES4	C27	EE2	62-1	1.25 / 3.34	IP40	PLA	c	2				
11.1.9193.30.00	24	3 / 26.5	100	3	20 / 177.01	24	E24	C26	F3	50-2	1.25 / 3.34	IP53	PLA	a	50				

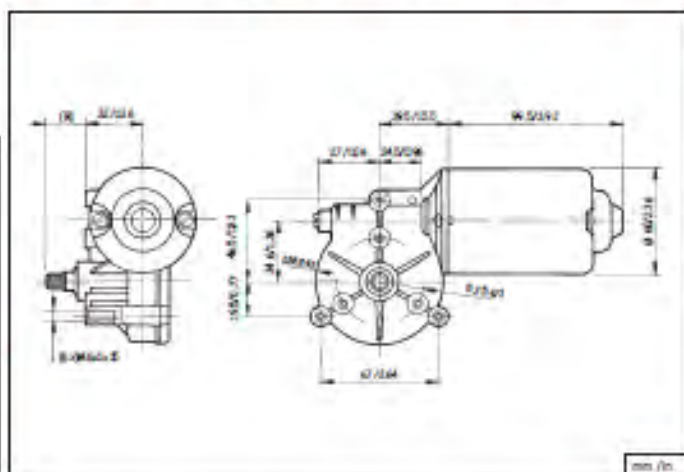
DOGA can develop for you on this series a customized version:
DOGA puede desarrollar para usted una versión a medida.

▼

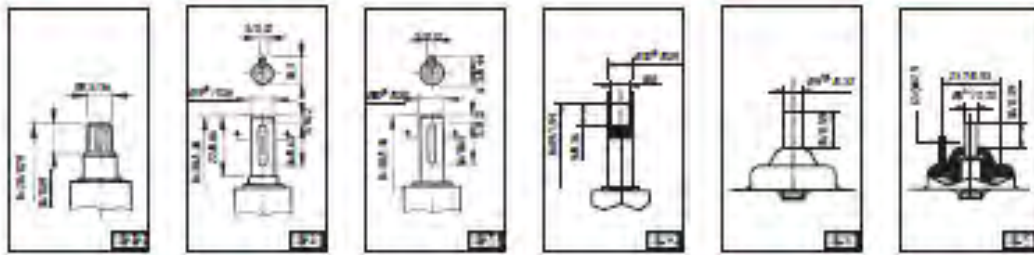
SELF-LOCKING / AUTO-BLOQUEO
BRONZE WHEEL / RUEDA DE BRONCE
RE-SYNCHRONIZED WHEEL / RUEDA DE CELOTEX
FRONT & REAR SHAFT / EJE DELANTERO Y POSTERIOR
HALL SENSING / SENSOR HALL

▲

and many more / y mucho más
 please contact us / por favor contáctenos

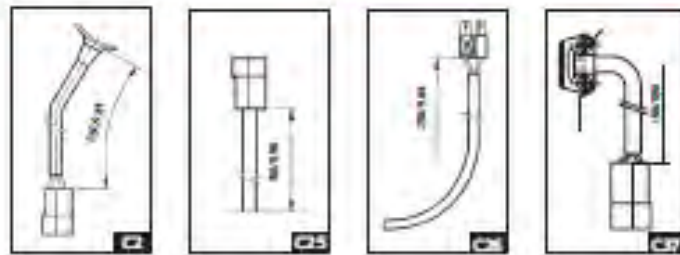


DRAFT - IZB

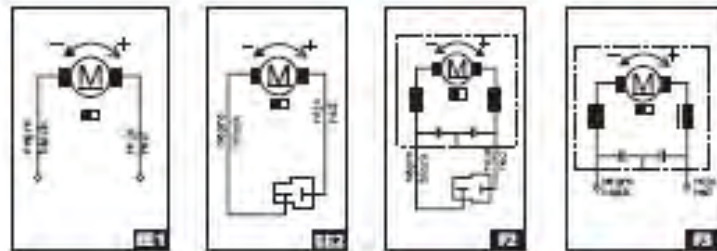


111

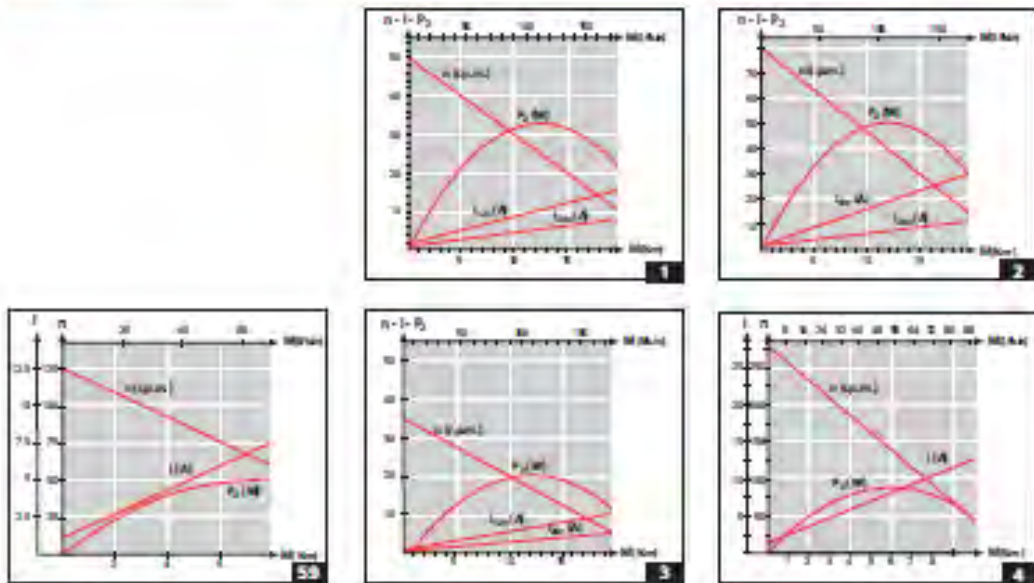
CORRECTION - CORRECTION



WIRING DIAGRAM - SCHEMA ELECTRIC



CURVES - CURVES



Appendix A.5: Wrist Conceptual Designs

The chain and sprocket drive, Concept 1, shown in Figure A.7 is attached to the wrist via the semi-sprocket. The motor drives the pinion sprocket which then drives the semi-sprocket using the chain. Both anti-clockwise and clockwise rotation is possible. The chain ends are fixed to the sprocket teeth using a revolute joint preventing the chain from losing contact with the semi-sprocket.

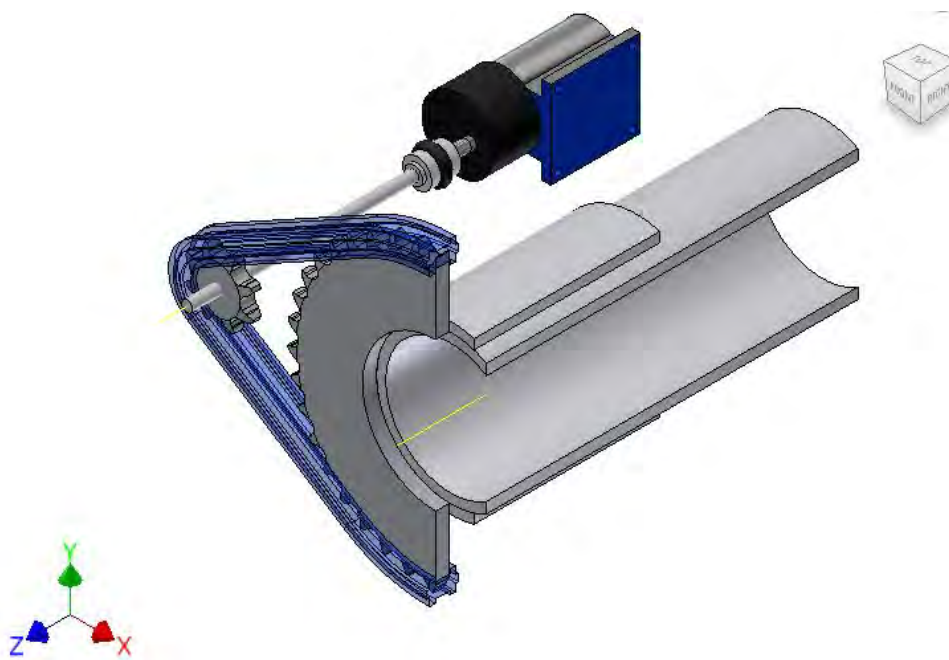


Figure A.7: CAD of the Wrists Mechanism's Concept 1.

The worm and bevel gear system, Concept 2, shown in Figure A.8 uses a worm gear to drive a gear attached to the wrist. A bevel gear system was used to change the axis of rotation so that the motor could be parallel to the forearm. The worm gear provides holding torque, allowing the gear system to be driven only and not be the driver in any unexpected circumstances.

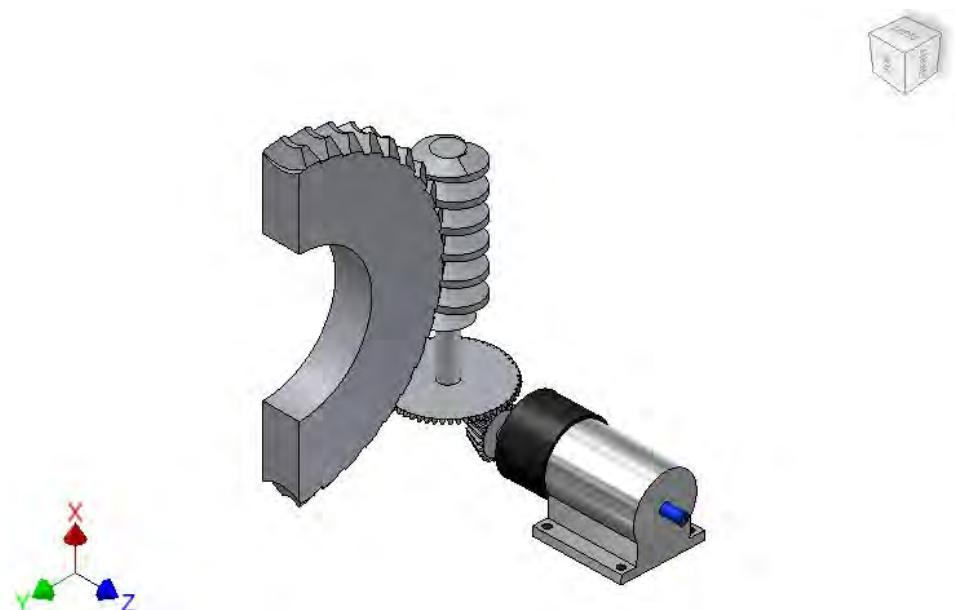


Figure A.8: CAD of the Wrists Mechanism's Concept 2

The spur gear drive system, Concept 3, shown in Figure A.9 has a pair of gears appropriately sized for the application. It is motor driven and can be constrained using a pin and slot configuration and a shaft with a key for the pinion.

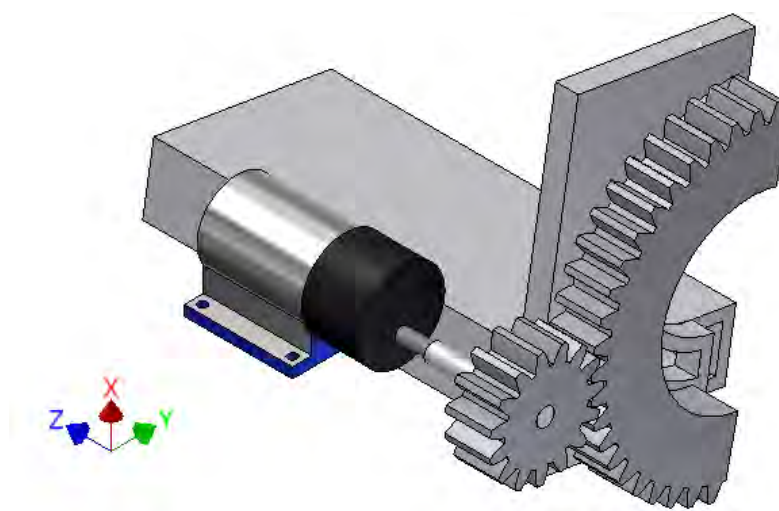


Figure A.9: CAD of the Wrists Mechanism's Concept 3

The three concepts were evaluated against the customer requirements using a selection matrix, shown in Table A.3. Each concept was compared to a reference concept with regards to how well each customer requirement was achieved. A weighted score was then achieved by the product of the rating given and the relative weight of each customer requirement. The weighted score was totalled and ranked by comparing each concepts weighted score. The highest ranked concept was then chosen to be developed.

Table A.3: Concept selection matrix

Selection criteria	Weight	Concept 1		Concept 2		Concept 3	
		Rating	Weighted score	Rating	Weighted score	Rating	Weighted score
Adjustability	8.33	3	0.2499	2	0.1666	3	0.2499
Weight	8.33	3	0.2499	5	0.4165	5	0.4165
Cost	13.9	3	0.417	1	0.139	4	0.556
Size	11.1	3	0.333	5	0.555	4	0.444
Comfort	19.4	3	0.582	5	0.97	5	0.97
maintenance	2.78	3	0.0834	3	0.0834	5	0.139
Aesthetics	0	3	0	4	0	5	0
Safety	22.2	3	0.666	5	1.11	4	0.888
Ability to lift objects	13.9	3	0.417	5	0.695	4	0.556
Total score			2.9982		4.1355		4.2194
Rank			3		2		1
Continue?			No		No		Develop

The process of generating concepts involved considering simplicity as a defining quality with regards to manufacture, kinematics and dynamics, and cost. A balance must be achieved between simplicity and meeting the customer requirements thus the concepts were created with common parts or modifications of common parts that can be found. The main concepts generated were a chain and sprocket drive, Concept 1, a worm and bevel gear drive, Concept 2, and a spur gear drive, Concept 3.

The spur gear drive system, Concept 3, was ranked the highest and hence this design was chosen to be developed. The spur gear drive showed a relatively good capability in accomplishing the customer requirements effectively. The worm and bevel gear system achieved a weighted score very close to that of the spur gear drive, showing that the worm and bevel gear system could be considered for development also.

The reason the worm and bevel gear system was not considered for development or to be merged with the spur gear drive was due to the relative cost of production despite the fact that this system proved to have the best rating concerning safety, the most important customer requirement.

Appendix A.6: C-gear Fatigue and Safety Factor Calculations.

For gear fatigue, the tangential force acting on the gear must be determined first using the torque supplied and the pitch circle diameter of the gear in question. For this case it is the c-gear.

$$Ft = \frac{2Mt}{d}$$

$$Ft = \frac{2 \times 0.59}{0.032}$$

$$Ft = 36.88\text{N}$$

The velocity of the gear was then calculated using the revolutions per minute and the diameter to determine the dynamic factor K_v .

$$v = \frac{\pi dn}{60}$$

$$v = \frac{\pi \times 0.032 \times 23}{60} = 0.0385\text{m/s}$$

$$K_v = \frac{3.05 + v}{3.05}$$

$$K_v = \frac{3.05 + 0.0385}{3.05}$$

$$K_v = 1.013$$

Other factors used were the overload factor, K_o , the load distribution factor, K_m , and the geometry factor J.

$$K_o = 1$$

$$K_m = 1.3$$

$$J_{Pinion} = 0.42$$

$$J_{gear} = 0.46$$

Using the stress equation shown below and the strength value the safety factor was then calculated.

$$\sigma = \frac{Ft}{mbJ} K_v K_o K_m$$

$$\sigma = \frac{36.88}{1 \times 0.01 \times 0.42} \times 1.013 \times 1.3 \times 1$$

$$\sigma = 11563.64 \text{ Pa}$$

$$S_n = 68.9 \text{ MPa @ } 5 \times 10^8 \text{ cycles}$$

$$S_f = \frac{S_n}{\sigma}$$

$$S_f = \frac{68.9 \times 10^6}{11563.64}$$

$$S_f = 5958.33$$

B. Appendix

Appendix B.1: Complex Jacobian Matrix and Positional Vector

The different rows of both the matrix and vector are illustrated in different colours. This matrix and vector are shown only to illustrate their extensive length. Solving these equations algebraically would be complicated and this complexity leads to the successful iterative method (DLS).

Positional Vector

p =

$$\begin{aligned}
 & [L3 * (\sin(\theta(4)) * ((8700286382685973 * \sin(\theta(1)) * \sin(\theta(3)))) / \dots \\
 & 9007199254740992 + (291404338770025 * \cos(\theta(1)) * \sin(\theta(2)) * \sin(\dots \\
 & (\theta(3))) / 1125899906842624 - \cos(\theta(1)) * \cos(\theta(2)) * \cos(\theta(3)) + \dots \\
 & (2^{1/2} * \cos(\theta(4)) * ((8700286382685973 * \cos(\theta(3)) * \sin(\theta(1)))) / \dots \\
 & 9007199254740992 + \cos(\theta(1)) * \cos(\theta(2)) * \sin(\theta(3)) + \dots \\
 & (291404338770025 * \cos(\theta(1)) * \cos(\theta(3)) * \sin(\theta(2))) / \dots \\
 & 1125899906842624) / 2 - \dots \\
 & (2^{1/2} * \cos(\theta(4)) * ((291404338770025 * \sin(\theta(1))) / 1125899906842624 - \dots \\
 & (8700286382685973 * \cos(\theta(1)) * \sin(\theta(2))) / 9007199254740992) / 2) + \dots \\
 & (2^{1/2} * L1 * ((8700286382685973 * \cos(\theta(3)) * \sin(\theta(1))) / \dots \\
 & 9007199254740992 + \cos(\theta(1)) * \cos(\theta(2)) * \sin(\theta(3)) + \dots \\
 & (291404338770025 * \cos(\theta(1)) * \cos(\theta(3)) * \sin(\theta(2))) / \dots \\
 & 1125899906842624) / 2 \dots \\
 & (291404338770025 * 2^{1/2} * L1 * \sin(\theta(1))) / 1125899906842624 \dots \\
 & (2^{1/2} * L1 * ((291404338770025 * \sin(\theta(1))) / 1125899906842624 \dots \\
 & (8700286382685973 * \cos(\theta(1)) * \sin(\theta(2))) / 9007199254740992) / 2 \dots \\
 & (8700286382685973 * 2^{1/2} * L1 * \cos(\theta(1)) * \sin(\theta(2))) / 9007199254740992; \\
 & \dots \\
 & L3 * ((2^{1/2} * \cos(\theta(4)) * (\cos(\theta(2)) * \sin(\theta(1)) * \sin(\theta(3)) \dots \\
 & - (8700286382685973 * \cos(\theta(1)) * \cos(\theta(3))) / 9007199254740992 \dots \\
 & (291404338770025 * \cos(\theta(3)) * \sin(\theta(1)) * \sin(\theta(2))) / \dots \\
 & 1125899906842624) / 2 \dots \\
 & \sin(\theta(4)) * ((8700286382685973 * \cos(\theta(1)) * \sin(\theta(3))) / \dots \\
 & 9007199254740992 \dots \\
 & (291404338770025 * \sin(\theta(1)) * \sin(\theta(2)) * \sin(\theta(3))) / \dots \\
 & 1125899906842624 + \cos(\theta(2)) * \cos(\theta(3)) * \sin(\theta(1)) \dots \\
 & (2^{1/2} * \cos(\theta(4)) * ((291404338770025 * \cos(\theta(1))) / 1125899906842624 \dots \\
 & (8700286382685973 * \sin(\theta(1)) * \sin(\theta(2))) / 9007199254740992) / 2) \dots \\
 & (2^{1/2} * L1 * (\cos(\theta(2)) * \sin(\theta(1)) * \sin(\theta(3)) \dots \\
 & (8700286382685973 * \cos(\theta(1)) * \cos(\theta(3))) / 9007199254740992 \dots \\
 & (291404338770025 * \cos(\theta(3)) * \sin(\theta(1)) * \sin(\theta(2))) / \dots \\
 & 1125899906842624) / 2 \dots \\
 & (291404338770025 * 2^{1/2} * L1 * \cos(\theta(1))) / 1125899906842624 \dots \\
 & (2^{1/2} * L1 * ((291404338770025 * \cos(\theta(1))) / 1125899906842624 \dots
 \end{aligned}$$

$$\frac{(8700286382685973 \sin(\theta(1)) \sin(\theta(2))) / 9007199254740992}{(8700286382685973 \cdot 2^{1/2} \cdot L1 \sin(\theta(1)) \sin(\theta(2))) / 9007199254740992} + \dots$$

$$L3 \cdot (\sin(\theta(4)) \cdot ((291404338770025 \cos(\theta(2)) \sin(\theta(3))) / \dots + \dots \\ 1125899906842624 + \cos(\theta(3)) \sin(\theta(2))) + \dots \\ (2^{1/2} \cos(\theta(4)) \cdot ((291404338770025 \cos(\theta(2)) \cos(\theta(3))) / \dots + \dots \\ 1125899906842624 - \sin(\theta(2)) \sin(\theta(3))) / 2 + \dots \\ (8700286382685973 \cdot 2^{1/2} \cos(\theta(2)) \cos(\theta(4))) / 18014398509481984 + \dots \\ (2^{1/2} \cdot L1 \cdot ((291404338770025 \cos(\theta(2)) \cos(\theta(3))) / \dots + \dots \\ 1125899906842624 - \sin(\theta(2)) \sin(\theta(3))) / 2 + \dots \\ (8700286382685973 \cdot 2^{1/2} \cdot L1 \cos(\theta(2))) / 18014398509481984];$$

Jacobian Matrix

J =

$$\begin{aligned} & [(2^{1/2} \cdot L1 \cdot ((291404338770025 \cos(\theta(1))) / 1125899906842624 + \dots \\ & (8700286382685973 \sin(\theta(1)) \sin(\theta(2))) / 9007199254740992) / 2 - \dots \\ & (2^{1/2} \cdot L1 \cdot (\cos(\theta(2)) \sin(\theta(1)) \sin(\theta(3))) - \dots \\ & (8700286382685973 \cos(\theta(1)) \cos(\theta(3))) / 9007199254740992 + \dots \\ & (291404338770025 \cos(\theta(3)) \sin(\theta(1)) \sin(\theta(2))) / 1125899906842624 \\ & 4) / 2 - (291404338770025 \cdot 2^{1/2} \cdot L1 \cos(\theta(1))) / 1125899906842624 - \dots \\ & L3 \cdot ((2^{1/2} \cos(\theta(4)) \cdot (\cos(\theta(2)) \sin(\theta(1)) \sin(\theta(3))) - \dots \\ & (8700286382685973 \cos(\theta(1)) \cos(\theta(3))) / 9007199254740992 + \dots \\ & (291404338770025 \cos(\theta(3)) \sin(\theta(1)) \sin(\theta(2))) / \dots \\ & 1125899906842624) / 2 - \dots \\ & \sin(\theta(4)) \cdot ((8700286382685973 \cos(\theta(1)) \sin(\theta(3))) / \dots \\ & 9007199254740992 - \dots \\ & (291404338770025 \sin(\theta(1)) \sin(\theta(2)) \sin(\theta(3))) / \dots \\ & 1125899906842624 + \cos(\theta(2)) \cos(\theta(3)) \sin(\theta(1))) + \dots \\ & (2^{1/2} \cos(\theta(4)) \cdot ((291404338770025 \cos(\theta(1))) / 1125899906842624 + \dots \\ & (8700286382685973 \sin(\theta(1)) \sin(\theta(2))) / 9007199254740992) / 2) - \dots \\ & (8700286382685973 \cdot 2^{1/2} \cdot L1 \sin(\theta(1)) \sin(\theta(2))) / 9007199254740992, \\ & \\ & L3 \cdot (\sin(\theta(4)) \cdot ((291404338770025 \cos(\theta(1)) \cos(\theta(2)) \sin(\theta(3)) \\ & (3))) / 1125899906842624 + \cos(\theta(1)) \cos(\theta(3)) \sin(\theta(2))) - \dots \\ & (2^{1/2} \cos(\theta(4)) \cdot (\cos(\theta(1)) \sin(\theta(2)) \sin(\theta(3))) - \dots \\ & (291404338770025 \cos(\theta(1)) \cos(\theta(2)) \cos(\theta(3))) / \dots \\ & 1125899906842624) / 2 + \dots \\ & (8700286382685973 \cdot 2^{1/2} \cos(\theta(1)) \cos(\theta(2)) \cos(\theta(4))) / \dots \\ & 18014398509481984) - \dots \\ & (2^{1/2} \cdot L1 \cdot (\cos(\theta(1)) \sin(\theta(2)) \sin(\theta(3))) - \dots \\ & \dots (291404338770025 \cos(\theta(1)) \cos(\theta(2)) \cos(\theta(3))) / 11258999068426 \\ & 24) / 2 + \dots \\ & (8700286382685973 \cdot 2^{1/2} \cdot L1 \cos(\theta(1)) \cos(\theta(2))) / 1801439850948198, \\ & \\ & L3 \cdot (\sin(\theta(4)) \cdot ((8700286382685973 \cos(\theta(3)) \sin(\theta(1))) / \dots \\ & 9007199254740992 + \cos(\theta(1)) \cos(\theta(2)) \sin(\theta(3))) + \dots \\ & (291404338770025 \cos(\theta(1)) \cos(\theta(3)) \sin(\theta(2))) / \dots \\ & 1125899906842624) - \dots \\ & (2^{1/2} \cos(\theta(4)) \cdot ((8700286382685973 \sin(\theta(1)) \sin(\theta(3))) / \dots \\ & 9007199254740992 + \dots \\ & (291404338770025 \cos(\theta(1)) \sin(\theta(2)) \sin(\theta(3))) / \dots \\ & 1125899906842624 - \cos(\theta(1)) \cos(\theta(2)) \cos(\theta(3))) / 2) - \dots \\ & (2^{1/2} \cdot L1 \cdot ((8700286382685973 \sin(\theta(1)) \sin(\theta(3))) / \dots \end{aligned}$$


```

-...
L3*(cos(theta(4))*(8700286382685973*cos(theta(1))*sin(theta(3)))/...
9007199254740992 -...
(291404338770025*sin(theta(1))*sin(theta(2))*sin(theta(3)))/...
1125899906842624 + cos(theta(2))*cos(theta(3))*sin(theta(1)) +...
(2^(1/2)*sin(theta(4))*(cos(theta(2))*sin(theta(1))*sin(theta(3))
(8700286382685973*cos(theta(1))*cos(theta(3)))/9007199254740992 +...
(291404338770025*cos(theta(3))*sin(theta(1))*sin(theta(2)))/...
1125899906842624)/2 +...
(2^(1/2)*sin(theta(4))*((291404338770025*cos(theta(1)))/1125899906842624 +...
(8700286382685973*sin(theta(1))*sin(theta(2)))/9007199254740992))/2);

```

0,

```

- L3*((2^(1/2)*cos(theta(4))*(cos(theta(2))*sin(theta(3))
(291404338770025*cos(theta(3))*sin(theta(2)))/1125899906842624))/2 +...
sin(theta(4))*(cos(theta(2))*cos(theta(3)) -...
(291404338770025*sin(theta(2))*sin(theta(3)))/1125899906842624 +...
(8700286382685973*2^(1/2)*cos(theta(4))*sin(theta(2)))/18014398509481984) -...
(2^(1/2)*L1*(cos(theta(2))*sin(theta(3)) +...
(291404338770025*cos(theta(3))*sin(theta(2)))/1125899906842624))/2 -...
(8700286382685973*2^(1/2)*L1*sin(theta(2)))/18014398509481984,

```

```

L3*(sin(theta(4))*((291404338770025*cos(theta(2))*cos(theta(3)))/...
1125899906842624 - sin(theta(2))*sin(theta(3)) -...
(2^(1/2)*cos(theta(4))*((291404338770025*cos(theta(2))*sin(theta(3)))/...
1125899906842624 + cos(theta(3))*sin(theta(2)))/2) -...
(2^(1/2)*L1*((291404338770025*cos(theta(2))*sin(theta(3)))/...
1125899906842624 + cos(theta(3))*sin(theta(2)))/2,

```

```

- L3*((2^(1/2)*sin(theta(4))*((291404338770025*cos(theta(2))*cos(theta(3)))/1
125899906842624 - sin(theta(2))*sin(theta(3)))/2 -...
cos(theta(4))*((291404338770025*cos(theta(2))*sin(theta(3)))/...
1125899906842624 + cos(theta(3))*sin(theta(2)))/2) +...
(8700286382685973*2^(1/2)*cos(theta(2))*sin(theta(4)))/18014398509481984];

```

Appendix B.2: Matlab workspace code.

```

% joint angle ranges

a=(-30:20:150);%4
b=(-150:20:-30);7%
c=(0:20:140);%8%135:360
d=(0:10:120);%7
e=0; % does not affect end-effector position.

p=b(end:-1:1);
b=p;

%twist angles

a1=0;
a2=-90;
a3=75;
a4=135;
a5=-90;

%link lengths
l1=0;
l2=0;

l3=0;
l4=0;
l5=0;

%link offsets
d1=0;
d2=0;
d3=-sqrt(2)*280;
d4=-280;%distance from GH joint to elbow joint.
d5=-350;%distance from elbow joint to center of end-effector.

count=0;
traj=zeros(2912,3);%stores position

%looping in range of constraints to produce multiple values.
for i = 1:4

    for j = 1:7

        for k = 1:8

            for l = 1:13

                % transformation matrices
T0l=[cosd(a(i))  -sind(a(i))  0  l1;
sind(a(i))*cosd(a1)  cosd(a(i))*cosd(a1)  -sind(a1)  -  sind(a1)*d1;
sind(a(i))*sind(a1)  cosd(a(i))*sind(a1)  cosd(a1)  cosd(a1)*d1;
0  0  0  1];

```

```

T12=[cosd(b(j))  -sind(b(j))  0  12;
sind(b(j))*cosd(a2)  cosd(b(j))*cosd(a2)  -sind(a2)  -sind(a2)*d2;
sind(b(j))*sind(a2)  cosd(b(j))*sind(a2)  cosd(a2)  cosd(a2)*d2;
0  0  0  1];

T23=[cosd(c(k))  -sind(c(k))  0  13;
sind(c(k))*cosd(a3)  cosd(c(k))*cosd(a3)  -sind(a3)  -sind(a3)*d3;
sind(c(k))*sind(a3)  cosd(c(k))*sind(a3)  cosd(a3)  cosd(a3)*d3;
0  0  0  1];

T34=[cosd(d(1))  -sind(d(1))  0  14;
sind(d(1))*cosd(a4)  cosd(d(1))*cosd(a4)  -sind(a4)  -sind(a4)*d4;
sind(d(1))*sind(a4)  cosd(d(1))*sind(a4)  cosd(a4)  cosd(a4)*d4;
0  0  0  1];

T45=[cosd(e)  -sind(e)  0  15;
sind(e)*cosd(a5)  cosd(e)*cosd(a5)  -sind(a5)  -sind(a5)*d5;
sind(e)*sind(a5)  cosd(e)*sind(a5)  cosd(a5)  cosd(a5)*d5;
0  0  0  1];

    % Forward Kinematics calculation
    T02=T01*T12;
    T03=T02*T23;
    T04=T03*T34;
    R=T04*T45;

    count=count+1;

    C = [R(1,4),R(2,4),R(3,4)];
    traj(count,1)=R(1,4);
    traj(count,2)=R(2,4);
    traj(count,3)=R(3,4);

        end
    end
end
end

plot3(traj(:,1),traj(:,2),traj(:,3),'.');
grid on
axis square

```

Appendix B.3: Calculation of the joint limited damping factor

$$\lambda_i = c \left[\frac{2\vartheta_i - \vartheta_{max} - \vartheta_{min}}{\vartheta_{max} - \vartheta_{min}} \right]^p + \frac{1}{w_i}$$

Given a joint constraint of -30 and +150 degrees for the maximum, ϑ_{max} , and minimum, ϑ_{min} , joint values respectively, this is the limitation of joint 1 of the final design. Three different desired joint values, ϑ_i , will be analysed. These values include -30, 100 and 150 degrees. Equating p to 2 and analysing the term $\left[\frac{2\vartheta_i - \vartheta_{max} - \vartheta_{min}}{\vartheta_{max} - \vartheta_{min}} \right]^p$ the following results were obtained.

$$\text{At } \vartheta_i = -30 \text{ degrees: } \left[\frac{2 \cdot -30 - 150 + 30}{180} \right]^2 = \left[\frac{-180}{180} \right]^2 = 1$$

$$\text{At } \vartheta_i = 100 \text{ degrees: } \left[\frac{200 - 150 + 30}{180} \right]^2 = \left[\frac{80}{180} \right]^2 = 0.2$$

$$\text{At } \vartheta_i = 150 \text{ degrees: } \left[\frac{300 - 150 + 30}{180} \right]^2 = \left[\frac{180}{180} \right]^2 = 1$$

Notice that when the desired joint angle is approaching the joint the joint limit the term goes to the value 1 and is below 1 within the range of the joint limits.

Appendix B.4: Comparison between JLDLS and DLS methods

Table B.1: Comparison of joint limited DLS and original DLS methods.

	X	Y	Z	Joint 1	Joint 2	Joint 3	Joint 4
JLDLS	-90	400	-30	81.97	-27.22	5.89	99.37
DLS				-206.80	-10.83	-204.19	-99.36
JLDLS	100	400	-100	32.85	-34.58	34.26	96.12
DLS				-149.07	-0.10	195.05	96.12
JLDLS	50	300	-397	-15.08	-24.05	78.74	75.46
DLS				-128.67	-264.96	206.18	284.54
JLDLS	100	300	400	21.49	-113.82	9.53	72.45
DLS				-97.51	196.05	339.02	72.45
JLDLS	500	100	200	-29.73	-129.34	54.69	59.63
DLS				-136.11	84.40	76.08	59.63
JLDLS	50	500	172	58.92	-70.17	0.52	65.53
DLS				-57.06	90.94	-24.46	-65.53
JLDLS	10	351	-35	50.16	-28.73	30.74	112.94
DLS				-38.34	48.59	91.97	112.93

Table B.1 illustrates the change in end-effector position from initial position X, Y and Z of 21.1mm, -3.9 mm and -629.6 mm respectively to the final tabulated X, Y and Z position. Joint angles which are not obeyed using the original DLS is printed in red. This is corrected with use of the JLDLS which is in bold print.

C. Appendix

Appendix C.1: Schematics of the ATmega 1280 and Arduino Board.

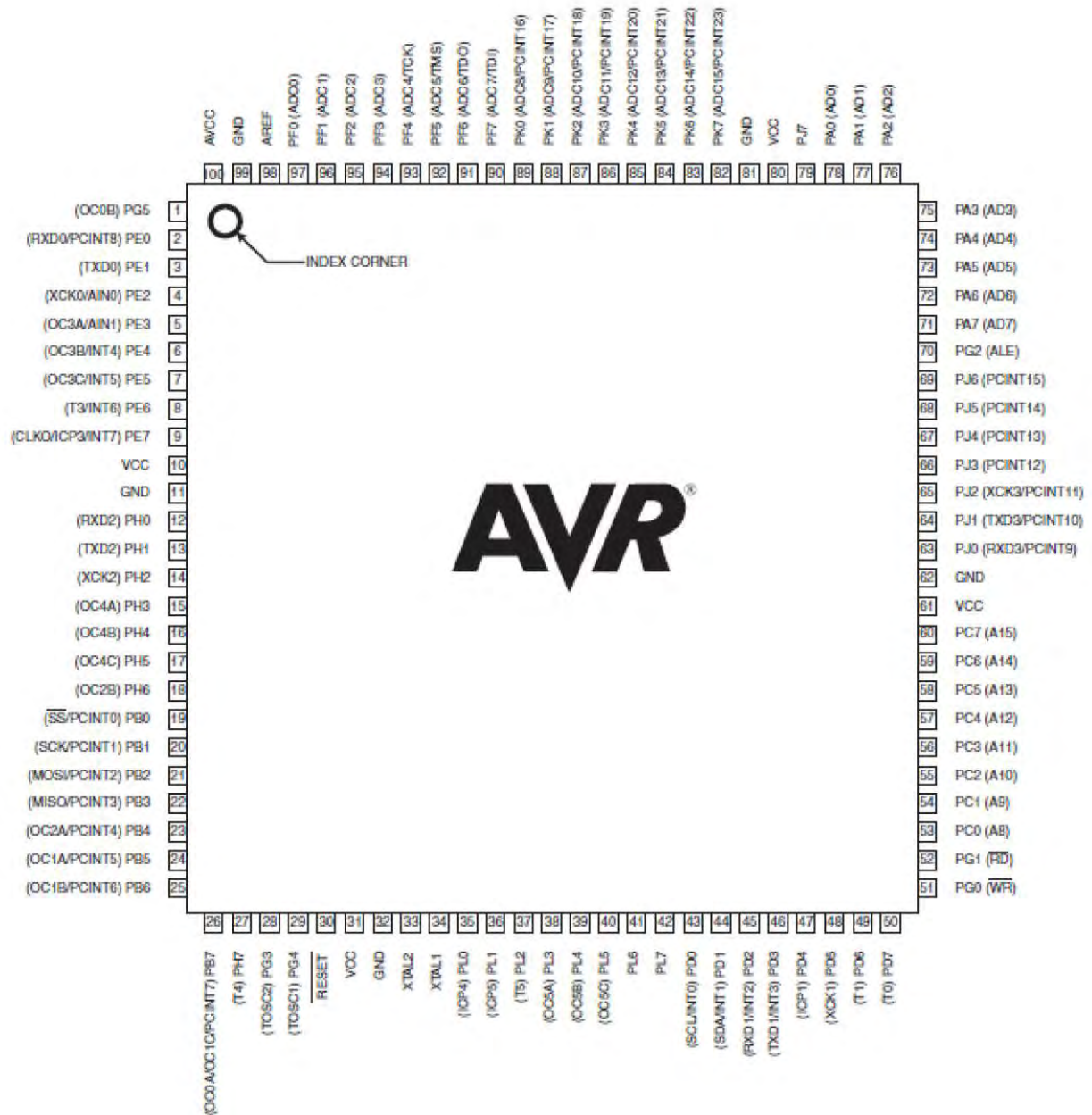


Figure C.1: Schematic of the AtMega1280 microcontroller.

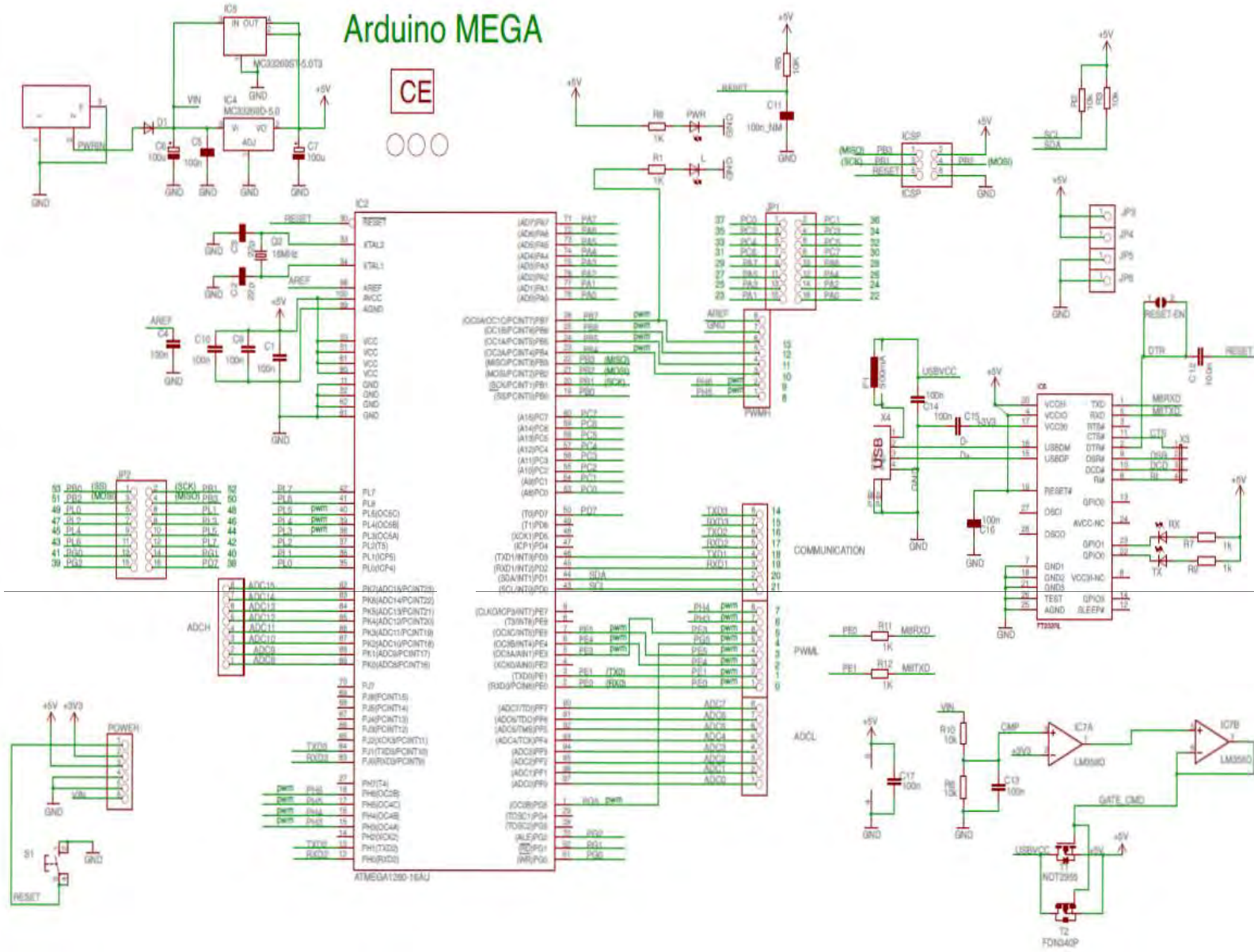


Figure C.2: Schematic relationship between the AtMega1280 microcontroller and the arduino inputs and outputs.

Appendix C.2: H-bridge Information

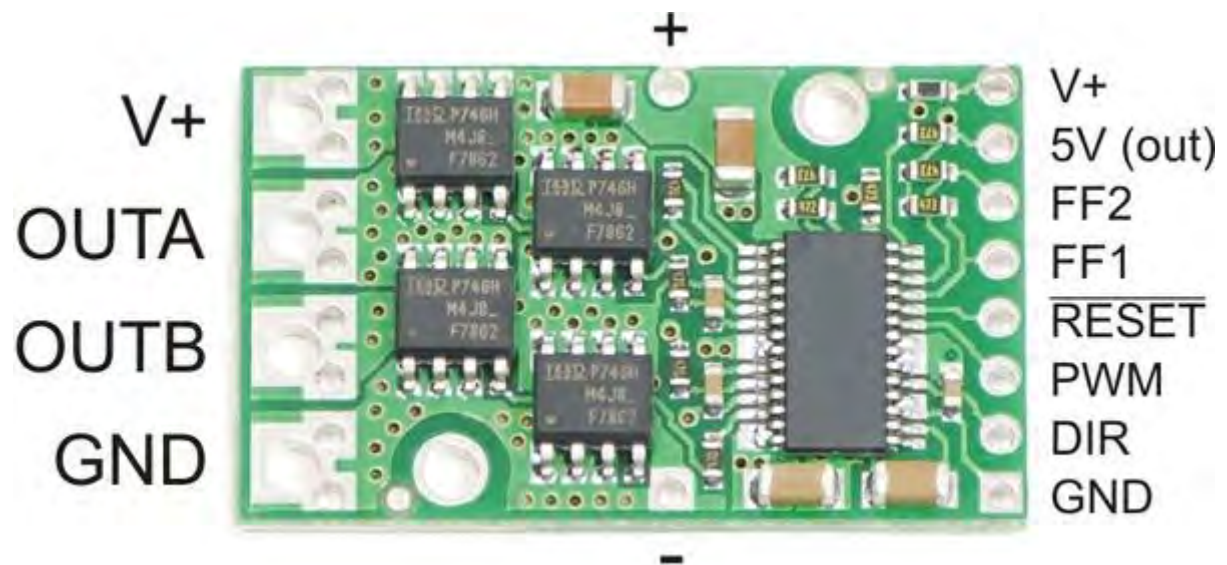


Figure C.3: Pololu H-bridge input and output ports.

Table C.1: Truth table for the Pololu H-bridge

PWM	DIR	OUTA	OUTB	Operation
H	L	L	H	Forward
H	H	H	L	Backward
L	X	L	L	Brake

H and L refers to High and Low respectively.

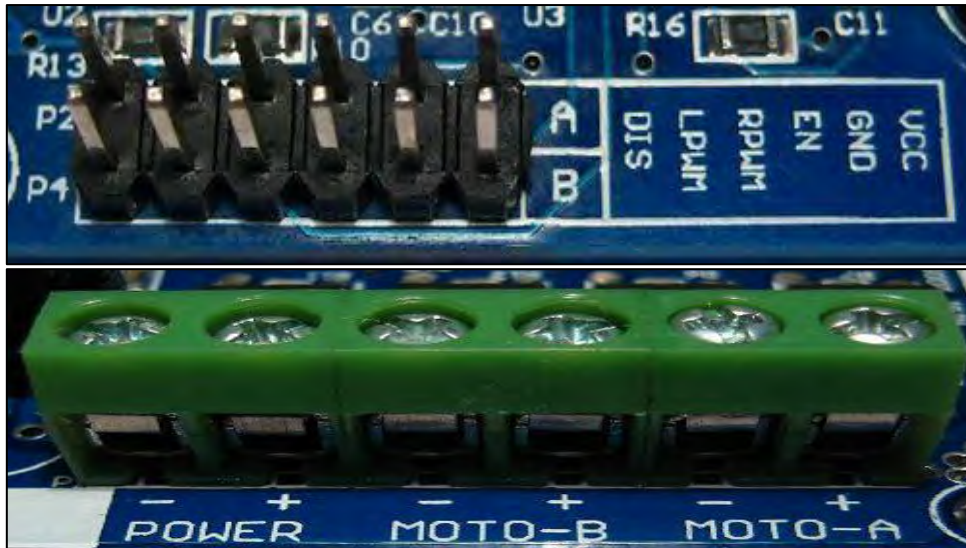


Figure C.4: Dual H-bridge input and output ports.

The Dual H-bridge does not consist of a direction pin instead it is controlled by two PWM pins for each motor.

Table C.2: Truth table for the Dual H-bridge

RPWM	LPWM	Operation
PWM	H	Forward
H	PWM	Backward
H	H	Brake

High represent a 100% duty cycle PWM signal.

Appendix C.3: Schematic of the FT232

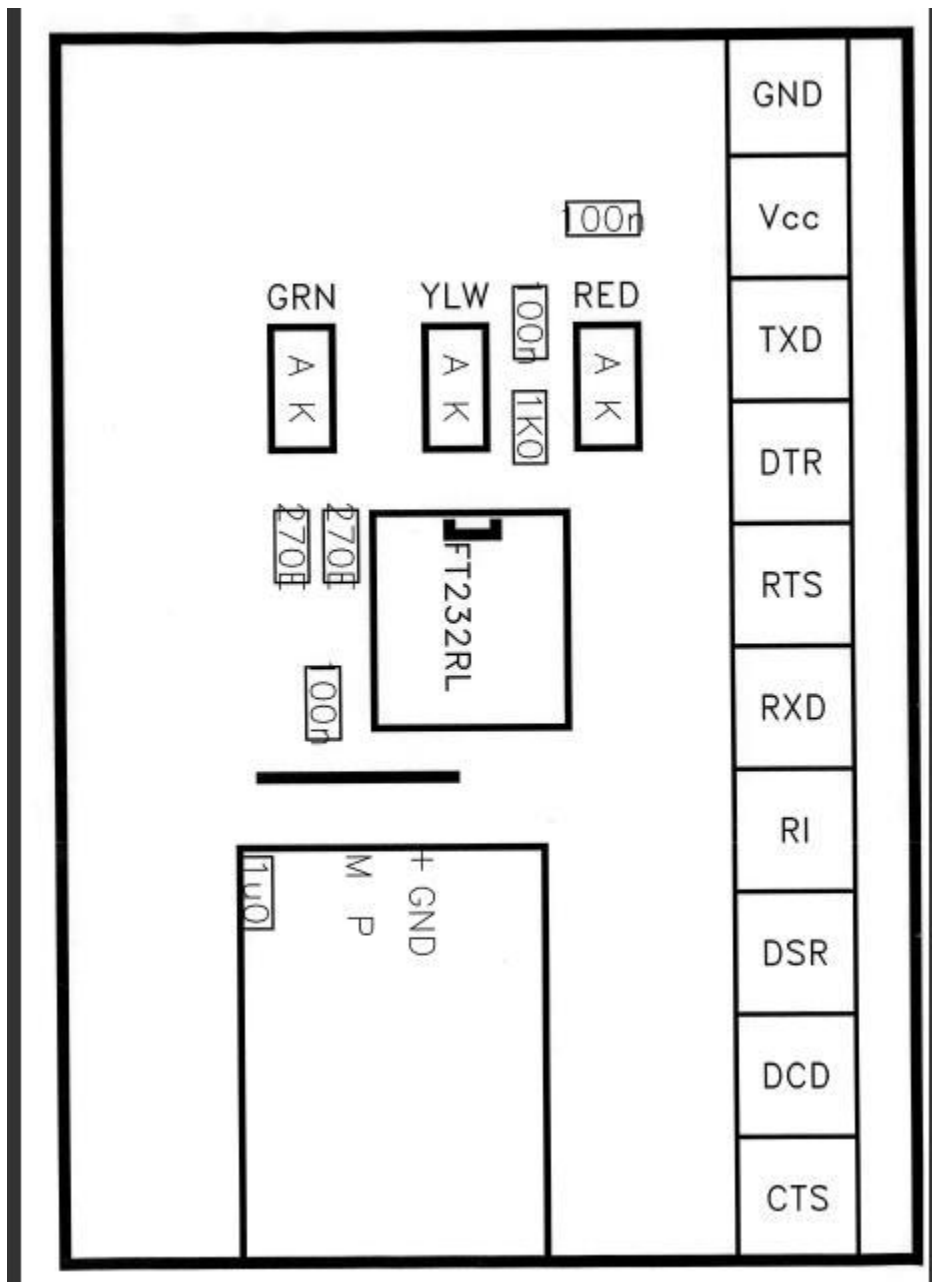


Figure C.5: Schematic diagram of the FT232 PCB.

D. Appendix

Appendix D.1: Sample of the GUI code

```

function calculate_Callback(hObject, eventdata, handles)
% hObject      handle to calculate (see GCBO)
% eventdata    reserved - to be defined in a future version of MATLAB
% handles      structure with handles and user data (see GUIDATA)
a=get(handles.Xt,'String');
b=get(handles.Yt,'String');
c=get(handles.Zt,'String');
a=str2num(a); %GUI X input
b=str2num(b); %GUI Y input
c=str2num(c); %GUI Z input

%Inverse Kinematics

L1=-280; % distance from GH joint to elbow.
L3=-350; % distance from elbow to center of end-effector.
d2r=pi/180;
N=100;
posit=zeros(N,5); % straight line graph to visualize angles (testing
purposes)

theta=[0 -pi/4 5*pi/12 0]'; %initial position.

i1=theta(1);
i2=theta(2);
i3=theta(3);
i4=theta(4);

count1=0;
count2=0;
count3=0;
count4=0;

for i=1:1

    %theta=[0.4 40*d2r 0.2 20*d2r]';

    t=[a; %required target position (X,Y,Z) inputted via GUI
        b;
        c];

    theta=posik(t,L1,L3,theta); %runs theta function
    p=poseik(L1,L3,theta); % calls complicated position variables.

    posit(i,1)=theta(1);
    posit(i,2)=theta(2);
    posit(i,3)=theta(3);
    posit(i,4)=theta(4);
    posit(i,5)=i;
end
figure(2);

```

```

clf;
plot(posit(:,5),posit(:,1),posit(:,5),posit(:,2),posit(:,5),posit(:,3),...
      posit(:,5),posit(:,4));

theta=theta/d2r;          % convert radians to degrees

%converting to change in angle

theta(1)=theta(1)-(i1/d2r);
theta(2)=theta(2)-(i2/d2r);
theta(3)=theta(3)-(i3/d2r);
theta(4)=theta(4)-(i4/d2r);

y = roundoff(theta,0); %roundoff function

n1=num2str(y(1));
n2=num2str(y(2));
n3=num2str(y(3));
n4=num2str(y(4));

% adding a '0' to values that are 2 digits or '00' to 1 digit numbers
% absolute negative numbers are taken and then '0' is added.

if str2num(n1) > 100 || str2num(n1) < -100
    if str2num(n1) < 0
        n1=num2str(abs(str2num(n1)));
        count1=count1+1;
    end
end
if str2num(n1) < 100 && str2num(n1) > -100
    if str2num(n1) < 10 && str2num(n1) > -10
        if str2num(n1)>0
            n1=['0',n1];
        else
            n1=num2str(abs(str2num(n1)));
            n1=['0',n1];
            count1=count1+1;
        end
    end
    if str2num(n1)>0
        n1=['0',n1];
    else
        n1=num2str(abs(str2num(n1)));
        n1=['0',n1];
        count1=count1+1;
    end
end

if str2num(n2) > 100 || str2num(n2) < -100
    if str2num(n2) < 0
        n2=num2str(abs(str2num(n2)));
        count2=count2+1;
    end
end
if str2num(n2) < 100 && str2num(n2) > -100
    if str2num(n2) < 10 && str2num(n2) > -10
        if str2num(n2)>0
            n2=['0',n2];
        end
    end
end

```

```
        else
            n2=num2str(abs(str2num(n2)));
            n2=['0',n2];
            count2=count2+1;
        end
    end
end
if str2num(n2)>0
    n2=['0',n2];
else
    n2=num2str(abs(str2num(n2)));
    n2=['0',n2];
    count2=count2+1;
end
end

if str2num(n3) > 100 || str2num(n3) < -100
    if str2num(n3) < 0
        n3=num2str(abs(str2num(n3)));
        count3=count3+1;
    end
end
if str2num(n3) < 100 && str2num(n3) > -100
    if str2num(n3) < 10 && str2num(n3) > -10
        if str2num(n3)>0
            n3=['0',n3];
        else
            n3=num2str(abs(str2num(n3)));
            n3=['0',n3];
            count3=count3+1;
        end
    end
end
if str2num(n3)>0
    n3=['0',n3];
else
    n3=num2str(abs(str2num(n3)));
    n3=['0',n3];
    count3=count3+1;
end
end

if str2num(n4) > 100 || str2num(n4) < -100
    if str2num(n4) < 0
        n4=num2str(abs(str2num(n4)));
        count4=count4+1;
    end
end
if str2num(n4) < 100 && str2num(n4) > -100
    if str2num(n4) < 10 && str2num(n4) > -10
        if str2num(n4)>0
            n4=['0',n4];
        else
            n4=num2str(abs(str2num(n4)));
            n4=['0',n4];
            count4=count4+1;
        end
    end
end
if str2num(n4)>0
    n4=['0',n4];
```

```
        else
            n4=num2str(abs(str2num(n4)));
            n4=['0',n4];
            count4=count4+1;
        end
    end
end

% adding a '+' to all positive values

if str2num(n1)==0
    n1=['0',n1];
end
if str2num(n2)==0
    n1=['0',n2];
end
if str2num(n3)==0
    n1=['0',n3];
end
if str2num(n4)==0
    n1=['0',n4];
end

if count1 > 0
    n1=['-',n1];
else
    n1=['+',n1];
end

if count2 > 0
    n2=['-',n2];
else
    n2=['+',n2];
end

if count3 > 0
    n3=['-',n3];
else
    n3=['+',n3];
end

if count4 > 0
    n4=['-',n4];
else
    n4=['+',n4];
end

%required protocol.

set(handles.Joint1,'String',n1);
set(handles.Joint2,'String',n2);
set(handles.Joint3,'String',n3);
set(handles.Joint4,'String',n4);
```

Appendix D.2: Protocol Retrieval of the Microcontroller

```
void dir(char* buffer) // Only occurs when interrupt detects a '#'

{
char angle1[4], angle2[4], angle3[4],angle4[4],angle5[4],angle6[4],speed[3],repe[2];
angle1[0]=buffer[1];
angle1[1]=buffer[2];
angle1[2]=buffer[3];
angle1[3]=buffer[4];
ref[1]=atoi(angle1);

angle2[0]=buffer[5];
angle2[1]=buffer[6];
angle2[2]=buffer[7];
angle2[3]=buffer[8];
ref[2]=atoi(angle2);

angle3[0]=buffer[9];
angle3[1]=buffer[10];
angle3[2]=buffer[11];
angle3[3]=buffer[12];
ref[3]=atoi(angle3);

angle4[0]=buffer[13];
angle4[1]=buffer[14];
angle4[2]=buffer[15];
angle4[3]=buffer[16];
ref[4]=atoi(angle4);

angle5[0]=buffer[17];
angle5[1]=buffer[18];
angle5[2]=buffer[19];
angle5[3]=buffer[20];
ref[5]=atoi(angle5);

angle6[0]=buffer[21]; // Grip part of the protocol
angle6[1]=buffer[22];
angle6[2]=buffer[23];
angle6[3]=buffer[24];
ref[6]=atoi(angle6);

speed[0]=buffer[25];
speed[1]=buffer[26];
speed[2]=buffer[27];
strength=atoi(speed);

repe[0]=buffer[28];
repe[1]=buffer[29];
repeat=atoi(repe);
```

```
initialize=1;           //flag to enable the initialize block in code
```

Appendix D.3: C-Code of the Physiotherapy Ramp Control

```
Kp=1.5;
Ki=0.2;
Kd=-20;

current=0;
currentprev=current;
ref=90;
error=ref-current;
errorprev=error;
integralerror=ref;
integralerrorprev=integralerror;
deltaerror=0;

proportional=Kp*error;
integral=Ki*integralerror;
derivative=Kd*deltaerror;

traj=zeros(1,4);%count current ref PWM

count=1;

PWM= proportional + integral + derivative;
if (abs(PWM)>127)
    PWM=127;
else
    PWM= proportional + integral + derivative;
end;

traj(count,1)=count;
traj(count,2)=current;
traj(count,3)=ref;
traj(count,4)=PWM;

while (current~=ref) && (norm(error)>1.0e-1)

    currentprev=current;

    if (abs(PWM)>20)
        PWM2=PWM/90;           %Linear Relationship
        current=currentprev+PWM2;
    else
        PWM2=0;
        current=currentprev+PWM2;
    end;

    errorprev=error;
    error=ref-current
    integralerrorprev=integralerror;
    if (integralerrorprev+error)>100
        integralerror=100;
    else
```

```
        integralerror=integralerrorprev+error;
    end;

    deltaerror=errorprev-error;

    proportional=Kp*error;
    integral=Ki*integralerror;
    derivative=Kd*deltaerror;

    if (abs (PWM)>127)
        PWM=127;
    else
        PWM= proportional + integral + derivative;
    end;

    count=count+1

    traj (count,1)=count;
    traj (count,2)=current;
    traj (count,3)=ref;
    traj (count,4)=PWM;

end

%Used to plot experimental plot against theoretical.

fileName='Testing.xlsx';
a=xlsread(fileName);
x=a(:,1);
y=a(:,2);
clf;
figure(1);

plot(traj(:,1),traj(:,2),x,y);
h = legend('Theoretical response','Experimental response',2);
grid on
xlabel('Iteration count');
ylabel('Current value');
```

Appendix D.4: Sample C-code

```

/* Defining controller gains
#define Kp 1.5
#define Ki 2/10
#define Kd 0

/* Initialize values
collision=0;
for (i=1;i<=5;i++)
{
    prev_error[i]=ref[i]-current[i];           //initialize
    integral_error[i]=0;                       //reset integral sum
};

while (1)
{
    if (initialize==1)                         //Reset values for re-entry of reference angles
    {
        collision=0;
        for (i=1;i<=5;i++)
        {
            ramp[i]=current[i];
            prev_error[i]=1;                   //initialize
            integral_error[i]=0;               //reset integral sum
        };
        windup=strength*2;
        initialize=0;
        timeout=0;
    };
    while ((initialize==0)&&(collision==0)&&(ref[1]!=current[1]||ref[2]!=current[2]||ref[3]!=current[3]||
        ref[4]!=current[4]||ref[5]!=current[5]))
    {
        for (i=1;i<=5;i++)                     //controller block
        {
            if (ramp[i]<ref[i]) ramp[i]++;      //driving ramp response
            if (ramp[i]>ref[i]) ramp[i]--;

            error[i]=ramp[i]-current[i];
            delta_error[i]=prev_error[i]-error[i];
            integral_error[i]=integral_error[i]+error[i];

            if (integral_error[i]>windup) integral_error[i]=windup; //limiting wind-up for each joint
            if (integral_error[i]<=-windup) integral_error[i]=-windup;

            PWM[i]=((error[i]*Kp)+(integral_error[i]*Ki)+(delta_error[i]*Kd));

            if (i==1||i==4||i==5)
            {
                if (PWM[i]>0) dir[i]=1;
                else if (PWM[i]<0)
                {
                    dir[i]=0; // make direction CCW
                    PWM[i] = -PWM[i]; // make PWM positive
                }
            }
        }
    }
}

```

```

    };
    if (PWM[i]>strength) PWM[i]=strength;           //limit comparator to TOP value
    }

    if (i==2||i==3)
    {
        if (PWM[i]>0)
        {
            RPWM[i]=PWM[i];                       //direction and PWM of 50A H-bridge
            LPWM[i]=0;                             //uses 2 PWM channels instead of dir channel
            if (RPWM[i]>strength) RPWM[i]=strength; //limit comparator to TOP value
        }
        else if (PWM[i]<0)
        {
            LPWM[i]=-PWM[i];
            RPWM[i]=0;
            if (LPWM[i]>strength) LPWM[i]=strength; //limit comparator to TOP value
        }
    }
};

    prev_error[i]=error[i];
};
//printf("\n\rPWM4 %d", PWM[4]);
PORTC.1=dir[1];                                 //Assigning H-bridge direction and PWM
OCR0A=PWM[1];
OCR2A=LPWM[2];                                  //Motor 2
OCR2B=RPWM[2];
OCR4AL=LPWM[3];                                 //Motor 3
OCR4BL=RPWM[3];
PORTC.4=dir[4];                                 //Motor 4
OCR0B=PWM[4];
PORTC.5=dir[5];                                 //Motor 5
OCR4CL=PWM[5];

    if (timeout==1)
    {
        printf("\n\rTimeout");
        /* Collision interrupt to check if change has occurred
        /* 'Change[j]' flag for each joint, if the flag of any joint is 0 then 'no change' warning
initialized.
        /* 'Collision' flags even if only one joint is stuck
        for (j=1;j<=5;j++)
        {
            if ((change[j]==0)&&(ref[j]!=current[j]))
            {
                printf("\n\rWarning: collision detected - joint %d", j); //report error if the destination is not
reached
                collision=1;                       // 'No change' flag (only if target not reached)
            }
        }
    };
    /* Collision flag is used to 'exit' while loop
    /* In the case that collision = 0 and ref = current, the loop will exit because ref = current.
    timeout=0; // Reset timeout, to read again when a change is not happening
    change[1]=0; // Reset change values, to register if change is still occurring
    change[2]=0;

```

```
change[3]=0;
change[4]=0;
change[5]=0;
};

OCR0A=0;           //zero the PWM to brake the motors in default code state
OCR0B=0;
OCR2A=0;
OCR2B=0;
OCR4AL=0;
OCR4BL=0;
OCR4CL=0;
};
}
```

Appendix D.5: Arduino Board and Pin Layout



Figure D.1: Arduino Mega 1280 Board.

Table D.1: Pin Layout for this Research Exoskeleton Design

ATMega 1280		Arduino Board Pin		Device
Port	Usage	Number	Description	
PE 0	USART0 RX	0	PWM	Computer receiver
PE 1	USART0 TX	1	PWM	Computer transmitter
PB 7	T0A PWM	13	PWM	Motor 1 PWM
PB 4	T2A PWM	10	PWM	Motor 2 LPWM
PH 6	T2B PWM	9	PWM	Motor 2 RPWM
PH 3	T4A PWM	6	PWM	Motor 3 LPWM
PH 4	T4B PWM	7	PWM	Motor 3 RPWM
PG 5	T0B PWM	4	PWM	Motor 4 PWM
PH 5	T4C PWM	8	PWM	Motor 5 PWM
PE 3	T3A PWM	5	PWM	Servo control
PE 5	T3C PWM	3	PWM	Servo control
PC 1	Digital out	36	Digital	Motor 1 direction
PC 4	Digital out	33	Digital	Motor 4 direction
PC 5	Digital out	32	Digital	Motor 5 direction
PD1	Ext Int 1	20	Digital	Encoder 1 channel A
PD2	Ext Int 2	19	Digital	Encoder 2 channel A
PD3	Ext Int 3	18	Digital	Encoder 3 channel A
PE4	Ext Int 4	2	PWM	Encoder 4 channel A
PD0	Ext Int 0	21	PWM	Encoder 5 channel A
PA 1	Digital in	23	Digital	Encoder 1 channel B
PA 2	Digital in	24	Digital	Encoder 2 channel B
PA 3	Digital in	25	Digital	Encoder 3 channel B
PA 4	Digital in	26	Digital	Encoder 4 channel B
PA 5	Digital in	27	Digital	Encoder 5 channel B

E. Appendix

Appendix E.1: Chauvenet's Criterion Sample Calculation for Encoder 4 Test.

Table E.1: Chauvenet's Criterion Test for Encoder 4.

x_i	28	30	30	31	29	29	29	29	30	30
$x_i - \bar{x}$	-1.5	0.5	0.5	1.5	-0.5	-0.5	-0.5	-0.5	0.5	0.5
$(x_i - \bar{x})^2$	2.25	0.25	0.25	2.25	0.25	0.25	0.25	0.25	0.25	0.25
$\frac{ d_i }{\sigma}$	0.692	0.231	0.231	0.692	0.231	0.231	0.231	0.231	0.231	0.231

The standard deviation and mean values were derived for encoder 4 as follows:

- $\sigma = \left(\frac{1}{N-1} \sum (x_i - \bar{x})^2 \right)^{0.5} = 2.166666667$
- $\bar{x} = 29.5$

The maximum $\frac{|d_i|}{\sigma}$ produced was 0.692 which was lower than the Chauvenet's Criterion of 1.96 therefore all the above encoder measurements were valid.